<1055>

MARTIN MARIETTA ENERGY SYSTEMS LIBRARIES

3 4456 0285925 3

CENTRAL RESEARCH LIBRARY
DOCUMENT COLLECTION

1

ORNL-4390
UC-25 – Metals, Ceramics, and Materials

FUELS AND MATERIALS DEVELOPMENT PROGRAM

QUARTERLY PROGRESS REPORT FOR PERIOD

ENDING DECEMBER 31, 1968

OAK RIDGE NATIONAL LABORATORY
operated by
UNION CARBIDE CORPORATION
for the
U.S. ATOMIC ENERGY COMMISSION

OAK RIDGE NATIONAL LABORATORY
CENTRAL RESEARCH LIBRARY
DOCUMENT COLLECTION
LIBRARY LOAN COPY
DO NOT TRANSFER TO ANOTHER PERSON
If you wish someone else to see this document, send in name with document and the library will arrange a loan.
UCN-7969
(3 3-67)

Printed in the United States of America. Available from Clearinghouse for Federal Scientific and Technical Information, National Bureau of Standards, U.S. Department of Commerce, Springfield, Virginia 22151
Price: Printed Copy $3.00; Microfiche $0.65

LEGAL NOTICE

This report was prepared as an account of Government sponsored work. Neither the United States, nor the Commission, nor any person acting on behalf of the Commission:

A. Makes any warranty or representation, expressed or implied, with respect to the accuracy, completeness, or usefulness of the information contained in this report, or that the use of any information, apparatus, method, or process disclosed in this report may not infringe privately owned rights; or

B. Assumes any liabilities with respect to the use of, or for damages resulting from the use of any information, apparatus, method, or process disclosed in this report.

As used in the above, "person acting on behalf of the Commission" includes any employee or contractor of the Commission, or employee of such contractor, to the extent that such employee or contractor of the Commission, or employee of such contractor prepares, disseminates, or provides access to, any information pursuant to his employment or contract with the Commission, or his employment with such contractor.

ORNL-4390

Contract No. W-7405-eng-26

METALS AND CERAMICS DIVISION

FUELS AND MATERIALS DEVELOPMENT PROGRAM QUARTERLY PROGRESS REPORT FOR PERIOD ENDING DECEMBER 31, 1968

Compiled by

P. Patriarca

Edited by

D. J. Rucker

MAY 1969

MARTIN MARIETTA ENERGY SYSTEMS LIBRARIES

3 4456 0285925 3

OAK RIDGE NATIONAL LABORATORY
Oak Ridge, Tennessee
operated by
UNION CARBIDE CORPORATION
for the
U.S. ATOMIC ENERGY COMMISSION

FOREWORD

This quarterly progress report describes research and development on nuclear fuels and materials performed at the Oak Ridge National Laboratory for the U.S. Atomic Energy Commission. With several exceptions, as noted below in the listing of specific programs, the work is sponsored by the Fuels and Materials Branch of the Division of Reactor Development and Technology. Classified aspects of the Nitride Fuels Development activity and work on fuels and materials for isotopic heat sources are reported separately.

The report is presented in five parts according to AEC Activity titles provided by the Fuels and Materials Branch, RDT.

Program Title	ORNL Division(s)	Person in Charge	Principal Investigator(s)
	I. Fuels and Claddings		
Development of Fast Reactor Oxide Fuels	Metals and Ceramics Chemical Technology Reactor	P. Patriarca	A. L. Lotts J. L. Scott R. E. Brooksbank
Development of High Performance LMFBR Fuels	Metals and Ceramics Reactor	P. Patriarca	J. L. Scott H. C. McCurdy A. L. Lotts
Fission-Gas Release and Physical Properties of Fuel Materials During Irradiation	Reactor Chemistry	O. Sisman	R. M. Carroll J. G. Morgan
Zirconium Metallurgy	Metals and Ceramics	J. R. Weir, Jr.	P. L. Rittenhouse
	II. Coolants		
Alkali-Metal Corrosion Studies	Metals and Ceramics Reactor	W. O. Harms	J. H. DeVan A. P. Litman

Program Title	ORNL Division(s)	Person in Charge	Principal Investigator(s)
III. Radiation Damage to Structural Materials			
Behavior of Refractory Materials Under Irradiation	Reactor Chemistry	G. M. Watson	G. W. Keilholtz
Fast-Neutron Irradiation Effects on Electrical Insulators*	Reactor Chemistry	G. M. Watson	G. W. Keilholtz
Mechanical Properties Research and LMFBR Cladding and Structural Materials Development**	Metals and Ceramics	J. R. Weir, Jr.	H. E. McCoy, Jr.
Radiation Effects in Alloys and Structural Materials	Solid State	D. S. Billington	M. S. Wechsler
IV. Techniques of Fabrication and Testing			
Tungsten Metallurgy	Metals and Ceramics	P. Patriarca	H. Inouye W. R. Martin G. M. Slaughter J. O. Stiegler H. E. McCoy, Jr.
Nondestructive Test Development	Metals and Ceramics	W. O. Harms	R. W. McClung
Joining Research on Nuclear Materials**	Metals and Ceramics	G. M. Adamson, Jr.	G. M. Slaughter

*Sponsored by Reactor Power Systems Branch, Division of Space Nuclear Systems.

**Partially sponsored by Liquid Metals Branch, Division of Reactor Development and Technology.

Program Title	ORNL Division(s)	Person in Charge	Principal Investigator(s)
Development of LMFBR Tubing Fabrication*	Metals and Ceramics	G. M. Adamson, Jr.	W. R. Martin
Development of Fuel Element Fabrication	Metals and Ceramics	G. M. Adamson, Jr.	J. V. Cathcart W. R. Martin R. W. McClung
V. Engineering Properties of Reactor Materials			
Physical and Mechanical Metallurgy of Refractory Alloys	Metals and Ceramics	P. Patriarca	H. Inouye R. W. McClung D. L. McElroy G. M. Slaughter H. E. McCoy, Jr.
Cladding Materials for Space Isotopic Heat Sources**	Metals and Ceramics	P. Patriarca	R. G. Donnelly H. Inouye

*Sponsored by Liquid Metals Branch, Division of Reactor Development and Technology.

**Sponsored by Reactor Power Systems Branch, Division of Space Nuclear Systems.

CONTENTS

Page

Summary xv

Part I. Fuels and Claddings

1. Development of Fast-Reactor Oxide Fuels 3
   - Preparation of $(U,Pu)O_2$ Fuels 4
   - Development of Fabrication Processes 4
     - Sphere-Pac 5
     - Pelletizing of Sol-Gel $(U,Pu)O_2$ 5
     - Capsule Fabrication 7
     - Sodium Filling System 13
   - Characterization of Sol-Gel $(U,Pu)O_2$ Fuels 17
     - Analytical Chemistry 17
     - Control of Oxygen-to-Metal Ratio of $UO_{2.00 \pm x}$ 19
     - Oxygen and Plutonium Redistribution in $(U,Pu)O_2$ in a Temperature Gradient 20
     - Calculation of the Thermodynamic Properties of the Pu-O System 21
     - Deformation of UO_2 22
   - Irradiation Testing of $(U,Pu)O_2$ Fuels 22
     - Uninstrumented Thermal-Flux Irradiation Tests . . . 23
     - ORR Instrumented Tests 25
     - Transient Testing of Sol-Gel $(U,Pu)O_2$ Fuels 27
     - Fast-Flux Irradiation Tests 28
     - Irradiation Test Calculations 29
2. Development of High-Performance LMFBR Fuels 34
   - Synthesis, Fabrication, and Characterization of Nitride Fuels 35
     - Synthesis and Fabrication of UN 35
     - Preparation of UN Pellets Containing ^{15}N 36
     - Synthesis, Fabrication, and Characterization of Mixed Nitrides 38
     - Characterization of UN and (U,Pu)N 40

Synthesis, Fabrication, and Thermodynamic Properties of Carbonitride Fuels 42

Manufacture of UC, UN, and U(C,N) from UO_2 42

Thermodynamic Investigations of High-Performance Fuel Systems 44

Chemical Effects of Nuclear Burnup on High-Performance Fuels 45

Temperature Gradient Effects on Compositions of High-Performance Fuels 48

Compatibility of Mixed-Nitride and Carbonitride Fuels with LMFBR Cladding Alloys 50

High-Temperature Properties of Vanadium Carbonitride Solutions 50

Measurements of the Physical Properties of (U,Pu)N Alloys 54

Studies of Thermal Conductance at Interface of Fuel and Cladding 55

Irradiation Testing of Nitride Fuels 57

3. Fission-Gas Release and Physical Properties of Fuel Materials During Irradiation 58

The Effect of Stored Energy in UO_2 and UN on In-Reactor Measurements of Thermal Diffusivity 58

Effect of Temperature, Fission Density, and Low Burnup on Release of Fission Gas from $(U_{0.75},Pu_{0.25})O_2$ 65

Effect of Temperature, Fission Density, and Burnup on Release of Fission Gas from Microspheres of $(U_{0.75},Pu_{0.25})O_2$ FFTF Fuel 68

Effect of Fission Density on Release of Fission Gas from Enriched Single-Crystal UO_2 Specimens 69

4. Zirconium Metallurgy 72

Fabrication and Texture Control of Zirconium Tubing . . 72

Texture Effects, Texture Development, and Anisotropy of Properties 76

Deformation and Annealing Textures in Zircaloy Tubing 76

Circumferential Texture Variations in Zircaloy Tubing 77

Yielding of Highly Textured Zircaloy Tubing 79

Part II. Coolants

5. Alkali-Metal Corrosion Studies 85

Mass Transfer of Interstitial Impurities Between Vanadium Alloys and Sodium 85

Oxygen Effects on the Compatibility of Vanadium and Sodium 85

Deoxidation of Vanadium by Molten Lithium 87

Interstitial Contamination Effects in Vanadium and Its Alloys 89

Compatibility of Stainless Steel and Insulation in LMFBR Systems 90

The Effect of Insulation on the Oxidation of Stainless Steel 91

Analysis of Mass Transfer Mechanisms in Loop Systems . . 93

Corrosion of Refractory Alloys in Lithium, Potassium, and Sodium 94

Forced Circulation Boiling Potassium Loop Tests (FCL-8) 94

Effect of Oxygen on Compatibility of Refractory Metals and Alkali Metals 95

Corrosion of Refractory Alloys by Lithium 100

T-111 Forced Circulation Loop (FCLLL-1) 104

Part III. Radiation Damage to Structural Materials

6. Behavior of Refractory Materials Under Irradiation 113

Irradiation Damage to Nonfissionable Refractory Materials 113

Refractory Metal Carbides 113

Effects of Irradiation on Carbides and Nitrides of Depleted Uranium 114

7. Fast-Neutron Irradiation Effects on Electrical Insulators . . 115

General Survey of Fast-Neutron Effects on Electrical Insulators 115

Irradiation of High-Density Commercial Al_2O_3 Products Considered for Thermionic Insulators 115

Fast-Neutron Damage to Large-Grained Translucent Alumina 115

Comparison of the Effects of Fast Neutrons on Several Commercial Alumina Products 118

8. Mechanical Properties Research and LMFBR Cladding and Structural Materials Development 121

Radiation Effects in Type 316 and Titanium-Modified Type 316 Stainless Steel 121

Results on Standard Types 316 and 316L Stainless Steel 121

Results on Titanium-Modified Type 316 Stainless Steel 123

Radiation Damage in Incoloy 800 127

Mechanical Properties Studies 127

Electron Microscopy Studies 129

Utilization of EBR-II 134

Examination of Stainless Steel and Nickel Irradiated in EBR-II 134

Mechanical Properties of Hastelloy N and Related Compositions 137

Experience with Modified Hastelloy N in the Molten-Salt Reactor Experiment 137

Influence of Irradiation Temperature on the Creep Properties of Hastelloy N 140

Aging of Modified Hastelloy N 144

9. Radiation Effects in Alloys and Structural Materials 148

Radiation Effects on Pressure-Vessel Steels 149

Radiation Hardening and Embrittlement in ASTM A 533-B Class 1 Steel 149

Investigation of Submerged Arc Weldment in HSST Plate 01 152

Characterization of HSST Plate 03 153

Radiation Effects in Iron 153

Part IV. Techniques of Fabrication and Testing

10. Tungsten Metallurgy 159

Primary and Secondary Working of Tungsten and Tungsten Alloys 159

Extrusion of Tungsten and Tungsten Alloys 159

Chemical Vapor Deposition of Tungsten Alloys 162

Deposition of Tungsten-Rhenium Sheet 162

Parametric Studies of the Tungsten-Rhenium Cedeposition Process 165

Effect of HF on Deposit Morphology 166

Chemical Vapor Deposition of Vanadium 167

Metallurgical Properties of Tungsten Alloys 168

Chemically Vapor Deposited Tungsten-Rhenium Alloys 168

Evaluation of Welds and Brazes in Tungsten Alloys . . . 170

Gas Porosity and Hot Cracking in Welds in Tungsten 170

Long-Time Creep-Rupture Properties of Tungsten Alloys 176

11. Nondestructive Test Development 177

Electromagnetic Inspection Methods (Eddy Currents) . . . 177

Analytical Studies 177

Probe Development 179

Ultrasonic Inspection Methods 179

Optical Visualization of Ultrasound 179

Frequency Analysis 182

Tuning Variables 182

Spectra Affected by Discontinuities 182

Integration of Spectral Energies 184

System Improvements 184

Penetrating Radiation and Holographic Inspection Methods 186

Radiation Attenuation Studies 186

Radiation Scattering Studies 186

12. Joining Research on Nuclear Materials 189

The Effect of Minor Variations in Chemical Composition on Weldability 189

Effect of Minor Elements on the Hot Ductility of Inconel 600 190

Effect of Certain Minor Elements on the Intermediate Temperature Ductility of Incoloy 800 . . . 192

Weldability of 18% Cr-8% Ni Class Stainless Steels 199

Development of Welding Procedures for Commercial and Modified Alloys 199

Joining Development in Support of Fast Flux Test Facility 199

The Effect of Defects on the Mechanical Properties of Weldments 203

13. Development of LMFBR Tubing Fabrication 204

Fabrication Studies on Type 316 Stainless Steel 204

Drawing of Type 316 Stainless Steel Tubing 204

Fabrication Studies on Titanium-Modified Type 304 Stainless Steel 205

Drawing of Titanium-Modified Type 304 Stainless Steel Tubing 205

Evaluation of Drawn Titanium-Modified Type 304 Stainless Steel Tubing 205

Biaxial Stress-Rupture of Titanium-Modified Type 304 Stainless Steel Tubing 213

14. Development of Fuel Element Fabrication 223

Fabrication Studies of Fuel Dispersion Plates 223

Investigations of Nonuniform Deformation in Simulated Fuel Plates 223

Fabrication of ATR-Type Fuel Plates 234

Fabrication of Plates Containing Burned U_3O_8 . . . 239

Grinding and Crushing of UAl_x Fuel 241

Roll Bonding of Unclad Type 6061 Aluminum 244

Irradiation Studies of Dispersion Plates 246

Preparation and Characterization of Test Plates . . 246

Postirradiation Examination of Miniature Fuel Plates 251

Studies of Fuel Plate Surfaces 258

Determination of Fuel-Plate Homogeneity 259

Scanner Calibration Studies 259

Radiographic Densitometry 261

Development of Ductile Dispersion-Strengthened Aluminum 266

Part V. Engineering Properties of Reactor Materials

15. Physical and Mechanical Metallurgy of Refractory Alloys . . 273

Basic Physical Metallurgy Studies 273

Solubility, Diffusivity, and Permeability of Interstitials in Refractory Metals 273

Development of Age-Hardening Refractory Alloys . . 274

Thermodynamics of Spinodally Decomposed Alloys . . 281

Long-Time, High-Temperature Mechanical Properties of Commercial Refractory Alloys 283

Molybdenum and Niobium Alloys 284

Welding and Brazing Development 285

Brazing Alloy Development 285

Welding of T-111 Alloy Forced Circulation Loop (FCLLL-1) 290

16. Cladding Materials for Space Isotopic Heat Sources 294

Studies of Commercial Superalloys 294

Interaction of Stress and Vacuum on Properties of Superalloys at Elevated Temperatures 294

Development of Improved Alloys 295

SUMMARY

PART I. FUELS AND CLADDINGS

1. Development of Fast Reactor Oxide Fuels

We fabricated five Sphere-Pac $(U_{0.8}Pu_{0.2})O_2$ capsules for irradiation in the Experimental Breeder Reactor II (EBR-II) and shipped them to the reactor. These double-walled capsules contain fuel with smear densities from 80 to 86% of theoretical density. Fine microspheres for Transient Reactor Test Facility (TREAT) irradiation were prepared. We developed a procedure for making 84% dense pellets for the transient tests to be conducted in the TREAT facility and prepared a sufficient quantity of low-density pellets for the first TREAT series.

We now have defined quantitatively both the accuracy and precision of the NITROX analysis for O in $(U,Pu)O_2$. A scheme has been devised for measuring the redistribution of U-Pu and O in mixed oxide in a temperature gradient. Thermodynamic calculations that will complement experimental work on thermal gradients are in progress. Studies of the plastic deformation of UO_2 have continued with emphasis on studies of long-term low-stress deformation. Comparative tests were made between ammonium diuranate (ADU) and sol-gel-derived UO_2.

Irradiation of the two Experimental Test Reactor (ETR) uninstrumented capsules, which contain Sphere-Pac $(U,Pu)O_2$, continued normally. One of these, operating at a linear heat rate of 18 kw/ft, will achieve its target burnup level of 5% fissions per initial metal atom (FIMA) during the next quarter. Alpha autoradiographs were obtained of selected cross sections of irradiated fuel from the other capsules in the ETR series.

Analysis of the temperature monitoring data from the first instrumented capsule of Sphere-Pac fuels has shown that the central temperature of the fuel decreased with time at a constant level of heat generation, which indicates the effects of fuel restructuring on integrated thermal conductivity. The phemonemon will be investigated further in the second capsule, which is now being fabricated.

The hazards analysis for the transient test capsules is almost complete. Thermal shock tests were begun out of reactor on microspheres; preliminary results indicate good mechanical stability with some off-gassing.

The hazards analysis for the Sphere-Pac test rods in the EBR-II Series I was submitted. Irradiation is scheduled to begin with EBR-II cycle 33.

2. Development of High Performance LMFBR Fuels

The facility for fabricating (U,Pu)N pellets by either hot or cold pressing and sintering was placed into operation. Typical contamination levels in the glove box atmosphere are 8 ppm moisture and 12 ppm O.

The relationships between lattice parameter and composition were established for V(C,N) solid solutions. These data are a prerequisite to the study of the compatibility of (U,Pu)(C,N) with claddings of vanadium alloys.

3. Fission-Gas Release and Physical Properties of Fuel Materials During Irradiation

We have been using a perturbation method to measure the thermal diffusivity of fuels during irradiation. The data have been unsatisfactory because of too much scatter and unexplainably low values. We found that stored energy was being released during the step changes in irradiation conditions and that this unsuspected energy source was causing the diffusivity to appear low.

Pellets of $(U,Pu)O_2$ fuel made to Fast Flux Test Facility (FFTF) specifications released fission gas in a way that indicated the specimen as manufactured contained a network of tiny cracks. These cracks were partially healed by irradiation at 1100°C, but an attempt to increase the healing rate by using higher temperatures and fission rates resulted in extensive cracking of the specimen. Spheres of $(U,Pu)O_2$ are now being irradiated.

Spheres of crystalline UO_2 broke because fission products concentrated at defects and generated enough stress to cause rupture. Post-irradiation metallography showed that the amount of breaking was as predicted by the amount of fission gas released during irradiation.

4. Zirconium Metallurgy

Twelve experimental fabrications of Zircaloy tubing were completed. Tubing was reduced to final size by tube reducing, cold drawing, swaging, and planetary swaging. Two experimental schedules, which required heavy sinking by swaging, were unsuccessful; all other operations, including sinking by drawing, were completed without difficulty.

Comparison of deformation and annealing textures of Zircaloy tubing showed that annealing can produce greater texture changes than previously observed. After annealing, we have found shift in the preferred position of the basal poles and decreases in texture intensity; in other instances, we have found only the commonly reported exchange of prism pole positions. These differences in behavior seem to be related to the nature of the deformation before the anneal.

Work on texture development, gradients, and variations is continuing with special attention to the materials produced in the experimental fabrication. We also examined six commercial fuel cladding tubes for circumferential texture variations. The variation in basal pole intensity was $> 30\%$ in five tubes and was $> 80\%$ in one tube. There were cyclic variations in four tubes.

Experimentation showed the influence of texture on the biaxial mechanical behavior of Zircaloy tubing. Depending on the texture present, the stress required to produce plastic yielding can vary by 50% or more for materials tested in the same stress state. It should be possible to use information of this type to select Zircaloy tubing with different textures that can optimize resistance to any particular set of operating stress conditions.

PART II. COOLANTS

5. Alkali-Metal Corrosion Studies

Effects of O on the corrosion of V by Na were evaluated at 600°C in capsules of Mo and stainless steel, respectively. In all tests, V gettered essentially all of the O present in the Na and showed a dark reaction product not found in previous tests with vanadium capsules.

Exposure of V to molten Li was found to reduce the oxygen content of the V significantly without manifesting other metallurgical changes. The nature and rate of interstitial changes produced during vacuum annealing were evaluated in pure V at 900°C. Pressures $\leq 10^{-7}$ torr are required to avoid significant changes in O and C.

We assembled oxidation test equipment for evaluating the compatibility of stainless steel and thermal insulation, both with and without the presence of Na. This new task is to guide the selection of containment piping and insulation for the Fast Flux Test Facility (FFTF) and future liquid-metal fast breeder reactor (LMFBR) systems.

Kinetic treatments describing mass transport in liquid metal systems were refined to include effects of solid-state diffusion. The resultant equations are being compared against available data for nickel-base alloys in Na.

Details are presented concerning the examination of a Nb–1% Zr helical induction pump used to circulate boiling K for 10,000 hr in an experiment in a loop of D-43 alloy. We traced the loss in performance near the end of the test to expansion of the outer pump sleeve away from the outer pump helix.

The effect of O on the compatibility of Nb with K was evaluated at 600°C. The presence of O in K leads to increased dissolution of the Nb by K. Also there is a critical concentration of O in Nb above which the Nb is penetrated by K.

The gettering-vacuum-fusion (GVF) technique for determining O in K and Na was compared against other analytical techniques. For concentrations between about 100 and 1000 ppm O, recoveries within 10% of the O added were obtained. At high concentrations of O, however, considerably

less O was recovered than was added. For K, this was the result of dissimilar-metal transfer between the molybdenum capsule and zirconium specimen, which led to the formation of Mo_2Zr and Mo. For Na, the cause appeared to be the formation of a poorly adherent ZrO_2 scale. Between about 25 and 100 ppm O, recoveries by the GVF and amalgamation analytical techniques were in good agreement.

We continued analysis of a T-222 thermal convection loop that had circulated Li for 3000 hr at 1350°C. Insert specimens from the loop showed a loss of O at all positions and an increase in N at the coldest position. Construction continued on a T-111 forced circulation liquid lithium test bed loop (FCLLL-1), designed to gain corrosion data on new refractory alloys for cladding fuel elements in space power systems cooled with Li. We leak checked the vacuum chamber and installed the loop in the chamber. Before assembly, we conducted corrosion tests on T-111 field welds and found them sufficiently free of contamination to waive the requirement for postweld annealing.

PART III. RADIATION DAMAGE TO STRUCTURAL MATERIALS

6. Behavior of Refractory Materials Under Irradiation

Hot-pressed and slip-cast monocarbides of Ti, Zr, Ta, Nb, and W were irradiated to fast-neutron fluences up to 4 to 5×10^{21} neutrons/cm^2 at 1000 to 1100°C, and explosion-pressed carbides were irradiated to a fluence of about 2.5×10^{21} neutrons/cm^2. None of the specimens showed changes in microstructure or lattice size. The maintenance of structural integrity and the absence of major property changes during irradiation are very encouraging for the applicability of carbides in high-temperature nuclear devices designed for long-term operation.

7. Fast-Neutron Irradiation Effects on Electrical Insulators

Metallographic examinations showed that increasing the temperature at which large-grained (25 μm) alumina is irradiated causes an increased amount of damage through grain-boundary separation. A reversal of this

trend begins only at temperatures of about 1000°C or above, presumably because of annealing in the reactor.

Results were obtained from a short-term irradiation [0.4 to 3.1×10^{21} neutrons/cm^2, (> 1 Mev)] of three commercial types of small-grained (< 10 μm) alumina and one commercial type of large-grained alumina at various temperatures from 400 to 1230°C. About half the specimens of the two small-grained types of alumina that contained the most impurities fractured during irradiation. Very little gross damage occurred to specimens of the highest purity small-grained type of alumina. In this irradiation, the impurity content appeared to be the predominant factor causing fracturing. The irradiation of an identical long-term assembly is continuing.

8. Mechanical Properties Research and LMFBR Cladding and Structural Materials Development

We have found that the mechanical properties of types 316 and 316L stainless steel are affected by irradiation and by thermal aging. Thermal aging causes an increase in the minimum creep rate, and irradiation reduces the fracture strain. Metallographic studies showed that the fracture mode in creep at 650°C changed from transgranular in aged samples to intergranular in irradiated materials. A similar examination of fractured samples of types 316 and 316L stainless steel modified with about 0.2% Ti revealed that the fracture mode was transgranular in both materials before and after irradiation.

Specimens of type 304 stainless steel and nickel 270 were irradiated in EBR-II to fluences of 1.4×10^{16} to 2.6×10^{19} neutrons/cm^2 (> 1 Mev) between 370 and 524°C. Electron microscope examination of several of the samples of type 304 stainless steel irradiated at various temperatures to a fluence of 2.6×10^{19} neutrons/cm^2 (> 1 Mev) showed that defect clusters were present after irradiation at 384 and 467°C but not at 524°C. Samples of nickel 270 irradiated at the same conditions contained voids over the temperature range of 384 to 524°C.

The fracture ductility at 650°C of a heat of Incoloy 800 containing 0.1% Ti and 0.12% C was reduced by aging at 500°C after solution annealing

at 1150°C. This aging resulted in lower fracture strains in the unirradiated and irradiated conditions. This embrittlement could be circumvented by annealing for 100 hr at 800°C after the 1150°C anneal, reducing the temperature of the solution anneal, and reducing the carbon content. Electron microscopy showed that the precipitate concentration and morphology vary with concentration of Ti and C. All of the precipitates extracted to date are of the $M_{23}C_6$ type.

Two heats of Hastelloy N modified with 0.5% Ti and 0.5% Hf have been exposed to the molten-fluoride-salt environment of the Molten Salt Reactor Experiment core for 9789 hr at 650°C. They received a thermal fluence of 5.3×10^{20} neutrons/cm^2 during this time. The postirradiation mechanical properties were measured and found to be much better than those for standard Hastelloy N under similar conditions. However, postirradiation tests on samples irradiated at higher temperatures in the Oak Ridge Research Reactor indicate that the Hastelloy N modified with Ti has very poor properties after irradiation at temperatures above 650°C. These experiments also included other materials, and we found that even vacuum-melted standard Hastelloy N was susceptible to this effect of irradiation temperature. Several alloys containing strong carbide formers such as Hf and Nb were not influenced by irradiation temperature. Our aging studies on the unirradiated titanium-modified alloy have been extended to aging times of 3000 hr at 650 and 760°C. Although the tensile and creep properties are responsive to heat treatment, the variations are too small to account for the temperature effect noted in irradiated samples.

9. Radiation Effects in Alloys and Structural Materials

The tensile and notch-impact properties of neutron-irradiated samples from a 12-in.-thick plate of ASTM A 533-B Class 1 steel have been measured as a function of irradiation temperature and depth in the plate. Based on a normalization of the results to a fluence of 9×10^{18} neutrons/cm^2 ($>$ 1 Mev), smaller increases in yield stress were observed for samples taken from regions closer to the plate surface, but a similar conclusion could not be reached for the increases in ductile-to-brittle transition temperature because of the inherent scatter in the notch-impact test data.

Notch-impact tests were conducted on weld metal from a full-thickness submerged-arc weld in a portion of a 12-in.-thick plate of ASTM A 533-B steel. No significant variation in properties was observed as a function of distance from the surface.

The effect of low-temperature irradiation and postirradiation annealing has been investigated on tensile samples of vacuum-melted iron containing less than 2 ppm N by weight and samples doped with 20 and 300 ppm N by weight. The results indicate that radiation hardening and radiation-anneal hardening increase with increasing nitrogen concentration, which is interpreted in terms of the trapping of N at defect clusters produced by radiation.

PART IV. TECHNIQUES OF FABRICATION AND TESTING

10. Tungsten Metallurgy

We completed the duplex extrusion of four powder-metallurgy tungsten tube shells at extrusion temperatures of 1250, 1450, 1650, and 1750°C. Specimens were cut from the extrusions to determine the effect of extrusion temperature on microstructure and working properties.

In our chemical vapor deposition (CVD) studies, a series of experiments was conducted to systematically determine the effect of various deposition variables on the uniformity of the thickness of W–5% Re sheet deposits. The results indicate that optimizing the deposition pressure between 10 and 100 torr will produce uniformly thick deposits. Experiments with the W–25% Re deposition system showed that the content of Re in the deposit was equal to that in the gas phase for deposition temperatures between 700 and 1200°C. Studies to determine the effect of HF on the surface morphology of tungsten deposits showed two unexpected results. The addition of HF to the inlet gas produced deposits that had a smoother surface, and the metal recovery was greater. In another CVD study, vanadium metal was deposited by the reaction of entrained VCl_3 and H_2 on an induction-heated graphite substrate at 1200 and 1300°C.

Preliminary bend tests of CVD W–5% Re showed that the material was very brittle as deposited because of grown-in porosity or inhomogeneous

alloying. However, after a 1-hr anneal at 2200°C, we found a DBTT of 125°C, which is lower than any other reported value for unworked W-Re alloys. An electron microscope fractographic study of fusion welds in powder-metallurgy, arc-cast, and chemically vapor-deposited W revealed that hot cracking in these materials is a result of stress-induced growth and a merging of very small gas bubbles at the grain boundaries at the high temperatures and stresses imposed during welding. Additional long-time creep-rupture data for unalloyed W was obtained at 1400, 1650, and 2200°C. The Larson-Miller constant calculated from these results was used to obtain an estimation of the creep-rupture curves at 1800 and 2000°C.

11. Nondestructive Test Development

We are developing new techniques and equipment for the nondestructive evaluation of materials and components. The major emphasis has been on eddy-current, ultrasonic, penetrating radiation, and holographic methods.

Our analytical work on electromagnetic phenomena has been directed in part to the solution of problems related to tubing inspection. We developed curves relating flaw sensitivity to inspection variables such as the thickness of the tubing wall and coil configuration and dimensions. We improved procedures for making miniature probe-coil assemblies.

An improved immersion tank and specimen-handling devices were fabricated and assembled for the ultrasonic schlieren system. Our continued investigations of frequency analysis included (1) observation of the effects of impedance-matching circuitry on the frequency spectra of transmitted pulses, (2) study of the effect of flaw size on the frequency spectra of reflections from rear surfaces, (3) development of a method for digital display of the integrated intensities of preselected frequency spectra, and (4) development of improved circuitry to achieve better ratios of signal to noise, which will allow measurements on much smaller signals.

Computer programs have been developed to aid in graphically plotting data from x-ray attenuation and radiographic densitometry studies. A

simple, unfocused collimator with goniometer capability has been constructed for gamma-ray scattering studies using multichannel analysis of energy spectra.

12. Joining Research on Nuclear Materials

We have found that S has a much more deleterious effect on the hot ductility of Inconel 600 heat-affected zones than does P. Furthermore, small additions of Mn do not improve the properties of compositions containing S. Our studies on alloys of the Incoloy 800 type show that some exhibit a ductility minimum at intermediate temperatures and then recover at elevated temperatures; other compositions exhibit a continuous decrease in ductility with increasing test temperature. All of the alloys that recovered ductility contained about 0.40 wt % Ti.

In support of the Fast Flux Test Facility (FFTF) primary vessel program, we are producing stainless steel weldments for irradiation by Battelle Northwest. The 130 specimens machined from submerged-arc welds have been delivered, and the preparation of gas metal-arc and shielded metal-arc welds is under way. We are also determining the effects of welding conditions on the occurrence of discontinuities.

13. Development of LMFBR Tubing Fabrication

Tubes of titanium-modified type 304 stainless steel have been fabricated; the resulting microstructure was influenced markedly by the processing variables. Pole figures were determined for the titanium-modified type 304L stainless steel after processing by several different schedules. The preferred orientation consisted of two components analogous to the $(011)[\bar{1}00]$ and $(322)[\bar{4}33]$ rolling textures. Transmission electron microscopy showed the presence of carbides and martensite in the cold-worked tubing.

Tube burst tests have been run on tubes of titanium-modified type 304L stainless steel at 600 and 700°C. The results indicated generally that the rupture life was increased and the fracture strain decreased by cold working. Annealed tubing failed at low strains when

flaws were observed, and cold-worked tubing failed at flaws that were too small to be detected by conventional techniques.

14. Development of Fuel Element Fabrication

In an effort to understand dogboning, we made high-speed movies of the deformation of simulated fuel plates during rolling. These studies confirmed previous theories on the importance of matching the mechanical properties of the core and frame materials. They also demonstrated that factors such as billet thickness, roll diameter, reduction per pass, core fit, and roll friction all play a part in dogboning. We established a mechanism that satisfactorily explains the occurrence of dogboning at both ends of a plate rolled in one direction.

Fuel plates with Advanced Test Reactor (ATR) geometry were then fabricated to demonstrate that dogboning can be reduced in actual fuel plates. Doubling the core thickness in plate 19 greatly reduced the dogboning. The use of a type 2219 aluminum insert at the core ends offered some improvement.

In miniature fuel plates with burned oxide fuel, the degree of dogboning and void concentration both increased when weaker cladding materials were used. Since it has been shown that irradiation performance of such plates is a function of as-fabricated void concentration, some suggested solutions to dogboning may cause poorer irradiation performance.

The use of roll crushers in the comminuting of UAl_3 continues to yield improved fuel recoveries. Varying the uranium concentration in the intermetallic from 69 to only 71 wt % caused a major difference in crushing characteristics. Under determined conditions, both types of fuel gave acceptable yields; however, the rejected material was in the form of oversize flake for the 69% material and −325 mesh fines for the 71% material.

While all parameters are not yet understood and unexplained variations in quality occur, we have shown it possible to roll bond type 6061 aluminum to itself. Even with reductions as low as 4:1, the percentage of interfacial grain growth was above 75%, and the percentage increased with increasing reduction.

Anodic coatings formed on type 6061 aluminum in a bath containing $TiO(KC_2O_2)_2$ plus citric and oxalic acids failed when exposed in a corrosion loop with a high heat flux across the sample. Similar samples had previously withstood static corrosion tests. Metallographic examination showed that all traces of the anodic coating had disappeared from the surface of the sample.

Mechanical property data were determined on the effect of oxide content and alloy additions (including Mg, Fe, Mo, Zr, Ti, and Cr) to Al. We found considerable increase in strength (for some alloys, up to 50% at 450°C) at all temperatures with some improvement in high-temperature ductility in all alloys with oxide contents similar to those of the usual sintered-aluminum-product alloys.

Miniature test plates prepared during the previous quarter are now being successfully irradiated in the Experimental Test Reactor (ETR). Both standard and instrumented miniature plates have been fabricated with nickel coatings on the surface for use in future loadings. The plating technique differs from ones previously tried in that a new cleaning procedure resulted in coatings capable of withstanding heat fluxes of 470 w/cm^2 in the loop tests.

Plates irradiated during the previous year were examined in the ORNL hot cells. Included were plates containing fuel loadings 25% greater than the present High Flux Isotope Reactor (HFIR) loadings with both high-fired and burned-oxide fuels; for comparison, plates with UAl_3 fuels also were run. All plates were in excellent condition with no evidence of matrix cracking, blistering, or any other indication of incipient failure. In the heavily loaded plates with the burned oxide, there was almost complete reaction between the fuel and matrix. The plates containing the UAl_3 fuel showed considerably more swelling than those with the oxide. In both cases, the swelling was shown to be an inverse function of the original void content of the plates.

PART V. ENGINEERING PROPERTIES OF REACTOR MATERIALS

15. Physical and Mechanical Metallurgy of Refractory Alloys

The hafnium-rich phase that precipitates from a rapidly quenched and aged alloy within the miscibility gap of the Nb-Hf system consists of very small, disk-shaped particles mutually perpendicular to each other; in slowly cooled and aged specimens the precipitates appear as coarse rosettes. The tensile strength of quenched and/or aged specimens of Nb–53% Hf ranges between 71 and 108 $\times 10^3$ psi with a ductility range between 0.6 to 12.1%. Curves for calculated solubility limit and chemical spinodal decomposition, based on the free energy of mixing of regular solutions, are compared with similar curves corrected for interactions of second nearest neighbors and clustering. The solubility is less and the spinodal curves are wider than the regular solutions.

Current measurements indicate that the solubility of N in W increases rather than decreases with temperature. The diffusivity, D, and solubility, S, obey the expressions

$$D = 1.29 \times 10^{-2} \exp(-42{,}300/RT) \text{ cm}^2/\text{sec}$$

and

$$S = 7.5 \times 10^{-2} \exp(-14{,}850/RT) \text{ torr}\cdot\text{liter cm}^{-3} \text{ torr}^{-\frac{1}{2}} .$$

The creep-rupture properties of SU-16 (Nb–11% W–3% Mo–2% Hf–0.08% C) were determined between 980 and 1205°C.

The development of brazing filler metals for joining refractory metals, ceramics, and graphite has continued. The Ti-V-Cr alloy system is particularly attractive in that compositions have been developed within it that will join all combinations of these materials. Compositions containing 25 to 48% Cr are better for Al_2O_3, whereas 5 to 25% Cr alloys are better for graphite. All seem to be useful for joining Ta. A complex forced circulation loop of T-111 alloy was successfully welded. It involved about 80 tungsten-arc welds, most of which were of the multipass, full-penetration type. No unusual problems were encountered.

16. Cladding Materials for Space Isotopic Heat Sources

Creep tests are being conducted to determine the minimum thickness of Haynes alloy No. 25 that will not be adversely affected by evaporation in vacuum to 800°C. We have found that increased surface area is responsible for enhanced evaporation of a specimen undergoing creep.

Ordered alloys with low vapor pressures, under study as improved cladding materials, have been fabricated into test specimens. Hardness tests at room temperature and elevated temperatures indicate superior strength in alloys exhibiting long-range order.

PART I

FUELS AND CLADDINGS

1. DEVELOPMENT OF FAST-REACTOR OXIDE FUELS

P. Patriarca A. L. Lotts

Of the various fuels that can be considered for a liquid-metal fast breeder reactor (LMFBR), the oxide fuels have the most advanced technology and the greatest potential for operating reliably at the burnups and heat ratings of interest for the early demonstration reactors. But the burnup and the heat rate are now limited to about 50,000 Mwd/metric ton and 16 kw/ft, respectively. These limitations are based on results of irradiations on fuels that are not necessarily optimized for thermal, burnup, and mechanical performance, but, experiments have not been performed to prototypic neutron fluences, which may impose additional limitations.

The capability of oxide fuels can possibly be improved by different fuel structures or different methods of void distribution in the fuels. We emphasize irradiating fuels with structures and void distributions different from those of the oxide fuels irradiated heretofore and compare these with reference fuels such as pellets derived from mechanically blended powders and coprecipitated material. The sol-gel process provides a variety of starting materials that can then be formed into different fuel structures by Sphere-Pac, vibratory compaction, pelletizing, or extrusion. The sol-gel process is ideal for reconstituting fuel after aqueous chemical processing of spent fuel elements. The combination of possible advantages of any particular sol-gel structure from a performance standpoint and the cost economies inherent in the sol-gel process make this program very interesting for obtaining total economies in the nuclear fuel cycle.

Therefore, the main object of the program is to extend the performance of oxide fuels and to economize processing, which, together, will result in an economically optimized fuel cycle.

Preparation of $(U,Pu)O_2$ Fuels

W. T. McDuffee[1]

So far, this work has primarily involved the preparation of the various sol-gel materials; it will later involve the purchase of coprecipitated and mechanically blended material. The $(U,Pu)O_2$ fuels are prepared by the sol-gel process in the Chemical Technology Division pilot plant as part of a larger ORNL program on sol-gel process development and demonstration.

We prepared about 170 g of $(U_{0.8},Pu_{0.2})O_2$ microspheres < 63 μm in diameter for use as the fine fraction in the TREAT fuel capsules. The large microsphere fraction (425 to 595 μm in diameter) was prepared earlier, but failure of a furnace tube destroyed the fine fraction made at that time.

We completed preliminary design of a larger column for forming spheres and of related equipment for use in preparing $(U,Pu)O_2$ and PuO_2 microspheres. A room in the pilot plant suitable for handling Pu was designated to house this equipment, and the preparation of this room to accept the equipment was started.

Development of Fabrication Processes

J. D. Sease

Fast reactors operating at high specific powers will require fuel pins of small diameter with fuel ranging from 80 to 90% of theoretical density and a high fissile loading. Our work is to develop procedures for Sphere-Pac, methods for pelletizing, and procedures for fabricating irradiation capsules. This quarter, we continued the development of methods for fabricating 85 and 91% theoretically dense pellets for TREAT irradiation and constructed five double-containment capsules for irradiation testing of sol-gel Sphere-Pac fuel in the Experimental Breeder Reactor II (EBR-II).

---

[1]Chemical Technology Division.

Sphere-Pac (W. L. Moore, R. B. Fitts)

Our equipment for Sphere-Pac loading of $(U,Pu)O_2$ microspheres was developed by practice loading thoria microspheres into dummy EBR-II fuel pins. Development was completed this quarter, and the equipment was used for loading EBR-II fuel pins.

We believe that the process has now reached the stage of development that will permit description of an optimized recipe for Sphere-Pac loading:

1. Weigh the proper amount of coarse and fine microspheres (4:1 ratio).
2. Apply 60-cps low-amplitude vibration to the fuel pin and load coarse microspheres.
3. Restrain the coarse microspheres with a screen funnel and infiltrate fine microspheres into the coarse bed.
4. Check bed height and add fine microspheres as required to adjust the height.

A complete description of the Sphere-Pac process was presented at the Fall Meeting of the American Ceramic Society in Pittsburgh, Pennsylvania.[2]

Pelletizing of Sol-Gel $(U,Pu)O_2$ (R. A. Bradley)

Sol-gel-derived $(U,Pu)O_2$ pellets are required for instrumented irradiation tests in the Oak Ridge Research Reactor (ORR) and for transient tests in the Transient Reactor Test Facility (TREAT). The transient tests in the TREAT require pellets with densities of 85 and 91% of theoretical and oxygen-to-metal ratios of 1.980 ± 0.005. The objective of this work is to develop the necessary fabrication procedures and to produce the pellets for these irradiation experiments.

The preparation of the $(U_{0.8},Pu_{0.2})O_2$ powder to be used for the TREAT pellets was described previously.[3,4] This quarter we investigated

---

[2]R. B. Fitts, A. R. Olsen, and J. Komatsu, "Sphere-Pac Fabrication of Sol-Gel Nuclear Fuel," paper presented at the Fall Meeting of the American Ceramic Society, Pittsburgh, Pa., October 6, 1968.

[3]W. L. Moore and R. A. Bradley, Fuels and Materials Development Program Quart. Progr. Rept. June 30, 1968, ORNL-4330, p. 7.

[4]R. A. Bradley, Fuels and Materials Development Program Quart. Progr. Rept. Sept. 30, 1968, ORNL-4350, pp. 5–7.

methods of calcining the powder to eliminate the volatiles, to reduce its surface area, and to stabilize its oxygen-to-metal ratio.

Calcination. — We conducted four preliminary calcination experiments to determine the effect of calcining temperature and atmosphere on the surface area and oxygen-to-metal ratio of the powder. In one experiment, the powder was oxidized in air at 600°C, reduced in Ar—4% H_2 at 600°C, and cooled in CO_2 to stabilize the oxygen-to-metal ratio at about 2.15 in the manner described by Lyon et al.[5] For the other three experiments, the powder was heated to 500, 700, or 900°C in Ar—4% H_2 and cooled in the same gas. Pellets were pressed and sintered from each batch of calcined powder to determine its sinterability. The powder from the oxidation-reduction-stabilization treatment (batch H.T. 12), which had a surface area of 7.1 m^2/g and an oxygen-to-metal ratio of 2.15, yielded 81.6% dense pellets. Pellets pressed from the powder and calcined at 500 and 700°C in Ar—4% H_2 were only about 72% dense, and the material calcined at 900°C could not be formed into pellets without the aid of a binder. The calcining conditions, characteristics of the powder, and densities of the test pellets are given in Table 1.1. Since the oxidation-reduction-stabilization treatment produced a powder with a surface area and oxygen-to-metal ratio in the desired range and also yielded pellets close to the desired density, we performed two similar calcining experiments. The powder was heated to 525 or 600°C in air, reduced at the same temperature in Ar—4% H_2, and cooled to room temperature in CO_2. The calcining conditions and characteristics of the resulting powder are given in Table 1.2.

The —325 mesh fraction of the calcined powder was pressed at 30,000, 35,000, or 40,000 psi and sintered into 82 to 87% dense pellets. The forming pressures, sintering conditions, and densities are shown in Table 1.3. From the relationship between forming pressure and sintered density, we determined the pressure required to produce 85% dense pellets.

---

[5]W. L. Lyon, C. M. Ryer, and C. N. Craig, "Laboratory Scale Preparation of Plutonia-Urania Fast Reactor Fuel," pp. 59—63, Vol 63 in "Preparation of Nuclear Fuels, Nuclear Engineering — Part XVIII," A. D. Trevebaugh and D. L. Keller, eds., Chem. Eng. Progr. Symp. Ser. 80, American Institute of Chemical Engineers, New York, 1967.

Table 1.1. Characterization of Urania-Plutonia Powder from Preliminary Calcining Experiments

Batch Number	Calcining Conditions	Oxygen-to-Metal Ratio	Surface Area (m^2/g)	Sintered Pellet Density (% of theoretical)
H.T. 12	600°C in air for 2 hr, Ar–4% H_2 for 16 hr, cooled in CO_2	2.15	7.1	81.6
H.T. 13	500°C in Ar–4% H_2 for 2 hr, cooled in Ar–4% H_2	2.30	17.7	72.9
H.T. 14	700°C in Ar–4% H_2 for 2 hr, cooled in Ar–4% H_2	2.18	13.7	71.0
H.T. 15	900°C in Ar–4% H_2 for 2 hr, cooled in Ar–4% H_2	2.02	4.1	Could not press into pellets without the use of a binder

We have made five sintering runs and produced about 100 pellets with densities of 85 ± 1%. All are free of cracks and have good surface appearance. The oxygen-to-metal ratio is 1.980, and the carbon content is < 50 ppm. The porosity is very fine and uniformly distributed. A photomicrograph of an 85% dense pellet made from the calcined powder is shown in Fig. 1.1. It appears that these pellets will be suitable for the TREAT fuel rods.

In summary, we have completed the development of the process for making 85% dense urania-plutonia pellets for transient tests in TREAT, and enough low-density pellets have been produced for the first four TREAT capsules. We expect that slight modification in the calcining and sintering conditions will allow us to make the 91% dense pellets for TREAT. This work is in progress and will be completed next quarter.

Capsule Fabrication (J. D. Sease, M. K. Preston, W. L. Moore)

During the quarter, our fabrication efforts were concentrated primarily on the construction of five capsules for the EBR-II. We continued the preparation of drawings, procedures, and hardware for irradiation capsules for the TREAT facility.

Table 1.2. Calcining Condition and Characterization of Urania-Plutonia

Batch Number	Calcining Conditions	Oxygen-to-Metal Ratio	NO_3 Content (wt %)		Carbon Content (wt %)	Surface Area (m^2/g)
			Kjeldahl	Colorimetric		
Granulated TREAT powder	Not calcined – tray dried at 100°C		0.12	0.47	0.58	29.3
H.T. 26	600°C in air for 1/2 hr, Ar–4% H_2 for 3 hr, cooled in CO_2	2.49	0.12	0.35	0.12	9.3
H.T. 27	525°C in air for 3 hr, Ar–4% H_2 for 17 hr, cooled in CO_2	2.30	a	a	0.31	11.7
H.T. 29	Same as H.T. 27	2.24	a	a	0.20	10.5
H.T. 35	Same as H.T. 27	a	a	a	a	a

[a]Results not received.

Table 1.3. Pressing and Sintering Conditions[a] and Densities of Urania-Plutonia Pellets

Batch Number[b]	Sintering Run	Forming Pressure (psi)	Density (% of theoretical) Green	Sintered
		$\times 10^3$		
		30	43.7	81.1
H.T. 26	57	35	44.7	82.7
		40	45.4	83.5
		30	43.3	81.7
H.T. 27	57	35	45.0	84.1
		40	45.3	87.3
		30	47.3	83.0
H.T. 27 and 29 blended	58	35	48.1	84.6
		40	48.9	84.2
H.T. 27 and 29 blended	59	35	47.8	83.7
H.T. 35	61	35	48.7	84.8
H.T. 35	62	35	48.7	86.0

[a]Heated at 300°C/hr to 1450°C and held 1 hr in flowing Ar. Gas changed to Ar–4% H_2 and held 4 hr.

[b]See Table 1.2.

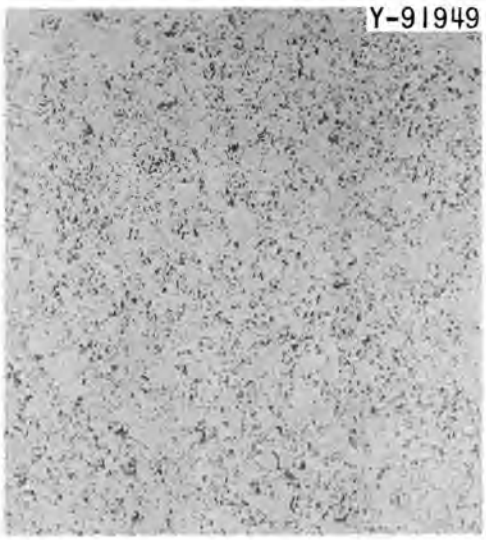

Fig. 1.1. Porosity Distribution in an 84% Dense Sol-Gel Urania-Plutonia Pellet. 100×.

EBR-II Capsules. — Five double-containment capsules for testing Sphere-Pac sol-gel fuel in EBR-II were completed and shipped to the reactor site. Our EBR-II capsules, which will be a part of a 19-capsule subassembly at the EBR-II, are of the design shown in Fig. 1.2.

The steps used in fabricating the EBR-II capsules are shown in Fig. 1.3. The capsule components were made from certified materials, and the tubing for the fuel pin was inspected for flaws by dye-penetrant and ultrasonic techniques. After being machined, all parts were inspected and cleaned in acetone and alcohol. All closure welds were inspected by radiography, helium leak testing, and dye-penetrant examination. Before loading the fuel, we covered the pins with plastic to minimize contamination of the outer surface of the cladding. The microspheres were loaded by the Sphere-Pac process.[6] We made gamma attenuation scans of the fueled portion of each pin to determine uniformity of the fuel bed. The EBR-II operators required the 16,000-psi fiber-stress test as a check of the integrity of the weld between adapter and capsule.

The data for capsule fabrication are summarized in Table 1.4. The high smear density for the fuel in capsule S-1-B apparently resulted from very dense seating of the coarse fuel bed. We attribute the low smear density of the fuel in capsule S-1-D to the lack of symmetry in the microspheres from fuel lot 101. The analytical chemistry data for the fuels are summarized elsewhere.[7]

A typical gamma attenuation scan of the fuel bed is shown in Fig. 1.4. The low density region at the top of the fuel column was the result of our not loading exactly the required ratio of coarse and fine microspheres. Except for 1/8 in. or less at the top of the fuel columns, density variations were within ±3% for the five capsules. There is little doubt that the 1/8-in. low-density regions at the top of the fuel pins can be eliminated through additional development.

---

[6]F. G. Kitts, R. B. Fitts, and A. R. Olsen, "Sol-Gel Urania-Plutonia Microsphere Preparation and Fabrication into Fuel Rods," Intern. Symp. Plutonium Fuels Technol., Scottsdale, Arizona, 1967, Nucl. Met. 13, 195–210, 1968.

[7]See W. H. Pechin, "Analytical Chemistry," pp. 17–18, this report.

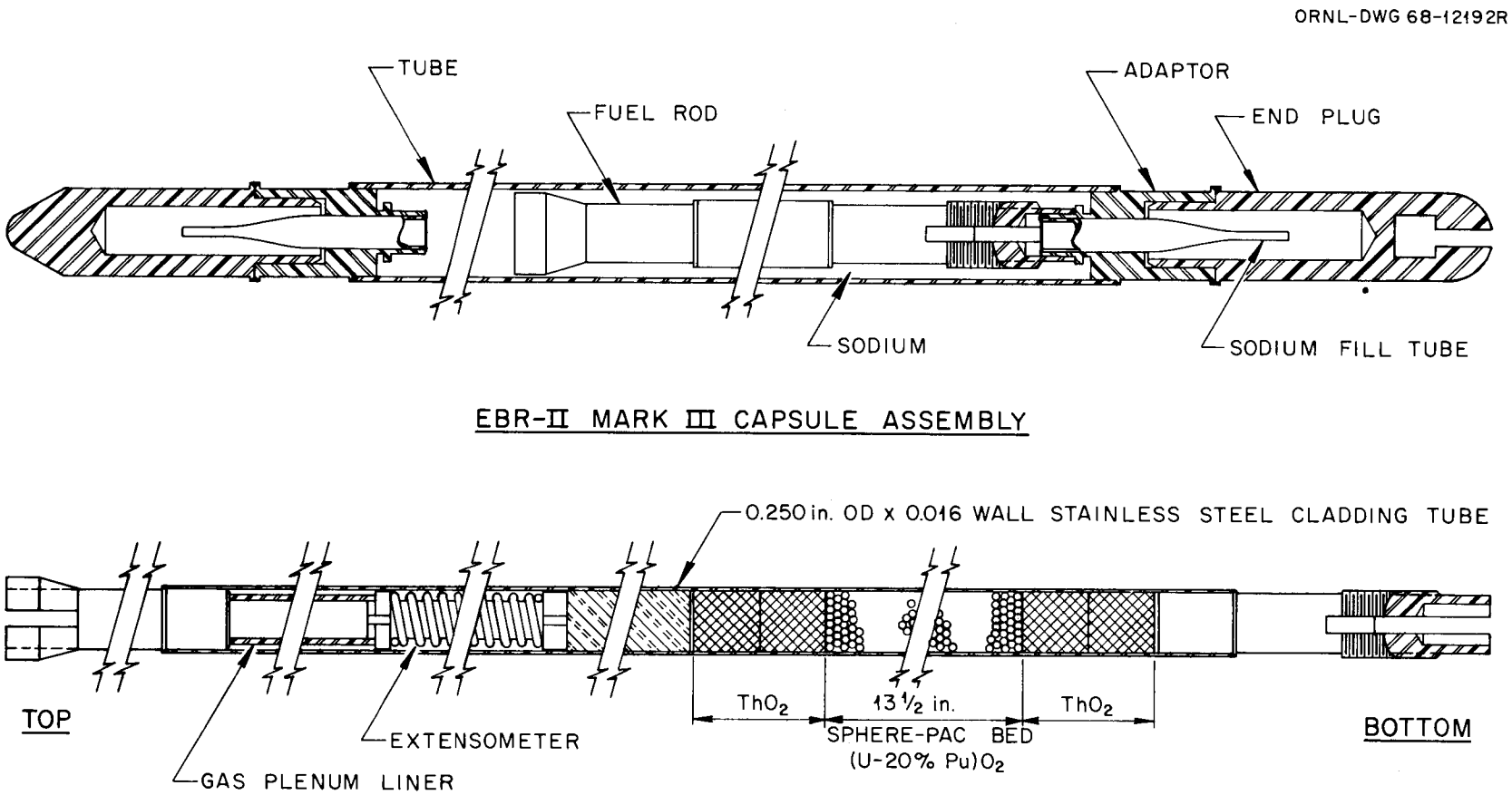

Fig. 1.2. Fuel Rod Assembly for Series I ORNL Oxide Fuels Tests in EBR-II.

ORNL-DWG 69-656

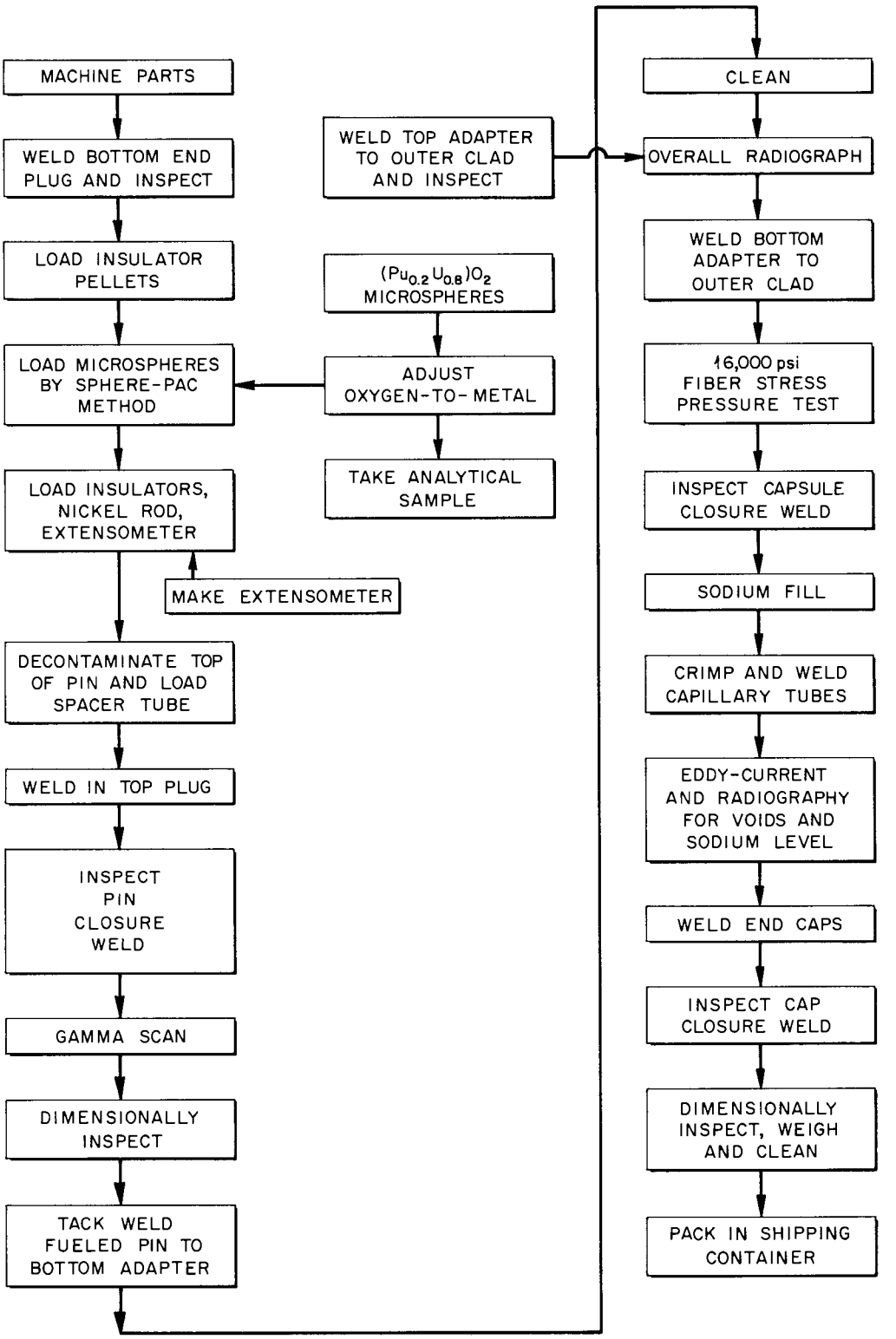

Fig. 1.3. EBR-II Fabrication Procedure.

Table 1.4. Summary of Data for EBR-II Capsule Fabrication

Capsule Number	Fuel Pin Number	Type Stainless Steel Cladding	Fuel Lot	Fuel Weight (g)	Fuel Smear Density (% of theoretical)	Oxygen in Sodium (ppm)
S-1-A	14-27-E	304	100	76.84	83.2	16
S-1-B	14-23-A	304	100	77.18	86.1	18
S-1-C	17-1	316	100	73.97	82.7	21
S-1-D	17-4-A	316	101	70.76	79.7	12
S-1-E	17-4	316	100	73.09	82.0	16

TREAT Capsules. — The irradiation capsules for testing the transient behavior of sol-gel fuel in the TREAT reactor are complex, instrumented capsules about 8 ft long and containing 12 thermocouples and 3 heater circuits. Detailed design of the TREAT capsule was approved, and preparation of fabrication procedures and data sheets was begun. We started fabricating the capsule hardware and started assembling the jigs and fixtures required for constructing the TREAT capsules.

Sodium Filling System

Sodium is required as the heat transfer medium in several of the capsules that will be used in the irradiation testing of fast reactor fuels; the problem of bonding Na was first encountered in these EBR-II capsules. Our method is to evacuate the piece to be bonded and fill with molten Na to the desired level in a closed pipe system. The layout of the system was detailed.[8] During the past quarter, the problems with the sodium-filling apparatus were resolved, and the five capsules for irradiation testing in EBR-II were satisfactorily sodium-bonded.

The maximum size allowed for bubbles in the molten Na for the EBR-II capsules was set at 1/6 in. in diameter. We inspected the sodium

[8]J. D. Sease, M. K. Preston, and W. L. Moore, Fuels and Materials Development Program Quart. Progr. Rept. Sept. 30, 1968, ORNL-4350, pp. 9–12.

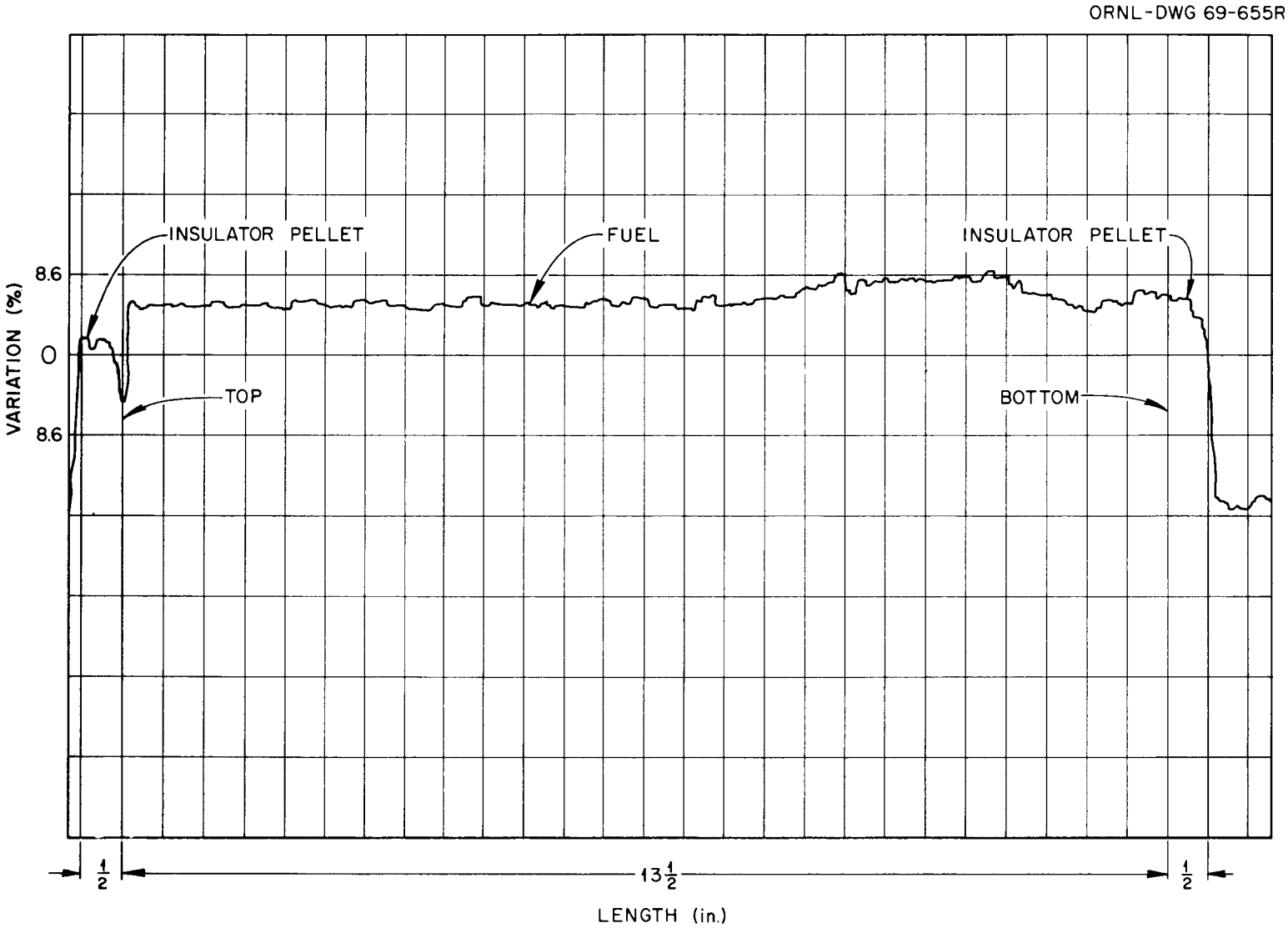

Fig. 1.4. Typical Gamma Attenuation Scan for EBR-II Capsule Fuel Bed.

bond with a phase-sensitive eddy-current device[9,10] and radiography of the solidified sodium. A typical readout from the eddy-current device is shown in Fig. 1.5. Because we inspected solidified Na and could not distinguish between bubbles and voids, we accepted bubble or void indications slightly larger than 1/16 in. in diameter. The reactor operators at the EBR-II site made the final inspection of the bond on molten Na.

The hot-trapped Na used in the sodium-filled rig contained 7 ppm O. Analytical results of the Na after it was charged into the five EBR-II capsules ranged from 12 to 21 ppm O (see Table 1.4).

The following filling technique was the most successful:

1. Connect the capsule into piping of sodium-fill rig, evacuate the capsule, and heat to 175°C.

2. Outgas the sodium supply at 260°C, reduce the temperature of the sodium supply to 175°C, and backfill at 4 psig He.

3. Fill the capsule under vacuum at 175°C to slightly above the desired fill level.

4. Increase the temperature of the capsule to 425°C under vacuum for 1 hr to cause wetting.

5. Lower the temperature of the capsule to 175°C under 4 psig He and adjust the fill height to the proper level, checking by eddy-current level probe.

6. Turn off the capsule furnace and allow the convection effect to zone cool the capsule to room temperature.

Loading of each of the EBR-II capsules took approximately 6 hr, not including the period for final cooling of the furnace from 175°C to room temperature.

---

[9]C. V. Dodd, "Recent Eddy-Current Development at the Oak Ridge National Laboratory," pp. 304–308 in Proceedings of the Fourth International Conference on Non-Destructive Testing, Butterworths, London, 1964.

[10]C. V. Dodd, "A Portable Phase-Sensitive Eddy Current Instrument," Mater. Evaluation 26(3), 33–36 (1968).

ORNL-DWG 69-925

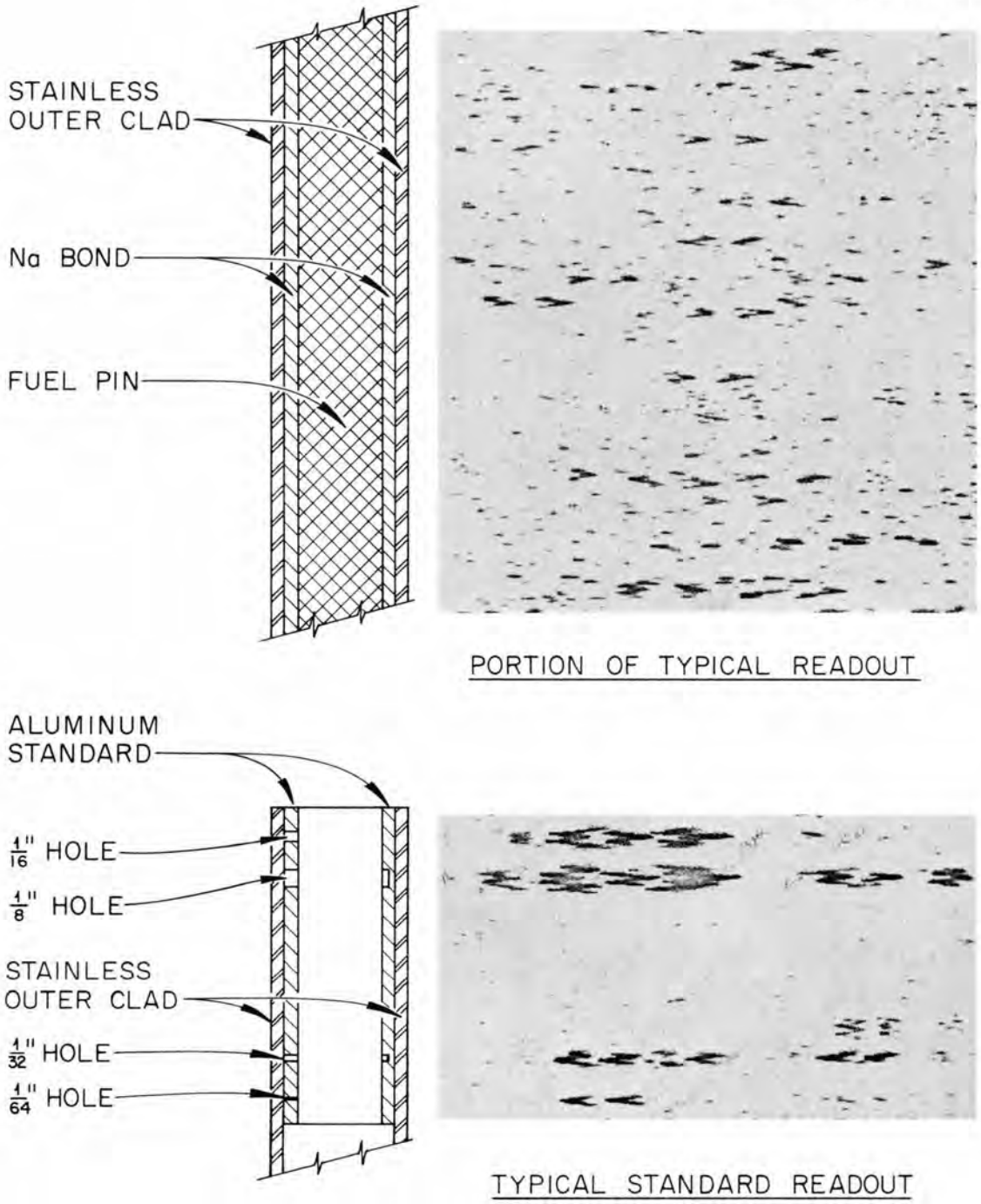

Fig. 1.5. Readout from Eddy-Current Void Detector.

Characterization of Sol-Gel $(U,Pu)O_2$ Fuels

W. H. Pechin

The development of sol-gel fuel fabrication requires characterization of both the chemical composition and the physical properties of the material to control the process and to determine which properties are important in the irradiation behavior. Thermodynamic studies will contribute to the development of the fuel process and will aid in predicting fuel performance for both irradiation testing and model studies.

Analytical Chemistry (W. H. Pechin)

Six lots of sol-gel fuel for Sphere-Pac, which are now being characterized, are summarized below:

Lot	Disposition
98	ETR capsule 43-116
99	ORR capsule SG-1
100	EBR capsules S-1-A, S-1-B, S-1-C, and S-1-E
101	EBR capsule S-1-E
102	TREAT (to be loaded)
103	ORR SG-2 (to be loaded)

The major results are complete for three of these lots and are listed in Table 1.5. The nitrogen colorimetric analysis was found to have an interference from U, so these values are being redetermined with a uranium separation. The colorimetric method is preferred because the nitrogen levels are near the limit of detection for the Kjeldahl method.

The standard deviation of the NITROX analysis was estimated from three different sets of data. The first set was from a series of 10 samples from a single batch of UO_2 analyzed on different days over a period of one month. This series, therefore, includes the day-to-day variation of the analysis. The standard deviation estimated from this series was ±0.0067 oxygen-to-metal-ratio units.

Table 1.5. Analytical Results Presently Available for Sol-Gel Fuel for Sphere-Pac

Analysis	Lot 99		Lot 100		Lot 101	
	Coarse	Fine	Coarse	Fine	Coarse	Fine
Chemical						
U, wt %	74.28	76.05	70.50	70.04	69.73	71.72
Pu, wt %	13.86	12.64	17.83	17.17	18.05	17.72
C, ppm	54.0	122.0	24.0	70.0	21.0	65.0
F, ppm	7.0	4.0	20.0	28.0	4.0	4.0
Cl, ppm	9.0	< 5.0	< 5.0	8.0	19.0	< 5.0
Oxygen-to-Metal Ratio						
Gravimetric	2.003		1.986	1.988	1.984	1.985
NITROX	1.989	1.942	1.991	1.984	1.981	1.981
Density, g/cm^3	10.86	10.61	11.10	10.83	10.77	10.90
Surface area, m^2/g	0.15	0.19	0.20	0.35	0.36	0.77
Gas evolution to 1700°C, cm^3/g	0.09	0.13	0.10	0.27	0.14	0.14

The second series was from nine determinations run at one time on a batch of material prepared by J. M. Leitnaker,[11] intended to have an oxygen-to-metal ratio of 2.00, and checked by x-ray diffraction. The standard deviation estimated from this series was ±0.0075 oxygen-to-metal-ratio units. The mean oxygen-to-metal ratio for this series was 1.999 with a 95% confidence interval of ±0.006 that indicated that the bias was within the limits +0.005 and −0.007 oxygen-to-metal-ratio units.

The third estimate was from the data of the control chart. The average standard deviation calculated from the last eight multiple determinations was ±0.0076 oxygen-to-metal-ratio units. A value of ±0.0072 for the standard deviation gives the 95% confidence interval of ±0.014 for one sample, ±0.010 for the average of two samples, and ±0.008 for the average of the three.

[11] J. M. Leitnaker, Fuels and Materials Development Program Quart. Progr. Rept. Sept. 30, 1968, ORNL-4350, pp. 14–18.

Control of Oxygen-to-Metal Ratio of $UO_{2.00 \pm x}$ (J. M. Leitnaker, K. E. Spear)

We have previously reported results of heating UO_2 at a $CO:CO_2$ ratio of 10:1. This particular gas mixture has been used as a defining quantity[12] for UO_2. That is, a sample of urania equilibrated with a 10:1 ratio of $CO:CO_2$ between 1000 and 1400°C will have an oxygen-to-metal ratio, by working definition, of 2.000 or 11.85% O. Three samples of the UO_2 equilibrated at 1400°C and cooled in the furnace to room temperature, as described previously,[11] were submitted to the Analytical Chemistry Division for oxygen analyses. Three determinations were made on each sample by the NITROX method. Results are listed in Table 1.6. The data of Table 1.6 show that the NITROX method is giving reliable results.

Table 1.6. Analyses of Equilibrated UO_2 Samples

Sample	Oxygen Content (wt %)			
	Test 1	Test 2	Test 3	Average
UO_2-14-16	11.84	11.85	11.82	11.84
A-5309-20	11.76	11.90	11.91	11.86
A-5309-24	11.80	11.82	11.86	11.83
				11.85 ± 0.014[a]

[a]Quoted error is one standard error of the mean.

Other compositions than the oxygen-to-metal ratio of 2.000 can be obtained by varying the $CO:CO_2$ ratio, which varies the oxygen potential. Table 1.7 illustrates for several temperatures and $CO:CO_2$ ratios the expected oxygen content of the urania phase.

The furnace now used cannot give accurate results on nonstoichiometric single-phase urania, since the samples are not quenched rapidly

[12]J. L. Markin and L.E.J. Roberts, "Thermodynamic Data for Uranium Oxides Between UO_2 and U_3O_8," pp. 693–711 in Thermodynamics of Nuclear Materials, International Atomic Energy Agency, Vienna, 1962.

Table 1.7. Oxygen-to-Uranium Ratios Expected with Various Conditions of Temperature and $CO:CO_2$ Ratios

Oxygen-to-Uranium Ratio	Temperature (°C)	Oxygen Potential (kcal/mole)	$CO:CO_2$ Ratio
2.01	1000	−58.9	1:100
	1200	−57.4	1:25
2.025	1200	−53.1	1:52
	1300	−52.1	1:17
2.05	1200	−48.8	1:110
	1300	−47.3	1:37

enough by being removed from the hot zone with a push rod; x-ray diffraction measurements show variation in the lattice size from the inside to the outside of the sample. Therefore, we are constructing a furnace from which samples can be dropped onto a copper block for more rapid quenching. We will determine the effect of the quenching rate on the sample as a guide to the experiments needed for $(U,Pu)O_2$ samples.

Oxygen and Plutonium Redistribution in $(U,Pu)O_2$ in a Temperature Gradient (J. M. Leitnaker, K. E. Spear)

The out-of-reactor compatibility of type 316 stainless steel with slightly substoichiometric oxides has been established,[13] and the results are in agreement with thermodynamic predictions.[14] In-reactor tests, however, indicated some reaction between fuel and cladding at temperatures between 500 and 600°C, temperatures lower than those proposed by current designs for fast breeder reactors. We believe major factors affecting fuel-cladding reactions will include fuel temperature gradients, the irradiation time, and the interface temperature. Our initial efforts are to understand the effects of thermal gradients in the fuel.

[13]T. Lauritzen and F. A. Comprelli, Trans. Am. Nucl. Soc. 10(2), 459 (1967).

[14]K. E. Spear, A. R. Olsen, and J. M. Leitnaker, Thermodynamic Applications to $(U,Pu)O_2$ Fuel Systems, ORNL-2494, in preparation.

Since the $(U,Pu)O_2$ phase can vary in both the U:P ratio and the oxygen-to-metal ratio, samples heated in a temperature gradient will exhibit gradients in both compositional variables. While these gradients have been the subject of several recent and continuing investigations at other laboratories, the mechanisms are unknown, and there is no general agreement on their extent.

We shall heat U-Pu-O samples in a temperature gradient and determine the composition as a function of temperature. These samples will be analyzed by an extension of the scheme for determining O in urania from measurement of the lattice.

A series of calibration curves will be prepared, relating lattice size to oxygen-to-metal ratio for various U:Pu ratios. These curves will be made from data on samples of known U:Pu ratio in which the oxygen-to-metal ratios have been adjusted to the desired values by equilibration with various $CO:CO_2$ ratios.

Calculation of the Thermodynamic Properties of the Pu-O System
(J. M. Leitnaker, K. E. Spear)

The thermodynamic properties of the Pu-O system are not well resolved. It appears that there is a basic discrepancy in the available thermodynamic data. Rand and Markin,[15] who have calculated the vaporization behavior of the U-Pu-O system, concluded that there was a minimum in the vapor-pressure curve that did not correspond to a congruently vaporizing composition. Since simple phase theory shows that this prediction cannot be true, something must be wrong with the data. We assume that the error lies in the less-well-known Pu-O system, though this is not certain.

We have begun analyzing the data relating to the Pu-O system, and discrepancies have become apparent. The principal ones are the assignment of the entropy of PuO_2 at 298°K and the vaporization behavior. These discrepancies are large enough to influence the calculated behavior of the Pu-O system and its interactions.

---

[15]M. H. Rand and T. L. Markin, "Some Thermodynamic Aspects of $(U,Pu)O_2$ Solid Solutions and Their Use as Nuclear Fuels," pp. 637–650 in Thermodynamics of Nuclear Materials, 1967, International Atomic Energy Agency, Vienna, 1968.

We have discussed the implications of the entropy assignment with H. L. Davis of ORNL. For now, it seems reasonable to try to calculate the crystal-field splitting of the Pu^{+4} levels. Davis will calculate this beginning next quarter. This calculation may indicate the probable levels, and from these, one can calculate the electronic contribution to the heat capacity of PuO_2 and thence the entropy contribution.

Deformation of UO_2 (C. S. Morgan, L. L. Hall, A. R. Olsen)

We have continued investigating the out-of-reactor deformation characteristics of UO_2 specimens prepared from sol-gel powder. Long-term low-stress (2140 psi) deformation tests were made at 1350 and 1400°C. As is seen in Fig. 1.6, the tests at slightly higher temperature exhibited more extensive deformation.

Specimens of UO_2 prepared from ammonium diuranate (ADU) powder were also tested for deformation to compare structural strength with specimens from sol-gel powder. Although the ADU specimens had a higher density than the specimens prepared from sol-gel (97% compared to 93% of theoretical), they exhibited slightly less resistance to deformation when subjected to a steady rate of compressive creep. It is well established that increasing the oxygen-to-metal ratio above 2.00 increases the deformation rate of UO_2 under a given stress. While the specimens were treated to give an oxygen-to-metal ratio of 2.00, the analytical results are not yet available, so final evaluation of these tests cannot be made.

Irradiation Testing of $(U,Pu)O_2$ Fuels

A. R. Olsen

The final evaluation of sol-gel-derived $(U,Pu)O_2$ fuels will be based upon their irradiation performance. The irradiation testing program is concentrating on comparative tests of the fabrication forms: Sphere-Pac, pellets, and extrusions. The program includes thermal-flux irradiations that permit use of instrumented capsules and achievement of high burnup levels in relatively short periods of time. These tests will provide supplemental information essential to the analysis of the fast-flux

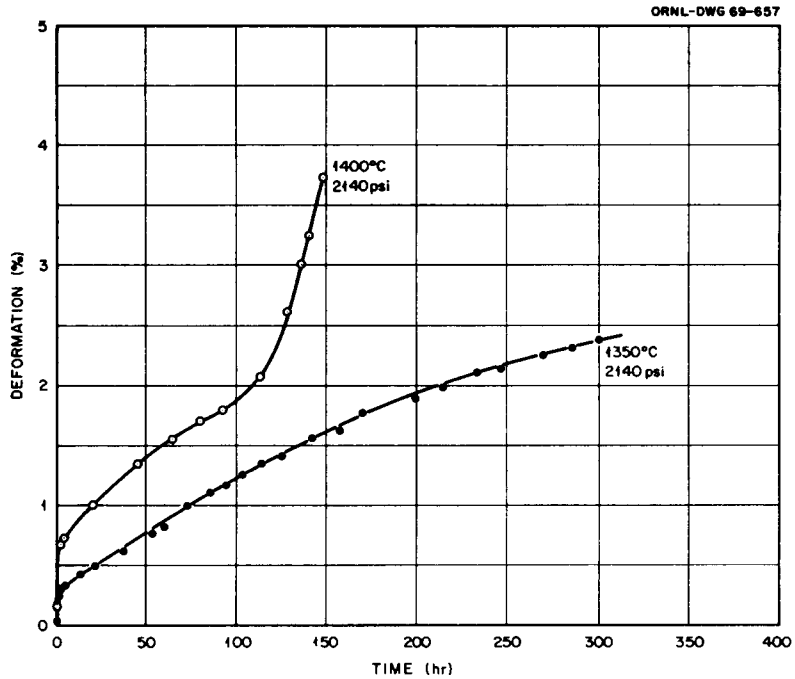

Fig. 1.6. Compressive Deformation of UO_2 Sol-Gel Pellets. Specimens were 0.16 in. in diameter, 0.33 in. high, and 93% of theoretical density.

irradiation tests, in which the radial fission-rate distribution and cladding damage are more typical of anticipated LMFBR operating conditions. The test program also includes transient tests to investigate fuel performance under abnormal operating conditions. The development of mathematical models to predict fuel behavior and of computer programs to perform the associated calculations is an integral part of the irradiation test program.

Uninstrumented Thermal-Flux Irradiation Tests (A. R. Olsen, J. Komatsu,[16] R. B. Fitts)

The status of the uninstrumented thermal-flux irradiation tests is given in Table 1.8. Two uninstrumented capsules are being irradiated in the Engineering Test Reactor (ETR), and two are undergoing postirradiation examination. Each capsule contains four test rods, each with a 3-in.-long fuel column.

---

[16]Guest scientist from Power Reactor and Nuclear Fuel Development Corporation, Tokai, Japan.

Table 1.8. Noninstrumented Irradiation Screening Tests of Sol-Gel-Derived Urania-Base Bulk Oxide Fuels

Experiment	Fuel		Number of Rods	Peak Burnup (% FIMA)[a]	Peak Linear Heat Rating (w/cm)	Current Status (12/31/69)
	Form	Composition				
43-99	Sphere-Pac	$(^{235}U_{0.8},Pu_{0.2})O_2$	2	1.8[b]	650[b]	Examined
43-100	Sphere-Pac	$(^{235}U_{0.8},Pu_{0.2})O_2$	2	1.7[b]	650[b]	Examined
43-103	Sphere-Pac	$UO_2(^{235}U_{0.2})$	3	5	690	Being examined
	Pellet	$UO_2(^{235}U_{0.2})$	1			
43-112	Sphere-Pac	$(^{238}U_{0.85},Pu_{0.15})O_2$	3	0.7	500	Being examined
		$UO_2(^{235}U_{0.2})$	1			
43-113	Sphere-Pac	$(^{238}U_{0.85},Pu_{0.15})O_2$	3	10[c]	500[c]	In reactor ≈ 6% FIMA
		$UO_2(^{235}U_{0.2})$	1			
43-115	Sphere-Pac	$(^{238}U_{0.85},Pu_{0.15})O_2$	3	5[c]	600[c]	In reactor ≈ 4% FIMA
		$UO_2(^{235}U_{0.2})$	1			

[a]FIMA = fissions per initial metal atom.

[b]These are preirradiated calculated values. Rods failed in reactor from overpowering at a peak burnup of 1.5% FIMA.

[c]These are target design values.

Examination in the hot cells has been concentrated on obtaining improved alpha autoradiographs. We have seen no gross segregation in any of the fuel sections examined. Both the alpha and beta-gamma autoradiographs will be analyzed in detail when the examination is complete.

Capsule 43-113, containing three Sphere-Pac fuel rods and one UO_2 pellet rod, has been exposed to about 20×10^{20} neutrons/cm^2. It is scheduled for removal at an exposure level of 43×10^{20} neutrons/cm^2. Capsule 43-115 is a duplicate of 43-113 but is operating at a linear heat rating of 600 w/cm (18 kw/ft) rather than 500 w/cm (14 kw/ft). The capsule has been exposed to a fluence of about 12×10^{20} neutrons/cm^2 and is scheduled for removal from the reactor during the next quarter when it achieves the target level of 15×10^{20} neutrons/cm^2.

A new capsule, 43-116, is being fabricated for irradiation for 2 to 3 ETR cycles. This capsule will contain four Sphere-Pac rods of $(U_{0.85},Pu_{0.15})O_2$ fuel to provide fuel for chemical dissolution studies.

ORR Instrumented Tests (R. B. Fitts)

The ORR instrumented irradiation tests are designed to monitor the thermal performance of test fuel rods. Temperatures of the cladding and fuel center and rates of heat generation in the fuel rod are continuously measured and recorded. These data will be used to evaluate the in-reactor thermal characteristics of various fuels and the effects of irradiation conditions upon the temperatures and rates of structural change within the operating fuels.

Capsule SG-1. — This first instrumented capsule contained sol-gel-derived $(U_{0.85},Pu_{0.15})O_2$ fuel fabricated by the Sphere-Pac technique. The main result from this test was, as planned, the verification of the capsule design by the achievement of desired cladding temperatures at the designed rates of heat generation. Fuel behavior has been partially analyzed, and a summary of the fuel central temperature, heat-generation rate, and smeared thermal conductivity[17] is given in Fig. 1.7. We calculated these conductivity values from temperatures measured at the center of

[17]R. B. Fitts, Fuels and Materials Development Program Quart. Progr. Rept. Sept. 30, 1968, ORNL-4350, pp. 25–29.

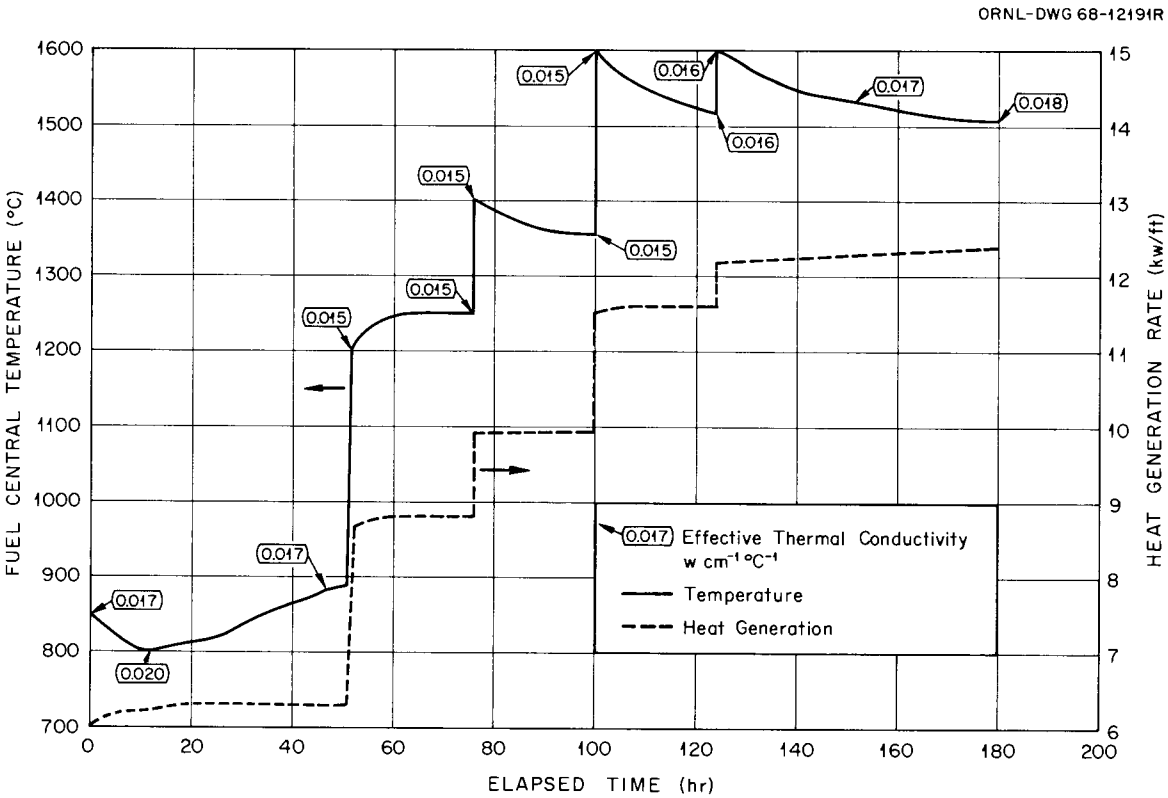

Fig. 1.7. History of First ORR Capsule SG-1 Operation.

the fuel and the surface of the cladding. From these data, it is apparent that the effective conductivity of the Sphere-Pac fuel is quite similar to that for pellet fuels of comparable smear density. The fuel central temperature is seen to decrease with time at constant heat generation for temperatures above 1250°C, and we believe that this decrease indicates the rate of fuel densification. The increase in central temperature with time after stepping to about 8.75 kw/ft and 1200°C appears to be associated with an increase in heat generation. The erratic behavior seen over the first 50 hr of operation at low temperatures is not understood but may be associated with the evolution and redistribution of impurity gases within the fuel rod.

We plan no further analysis of fuel behavior in this capsule, since it was operated to gain data on capsule operation rather than fuel behavior.

Capsule SG-2. — The fuel rods for this capsule are being loaded with Sphere-Pac $(U_{0.8},Pu_{0.2})O_2$ from a batch of fuel that will also be

used for the first series of TREAT tests.[18] This capsule will initially be operated at central fuel temperatures below 1000°C to obtain data for comparison with out-of-reactor data, most of which is for lower temperatures, and in particular with that being developed for Sphere-Pac fuels.[19] The final period of operation will be at a temperature where fuel restructuring is occurring (1200 to 1400°C) for direct correlation of postirradiation structure with operating fuel temperature.

Transient Testing of Sol-Gel $(U,Pu)O_2$ Fuels (C. M. Cox)

The purpose of the transient testing program is to investigate the behavior of sol-gel-derived $(U,Pu)O_2$ fuels under conditions simulating accidental power excursions. These experiments will be performed at the TREAT.

The hazards analysis for the first four experiments with fuel that was not preirradiated is about 75% complete.

A series of calculations of transient heat transfer have been performed to define the desired transient conditions for the first experiments. Typical TREAT transients with initial reactor periods of 155 and 200 msec have been assumed. These are "clipped" by control rod insertion to vary the integrated power. Calculations for the 155 msec case indicate that as little as 25% variation in integrated power can give the desired range of melting of fuel volume, 25 to 75%. Since variations of 15% in the desired as opposed to the resulting transient pulses are common in this reactor, close experimental control is impossible. Judging from experimental data from other investigators, we expect these fuel rods to fail by melting of the cladding if the melting of the fuel volume in any cross section exceeds about 70%. Under these conditions, the peak temperatures calculated for the cladding are several hundred degrees below melting. We predict, however, that the fuel surface temperature will be above the melting point for the cladding material, and failure can be expected. This is consistent with motion-picture

---

[18]See C. M. Cox, "Transient Testing of Sol-Gel $(U,Pu)O_2$ Fuels," pp. 27–28, this report.

[19]Peter Spindler, Fuels and Materials Development Program Quart. Progr. Rept. June 30, 1968, ORNL-4330, p. 16.

observations of water- and gas-cooled experiments that show that failure begins in localized hot spots.

We have performed three scoping experiments on thermal shock with 400-μm-diam 99% dense sol-gel-derived UO_2 microspheres obtained from the Chemical Technology Division. Spheres were dropped into an induction furnace at 1200, 1600, and 1900°C, held at temperature for 7 sec, and cooled at 3 to 10°C/sec. The experiments were performed in a dynamic vacuum with a pressure less than 2×10^{-5} torr before the microspheres were introduced. Off-gassing was apparent in all cases from momentary increases in the pressure of the system, but metallographic examination showed no cracks.

Fast-Flux Irradiation Tests (A. R. Olsen, C. M. Cox)

The five encapsulated tests of Sphere-Pac sol-gel $(U,Pu)O_2$ fuels for the EBR-II Series-I group have been fabricated. The hazards analysis for these tests was submitted and is apparently acceptable pending final nondestructive testing of the capsules.

Since the EBR-II cycle schedule was changed to move a planned, extended shutdown from before to after cycle 32, the irradiation of subassembly X050, which will contain these capsules, was rescheduled to start with cycle 33. In addition to the sol-gel Sphere-Pac capsules, this subassembly will contain two pins with mixed carbide fuel, four capsules containing samples of structural materials, and eight other capsules containing oxide fuels. The subassembly will be irradiated in the 4-N2 position to a proposed 5500 Mwd irradiation exposure. The exposure is controlled by the additional irradiation increment required to bring some of the oxide pins previously irradiated in subassembly XG05 up to their target exposure level. Based on the proposed loading diagram and the assembled fuel rod parameters, we are beginning calculations to predict the burnup level that will be achieved by the sol-gel capsules during this exposure.

We have continued our reactor physics analysis of the EBR-II to compare the effects of the P_0 vs P_1 vs P_3 scattering approximations using

the ANISN neutron transport code.[20] The fission rate distributions predicted using P_3 or P_1 scattering are within 0.5% of each other and agree adequately with experimental data, but the values from the P_0 case with no transport correction differ by as much as 13% from the other calculations.

Irradiation Test Calculations

Comparison of Thermal-Flux and Fast-Flux Thermal Gradients (R. B. Fitts). — Much of the initial irradiation testing of fast-reactor fuels is being carried out in thermal-flux reactors because of the limited space available for fast-flux testing. Since the two types of fluxes produce different distributions of fissioning and temperature for a given rate of heat generation, there is some question about the validity of testing fast-reactor fuels in the thermal flux. A comparison of the two has been made on the basis of the radial fission rate and temperature profiles expected to exist in operating $(U_{0.85},Pu_{0.15})O_2$ fuels. The PRØFIL computer code[21] was used to calculate the temperatures and thermal restructuring of the fuel. The 0.230-in.-OD fuel was initially at 80 or 87% of theoretical density and operating at a surface temperature of 750°C. The calculations assumed density changes such that all fuel between 1400 and 1750°C became 94% dense and all above 1750°C became 97% dense. Such restructuring has been observed to occur within the first few hours of irradiation testing.[22] Heat generation within the fuel was assumed to be 180 Mev/fission plus 0.5 w/g gamma heat. The initial fission rates were assumed uniform for the fast-flux case. They were based upon the flux depression predicted by the ANISN neutron transport code[20] for a typical ETR flux spectrum in the reflector region for the

---

[20] W. W. Engle, Jr., A User's Manual for ANISN, K-1693 (March 1967).

[21] C. M. Cox and F. J. Homan, PRØFIL — A One-Dimensional FORTRAN IV Program for Computing Steady-State Temperature Distribution in Cylindrical Ceramic Fuels, ORNL-TM-2443 (March 1969).

[22] G. Testa *et al.*, Trans. Am. Nucl. Soc. 11(2), 494 (1968).

case of thermal flux. The thermal conductivity of the fuel was assumed to be that given by W. E. Bailey et al.[23]

In Fig. 1.8 the relationship between the fuel central temperature and heat generation rate is shown for fast- and thermal-flux irradiations. It is interesting to note that an increased initial fuel density at linear heat ratings above about 10 kw/ft increases the peak fuel temperature after in-reactor restructuring despite the higher initial fuel thermal conductivity of the higher density material. This is the result of less restructuring in the peripheral fuel regions as calculated by the current step densification model. Figure 1.9 allows comparison of the predicted density, fission rate (heat generation) profiles, and temperature profiles for a fuel, initially 80% dense, operating in a thermal and a fast flux.

[23]W. E. Bailey et al., "Thermal Conductivity of Uranium-Plutonium Oxide Fuels," pp. 293–308 in Intern. Symp. on Fuels Technol., Nucl. Met. 13, AIME, New York (1968).

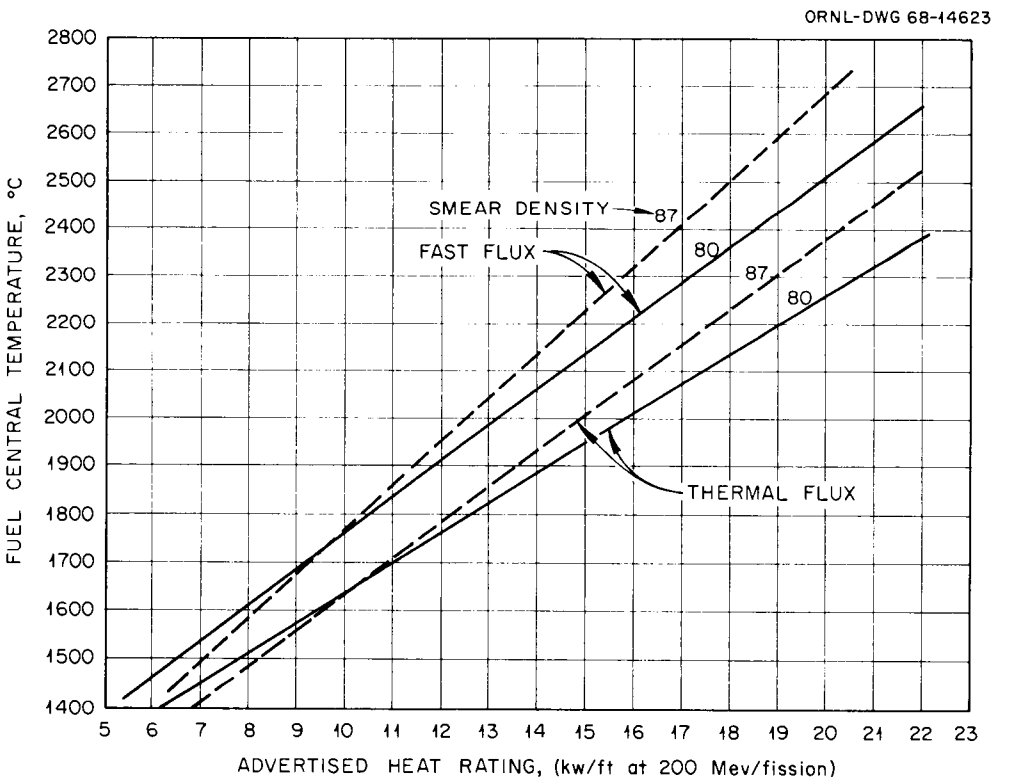

Fig. 1.8. Fuel Central Temperature During Fast- and Thermal-Flux Testing Versus Advertised Heat Rating.

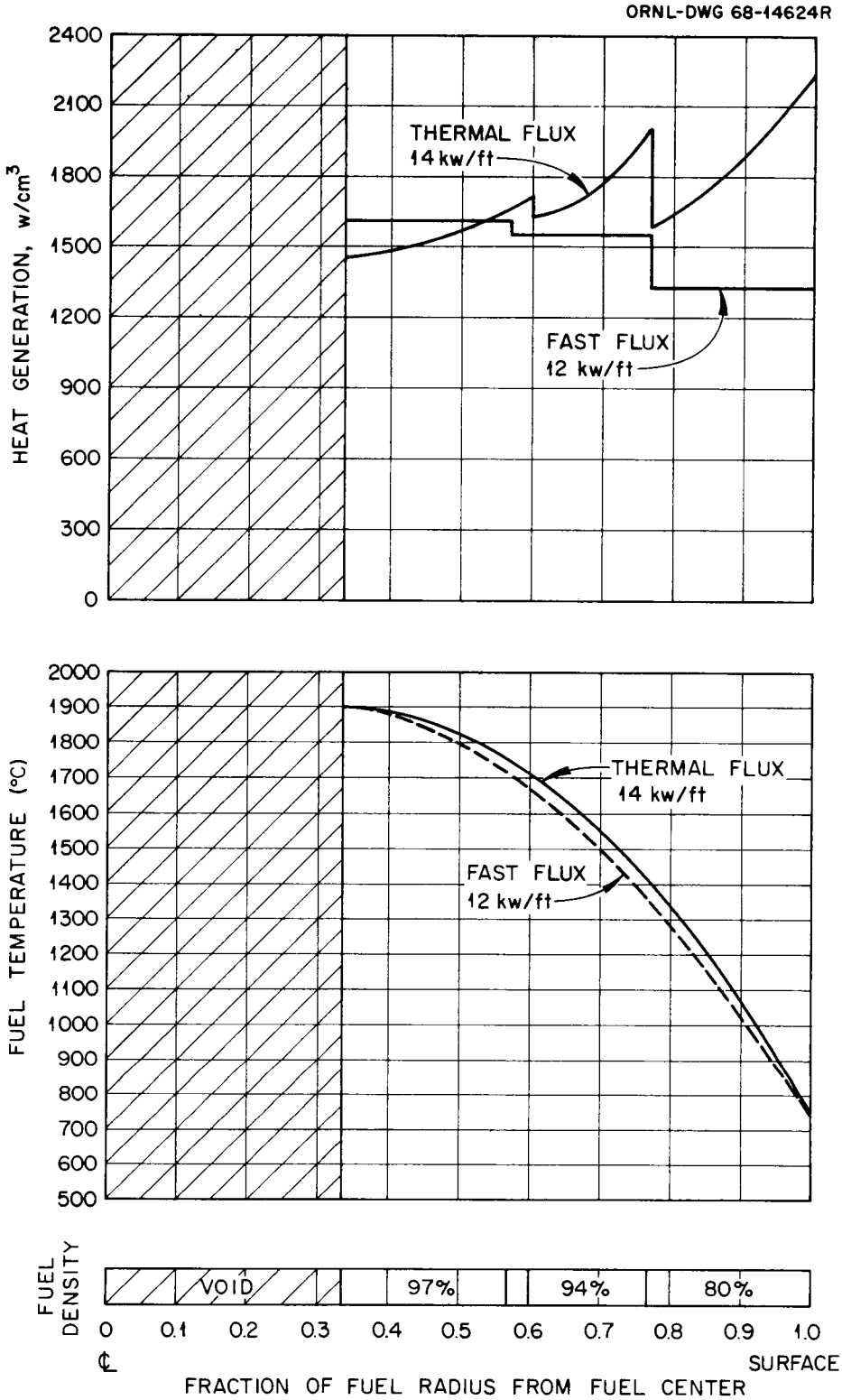

Fig. 1.9. Comparison of Calculated Fuel Temperatures and Heat Generations for Fast- and Thermal-Flux Irradiation of $(U_{0.8},Pu_{0.2})O_2$.

In accordance with Fig. 1.9, a 1900°C central temperature requires operation at about 12 kw/ft in a fast flux and 14 kw/ft in the thermal flux. Similar analyses have been made previously. Those reported by workers at General Electric[24] were performed some time ago and apparently did not include the effects of fuel densification, which causes significant changes in the calculated temperatures. The recent work of Sayles[25] appears to be based upon an analysis similar to that used here, but insufficient information is presented in his paper to perform the comparison that we desired.

These calculations predict that fuel temperature profiles are very similar in fast- and thermal-flux tests if the rates of heat generation are properly chosen. No great differences in thermal gradient are to be expected, and the fuel structures will therefore be very similar until significant fission products accumulate to alter the characteristics of the fuel. The most important difference, in terms of fuel behavior, is probably the generation of a much greater portion of the fission products in the cooler regions near the surface of the fuel during thermal-flux testing. This difference in distribution would be expected to influence the chemical and mechanical interactions between fuel and cladding, though the degree of this effect is not known.

It appears from our analysis, which considers only the fuel behavior and not the effects of exposure to fast neutrons on the mechanical properties of the cladding, that thermal-flux testing of fast-reactor fuels is quite adequate for lower burnup evaluations of such factors as in-reactor fuel restructuring, thermal conductivity, and basic compatibility of fuel and cladding. Long-term tests to prototypic burnups can be carried out in a thermal flux but are subject to careful interpretation and require confirmation in fast-flux tests.

---

[24] Fast Ceramic Reactor Development Program, Sixteenth Quart. Rept., August–October 1965, GEAP-4982, p. 4-4 (January 1966).

[25] C. W. Sayles, Trans. Am. Nucl. Soc. 11(2), 509–510 (1968).

Computer Code for Thermal Expansion of Fuel and Cladding (C. M. Cox, F. J. Homan). — The PRØFIL code for describing temperature distributions in ceramic fuel pins has been extended to include the cladding. The new code, called FMØDEL, includes thermal expansion of the fuel and cladding and a modified Greenwood-Speight[26] model for fuel swelling. The FMØDEL code is being expanded to include an analysis of stress and strain.

---

[26]G. W. Greenwood and M. V. Speight, J. Nucl. Mater. 10(2), 140–144 (1963).

2. DEVELOPMENT OF HIGH-PERFORMANCE LMFBR FUELS

P. Patriarca J. L. Scott

The goals of this program are to investigate the properties and behavior of those uranium- and plutonium-based ceramic fuels that we term conductors — such as the mononitrides, carbonitrides and monocarbides — and to compare their potential as Liquid Metal Fast Breeder Reactor (LMFBR) fuel with that of $(U,Pu)O_2$, which by comparison is an insulator. Since the thermal conductivity of the ceramic conductors is about ten times that of $(U,Pu)O_2$, it is theoretically possible to operate a conductor at ten times the power density with the same temperature at the center of the fuel. In practice, heat-transfer limitations, thermal stresses in the cladding, and high rates of swelling at high temperatures limit the power density that can be achieved with thermal conducting fuels to about two or three times that of $(U,Pu)O_2$ — still a challenging improvement. Additionally, the margins for transient overpower in the ceramic conductors are much higher than those for $(U,Pu)O_2$.

We seek to provide the information necessary for evaluating the true potential of nitrides, carbonitrides and carbides in comparison to each other and to mixed oxides. We need to define the structures, composition, and quality control required to achieve 150,000 Mwd/ton at peak linear heat ratings of 30 to 50 kw/ft. We must also demonstrate the possibility of a low-cost fuel cycle for manufacturing fuel with the needed properties. And since austenitic stainless steel is a poor conductor of heat, we seek to establish the physical and thermodynamic criteria for the new cladding material that will probably be required to exploit the conducting fuels.

Our work is now oriented toward fabricating and characterizing (U,Pu)N with controlled low or high porosity distributed in different ways. The requisit void volume in a fuel pin may be provided in several ways if dense fuel is used, such as by a large sodium-filled gap between fuel and cladding or by dished or annular pellets. It may also be provided by the internal porosity of low-density fuel pellets. We use both hot pressing and cold pressing and sintering. In our characterization work, emphasis is being placed on reliable chemical analyses of U, Pu, C,

O, and N. We have glove boxes with less than 20 ppm O and 10 ppm moisture that allow us close control of oxygen content, and we have facilities in operation for x-ray, metallographic, thermogravimetric (TGA), and differential thermal (DTA) analyses. We are also assessing the effects of temperature gradient and burnup on the activities of N, C, and O. Finally, we are developing the information needed to design the decisive experiments that will demonstrate the best type of pin for meeting LMFBR requirements.

Synthesis, Fabrication, and Characterization of Nitride Fuels

Synthesis and Fabrication of UN (R. A. Potter, V. J. Tennery)

We continued with the routine synthesis of UN powder from which we pressed and sintered specimens for distribution to various groups concerned with measurements of physical properties and with irradiation testing. We also made several experiments that will help us better understand the physical character of the synthesized material. For some time, we have been aware of a temperature gradient in our synthesis rig. Although we did not make quantitative measurements of the gradient, we did perform an experiment that indicated the effects of the gradient on the synthesized powder and on the sintered product made from the powder. The experiment, though simple, resulted in some rather unexpected revelations.

By systematic sampling and x-ray analysis of our synthesized product, we found that powder from what had been the cold end of the reaction vessel during synthesis consisted of the higher nitride, $UN_{1.5}$-$UN_{1.75}$. Samples from what had been the intermediate- and high-temperature zones were mixtures of UN and higher nitride. Although the x-ray analyses of the powder samples did not indicate the presence of O, we observed second-phase uranium oxide by both metallographic and x-ray analyses of sintered specimens prepared from the powders.

During the qualitative metallographic examination of the sintered specimens, we found considerably more oxide in the microstructure of samples prepared from the higher nitride than in those from the mixtures

of UN and the higher nitride. This was reasonable, since the powder with the higher nitride came from that part of the reaction vessel where the gases used for the synthesis enter. Furthermore, the higher nitride, having been exposed to less heat than the mixture, has greater surface area and not only serves as an efficient "getter" of contaminants in the gas stream but is more susceptible to oxidation during handling after removal from the synthesis rig. We do not yet understand all the ramifications of the characteristics associated with the higher nitride prepared by our synthesis process, but our results from sintering trials show that it is an extremely active material that can be sintered nearly to the theoretical density of UN. For comparison, microstructures of sintered UN prepared from the higher nitride and from the mixture of UN and the higher nitride are shown in Fig. 2.1.

We are still trying to develop reliable methods to better characterize our synthesized powder; in the meanwhile, we must rely on qualitative results and observations to control our production of samples.

Preparation of UN Pellets Containing ^{15}N (R. A. Potter, T. G. Godfrey)

Of concern to the use of nitride fuels for the LMFBR is the generation of helium gas within the fuel through the $^{14}N(n,\alpha)^{11}B$ reaction and the corresponding loss of neutrons. Recently we found that the use of $U^{15}N$ fuel in an LMFBR, with proper recycle of the $^{15}N_2$, may be economically feasible because of the increased neutron economy and reduced fuel inventory.[1] Therefore, high- and low-temperature irradiation experiments (ORNL 41-41) to fluences of 2 to 4×10^{21} neutrons/cm^2 (> 1 Mev) are to be conducted to compare directly the effects of fast neutrons on four candidate fuels: $U^{14}N$, $U^{15}N$, UC, and $U(C_{0.5}N_{0.5})$.

We fabricated the $U^{14}N$ and $U(C_{0.5}N_{0.5})$ specimens by our usual techniques, cold pressing followed by sintering. The UC specimens are to be arc-cast. We have received from the CMF Division of Los Alamos Scientific Laboratory the first of two shipments of $^{15}N_2$ necessary

[1]J. L. Scott and W. O. Harms, Metals and Ceramics Div. Ann. Progr. Rept. June 30, 1966, ORNL-3970, p. 91.

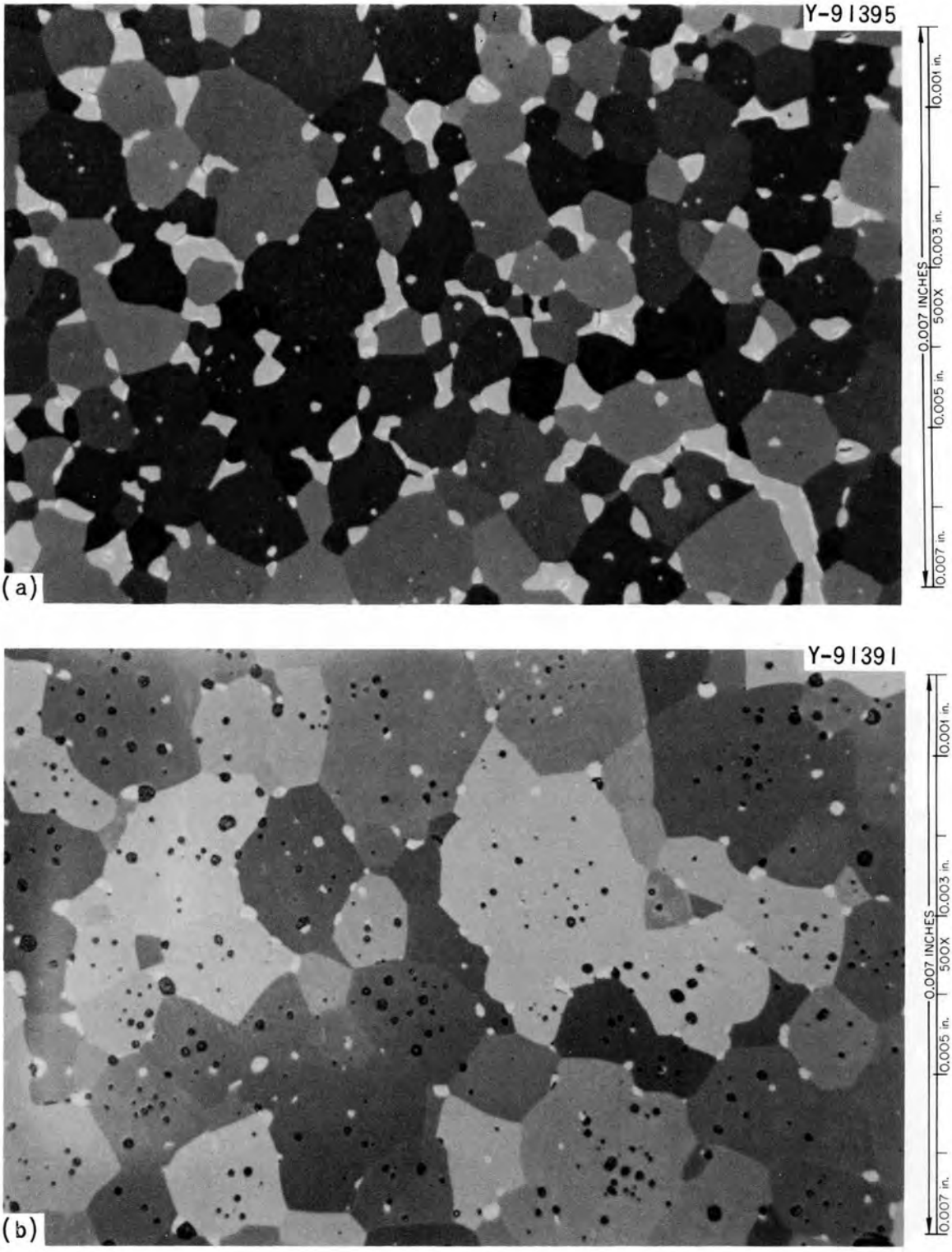

Fig. 2.1. Microstructures of UN Specimens Prepared From Selected Samples of Nitride Powders. Gray phase is UO_2. (a) Nearly theoretically dense specimen prepared from $UN_{1.5}$-$UN_{1.75}$ powder. (b) A 95.5% dense specimen prepared from a mixture of $UN_{1.5}$-$UN_{1.75}$ and UN. Etchant: 30 parts lactic, 10 parts HNO_3, 1 part HF acids.

for fabrication the $U^{15}N$ specimens. The mass spectrometer analysis of the gas is given below:

H_2	300 ppm	O_2	30 ppm
H_2O	100 ppm	A	< 30 ppm
$^{14}N_2$ + CO	1500 ppm	CO_2	30 ppm
$^{15}N_2$	99.79%		

This analysis indicates that the N_2 is 99.89% enriched in $^{15}N_2$ and is exceptionally clean.

To prepare the apparatus we use to synthesize nitrides for use with the $^{15}N_2$, we modified it so that it accepts a specially fabricated gas system consisting of a fresh Nb–1% Zr getter and new or refurbished valves and hardware. This new gas system will also be used on the sintering furnace to assure minimum contamination and maximum conservation of the $^{15}N_2$. A system of molecular-sieve pumps will remove $^{15}N_2$ from the sintering furnace and transfer it back to the original gas cylinders.

A 540-g rod of depleted U was cleaned and readied for the synthesis process, which will begin soon. The dies for cold pressing irradiation test specimens are on hand.

Because of the uniqueness of this material and because enough $^{15}N_2$ is available for only one sintering run, all of the synthesized powder will be fabricated into pellets for possible use in future experiments.

Synthesis, Fabrication, and Characterization of Mixed Nitrides
(E. S. Bomar, Ji Young Chang)

Our goal is to synthesize high-purity (U,Pu)N powder and fabricate it into a variety of shapes, sizes, and densities for determination of physical and mechanical properties and for irradiation testing. Synthesis involves hydriding, dehydriding and nitriding of plutonium and prealloyed powders. Fabrication includes both hot pressing and cold pressing followed by sintering.

We completed the metallographic examination of the first 3/8-in.-diam × 1/4 in.-long hot-pressed UN specimens that were prepared during the last report period and found the grain size to be extremely

small compared with that of sintered material of comparable density. The starting powder had about 5000 ppm O contamination that resulted in a second phase, shown in Fig. 2.2. These pellets were pressed at 6200 psi at 1450°C and were essentially fully dense. A pellet of the same size that was pressed at 2100 psi had a density of about 90% of theoretical.

We also continued the synthesis of UN to obtain experience in preparation for work with (U,Pu)N. The existing tube furnaces will accommodate 50- to 70-g batches of the nitride. A charge of metallic U can be converted to UN in a 1 1/2-day cycle. We believe the experience gained from preparing five batches of UN is sufficient to allow us to begin work with the mixed nitride, though considerable experimentation is still needed to optimize the synthesis procedure.

We introduced Pu into the Interim Plutonium Facility in mid-December when two cannisters containing 950 and 1025 g of Pu, respectively, were successively unloaded and bagged into a glove box for weighing and

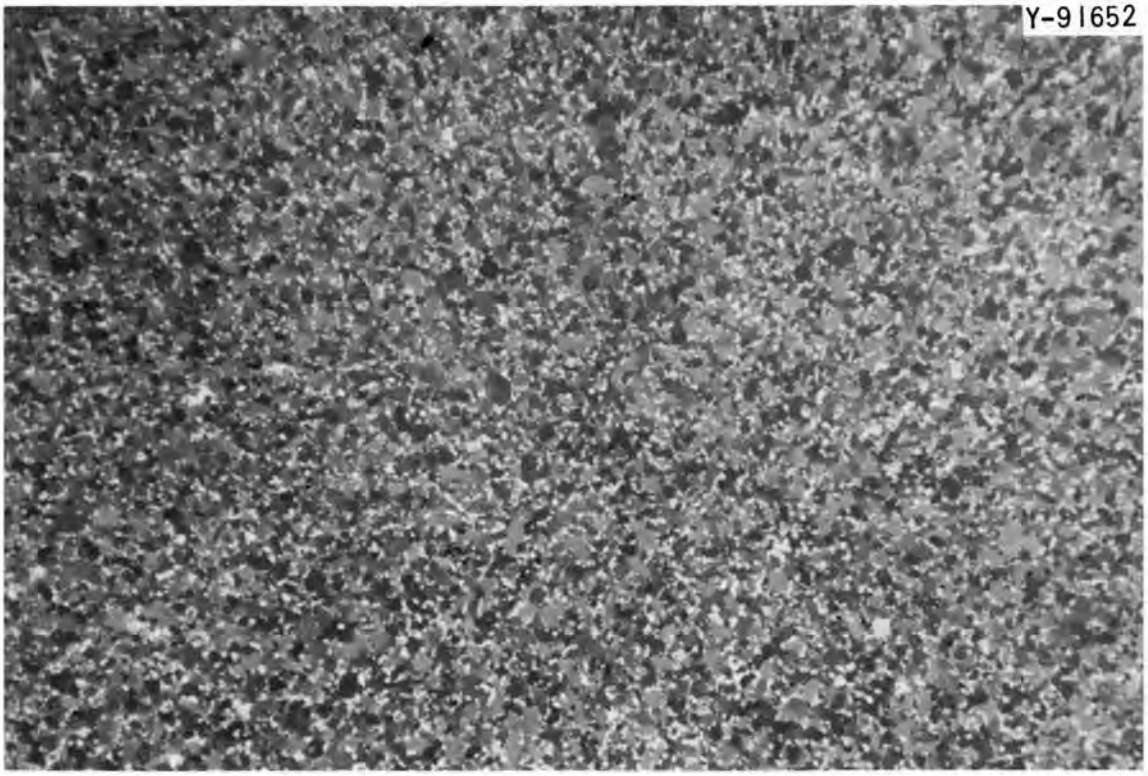

Fig. 2.2. Microstructure of Hot-Pressed UN Containing 5000 ppm O. Lightest colored phase is UO_2. Almost no porosity is visible. Etched with 90 Lactic, 30 HNO_3, 3 HF for 50 sec. 800X.

subdividing. These items had been stored in the storage vault in the ORNL Accountability Office for over a year. The metal had oxidized considerably; 35 g of fine oxide powder was removed from one container and 50 g from another. Each batch of metal was divided into four approximately equal portions, which were placed into metal capsules sealed with O-rings; that portion not needed for near-term research was returned to the storage vault. The Analytical Chemistry Laboratory removed the adherent oxide from the metal with an HCl solution. Since we were unable, with equipment now in our glove box, to break the metal chunks into smaller pieces suitable for preparation of an alloy with U, we melted the Pu under vacuum in an elongated graphite boat coated with Y_2O_3.

The high level of moisture observed in the glove box containing the tube furnaces used for synthesis and sintering work was traced to a very small defect in a soldered fitting. This was corrected so that the level of moisture for this box, which has a volume of about 45 ft^3, was below 10 ppm when the entering Ar contained about 3 ppm. The additional experience acquired by the operators and the additional conditioning of the glove boxes has resulted in a further lowering of the average level of impurities in the atmosphere for our glove boxes. Even while work was being done in the boxes, we recently observed typical values of 8 ppm moisture and 12 ppm O at an argon flow rate that changed the atmosphere in each box once per hour; the supply Ar at that time contained 2 ppm moisture and 2 ppm O.

Characterization of UN and (U,Pu)N (V. J. Tennery, R. A. Potter)

X-ray Techniques and Facilities for Inert-Atmosphere Glove Box. — Our work was directed toward techniques for preparing specimens for x-ray examination in the diffractometer and the powder camera within an inert-atmosphere glove box. An objective is to perfect the techniques so that they will be applicable to specimens containing Pu and yet will produce packages that have essentially no exterior contamination, since the diffractometer must remain essentially uncontaminated even though it is within a glove box and since the powder camera will actually be used outside a glove box. One promising technique for diffractometer specimens

involves mixing the sample powder with an amyl acetate-parlodian solution and casting the mixture into machined aluminum holders that lie on a very smooth Teflon surface. With a proper concentration of parlodian in the amyl acetate, the mixture shrinks very little, and as the amyl acetate evaporates, a very smooth, solid, diffracting surface is produced in which the powder particles are all entrapped in parlodian. A mechanically strong specimen is produced, and the technique greatly reduces the contamination hazard due to powder particles falling onto the x-ray equipment. For specimens containing Pu, these sample holders will be permanently encased in a suitable thin plastic bag before being introduced into the goniometer glove box.

For work involving the Debye-Scherrer x-ray diffraction camera, we obtained micromanipulators for handling the delicate capillaries and for sealing them by fusing the glass walls of the capillary to form the primary containment. The loaded capillary is placed into a suitable holder, and a gelatin capsule is placed over the capillary and sealed to the base to form the secondary containment. This assembly, which is not contaminated on the outside, is then removed from the glove box and mounted in a Debye-Scherrer camera that has a removable film cassette. The capillary assembly is properly aligned optically in the camera by means of a goniometer before the x-ray exposure.

All of the equipment for this x-ray facility was obtained except for one of the cameras and the mounting table for the x-ray tube for camera work, which will be located outside the glove boxes.

Chemical and Metallographic Analyses of UN. — Due to persistent difficulties in obtaining consistent chemical analyses of UN specimens, particularly for nitrogen and oxygen content, we have begun a comparative experiment to determine precisely what needs to be done to the analytical techniques to provide routine, reliable analyses of these materials. As an initial part of this experiment, we prepared a set of sintered UN specimens that were characterized as having small traces of UO_2 in the microstructure. Specimens from this group will be sent in helium-filled capsules to three outside sites and to the Analytical Chemistry Division for analysis of U, N, C, and O. Quantitative

metallography is being performed on the control samples from this group of specimens to establish the concentration of UO_2 in the microstructure. If the chemical analyses for O are reliable, the difference between the oxygen concentrations determined chemically and metallographically should establish within reasonably narrow limits the amount of O that was present in the nitride and not visible as a second phase. This O presumably would be within the mononitride crystal structure.

Purification and Control of Inert Atmosphere for Glove Boxes. — To determine the practical limit to which O can be excluded from the process of nitride synthesis, using the present apparatus, we purchased a commercial purifier for glove-box atmospheres that will soon be installed on the glove boxes now used for large batches. The boxes can now be maintained with argon atmospheres with typical purities of 10 to 15 ppm O_2 and 5 to 15 ppm moisture when the gloves are extended. Working in the gloves causes the moisture level to rise. The new purifier should produce a box atmosphere containing essentially no O_2 or moisture. Another possible source of contaminating O_2 is the purified gases used in the synthesis operations. We are studying these for ways to ensure improved gas purity at reasonable cost. An obvious remaining source for contamination by O in the nitride synthesis and fabrication process is the U. Steps are being taken to establish the concentrations of O in the U that is used and to attempt to correlate these quantities with the levels of O measured in the synthesized nitride powders.

Synthesis, Fabrication, and Thermodynamic Properties of Carbonitride Fuels

Manufacture of UC, UN, and U(C,N) from UO_2 (T. B. Lindemer, J. M. Leitnaker)

We are studying the kinetics of the conversion of sol-gel UO_2 to uranium carbides, nitrides, and carbonitrides to determine the mechanisms that control the rate of the conversion processes. This information is fundamental to the design and economic analysis of reactor fuel cycles.

Kinetics of the UC_2-N_2 Reaction. — During the previous two quarters we studied the kinetics of the reaction of N_2 with microspheres of UC_2

(nominal dicarbide) to produce U(C,N) (ref. 2,3). This phase of the study generally involved the reaction of UC_2 that orginally contained 1 vol % free C. We found that the reaction was controlled at the interface between UC_2 and U(C,N). About 4% of the particles, however, did not originally contain any free C. These particles reacted differently, and the reaction rate was about 50% of that for the majority of the particles. We were not able to determine the rate-controlling mechanism for the particles that did not contain free C because they did not occur in sufficient numbers in our samples. We are now adapting the investigation for the study of these particles; we expect the additional information to explain some of the behavior observed in the companion studies of the kinetics and thermodynamics of reactions in the U-C-N system.

We have developed several new procedures and materials for this continued investigation. A principal change in procedure was a redesigning of the fluidized reaction bed and of the sampling devices so that larger samples could be obtained at a given time during the reaction. This system is now operable. We will mount 900 microspheres from each of these samples so that we can measure the 30 to 40 microspheres that are free of initial C and analyze the results with our models for the kinetics of reactions in spheres. Additional UC_2 has also been ordered and received from Gulf General Atomic. About 25% of this material is microspheres without free C, and this increased percentage will facilitate our examination procedures. In addition, we will compare the kinetic behavior of the UC_2 from the two different sources to determine whether there are any significant compositional effects.

UO_2-C-N_2-H_2 Reactions. — In the basic studies of the UC_2-N_2 reaction, we observed that the C in the system acted as a short-circuit path along which N_2 could migrate into and react with the interior of the UC_2 microsphere.[3] This mechanism is also implied in the synthesis of U(C,N) via

---

[2]T. B. Lindemer, Fuels and Materials Development Program Quart. Progr. Rept. June 30, 1968, ORNL-4330, pp. 32–39.

[3]T. B. Lindemer and J. M. Leitnaker, Fuels and Materials Development Program Quart. Progr. Rept. Sept. 30, 1968, ORNL-4350, pp. 39–47.

the reaction of UO_2-C sol-gel shards with N_2 (ref. 4). We also noted that H_2 was very effective in stripping the C produced in the UC_2-N_2 reactions.[3] We are now applying this information to the conversion of UO_2-C sol-gel microspheres to determine if the process described in ref. 4 can be improved. Our present experiments involve reacting microspheres containing controlled amounts of C in excess of that necessary for the conversion of UO_2 to U(C,N); this excess C may provide a short-circuit path for the N_2 at all stages of the reaction. The excess C is then removed via reaction with H_2. Our experiments, which are very preliminary, demonstrate the validity of our concepts, but we have yet to optimize the time and temperature variables.

Thermodynamic Investigations of High-Performance Fuel Systems

K. E. Spear

The goal of our thermodynamics program for high-performance fuels, the carbides, nitrides, and carbonitrides, is to be able to predict the limiting equilibrium behavior of heat-transfer bonding between fuel and cladding in fast-reactor environments. Our experiments, though limited to measurements out of reactor, are of value for defining and understanding the factors affecting fuel performance.

These experiments involve the interactions of fuel and cladding, fuel burnup, temperature gradients, impurities in the fuel, and methods for tailoring the fuel to force thermodynamic compatibility. Our investigations in these areas are designed to give basic information on the problems of containment for fuel in a fast reactor. Priority is being given to sodium-bonded fuel in austenitic stainless steels and vanadium-based alloys.

---

[4] J. M. Leitnaker, R. L. Beatty, K. Notz, K. E. Spear, and T. B. Lindemer, Fuels and Materials Development Program Quart. Progr. Rept. June 30, 1968, ORNL-4330, pp. 28–31.

Chemical Effects of Nuclear Burnup on High-Performance Fuels
(K. E. Spear, J. M. Leitnaker)

The ability to predict and understand the equilibrium chemical interactions of a reactor fuel requires, among other things, a knowledge of the effects of nuclear burnup on the fuel. Our calculations of these effects on mixed (U,Pu)N and (U,Pu)C fuels are reported here.

The fissioning of Pu in (U,Pu)N or (U,Pu)C fuels not only forms fission products but also releases the atom of N or C that was bound to the Pu. The final state of this released atom depends on its relative affinity for the produced fission products and remaining fuel. We have used avilable thermodynamic and phase data to calculate the equilibrium chemical state of nitride and carbide fuels in a fast reactor environment.

We have listed in Table 2.1 the relative concentrations of atoms in $(U_{0.8}Pu_{0.2})N$ and $(U_{0.8}Pu_{0.2})C$ fuels after zero time, six months, and two years at full power of 185 Mw/ton. We assumed that the ^{239}Pu formed from ^{238}U is equal to 0.9 times the ^{239}Pu fissioned. We also assumed the ^{14}N burnup to form ^{4}He and ^{11}B to occur at 4.6% of the rate of the fissioning of the heavy metal atoms.

In Table 2.2, we have given the distribution of bound N and C in nitride and carbide fuels after zero time, six months, and two years at full power of 185 Mw/ton. There are several uncertainties in the data listed there, however. For example, we assumed the B would form BN. It may be that the ZrB_2 is the stable species with the N from BN and part of the ZrN being bound as additional U_2N_3. Also, intermetallics such as $ZrPd_3$ may form. The result would be the formation of more U_2N_3 or U_2C_3 than we have calculated. The uncertainty listed in the amount of rare earth sesquicarbide $[(R.E.)_2C_3]$ formed is most likely not real since the $(R.E.)_2C_3$ and $(U,Pu)_2C_3$ probably form a solid solution. Also, since the thermodynamic stabilities of $(R.E.)_2C_3$ and $(U,Pu)_2C_3$ are so close to

Table 2.1. Relative Atomic Concentrations of Elements in a Nitride or Carbide Fast-Reactor Fuel as a Function of Time at Full Power (185 Mw/ton)

Elements	Number of Atoms		
	0 Time	6 Months	2 Years
	Major Elements in Fuel		
^{238}U (ref. a)	8000	7670	6680
^{239}Pu (ref. a)	2000	1963	1853
^{12}C	10,000	10,000	10,000
or			
^{14}N (ref. b)	10,000	9983	9933
^{4}He or ^{11}B (ref. b)		17	67
	Major Fission Products[c]		
Kr		9	37
Rb		5	19
Sr		16	57
Y		6	25
Zr		74	275
Nb		4	6
Mo		77	342
Tc		21	81
Ru		86	311
Rh		14	73
Pd		38	177
Ag		10	38
Cd		3	15
Te		12	45
I		10	37
Xe		82	330
Cs		72	288
Ba		25	100
La		21	83
Ce		52	172
Pr		17	77
Nd		51	225
Pm		7	22
Sm		11	53
Eu		3	10
Gd		3	13

[a]We assumed the Pu formed from U is equal to 0.9 times the Pu fissioned.

[b]The formation of He and B from N occurs at about 4.6% of the rate of fissioning of heavy metal atoms.

[c]Concentrations of fission products were calculated with the use of a computer program from Hanford converted by E. D. Arnold of the Chemical Technology Division, ORNL.

Table 2.2. Distribution of Bound Nitrogen in a (U,Pu)N and Bound Carbon in a (U,Pu)C Fast Reactor Fuel as a Function of Time at Full Power (185 Mw/ton)[a]

Compound[b]	Number of Nitrogen or Carbon Atoms		
	0 Time	6 Months	2 Years
(U,Pu)N	10,000	9519	7999
U_2N_3		171	801
BN		17	67
Sr_3N_2		10	38
YN		6	25
ZrN		74	275
NbN		4	6
BaN_2		17	67
(R.E.)N (ref. c)		165	655
(U,Pu)C	10,000	9569-2X (ref. d)	8201-2X (ref. d)
$(U,Pu)_2C_3$		96 + 3X	498 + 3X
Y_2C_3		9	37
ZrC		74	275
NbC		4	6
$(R.E.)_2C_3$ (ref. c)		248-X	983-X

[a]The atomic concentrations of the elements that were used are given in Table 2.1.

[b]In deciding which compounds would form, we made the following assumptions: (1) none of the compounds that are listed as nitride or carbide formers are bound as intermetallics, (2) solid solution or ternary compounds involving fission products are not important for these calculations, and (3) no interaction with or loss of material through the cladding material occurs.

[c]R.E. signifies the rare earth elements, La, Ce, Pr, Nd, Pm, Sm, Eu and Gd.

[d]The uncertainties in terms of X are caused by the fact that the stabilities of $(U,Pu)_2C_3$ and $(R.E.)_2C_3$ are identical within the error limits of the measured values.

being the same, the activity of C in the system is essentially independent of whether it is in the form of $(R.E.)_2C_3$, $(U,Pu)_2C_3$, or a solution of the two.

Our calculations show that the activities of N and C in (U,Pu)N and (U,Pu)C fuels increase with nuclear burnup. Rand and Markin[5] have similarly shown that the oxygen-to-metal ratios of $(U,Pu)O_{2-x}$ fuels increases with burnup. This effect of burnup on the activities of nonmetals in ceramic fast-reactor fuels can result in compatibility problems not encountered with the fuel at zero burnup. Thus, our calculations emphasize the importance of considering burnup effects in analyses of containment for ceramic fuel for any type of reactor.

Temperature Gradient Effects on Compositions of High-Performance Fuels (K. E. Spear, J. M. Leitnaker)

The effects of temperature gradients on $(U,Pu)O_2$ fuels have been studied by several investigators;[6–10] as far as we know, however,

---

[5] M. H. Rand and T. L. Markin, Some Thermodynamic Aspects of $(U,Pu)O_2$ Solid Solutions and Their Use as Nuclear Fuels, AERE-R-5560 (August 1967); also pp. 637–650 in Thermodynamics of Nuclear Materials, International Atomic Energy Agency, Vienna, 1968.

[6] M. H. Rand and L.E.J. Roberts, "Thermochemistry and Nuclear Engineering," pp. 3–31 in Thermodynamics of Nuclear Materials, International Atomic Energy Agency, Vienna, 1966.

[7] T. L. Markin and E. J. McIver, "Thermodynamic and Phase Studies for Plutonium and Uranium-Plutonium Oxides with Application to Compatibility Calculations," pp. 845–857 in Plutonium 1965, ed. by A. E. Kay and M. B. Waldron, Chapman and Hall, London, 1967.

[8] T. L. Markin, "Thermodynamic Data for Uranium and Uranium/Plutonium Oxides Applied to Fuel Preparation Problems," pp. 43–49 in Preparation of Nuclear Fuels, Nuclear Engineering – Pt. XVIII Chem. Eng. Progr. Symp. Ser., 63(80), American Institute of Chemical Engineers, New York (1967).

[9] R. E. Fryxell and E. A. Aitken, Trans. Am. Nucl. Soc. 8, 381–382 (1965).

[10] J. A. Christensen, Stoichiometry Effects in Oxide Nuclear Fuels, BNWL-536 (December 1967).

similar studies have not been attempted on carbide or nitride fast-reactor fuels. We have just begun to consider possible effects of temperature gradients on these advanced fuels; thus far, we have considered only the effects on the nonmetallic components in the fuel.

As a first approximation for a nitride fuel, we have assumed that the system will maintain a constant pressure of N_2. This approximation should be fairly accurate if there is interconnected porosity throughout the fuel.

To determine if the temperature gradient may cause the formation of free metal at the center of the nitride fuel system, the following simple analysis may be made. The usual type of log P_{N_2} versus 1/T plot (where P is pressure and T is temperature) for the reaction

$$(U,Pu)(\ell) + 1/2\ N_2(g) \rightarrow (U,Pu)N(s) \tag{2.1}$$

may be made along with those for the reactions

$$2UN(s) + 1/2\ N_2(g) \rightarrow U_2N_3(s) \tag{2.2}$$

$$M(s) + 1/2\ N_2(g) \rightarrow M_xN(s) \tag{2.3}$$

where M(s) is a metallic component of the cladding material. In these three reactions, the activities of the condensed phase must not be forgotten when log P_{N_2} is calculated. One then draws a constant-pressure line (parallel to the 1/T axis) that intersects the log P_{N_2} vs 1/T curve for Reaction (2.1) at the temperature of the center of the fuel pin. If the constant-pressure line intersects the curve for Reaction (2.2) at a temperature equal to or greater than that at the interface between fuel and cladding, $U_2N_3(s)$ can form at this temperature and $(U,Pu)(\ell)$ can form at the center of the fuel pin. Similarly, if the constant-pressure line intersects the curve for Reaction (2.3) at a temperature equal to or greater than that of cladding, the cladding element can be nitrided and $(U,Pu)(\ell)$ can occur at the center of the fuel pin.

As a first approximation for a carbide fuel, we assume transport of the C in the gaseous phase by the reaction

$$CO_2(g) + C[in(U,Pu)C_x] \rightarrow 2CO(g) \tag{2.4}$$

Carbon may be transported from a hot to a cool region by this reaction. Plots of carbon potentials versus temperature for constant CO_2:CO ratios and constant total pressure of these species need to be compared with carbon potentials for various compositions of mixed carbide fuels. With the help of these comparisons, one could determine changes in fuel composition caused by the temperature distribution across a fuel pin. The reason for having to specify the total pressure as well as the CO_2:CO ratio may be seen by calculating the activity of C by the following equations:

$$P_{CO_2}/P_{CO} = Q = \text{constant} \tag{2.5}$$

$$P_{CO_2} + P_{CO} = P = \text{constant} \tag{2.6}$$

$$K_{eq} = [P^2_{CO}/P_{CO_2}]\ [1/a_C] \tag{2.7}$$

where P is the pressure, Q is the ratio constant, K_{eq} is the equilibrium constant for Reaction (2.5) and a_C is the activity of C. The activity of C is equal to

$$a_C = P/[K_{eq}Q(Q + 1)] \tag{2.8}$$

at a constant temperature. Thus, both P and Q need to be specified to fix the carbon activity at each temperature.

Compatibility of Mixed-Nitride and Carbonitride Fuels with LMFBR Cladding Alloys

High-Temperature Properties of Vanadium Carbonitride Solutions
(K. E. Spear, J. M. Leitnaker)

Investigations of the properties of carbon-rich vanadium carbonitride solid solutions at high temperatures were reported previously.[11] The further studies of this system summarized here are part of a continuing

[11]K. E. Spear and J. M. Leitnaker, Fuels and Materials Development Program Quart. Progr. Rept. June 30, 1968, ORNL-4330, pp. 43–49.

program for investigating the chemical and thermodynamic properties of advanced fuel and cladding systems of interest for the LMFBR program. Of particular interest in the V-C-N system are interactions between fuel and cladding and additions to fuels to force compatibility.

The lattice parameters of V(C,N) solutions in equilibrium with C and N_2 have been determined for nitrogen pressures of 50, 100, 300, and 600 torr and 1200 to 1600°C. The equilibrium reaction may be written as

$$VC[\text{in } V(C,N)] + 1/2\ N_{2(g)} \rightleftharpoons VN[\text{in } V(C,N)] + C(s). \qquad (2.9)$$

Earlier results for nitrogen pressures of 600 torr indicated that VC reacts with N_2 reversibly to produce V(C,N) solutions and C in a form thermodynamically more active than graphite. The present results for nitrogen pressures of 50, 100, and 300 torr are also consistent with the assumption that an active form of C is produced in the reaction of VC plus N_2.

In addition to studies of pressure, chemical analyses and measurements of temperature and lattice parameter were made on 30 samples of V(C,N). These data, along with x-ray data, have been combined into a plot of lattice parameter versus composition.

The annealing experiments were performed with an apparatus described previously[12] and a graphite crucible containing two isolated chambers. One chamber of the twin crucible was loaded with about 1 g of a mixture of VN and graphite, and the other chamber was loaded with about 1 g of VC containing free C. Our apparatus let us keep the temperature and pressure of an experiment constant within ±3°C and ±1 torr, respectively. The lattice parameters were calculated from data measured with a Debye-Scherrer x-ray powder diffraction camera to an average accuracy of about ±0.0004 A.

The combined oxygen and metallic impurities in the carbonitrides were determined to be less than 0.1 wt %. The V and total C in the samples were determined by combustion analysis and collection of the CO_2 produced. We assumed the balance to be N.

---

[12]J. M. Leitnaker, "The Ideality of the UC-UN Solid Solution," pp. 317–330 in Thermodynamics of Nuclear Materials, 1967, International Atomic Energy Agency, Vienna, 1968.

The data for temperature, pressure, and lattice parameter are summarized in Fig. 2.3. The dependence of the lattice parameter on starting material is also illustrated by this graph.

The relationship between lattice parameter and composition for V(C,N) solutions is shown in Fig. 2.4. The data of Brauer and Schnell[13] are also shown on this plot. The composition axis is represented by the N:V molar ratio rather than, for example, the N:(N + C) molar ratio in the solid solution, because the samples all contained free C and thus far, only the total C in each sample has been determined.

The shape of the curve showing lattice parameter versus composition, for V(C,N) solutions given in Fig. 2.4, is rather unusual. Our data extend only over the N:V range of zero (pure VC) to 0.33. The more nitrogen-rich solutions in equilibrium with free C are difficult to prepare because of the high pressures (> 1 atm N_2) and/or low temperatures (< 1200°C) required. Attempts to reach equilibrium by heating for 160 hr at about 1 atm N_2 and 1100°C were unsuccessful because of the slow reaction kinetics.

The data in Figs. 2.3 and 2.4 can be used together to give the experimental conditions necessary for preparing V(C,N) solutions with the maximum ratio of nonmetal to metal. These data along with a knowledge of the C:V ratio in a sample give the maximum conditions of temperature and pressure that can be used before free C is precipitated. Such information could be of great importance in making use of $V(C,N)_{1-x}$ solutions as buffering agents in a carbonitride fuel.

Since the previous report,[11] studies of V(C,N) solutions have given results consistent with our earlier conclusion that VC reacts with N_2 to produce V(C,N) plus a form of C more active than graphite.

We have discussed elsewhere[14] some of the implications of our postulation that a high-energy form of C may result from any decomposition

---

[13]G. Brauer and W. D. Schnell, J. Less-Common Metals, 7, 23–30 (1964).

[14]K. E. Spear and J. M. Leitnaker, "The Formation of Actine Carbon in Twin Crucible Studies of Vanadium Carbonitride Solutions," accepted for publication in The Journal of the American Ceramic Society.

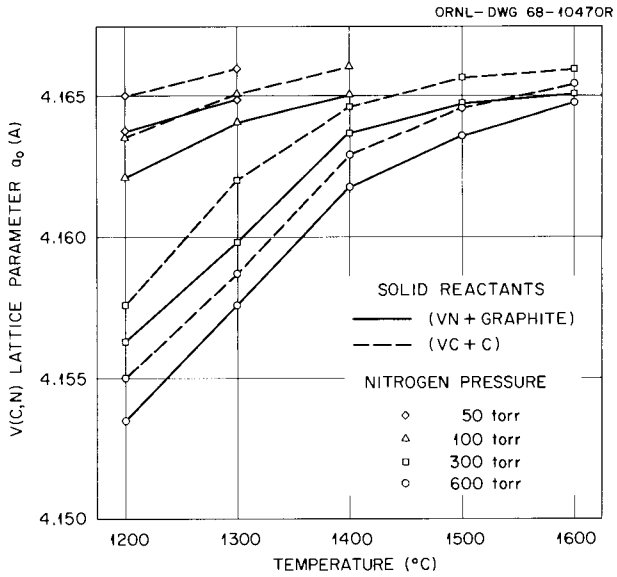

Fig. 2.3. Relationships Among Lattice Parameter, Temperature, Pressure, and Solid Reactants for V(C,N) Solid Solutions in Equilibrium with Carbon and Nitrogen Gas.

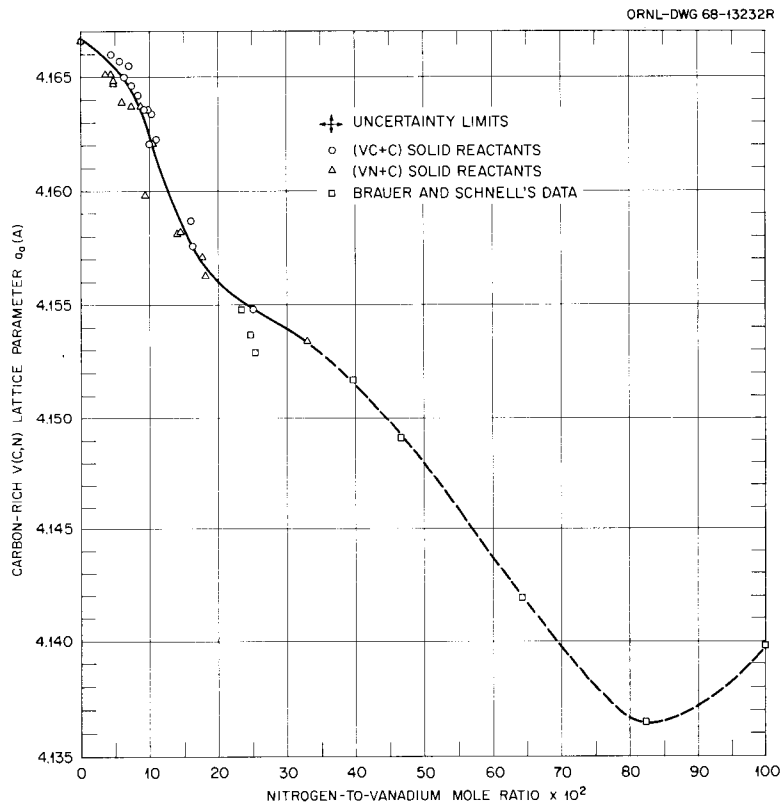

Fig. 2.4. Relationship Between Lattice Parameter and Composition for V(C,N) Solid Solutions in Equilibrium with Carbon and Nitrogen Gas. Ref.: G. Grauer and W. D. Schnell, J. Less-Common Metals, 7, 23–30 (1964).

or reaction leading to free C. The examples given concern (1) the vaporization of metal carbides to give gaseous metal atoms and free C and (2) the transition temperature for the solid-state decomposition of nominal UC_2 to U_2C_3 and free C.

Measurements of the Physical Properties of (U,Pu)N Alloys

S. C. Weaver D. L. McElroy

Because of the importance of knowing temperature distribution to predict irradiation behavior, we are beginning a study of the thermal conductivity of (U,Pu)N alloys. Fuel swelling, release of fission gas, distribution of fission products, redistribution of Pu, and other effects of irradiation very strongly depend on the temperature distribution and, therefore, the thermal conductivity of the fuel. Although a few studies have been made on the thermal conductivity of (U,Pu)N alloys, studies on well-characterized material over a wide range of temperatures and compositions have not been made. We will study the effects of fuel density, including the effects of pore size and shape; the effect of impurities, such as C and O; and the effects of varying compositions of U and Pu.

The equipment being designed includes (1) an electrical resistivity apparatus for measuring electrical resistivity and the absolute Seebeck coefficient, (2) an absolute heat flow apparatus for measuring thermal conductivity, electrical resistivity, and Seebeck coefficient, and (3) a comparative heat flow apparatus for measuring thermal conductivity. This equipment, plus auxiliary equipment to be included, will have a measurement capability as shown below:

Box I — Electrical Resistivity Apparatus and Auxiliary Equipment

1. 1700°K annealing in 5×10^{-7} torr vacuum or inert gas
2. Electrical resistivity, 300 to 1700°K
3. Thermopower, 300 to 1700°K
4. Electrical resistivity, knife edges, 300°K
5. Electrical resistivity, eddy current, 300°K
6. Electrical resistivity, eddy current, 4.2 to 300°K

7. Electrical resistivity, 4.2 to 300°K
8. Thermopower, 4.2 to 300°K
9. Density, 300°K

Box II — Comparative Heat Flow and Absolute Heat Flow Apparatuses

1. Thermal conductivity, 300 to 500°K
2. Contact thermal resistance, 300°K, 4000 psi
3. Thermal conductivity, 77 to 500°K
4. Thermopower, 77 to 500°K
5. Electrical resistivity, 77 to 500°K

All of this equipment must be enclosed in glove boxes. Electrical leads from the boxes will be fed through the ceiling to the room above the Interim Plutonium Facility, where all of the instrumentation will be placed.

The equipment for measuring thermal conductivities, is limited to 500°C, but electrical resistivity measurements can be made to 1700°C and possibly to 2000°K if desired. Because the electronic contribution to the thermal conductivity is significant for (U,Pu)N alloys at high temperatures, we should be able to calculate the thermal conductivity at high temperatures from low-temperature data for thermal conductivity and from low- and high-temperature data for electrical resistivity.

Costs have been estimated, and the designing of equipment has begun. We are searching the literature for existing data.

Studies of Thermal Conductance at Interface of Fuel and Cladding
(R. K. Williams, D. L. McElroy)

We have obtained data on the thermal contact resistance of three additional interfaces between UN and Mo, a V–15% Cr–5% Ti alloy, and annealed Cu. In these experiments, conducted in vacuum, the temperatures at the interfaces ranged from 40 to 60°C and the compressive stress was varied from 150 to about 5000 psi. All our results on interfaces between UN and a metal are compared in Table 2.3. Data for the interfaces with Mo and V–15% Cr–5% Ti do not differ significantly from the results previously reported for interfaces with type 302 stainless steel. The interface with Cu has a lower interfacial resistance (R_c), but the

Table 2.3. Comparison of Thermal Contact Resistance at 50°C in Vacuum for Interfaces Between UN and Various Metals

Stress (psi)	Thermal Contact Resistance ($°C \cdot cm^2/w$)						
	Annealed Type 302 Stainless Steel	"Half Hard"[a] Type 302 Stainless Steel	"Full Hard"[a] Type 302 Stainless Steel	Mo	V–15% Cr–5% Ti	Annealed Cu	Annealed Cu (ref. b)
100	14.0	16.8	14.6	18.2	12.8	9.0	5.0
1000	1.9	2.4	2.2	2.5	1.8	1.0	0.5

[a]Mill designation.

[b]After 48 hr at 5000 psi.

results are not as low as those previously found for the interface between tool steel and Cu. Also, the R_c of the interface between UN and Cu seems to show hysteresis effects, the R_c values decreasing by half after prolonged application of a 5000-psi stress. This possibility is being investigated further.

Irradiation Testing of Nitride Fuels

S. C. Weaver

As one step in preparing irradiation test capsules, we are studying the problem of sodium bonding of fuel to the cladding. Our approach is to (1) cast the Na into a rod, (2) insert the Na into either the fuel pin or containment vessel, whichever is being bonded, (3) place the fuel or fuel rod on top of the Na, (4) heat the Na to seat the fuel or fuel pin, (5) make the closure weld, (6) heat the fuel pin or capsule; and (7) ultrasonically vibrate the assembly to eliminate voids.

This approach to sodium bonding called for a slight redesigning of the capsule. Parts were fabricated to test this procedure.

We are preparing the proposal for approval-in-principle required for testing fuel pins in EBR-II.

3. FISSION-GAS RELEASE AND PHYSICAL PROPERTIES OF FUEL MATERIALS DURING IRRADIATION

O. Sisman

The purpose of this work is to measure the parameters that control the release of fission gas from highly characterized nuclear fuels. These parameters are evaluated in terms of a generalized model to predict release from operating fuel materials. Thermal diffusivity is measured in-reactor in analogous experiments.

The Effect of Stored Energy in UO_2 and UN on In-Reactor Measurements of Thermal Diffusivity

R. M. Carroll R. B. Perez

We have found that the use of a perturbation method to measure thermal diffusivity in UO_2 and UN specimens during irradiation gives erratic and spurious values because of the storage and release of energy. This report describes the process by which energy is stored and released and the effect this process may have on measurements of thermal diffusivity.

The thermal diffusivity of UO_2 cannot be measured by conventional techniques during an irradiation at realistic levels of fission power, for thermal stresses will break the specimen unless thin cross sections are used. This prohibits, for example, steady-state measurements involving thick cylinders of UO_2 with thermocouples embedded at different locations. We have been measuring thermal diffusivity by means of a thin, cylindrical specimen with a thermocouple that measures central temperature. The generation of fission heat in the fuel specimen is changed stepwise by moving the specimen into a region of higher flux in the reactor. The resulting rise in the temperature of the specimen and its surroundings is measured as a function of time (after the step change) by an automated data logger.[1]

---

[1]R. B. Perez *et al.*, Reactor Chemistry Div. Ann. Progr. Rept. Dec. 31, 1967, ORNL-4229, pp. 138–141.

The initial results of computer processing of the data for UO_2 specimens showed that the values of thermal diffusivity appeared too low to be realistic. This implied that the heat source was larger than calculated. From theory, we had assumed that heating by any sources other than fission could be neglected in comparison to fission heating, but our discovery that our heat source was probably larger than calculated made it necessary that we measure the amount of the nonfission heating. We found that the amount, though somewhat larger than calculated,[2] would not account for the unknown heat source. Moreover, our calculated values for thermal diffusivity were more erratic than our precision of measurement would indicate, and the values did not vary smoothly with temperature as would be expected.

These problems seemed so insurmountable that we were on the verge of abandoning the method when we found that one of the heating curves for a UN specimen showed a sudden rise of temperature at the center of the specimen [see Fig. 3.1(a)]. This was not a spurious signal, for the thermocouple in the capsule just outside the specimen recorded the same pulse but at a lower amplitude [see Fig. 3.1(b)]. The lines through the data of Fig. 3.1(a) and (b) represent a computer fit of a single exponential equation to the data beginning 30 sec after the start of the pulse.[2] We concluded that the most likely explanation of the temperature rise was that stored energy was suddenly released. The phenomenon of energy stored in materials by irradiation is well known, and stored energy has been found in irradiated UO_2 by postirradiation measurements.[3] The consensus, however, was that most of the stored energy was released well below the operating temperatures of 700 to 1300°C where we were trying to measure thermal diffusivity.

The mechanism postulated for the storage and release of energy is based on a process similar to that for the release of fission gases from

---

[2]R. M. Carroll and R. B. Perez, Fuels and Materials Development Program Quart. Progr. Rept. Sept. 30, 1968, ORNL-4330, pp. 54–58.

[3]G. J. Dienes (ed.), Studies in Radiation Effects on Solids, p. 189, vol 2, Gordon and Breach, 1967.

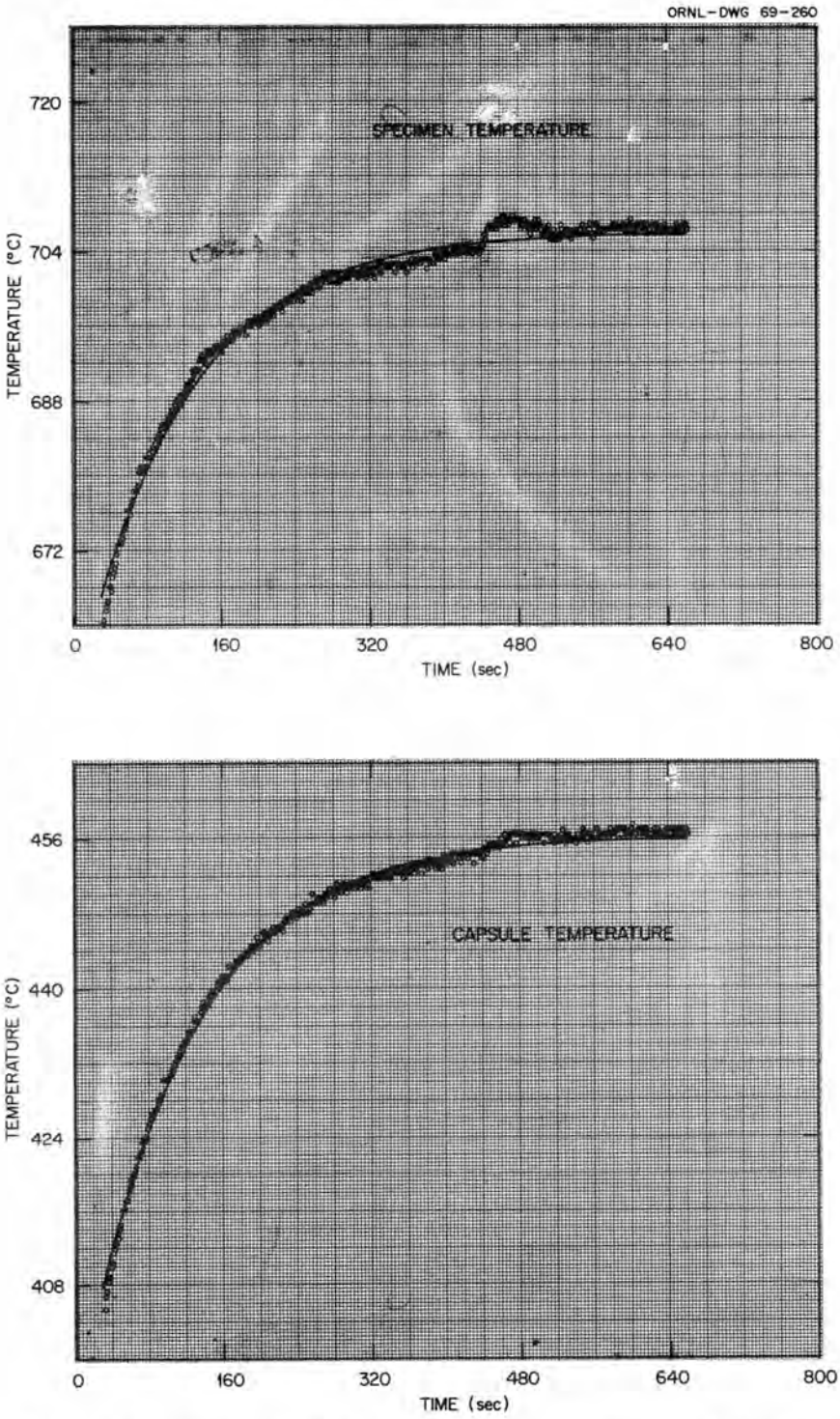

Fig. 3.1. Computer Plot of Rise in Temperature of UN Specimen as Function of Time After Step Increase in Fission Power. (a) As measured by thermocouple at center of specimen. (b) As measured by thermocouple in capsule surrounding specimen.

nuclear fuels:[4] a fraction of the kinetic energy of the fission fragments is transformed into potential energy by deformation of the lattice (the creation of point defects). The concentration of defects is the result of a dynamic equilibrium between formation by fission fragments and annealing by temperature. The rate of annealing is assumed to have the form of an Arrhenius equation and (from measurements of the release of fission gas) to have an activation energy of about 2 kcal/mole (ref. 5).

Although one would expect the great majority of the defects to be annihilated at lower temperatures, during power production (at any temperature) a dynamic equilibrium is reached between production and annealing processes so that more energy is available during irradiation than would be indicated by measurements after irradiation. Thus, when the temperature of the specimen is suddenly increased, the shift of the equilibrium defect concentration caused by the increased annealing rate will cause a momentary release of heat. This heat, released during the rise in temperature, causes the temperature of the specimen to increase more rapidly than would be expected.

It would appear that the data of Fig. 3.1(a) and (b) were rather freakish because the release of energy was triggered when the temperature of the specimen was changing slowly. This phenomenon, however, led us to reexamine our older data, and we could see from the shape of the heating curves that as the power was step-increased the curve for time and temperature showed small but significant variations from the expected smooth increase in temperature.

This argument thus predicts that if the fission power in a fuel specimen were suddenly increased, resulting in a temperature rise, more energy would be released for a short time than could be accounted for by the increase in fission power. The energy release would cause the temperature of the specimen to rise faster but would not affect the

---

[4]R. M. Carroll and O. Sisman, Nucl. Sci. Eng. 21, 147 (1965).

[5]R. B. Perez et al., "A Dynamic Method to Study In-Pile Fission-Gas Release," Trans. Am. Nucl. Soc. 11(1), 271–272 (1968).

equilibrium temperature (which reflects a steady-state balance between heat production and heat loss). Conversely, if the fission power were suddenly decreased, the temperature of the specimen would drop faster than would be expected because of the energy absorption required to reestablish the concentration of point defects. Either the rapid rise or fall of temperature might be falsely interpreted as being caused by a lower thermal diffusivity in the specimen during irradiation.

It follows from the arguments above that the dependence of the fuel temperature on time is not reversible when the power generation of the fuel is changed reversibly. That is, the temperature profile between identical initial and final temperatures depends on whether one deals with a heating or cooling pulse.

We measured the temperature-time behavior of a UN specimen when the neutron flux level of the specimen was step increased from 4.0 to 4.9×10^{12} neutrons cm^{-2} sec^{-1}; this resulted in a rise in temperature from 1018 to 1173°C. After equilibrium was reached, the specimen was step withdrawn to reverse the conditions. After the original conditions were reestablished, we repeated the first process of stepwise increase (see Fig. 3.2).

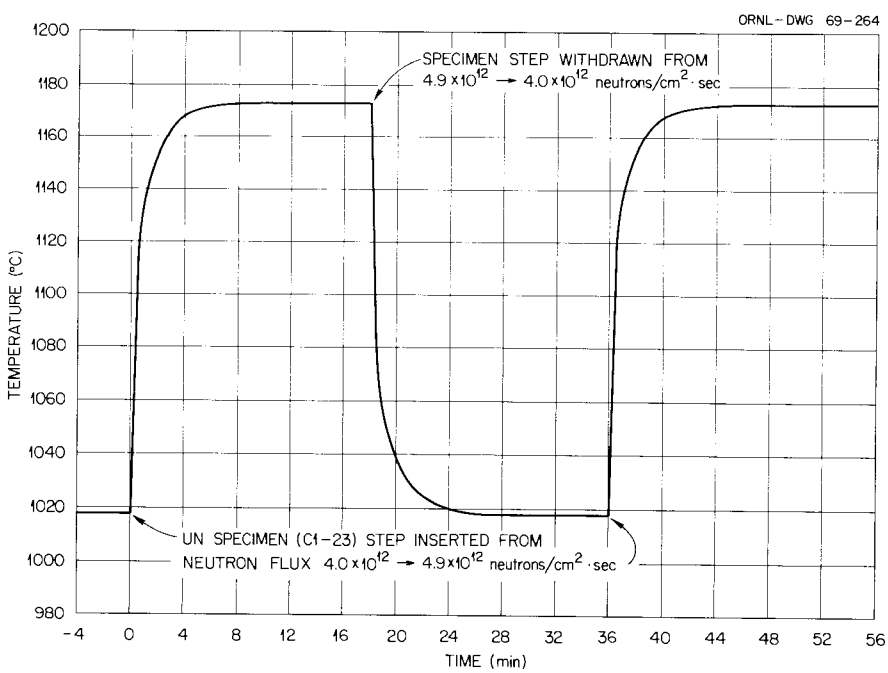

Fig. 3.2. Temperature Response of UN Specimen to Step Change of Fission Rate.

Using the data of Fig. 3.2, we compared the heating rise, $T_h(t)$, with $T_h'(t)$. The value of $T_h'(t)$ was obtained from the cooling step, $T_c(t)$, by the relation

$$T_h'(t) = T_{initial} + T_{final} - T_c(t) \quad . \tag{3.1}$$

In the absence of stored energy release both temperature profiles, $T_h(t)$ and $T_h'(t)$, should coincide. The resulting curve (shown in Fig. 3.3), however, exhibits the behavior typical of history-dependent phenomena. Both heating curves of Fig. 3.2 did indeed coincide as $T_h(t)$ on Fig. 3.3 while $T_h'(t)$ (obtained from the cooling curve) showed a significant deviation.

The area of the hysteresis cycle is proportional to the difference, ΔE, of energy released per unit volume from defects that anneal during the heating and cooling step:

$$\int_{T_{initial}}^{T_{final}} dt\ [T_h(t) - T_c(t)] = \frac{L_o\ (\alpha)}{\rho\ c\ \kappa} \Delta E \ , \tag{3.2}$$

where ρ, c, and κ are, respectively, the density, specific heat, and the thermal diffusivity of the fuel and $L_o\ (\alpha)$, in square centimeters, is a geometric factor depending on the curvature, α (cm^{-1}), of the spatial distribution of temperature in the specimen. The parameters $L_o\ (\alpha)$, c, and κ can be evaluated by an analysis of the cooling and heating steps; hence, Eq. (3.2) offers a method for evaluating the released energy.

The presence of an energy release during the time that the rate at which point defects are annealed exceeds the rate at which they are produced (an increase of specimen temperature) or the presence of an energy absorption when the annealing rate is less than the production rate (specimen cooling) will affect the measurement of thermal diffusivity during irradiation when a temperature transient method is used. The time required for the defect concentration to reach an equilibrium

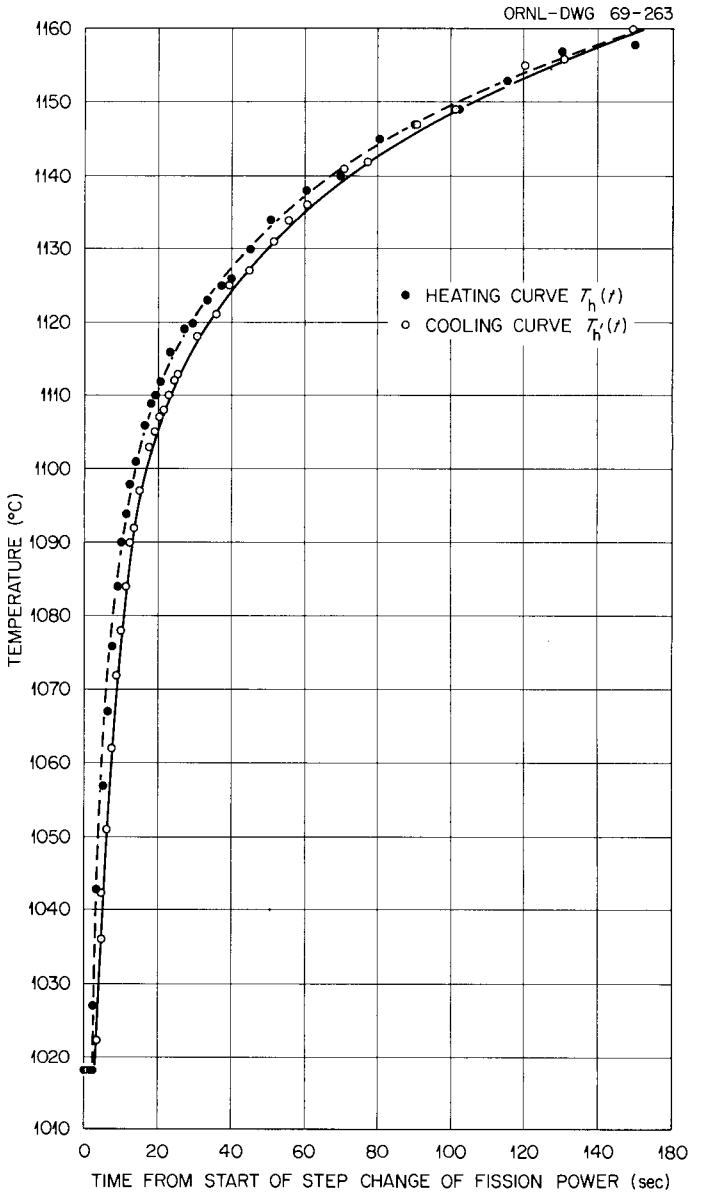

Fig. 3.3. Time Dependence of Temperature Change of UN Specimen When Fission Power Was Step Changed in a Reversible Manner.

production-decay will obviously depend upon the temperature of the specimen. The amount of energy released (or stored) during temperature transients will depend on fission density, specimen temperature, and the magnitude of the perturbation of temperature and fission density. However, since the energy release is reversible (see Figs. 3.2 and 3.3), the amount of energy released as well as the thermal diffusivity should be determined by pairs of measurements of the heating and cooling curves.

Effect of Temperature, Fission Density, and Low Burnup on Release of Fission Gas from $(U_{0.75},Pu_{0.25})O_2$

R. M. Carroll J. G. Morgan

Two pellets of high-density (97% of theoretical density) mixed oxide made to Fast Flux Test Facility (FFTF) specifications from test batch MJB-6 were supplied by M. J. Barr and Harlan Anderson of Battelle Northwest. These pellets were selected because each was fabricated with a 0.127-cm-diam axial hole that allows a thermocouple to be inserted to measure the maximum temperature in the pellet. With the exception of the axial hole (and a slightly higher density), the 0.54-cm-OD by 0.58-cm-long pellets were of the same composition as FFTF production pellets. Two of the pellets were stacked in a tungsten container and loaded into a capsule as previously described.[6]

The specimen was at first irradiated at low flux (1×10^{12} neutrons cm^{-2} sec^{-1}) and low temperature (480 to 350°C). Even at these low temperatures, the gas release appeared to depend on temperature. The temperature dependence, however, was obscured by the rapid decrease in gas release as the irradiation progressed. Such decreases with initial radiation are often observed and seem to indicate a surface reorientation brought about by fission at the surface.

The release of isotopes with short half lives (^{85m}Kr, ^{88}Kr, ^{87}Kr, and ^{138}Xe) was measured for a series of different neutron flux levels from 1.1 to 5.6×10^{12} neutrons cm^{-2} sec^{-1} and for temperatures from 350 to 1130°C. Since the isotopes with short half lives reach equilibrium quickly, we could measure equilibrium release rates after only about 20 hr irradiation time. A comparison of the fractional release rates of these isotopes showed that they were in the proportions that would be expected for a diffusion process. When the fission rate was increased, the rate at which the fission gas escaped increased proportionally. This result also indicated a process of escape by diffusion

---

[6]R. M. Carroll and H. E. Robertson, Fuels and Materials Development Program Quart. Progr. Rept. Sept. 30, 1968, ORNL-4350, pp. 76–77.

with little or no trapping. When the specimen was suddenly cooled, (see Fig. 3.4) a burst of gas was released, and gas continued to dribble from the specimen although the specimen was cool and at a low fission rate.

These results showed that the gas escaped by diffusion from small, interconnected pores or from small cracks. The passages must have been small to give the diffusion character to the gas and yet allow the gas to continue to dribble slowly out of the specimen. If the gas had diffused through the fuel matrix, the release would have stopped at once when the fuel specimen was withdrawn from the neutron flux and cooled.

It is unlikely that the high-density $(U,Pu)O_2$ fuel contained much interconnected porosity. Therefore, it is most likely that the specimens contained a network of very small fractures or cracks.

The fractional gas release rate generally tended to decrease as the irradiation progressed, although there were occasional bursts (especially during temperature changes) that indicated cracking of the specimen

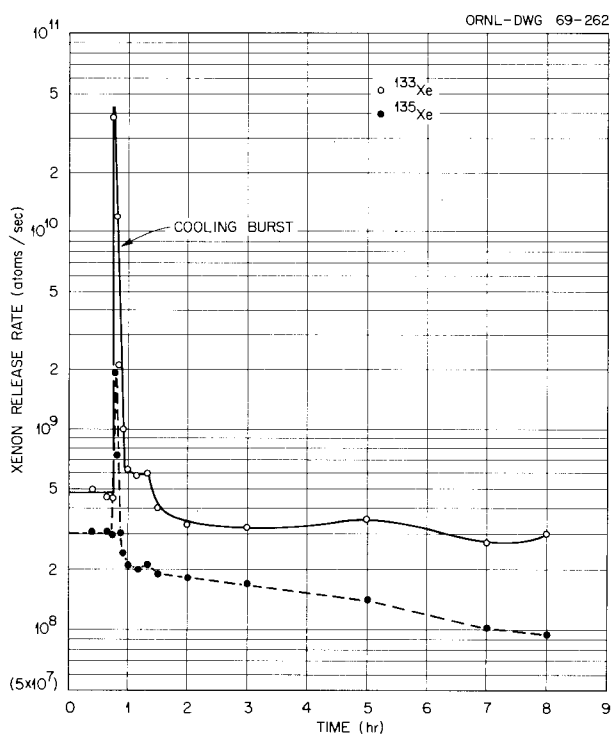

Fig. 3.4. Gas Release During Cooling of $(U,Pu)O_2$ Specimen C1-24 from 980 °C to Nearly Equal to 200 °C by Withdrawing Specimen from Flux.

(see Fig. 3.4). After 6×10^{19} fissions/cm^3 burnup, the gas release rate was only about 17% of what it was originally. The gas release decreased more quickly when the specimen was at its highest temperature (about 1100°C). This caused us to speculate that the network of fine cracks was being destroyed by sintering.

In an attempt to heal the cracks at a faster rate, we inserted the specimen into a neutron flux of 9.5×10^{12} neutrons cm^{-2} sec^{-1} (the previous high flux had been 5.6×10^{12} neutrons cm^{-2} sec^{-1}). The increased fission rate caused the temperature of the specimen to rise to 1450°C, about 300°C higher than previously. These conditions were maintained for only about 20 min before extremely high rates of fission-gas release reached the upper limit of activity tolerance set for the experiment. It should be noted that there was a 17-min delay required for the fission gas to flow from the reactor to the detector; thus, the specimen released gas as soon as it was subjected to the higher levels of flux and temperature.

Analysis of the residual gas after the specimen was withdrawn showed that a great deal of iodine had been emitted during the burst. Duplicating irradiation conditions just before the burst, we found that the rate of fission-gas release had been increased about an order of magnitude by the 20-min irradiation at 1450°C and 9.5×10^{12} neutrons cm^{-2} sec^{-1}. We therefore conclude that the combination of thermal stresses and stresses caused by trapped fission products caused the fuel structure to crack extensively, probably along the network of fractures initially present in the fuel. Further irradiation was carried on at 1140°C (the maximum we could achieve without the fission-gas activity exceeding the hazard limits of the experiment). Since the release of gas continued to increase with further irradiation, especially with small thermal changes, the irradiation was stopped. At the end of the reactor cycle, the specimen will be removed to a hot cell for examination.

From the irradiation behavior of the specimen we conclude that even before irradiation began it was filled with microcracks that were most likely caused by the heat treatment of this special batch of fuel. The microcracks provided the means of escape for the fission gas generated

during irradiation. The sintering of the cracks during irradiation accounted for a large part of the dramatic reduction in the release of fission gas as irradiation progressed. The reduction of gas release continued until a momentary high temperature (1450°C) caused the specimen to break into small pieces. Since the gas release shows the physical characteristics of this specimen from a special batch rather than the characteristics of the fuel in general, it would not be proper to draw conclusions from the results of this test about the behavior of the FFTF fuel.

Effect of Temperature, Fission Density, and Burnup on Release of Fission Gas from Microspheres of $(U_{0.75},Pu_{0.25})O_2$ FFTF Fuel

R. M. Carroll H. E. Robertson

We obtained about 60 spherical pellets of FFTF composition $(U,Pu)O_2$ fuel from Battelle Northwest. These spheres, unlike the special specimens discussed above, are from a production batch (ME-21) of FFTF candidate fuel. The spheres were made by grinding broken pieces of fuel pellets by centrifugal air-blast process until the particles were roughly spherical.

Since the grinding process did not produce spheres of exactly uniform size, we manually selected the best matched spheres. For the test batch, we chose 21 spheres ranging from 793 to 1030 μm in diameter and with an average diameter of 903 μm. The selected spheres had an average diametral deviation of 1.6% (deviation from the average of five different measurements). Thus the grinding process produced spheroids varying about 10% in diameter and about 1.6% in spheroidicity.

The 21 spheroids, weighing a total of 0.0784 g, were loaded into a tungsten holder and placed in capsule C1-25. This capsule is scheduled for insertion into the reactor during the shutdown on January 12, 1969.

We expect to compare the response of these specimens with that of the high-density $(U,Pu)O_2$ pellets described above and with that of single-crystal UO_2 specimens.

Effect of Fission Density on Release of Fission Gas from Enriched Single-Crystal UO_2 Specimens

R. M. Carroll

The irradiation behavior of these specimens was reported.[7,8] We predict from the characteristics of the gas and from the way it was released that the spheres subdivided so as to increase the surface area available for gas release. We reasoned that fission products concentrated at subgrain boundaries generated enough stress to break the particles. The amount of gas released indicated that each original particle was divided into about 1000 pieces. Since the original spheres were only 0.0997 cm in diameter this would indeed give the impression that the specimens degenerated into powder.

Postirradiation metallographic examination showed that the original 0.1-cm-diam spheres (see Fig. 3.5) subdivided along what appeared to be lines of crystal orientation. The typical appearance of the spheres after irradiation is shown in Fig. 3.6. The gas trapped in the spheres formed the closed voids seen as dark spots, and the solid impurities are seen as small white spots.

Since the fragments of the spheres were cast into plastic for metallographic examination, we cannot determine their orientation or whether a segment shows the midplane of a sphere. Thus we cannot use the radius of curvature of the segments of spheres to determine if swelling occurred.

From the appearance of the fractures and the microstructure, we conclude that our prediction based on the characteristics of the gas release was correct and that the fractures were caused by burnup effects rather than any chemical reaction with the sweep gas.[8]

---

[7]R. M. Carroll, O. Sisman, and R. B. Perez, Nucl. Sci. Eng. 32(3), 430–431 (1968).

[8]R. M. Carroll et al., Fuels and Materials Development Program Quart. Progr. Rept. June 30, 1968, ORNL-4330, pp. 54–55.

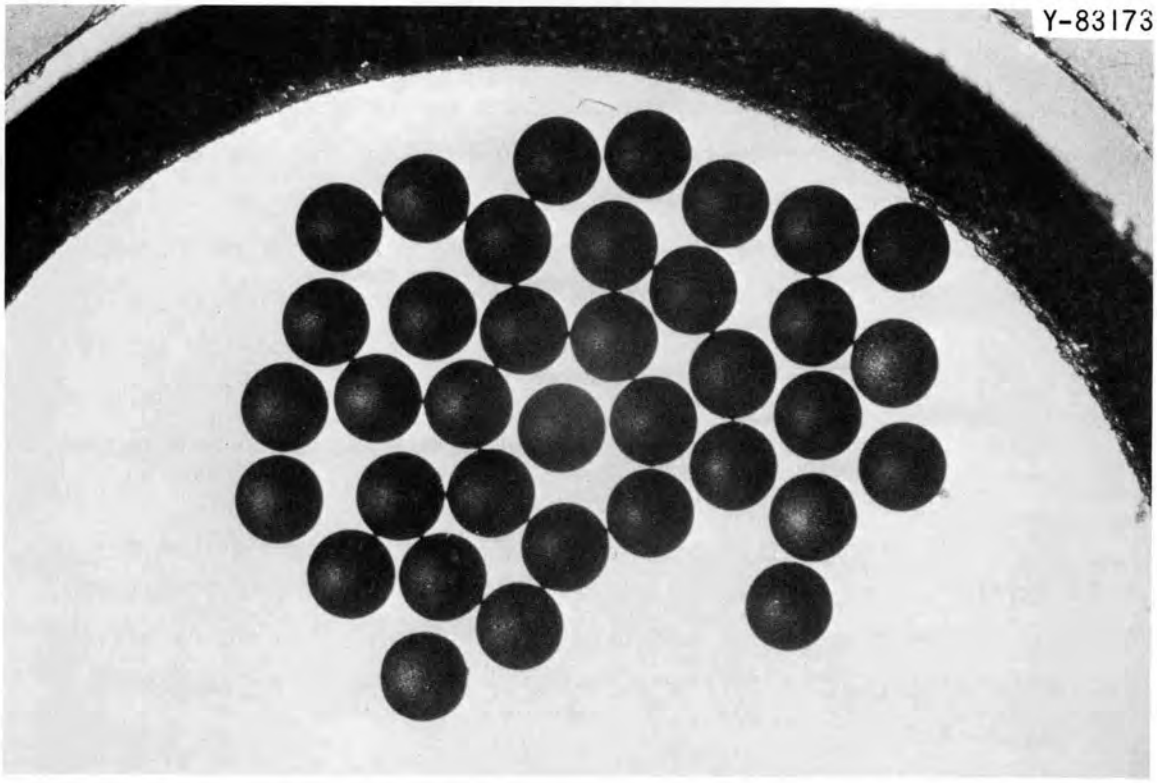

Fig. 3.5. Single-Crystal UO_2 Spheres, 0.0997 cm in Diameter, Before Irradiation.

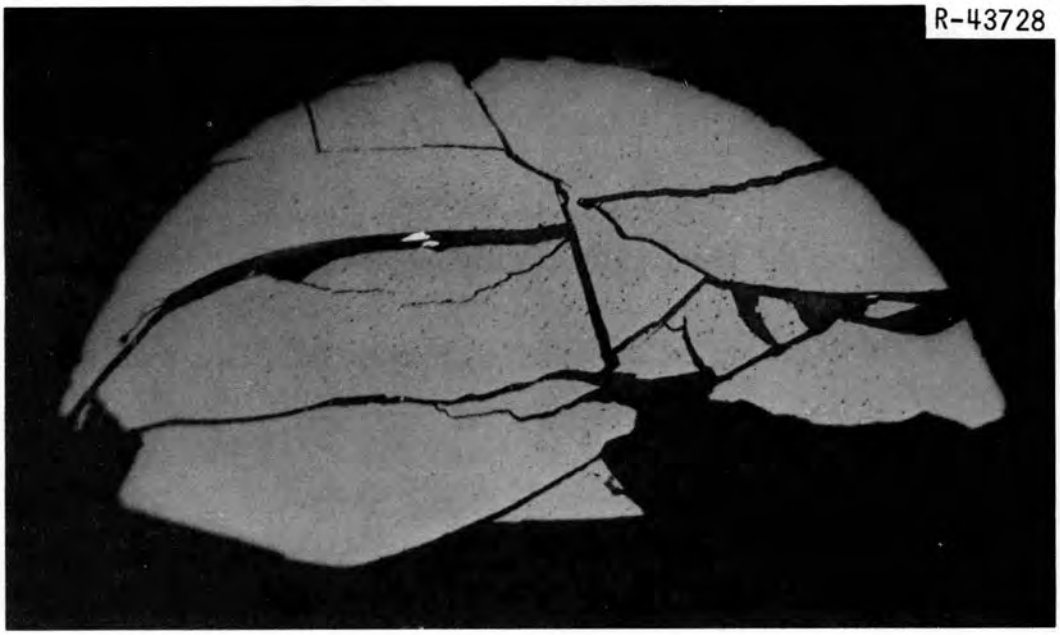

Fig. 3.6. Typical Appearance of Sectioned Fragments of UO_2 Spheres After Irradiation. 200×.

4. ZIRCONIUM METALLURGY

J. R. Weir, Jr. P. L. Rittenhouse

The object of this program is to optimize the properties of zirconium alloy tubing used in nuclear reactors by study of fabrication procedures and their interaction with crystallographic deformation modes. Rather than following the usual practice of designing fuel element cladding on the basis of minimum strength values, we are attempting to control the crystallographic texture in the tubing to permit the strongest direction in the tubing to be matched against the highest service stress. This technique can also be used to control the orientation of potentially embrittling hydride platelets that form from absorption of H_2 that is released by corrosion. Success in this program can reduce the cost of producing nuclear power by making possible longer core life, higher operating temperatures, and the use of tubing with thinner walls.

Fabrication and Texture Control of Zirconium Tubing

T. M. Nilsson

We completed the last five of the twelve schedules planned in our study of tubing fabrication.[1] Three of these five were reduced to final size (0.59-in. OD × 0.53-in. ID) by cold drawing. The starting material was tube-reduced tubing of the following dimensions: 0.886-in. OD × 0.786-in. ID, 0.886-in. OD × 0.736-in. ID, and 0.886-in. OD × 0.567-in. ID. Tubes were reduced to the final size in steps of about 20% (in two passes) with intermediate anneals of 2 hr at 730°C.

We also tried to produce tubing by swaging and by planetary swaging. The starting material in both cases was 0.886-in. OD × 0.786-in. ID. Neither of these schedules was satisfactory. Ordinary swaging broke the

[1]T. M. Nilsson, Fuels and Materials Development Program Quart. Progr. Rept. Sept. 30, 1968, ORNL-4350, pp. 79–81.

tubing during the third step of 20% reduction in spite of annealing 2 hr at 730°C between steps. Planetary swaging was even less successful: the tubes broke during the second rather than the third step. We tried to increase the total permissible work by decreasing the reduction per pass from 10 to about 5%, but this also failed. Almost all of the cracks in the broken tubes started on the inside walls. There were some smaller cracks on the outside walls of the tubes reduced by planetary swaging (Fig. 4.1), but the majority were on the inside walls. After ordinary swaging, there were cracks only on the inside walls (Fig. 4.2).

We earlier[1] reported successful swaging and planetary swaging of similar Zircaloy (Zr–1.45% Sn–0.1% Cr–0.2% Fe) tubes with similar area reductions. In those cases, however, the working process was primarily one of wall thinning, while sinking predominates in the present schedules. During wall thinning, the tubing has solid support from the mandrel, and compressive stresses are high compared to the tensile stress.

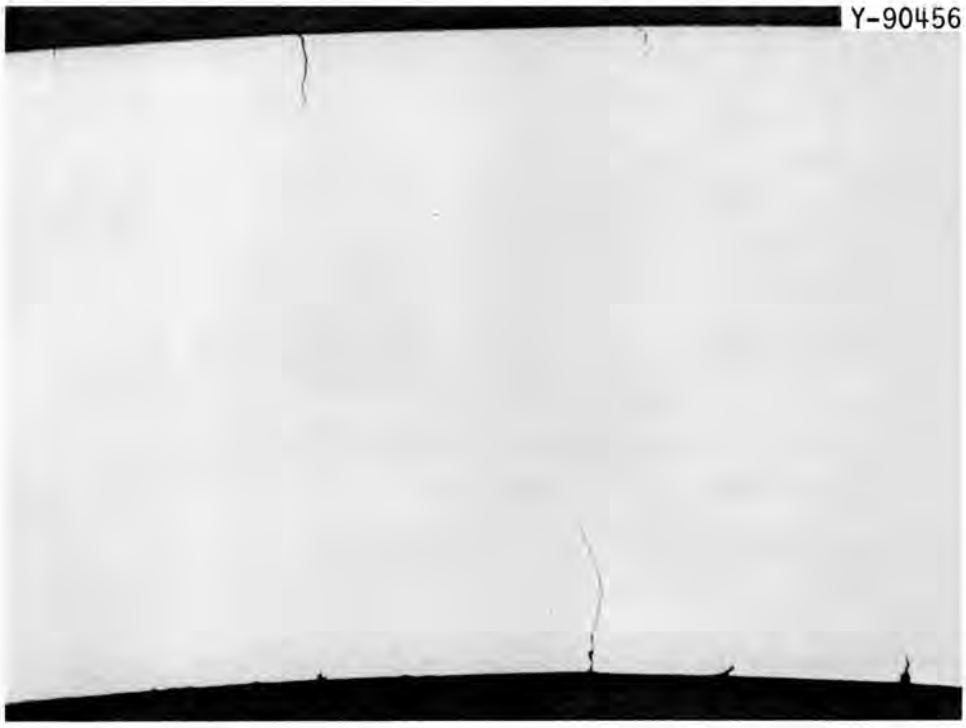

Fig. 4.1. Wall Section of Planetary-Swaged Zircaloy Tubing. Cracks can be seen on both the inside and outside of the wall after 27% working. One intermediate anneal, 2 hr at 730°C. 100×.

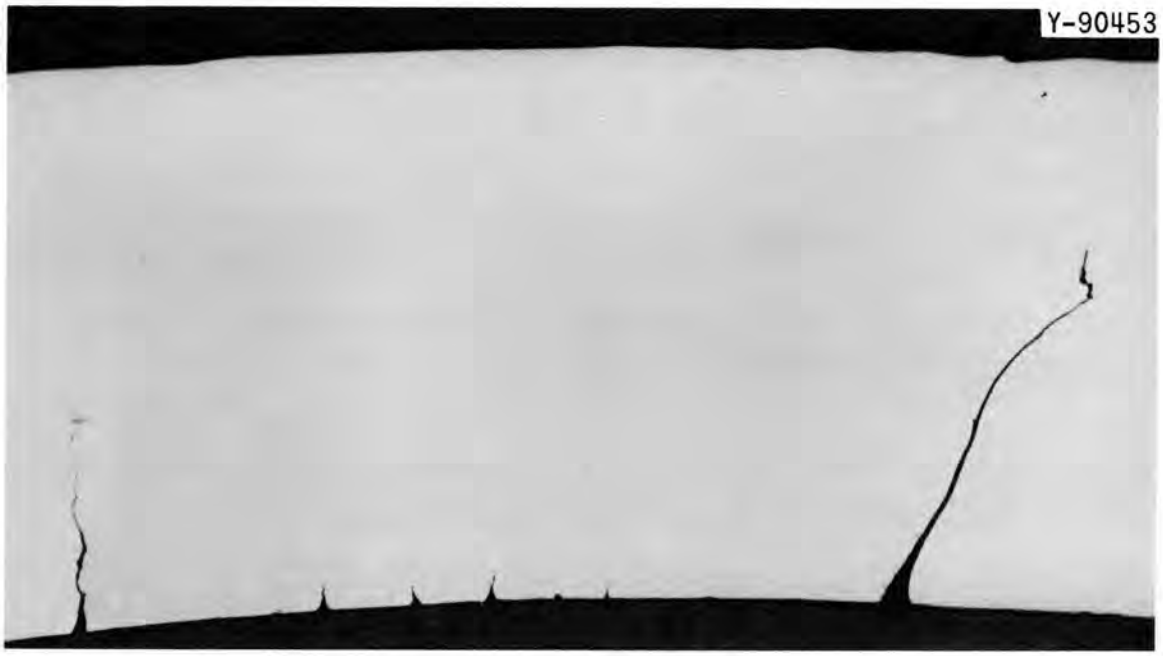

Fig. 4.2. Wall Section of Swaged Zircaloy Tube. The tube was worked about 60% with two intermediate 2-hr anneals at 730°C. No cracks were found on the outer surface of the tube. 100×.

This is probably the reason for the higher workability in the earlier swaging schedules. Sinking is successful in mandrel drawing because the deformation of the workpiece is less abrupt than in swaging — the entrance angle of the die is only 16°.

The grain sizes of the finished tubes of schedules V through XII are listed in Table 4.1. Grain sizes for schedules I through IV, which were tube reduced only, were reported earlier.[1] The grain size after annealing appeared to depend only on the amount of cold work. The critical amount of cold work needed to provide a fine grain size was not determined exactly but is > 20 but < 54%. In schedules V through XII, the tubes were reduced only 20% between anneals. The table shows, however, that the grain size does become relatively fine after a number of small reductions and anneals. The following variables seem to be of minor or no importance in determining grain size: direction of drawing (see schedule VI), cold working technique (see schedules VI, VII, and VIII), the type of reduction, or the Q ratio (i.e., the ratio of the reduction in wall thickness to the reduction in diameter).

Table 4.1. Grain Size of Finished Zircaloy-4 Tubing as a Function of Fabrication Variables

Schedule	Tube Identification Number	Dimensions (in.)				Method of Reduction	Average Q Ratio[a]	Number of Reductions of About 20%	ASTM Grain Size[b]
		Original		After Reduction					
		ID	OD	ID	OD				
V	7-34	0.576	0.886	0.535	0.595	Drawing	High	8	7 1/2
VI	3-3A	0.540	0.636	0.533	0.591	Drawing	High	2	8 1/2
	3-12A2	0.540	0.636	0.533	0.593	Drawing[c]	High	2	8 1/2
VII	3-12B1	0.540	0.636	0.536	0.588	Planetary Swaging	High	2	9
	3-12B3	0.540	0.636	0.536	0.590	Planetary Swaging	High	2	9
VIII	5-3B	0.540	0.636	0.535	0.591	Swaging	High	2	8 1/2
IX	4-12B2	0.736	0.886	0.535	0.595	Drawing	Medium	5	7 1/2
X	2-12B1	0.786	0.886	0.535	0.591	Drawing	Low	4	7
	5-25	0.786	0.886	0.535	0.591	Drawing	Low	4	7
XI	2-12C	0.786	0.886	0.710	0.787	Planetary Swaging		1[d]	9[e]
XII	2-12A2	0.786	0.886	0.630	0.688	Swaging		3[d]	8

[a]The Q ratio is the ratio of the reduction in wall thickness to the reduction in diameter.

[b]After final 2-hr anneal at 730°C.

[c]All tubes except 3-12A2 were worked in the same direction as during tube reducing. Tube 3-12A2 was worked in the opposite direction.

[d]Cracked.

[e]No final heat treatment.

Texture Effects, Texture Development, and Anisotropy of Properties

Deformation and Annealing Textures in Zircaloy Tubing (E. Tenckhoff)

The annealing textures in Zircaloy tubing are much more complicated than those of pure zirconium sheet. We found it important to determine the basal pole figure as well as the prism pole figure. Although annealing has not before been observed to cause a shift of basal poles, our investigation shows that annealing can — but need not necessarily — cause a shift of basal poles toward the radial direction and a drop in texture intensity. We find in the prism pole figures either the features and development of annealing textures as described for rolled Zr or a continuous, smeared distribution of prism poles between the $\langle 10\bar{1}0 \rangle$ and $\langle 11\bar{2}0 \rangle$ directions.

The following results for drawn tubes and extruded tubes are examples of the differences in annealing behavior. First, for tubes cold drawn in six passes to 50% reduction in area, the basal poles have a preferred position of ±40 to 60° from the radial toward the tangential direction. The $\langle 10\bar{1}0 \rangle$ direction is parallel to the axial direction. Annealing 45 min at 700°C changes the preferred position of basal poles to the radial direction and also weakens the texture intensity by 50%. The prism poles then have nearly a random distribution, with perhaps a slight emphasis of $\langle 10\bar{1}0 \rangle$ in the axial direction.

In the basal pole figure for an extruded and annealed tube, we found no change from the deformation texture, even though the deformation texture was very similar to that of the drawn tubing given identical annealing. The prism pole figure shows the annealing texture usual for rolled Zr. In the extruded tubes, we repeatedly found an additional splitting of the basal poles toward the axial direction when the reduction in wall thickness was > 90%. Annealing did not change this splitting. We assume that this splitting resulted from basal slip during the hot-extrusion process.

We cannot yet explain the different annealing behaviors; more systematic examinations are necessary. But it is worthwhile noting that the drawn tubes were deformed cold, while the extruded tubes were

processed warm. Some amount of recrystallization during the extrusion may have induced a texture that could not be changed by further annealing.

Circumferential Texture Variations in Zircaloy Tubing (D. O. Hobson)

Last quarter we reported the texture variations found around the circumference of tubing experimentally fabricated by tube reducing and ascribed these variations to a number of incidents in the history of the tubing. We have recently examined tubes fabricated by swaging, drawing, and planetary swaging of starting materials from various stages of the earlier schedules for experimental tube reducing. We analyzed the circumferential texture variations and related them to the history. The textures produced by tube reduction were quite strong, and we found that whether or not subsequent fabrication affected the prior texture depended on the kind of fabrication. Reductions such as drawing and, to a lesser extent, planetary swaging introduced no new variations of their own but did reduce the amplitude of the variations of the old textures. Ordinary swaging imposed strong new texture variations that obliterated the old textures. A cyclic texture variation produced by one of the tube-reducing schedules remained even after two drawing passes; the amplitude was much reduced, but the cyclic variation could still be seen.

Radial basal pole intensity scans for the tubes at various stages of the fabrication processes were averaged to obtain values corresponding to the center points of conventional pole figures of the surfaces of the tubes. We have attempted various correlations between these average values of radial intensity and such fabrication variables as reduction in area, reduction in diameter, reduction in wall thickness, and Q ratio. So far, we have found no correlation with any of these variables, either alone or in combination. We did find a correlation, however, when we plotted average radial intensity versus the thickness of the tubing wall. Such plots are shown in Figs. 4.3 and 4.4.

Figure 4.3 shows the data for three tube-reduced and drawn materials. The data points at the heaviest wall thickness represent the tube-reduction step, and the others represent the drawing steps. The numbers above the data points show the percentage of reduction in area.

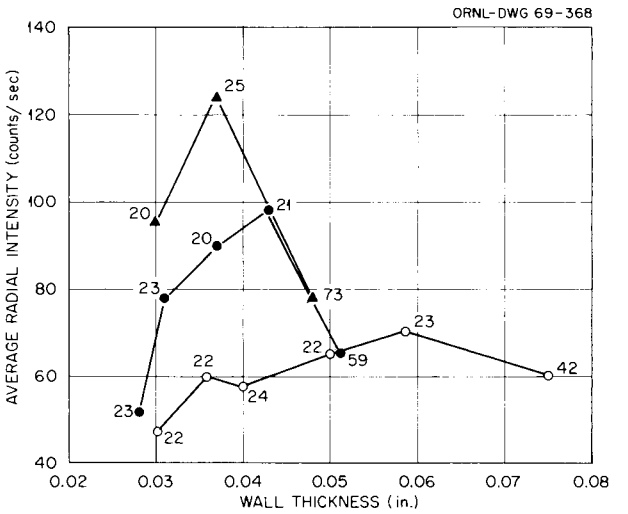

Fig. 4.3. Average Radial Intensity Versus Wall Thickness of Cold-Drawn Zircaloy Tubing.

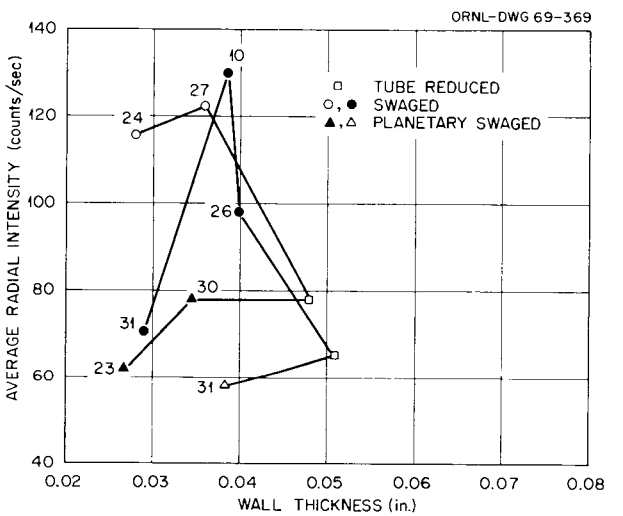

Fig. 4.4. Average Radial Intensity Versus Wall Thickness of Swaged Zircaloy Tubing.

For each of the three drawing schedules, the average intensity increased on the first drawing step over the previous value for tube reducing. The intensity then decreased with each successive drawing pass.

Figure 4.4 gives the data for tubes fabricated by tube reducing followed by either conventional or planetary swaging. In general, the intensity varies as in Fig. 4.3. There are two exceptions, however. The tubes reduced by planetary swaging did not show an increase in

intensity on the first pass after tube reducing; we do not yet know the cause. The one schedule for which we have data for two passes of planetary swaging shows the expected decrease on the second pass. The second exception occurs on the second pass of one of the conventional swaging passes: there is an anomalous increase in intensity, probably due to the light reduction in area (10%) that worked only the surface of the tube.

The data presented here represent only the surfaces of the tubing. We shall obtain more complete information, about both the surface and various layers through the tube walls, by conventional pole-figure techniques. We believe that the simple relationship between average radial intensity and wall thickness is not the correct correlation but that a more complex relationship exists.

We examined six fuel cladding tubes from four different vendors, for circumferential variations. No statistical interpretation can be made from this small number of samples, but it is interesting that five of the six tubes had enough variation in texture that, based upon the behavior of previous tubes, nonuniform mechanical properties would be expected. The most uniform commercial tube showed about 15% spread in radial basal pole intensity and no cyclic variation. The other tubes showed variations from 30 to 83%. Cyclic behavior was evident in four tubes; one of these four showed a regular six-cycle variation.

Yielding of Highly Textured Zircaloy Tubing (P. L. Rittenhouse)

It is well known that the uniaxial strength properties of the Zircaloys are highly anisotropic and dependent on texture, but there has been very little reported on biaxial behavior as related to texture. Consider the three basal pole figures shown in Fig. 4.5. These are typical of the wide variation that can occur in Zircaloy tubes from different lots. The basal poles may be concentrated at the radial (R) or tangential (θ) directions or between the two. The biaxial yield surfaces for these tubes have been determined, but let us consider only the effect of the texture in these three tube materials on the yield behavior under stress states of ±1. In the stress state +1, the axial stress and the tangential stress (or hoop stress) are of equal value and are both

ORNL-DWG 69-255

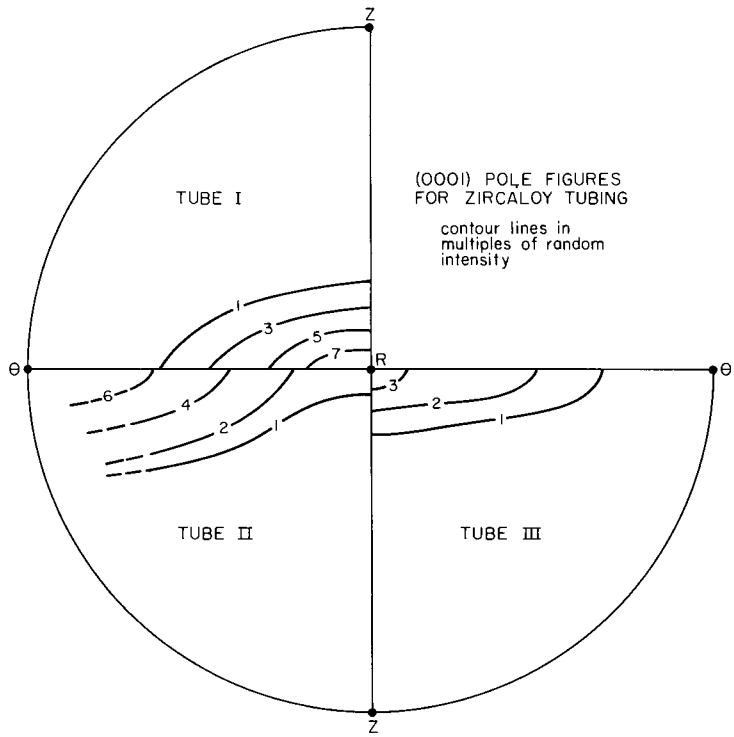

Fig. 4.5. Basal Pole Figures for Three Lots of Zircaloy Tubing. R, θ, and Z correspond to the radial, tangential, and axial directions of the tubing.

tensile. The axial stress in the stress state −1 is tensile, but the tangential stress, although of the same absolute value, is compressive.

The three tubes have about the same yield strength in uniaxial tension – 60,000 psi – so that yield criteria developed and used for isotropic materials predict identical biaxial behavior for the three. Tube I, however, has the highest value for yield at the stress state +1 and the lowest at −1 (see Table 4.2). This is just reversed for Tube II. Tube III has yield values intermediate to the other tubes in both stress states. The differences in the strengths of the three tubes are, of course, the result of the texture differences. For example, when the stress state is +1 there are equal tensile stresses along the tube axis, Z, and the tangential direction, θ. The applied stress in the radial direction, R, is zero. This stress state can be considered equivalent to a combination of two simpler stress states. The first of these is a

Table 4.2. Yield Stresses for Zircaloy Tubing at Two Stress States

Tube	Stress at 0.2% Yield (psi)	
	$\frac{\text{Axial Stress}}{\text{Tangential Stress}} = +1$	$\frac{\text{Axial Stress}}{\text{Tangential Stress}} = -1$
I	90,000	34,000
II	60,000	47,000
III	77,000	40,000

stress state of hydrostatic tension, which produces no distortion deformation, and the second is a uniaxial compression parallel to the tube radius. For the tube to yield, it must deform or elongate in the plane of the applied tensile stresses, and this deformation must be accommodated by wall thinning. In material with a texture like that of Tube I (basal poles parallel to the tubing radius), wall thinning must occur primarily by compression twinning. Since this mode of deformation requires a very high applied stress, it is not surprising that Tube I is highly resistant to yielding in the +1 stress state. In Tube II, the deformations in the +1 stress state (axial elongation and wall contraction) can occur by prism slip, and the applied stress required for yielding is much lower than that for Tube I. Tube III, as would be expected from its texture, is intermediate in strength.

The same reasoning can explain why Tube II has the highest yield strength in the −1 stress state. For optimum strengthening, the basal poles must be concentrated in the plane containing the axial and tangential directions.

These and similar facts illustrate quite dramatically the influence of texture on yielding behavior. They should allow us to use Zircaloy tubing of optimum properties for any particular application by matching texture and stress state.

PART II

COOLANTS

5. ALKALI-METAL CORROSION STUDIES

W. O. Harms J. H. DeVan A. P. Litman

The purpose of this program is to investigate the chemical and metallurgical effects produced in structural materials during exposure to alkali metals. The program is designed to guide the selection of container materials for sodium-cooled fast breeder reactor systems and lithium-cooled space power reactor systems in which K serves as the Rankine-cycle working fluid. Forced circulation loop experiments of engineering scale are included in the test program.

Mass Transfer of Interstitial Impurities Between Vanadium Alloys and Sodium

Although vanadium alloys are highly resistant to dissolutive attack by Na, they are quite reactive with nonmetallic impurities in Na, particularly with C, N, and O. Accordingly, we are investigating the mechanisms by which vanadium alloys are attacked in Na at impurity levels typical of service conditions in a reactor. Our program is concerned with four basic aspects of the oxidation process for vanadium alloys in Na: (1) the partitioning of O between vanadium alloys and Na; (2) the effects of alloying additions of Cr and Zr on the diffusion coefficient of O in V; (3) the effects of Cr and Zr in V on the oxide formed and on the dissolution of the alloys in Na; and (4) the solubility of V in Na as affected by the presence of O in either metal. We are also examining the kinetics of the transfer of C and N between vanadium alloys and types 304 and 321 stainless steel in a sodium circuit.

Oxygen Effects on the Compatibility of Vanadium and Sodium (R. L. Klueh)

We previously reported[1] on oxygen uptake by vanadium specimens contained in vanadium capsules at 600 and 800°C. Similar tests were made

[1]R. L. Klueh, Fuels and Materials Development Program Quart. Progr. Rept. Sept. 30, 1968, ORNL-4350, pp. 87–91.

at 600°C with a vanadium specimen in capsules of Mo and type 304 stainless steel. We chose Mo because it is relatively inert to oxygen interaction, and stainless steel because of its interest for liquid-metal fast breeder reactor (LMFBR) applications.

Except for the capsule material, the experimental system and test procedure were the same as described earlier.[1] Table 5.1 shows the weight gained by vanadium specimens as a function of the amounts of Na_2O added to the Na before test. As in the case of the all-vanadium systems,[1] weight was gained in proportion to the amounts of Na_2O added to the Na. Unlike the all-vanadium systems, however, which had no reaction products, the specimens exposed to Na with high oxygen content in these later tests had a dark surface scale. The scale on those contained in molybdenum capsules were quite black, while those contained in stainless steel were dark gray.

These specimens have now been submitted for metallographic and chemical analyses, and we are attempting to determine the nature of the scales.

Table 5.1. Weight Changes of Vanadium Specimens Exposed To Sodium Containing Various Amounts of Na_2O at 600°C

Container Material	Initial Oxygen Content of Sodium[a] (ppm)	Specimen Weight Gain[b] (mg)
Molybdenum	50	1.3
	450	5.0
	1000	8.9
	1800	14.6
	4000	14.3
Type 304 Stainless Steel	50	0.5
	550	3.8
	1100	7.6
	2050	11.2
	4000	20.6

[a]Oxygen added as Na_2O.

[b]Specimen size: $1 \times 1/2 \times 0.065$ in.

Deoxidation of Vanadium by Molten Lithium (J. H. DeVan)

We have been examining techniques for altering the oxygen content of V without affecting other chemical or metallurgical properties of the metal. The ability to adjust the oxygen content of V would facilitate our investigation of the role of O in the process of corrosion by Na.

Though the concentration of O can be increased above that in as-received V by heat treatment in an environment of low-pressure O, the reverse process is more difficult, as attested by the problem of manufacturing V with low oxygen content. However, a potential technique for deoxidizing V was suggested by the results of lithium capsule tests conducted by DiStefano[2] in which he evaluated the effect of interstitially dissolved O on the corrosion resistance of V in Li. His studies were carried out in 0.62-in.-OD × 0.030-in.-wall-thickness × 4.0-in.-long vanadium capsules, each of which contained a vanadium coupon submerged in 3 in. of Li. He found that V containing even as much as 2200 ppm dissolved O was completely resistant to attack by Li at 800°C. More significantly, however, the initial oxygen content of all vanadium specimens, which ranged from 400 to 2200 ppm before test, was reduced to about 100 ppm after test. The level of N in the V in some cases went up and in other cases remained unchanged.

Based on these results, we recently exposed a set of vanadium tubes, end caps, and specimens to molten Li to provide low-oxygen vanadium capsules for our proposed sodium corrosion tests. The cross sections of the vanadium components ranged from 0.049 to 0.060 in. The reaction vessel used for the treatment was constructed from 2.5-in.-OD Nb–1% Zr tubing and is pictured with the vanadium components in Fig. 5.1. To augment the gettering capability of the Li and to counteract the possibility of N being picked up by the V, we also incorporated a coil of zirconium foil around the vanadium components. The vessel was filled with 280 g of filtered Li and heated for 100 hr at 800°C. The Li was then discharged from the vessel, and residual Li was removed by flowing liquid ammonia through the inlet and outlet lines to the vessel until no color change

[2]J. R. DiStefano, Corrosion of Refractory Metals by Lithium, ORNL-3551 (April 1966), pp. 68–69.

Fig. 5.1. The Nb–1% Zr Reaction Vessel (Left) Used to Lithium-Treat Vanadium Capsule Components (Right). Corrugated zirconium foil (center) was placed against vessel wall, surrounding vanadium components.

could be detected in the ammonia. The vessel was then opened, and the Li, the vanadium components, and the zirconium getter strip were chemically analyzed. The analytical results for the V appear in Table 5.2. In the case of the vanadium tubes, the analyses reflect the results of samples taken from each end and the middle of one tube. The oxygen level of all vanadium components decreased to below 100 ppm. The zirconium foil gained O roughly commensurate with the amount of O lost by the V. The nitrogen level of the V increased slightly despite the presence of zirconium foil. No chemical differences were detected among samples taken from different longitudinal positions on the vanadium tube. However, removal of 5- and 10-mil layers from the inside and outside surfaces reduced both the oxygen and nitrogen levels (Table 5.2). No metallographic changes were noted in the V, and the metallic impurities (including Li) were the same in vanadium samples before and after test.

These results indicate that lithium treatment could be used to reduce the oxygen level of commercially produced V whenever cross sections

Table 5.2. Effect of Zirconium-Gettered Lithium on Interstitial Content of Vanadium Metal After 100 hr at 800°C

Condition of Metal	Interstitial Content, ppm			
	O	N	H	C
3/4-in.-OD × 0.05-in.-Wall-Thickness Tubing				
As received[a]	1470	580	6	200
Lithium treated[a]	87	850	<1	230
Lithium treated, 5 mils machined from outer and inner surfaces	65	610	<1	200
Lithium treated, 10 mils machined from outer and inner surfaces	69	600	<1	220
3/4-in.-diam × 0.06-in. End Caps				
As received	1600	320	<1	470
Lithium treated	90	430	<1	470

[a]Average of three analyses.

are conducive to diffusion of O out of the V in reasonable periods of time. We are now evaluating the effects of time, temperature, and oxygen content of the Li on the kinetics of vanadium deoxidation.

Interstitial Contamination Effects in Vanadium and Its Alloys
(R. L. Wagner)

Interstitial contaminants in vanadium alloys significantly affect their metallurgical and mechanical properties. We are now evaluating the effects of alloying elements on the nature and rate of interstitial contamination of the following vanadium alloys in terms of temperature and vacuum conditions: V–5% Cr, V–10% Cr, V–15% Cr, V–1.5% Zr, V–5% Zr, V–10% Zr, and V–20% Ti. Reference studies on unalloyed V were begun at 500 and 900°C. As shown in Table 5.3, a 1-hr anneal at 900°C at 10^{-7} torr did not change the interstitial chemistry, but after 100 hr there was evidence of some decarburization. After 100 hr at 3×10^{-6} torr, the C decreased 60 ppm and the O increased 150 ppm. No weight change was

Table 5.3. Effect of Vacuum Exposure on the Interstitial Content of Vanadium[a]

Condition	Time (hr)	Pressure (torr)	Interstitial Analyses, wt %			
			C	N	H	O
As received			0.032	0.053	0.0007	0.021
Tested at 500°C	300	5×10^{-8}	0.034	0.051	0.0003	0.025
Tested at 900°C	1	1×10^{-7}	0.032	0.052	0.0002	0.022
Tested at 900°C	100	2×10^{-7}	0.029	0.053	0.0001	0.024
Tested at 900°C	100	3×10^{-6}	0.026	0.054	0.0002	0.036

[a]0.007-in.-thick foil.

observed for any of the samples after annealing. Related experiments[3] using this same equipment have extablished the major gaseous impurities to be H_2, C, N_2, H_2O, and CO_2.

We are evaluating other temperature and vacuum conditions and the value of protective wrapping with Ta. A furnace with a temperature gradient from 350 to 900°C is being set up to allow us to test several samples simultaneously and to vary the composition of our vacuum atmosphere.

Compatibility of Stainless Steel and Insulation in LMFBR Systems

A. P. Litman

We are studying the compatibility of stainless steel and thermal insulation, with and without the presence of Na, to guide the selection of containment piping and insulation for the Fast Flux Test Facility (FFTF) and future LMFBR systems. A comprehensive study of the literature will be followed by testing of types 304, 316, and 321 stainless steel between 370 and 760°C in air and in inert gas in contact with insulations and Na.

[3]H. Inouye, Contamination of Refractory Metals by Residual Gases in Vacuums Below 10^{-6} Torr, ORNL-3674 (September 1964).

The Effect of Insulation on the Oxidation of Stainless Steel
(C. D. Bopp)

During this reporting period, we completed the assembly of our oxidation test apparatus, which is shown in Fig. 5.2. This apparatus will be used both for the first part of this study, which deals with compatibility of thermal insulation in contact with stainless steel, and for the second part of the program, which deals with the effect of a small leak on the corrosion of the system.

We are testing relatively large specimens, 3/4-in.-diam × 5-in. long tubes, to simulate more closely actual LMFBR container materials and to match the sensitivity of an available chromatograph. During oxidation, the O_2 consumed and the H_2 generated (in moist air) are measured with a gas chromatograph. A measure of the permeability of the insulation is obtained from the pressure drop across the manometer shown in Fig. 5.2. After test, the tube specimen is removed, weight changes are recorded before and after the scale is removed, and the specimen is metallographically examined.

The test arrangement used for our first experiment with type 316 stainless steel tube is shown in Fig. 5.3. Ceramic filler pieces will be used in future tests to reduce the volume of the oxidation tube and the moisture meter, but they were not available for this preliminary test. The degree of stagnation of the atmosphere produced by the insulation was therefore less than we would have liked (see Fig. 5.2), since stagnation may accelerate oxidation (i.e., produce catastropic oxidation) by confining either MoO_3 vapor from materials that contain Mo or volatile substances from certain types of insulation. After 300 hr at 800°C in dried air (passed over $CaSO_4$ at 25°C), the metal loss from a specimen after removal of the scale was 8 mg/cm^2, and the scaling did not appear to be any more severe on the portion of the tube in contact with Kaowool. This rate of scaling is of the same magnitude as that found by others[4] at 870°C. We are conducting a test at the same temperature, 800°C, in

[4]A. de S. Brasunas, J. T. Gow, and O. E. Harder, "Resistance of Iron-Nickel Chromium Alloys to Corrosion in Air at 1600–2200°F," pp. 129–152 in Symposium on Materials for Gas Turbines, Buffalo, New York, June 24–26, 1946, Philadelphia, 1946.

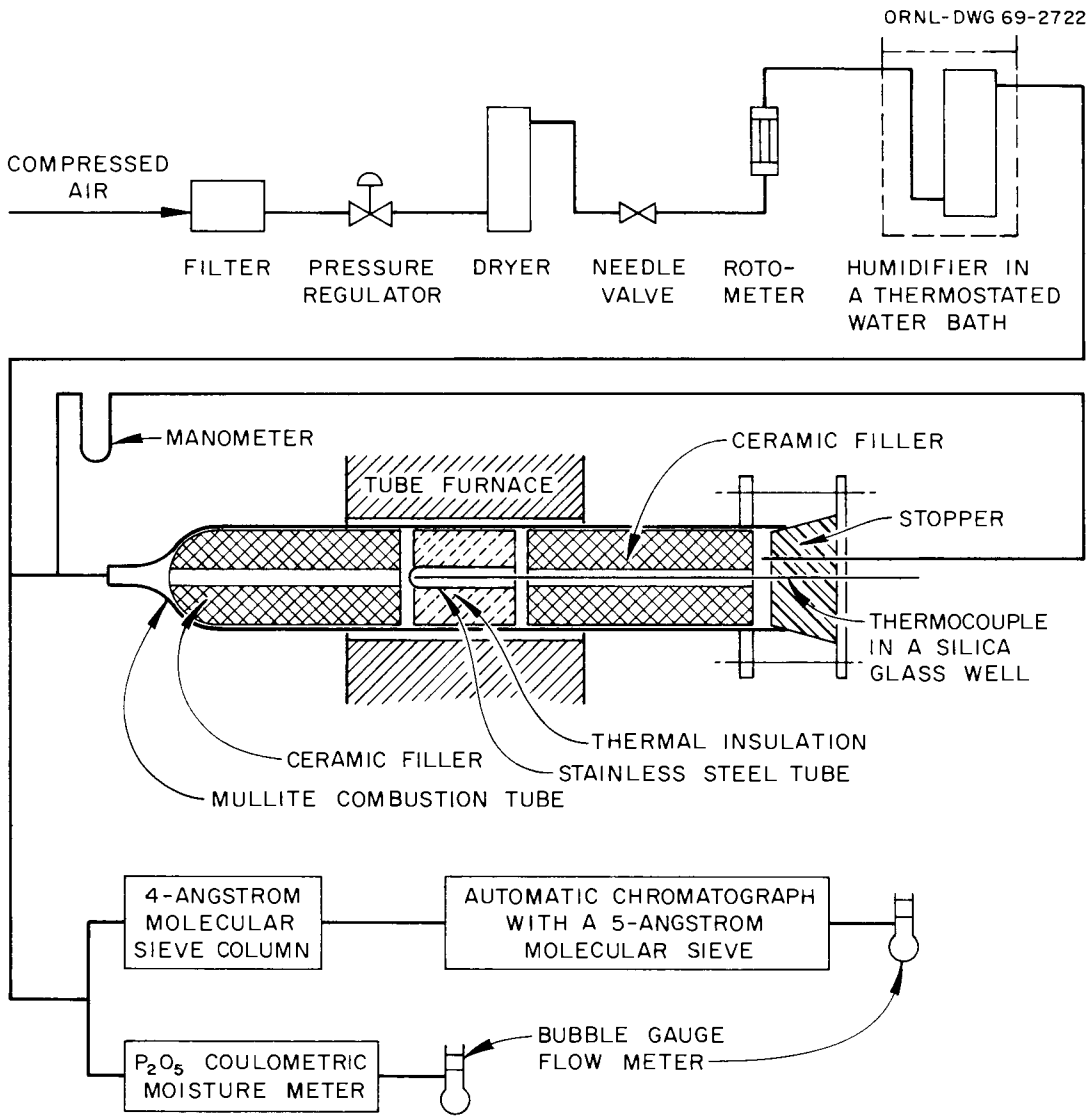

Fig. 5.2. Schematic Diagram of Apparatus for Insulation-Stainless Steel Compatibility Test.

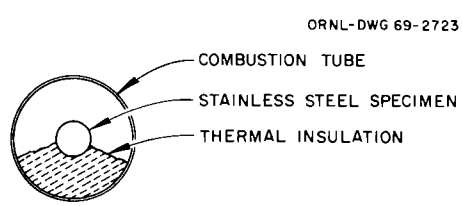

Fig. 5.3. Configuration for Preliminary Test of Interaction Between Stainless Steel and Thermal Insulation.

moist air (saturated with water vapor at 20°C), and the preliminary data for oxygen consumption indicate that the scaling rate is not much greater than in dry air.

Analysis of Mass Transfer Mechanisms in Loop Systems

R. B. Evans III

At the present stage of technology, mathematical treatments of mass transport in alkali metals stop short of considering solid-state diffusion effects. Since past studies at ORNL have underscored the importance of solid-state diffusion to mass transport at high temperatures, we are attempting to factor this added transport step into existing classical dissolution-deposition treatments.[5–7] The resultant equations are being compared against experimental findings for nickel- and iron-base systems operated with Na both at ORNL and at other laboratories.

In order to handle the rather complicated temperature profiles of these experimental systems, we have set up a computer program that allows us to divide the system into an arbitrary number of segments, across any one of which temperature can be assumed to vary linearly with distance along the loop.

There are several obstacles to acquiring a definitive treatment of existing experimental information, and these are worth noting for future experimental designs. The most serious difficulties stem from complicated geometry and temperature profiles, the uncertainty as to supersaturation effects, and the confusion about whether solute is carried in

---

[5]J. J. Keyes, Jr., Some Calculations of Diffusion Controlled Thermal Gradient Mass Transfer, ORNL-CF-57-7-115 (July 22, 1957).

[6]L. F. Epstein, "Static and Dynamic Corrosion and Mass Transfer in Liquid Metal Systems," Vol. 53, p. 67 in Liquid Metals Technology, Part 1, Chem. Engr. Progr. Symp. Ser. 20, American Institute of Chemical Engineers, New York, 1957.

[7]W. R. Grimes, G. M. Watson, J. H. DeVan, and R. B. Evans, "Radio-Tracer Techniques in the Study of Corrosion by Molten Fluorides," pp. 559–574 in Conference on the Use of Radioisotopes in the Physical Sciences and Industry, September 6–17, 1960 Proceedings Vol. III, International Atomic Energy Agency, Vienna, 1962.

part as particulate matter. Finally, in many systems there have not been enough determinations of weight change to yield a reliable measure of mass transport rates at every loop position.

In order to supplement the existing information on weight change for the several nickel alloy-sodium systems operated at ORNL,[8] we are submitting specimens from several loops for microprobe analysis. Concentration profiles of the alloy constituents in the loop walls and in crystalline deposits should shed considerable light on the mechanism involved and on the kind of mathematics one might use (even semiempirically) to describe corrosion rates in this particular system.

Corrosion of Refractory Alloys in Lithium, Potassium, and Sodium

J. H. DeVan A. P. Litman W. R. Huntley

Requirements for auxiliary electricity or ion propulsion for space vehicles necessitate power plants of high efficiency that will operate at high temperatures. For these applications, nuclear power systems have been proposed in which alkali metals are used to transfer heat, drive a turbogenerator, and lubricate rotating components. Accordingly, we are investigating the corrosion properties of candidate alkali metals, primarily Li and K, under conditions of interest for space applications. Because of the relatively high temperatures (>1000°C), the investigation is concerned largely with refractory-metal container materials.

Forced Circulation Boiling Potassium Loop Tests (FCL-8)
(C. W. Cunningham, B. Fleischer)

Loop FCL-8, constructed of the niobium alloy D-43, is the third and final test in a series of forced convection loops designed to evaluate the effects of boiling potassium and potassium vapor at high velocity on niobium-base alloys and on TZM alloy. The loop completed 10,000 hr of operation in June 1968, and metallurgical examination is in progress.

---

[8]J. H. DeVan, "Corrosion of Iron- and Nickel-Base Alloys in High-Temperature Sodium and NaK," pp. 643–659 in Alkali Metal Coolants (Proceedings of a Symposium, Vienna, 28 November – 2 December 1966). International Atomic Energy Agency, Vienna, 1967.

We have destructively examined the two-pass helical induction pump from loop FCL-8 to ascertain the reason for the drop in pump efficiency[9] encountered during test. Examination showed that the 2.2-in.-OD outer shell of the pump had expanded to produce a gap of 0.035 in. between the inner surface of this shell and the adjoining helix assembly. This allowed a considerable part of the K flowing through the pump to bypass the outer helix. The growth of this outer shell indicates that it operated at a much higher temperature than measured at the inlet and outlet pumps. The explanation for the higher temperature we now believe is associated with the unique economizer capability of the two-pass reentrant helical pump cell, which features two concentric helical flow passages separated by a single wall of Nb–1% Zr alloy. This configuration can act as a regenerative heat exchanger for the transfer of energy deposited in the pump cell by the drive motor during normal operation. Consequently, even though the pump inlet temperature was nominally about 595°C and the outlet temperature was about 720°C, our calculations show that the central portions of the pump cell wall could have exceeded 980°C. The creep rate of Nb–1% Zr at this temperature under the pressure load of the pump would be on the same order as that observed for the outer shell (1.6×10^{-6} hr^{-1}). Future pumps of this design must provide a temperature capability considerably above the proposed inlet-outlet temperature range.

Effect of Oxygen on Compatibility of Refractory Metals and Alkali Metals (R. L. Klueh)

Oxygen Effects in the Niobium-Potassium System. – In our studies to compare the effect of O in the different refractory metal-alkali metal systems,[10] we have completed further tests on the Nb-O-K system. Five capsules containing specimens of unoxidized Nb were exposed to K with several oxygen levels, and two capsules containing specimens of Nb with 580 and 1400 ppm O, respectively, were exposed to K with about 100 ppm O.

---

[9]B. Fleischer and C. W. Cunningham, Fuels and Materials Development Program Quart. Progr. Rept. June 30, 1968, ORNL-4330, pp. 91–93.

[10]R. L. Klueh, Fuels and Materials Development Program Quart. Progr. Rept. Sept. 30, 1968, ORNL-4350, p. 125.

All tests were conducted for 500 hr at 600°C by procedures described previously.[11] Results are shown in Table 5.4.

The surfaces of specimens exposed to K with high oxygen content appeared dull after test, but none of them appeared to have a scale. All specimens lost weight. The two specimens oxidized before test lost considerable O, while unoxidized specimens changed little in K with either high or low oxygen content.

Metallographic examination of the two oxidizied specimens indicated that they had been penetrated by the K. The penetration was much less severe than for similarly oxidized tantalum specimens exposed to K or for niobium specimens exposed to Na at 600°C. Since we believe penetration involves the formation of a compound containing O, the final concentration of O in the penetrated specimens may include O in the form of a corrosion product as well as O dissolved in Nb.

[11]R. L. Klueh, Fuels and Materials Development Program Quart. Progr. Rept. June 30, 1968, ORNL-4330, p. 142–146.

Table 5.4. Effect of Oxygen on Compatibility of Niobium and Potassium

Oxygen in Potassium Before Test[a] (ppm)	Oxygen in Niobium (ppm)		Weight Change[c] (mg)	Niobium in Potassium After Test (ppm)
	Before[b]	After[b]		
100	70	64	−0.2	960
530	70	68	−0.2	1060
1000	70	58	−1.1	2190
2030	70	57	−2.9	3380
3900	70	71	−7.0	3600
100	580	420[d]	−1.2	885
100	1400	520[d]	−5.5	1130

[a]Oxygen added as K_2O to K already containing about 100 ppm O.

[b]Determined by vacuum-fusion analysis.

[c]All specimens were about 1 × 1/2 × 0.04 in.

[d]Microstructures show that K penetrated these specimens.

Specimens with normal levels of O before test showed no significant metallographic changes. Microhardness profiles for these specimens indicated that the oxygen concentration was uniform across the specimen, and diffusion calculations confirmed that the oxygen concentration should have attained equilibrium across the specimen under our test conditions.

Partitioning of Oxygen Between Potassium and Zirconium and Between Sodium and Zirconium. — We demonstrated[12] that the equilibrium distribution coefficient for the partitioning of O between Zr and K or Na (atom fraction of O in Zr divided by atom fraction of O in alkali metal) is large enough to be considered infinite. Therefore, when Zr is exposed to the liquid metal, the amount of O originally present in the liquid, $C_O^{(A)}$, is given by

$$C_O^{(A)} = \Delta C_O^{(Zr)} \frac{W_{Zr}}{W_K} , \qquad (5.1)$$

where $\Delta C_O^{(Zr)}$ is the O gettered by the Zr and W_{Zr} and W_A are the weights of Zr and alkali metal, respectively.

We are evaluating the applicability of Eq. (5.1) for the analysis of O in K and Na. Our technique consists of exposing a given amount of alkali metal to a zirconium coupon in a molybdenum container for 100 hr at 815°C. After test, the capsules are inverted and quenched, the specimens are removed and cleaned in alcohol, and $\Delta C_O^{(Zr)}$ is determined by vacuum-fusion analysis. The technique has been referred to as a gettering-vacuum-fusion (GVF) analysis. Table 5.5 shows the results of evaluations of the K by the GVF technique; in these tests, known amounts of O were added to the K before test, and the amount of O recovered by the Zr was checked against the amount added. For oxygen concentrations up to about 1000 ppm, the amount recovered was within 10% of the amount added. At higher oxygen concentrations, however, the percentage recovered decreased significantly. Results of similar tests for Na are shown

[12] R. L. Klueh, Fuels and Materials Development Program Quart. Progr. Rept. Sept. 30, 1968, ORNL-4350, pp. 126–127.

Table 5.5. Oxygen Recovered from Potassium by Gettering-Vacuum-Fusion Analysis[a]

Total Oxygen[b] (ppm)	Oxygen Content in Zirconium (ppm)	Percent Oxygen Recovered by Zirconium
385	407	105
625	595	95
820	900	91
1125	800	71
1575	1000	64
2200	950	43
3000	1300	43

[a]All tests were made at 815°C for 100 hr on 0.04-in.-thick zirconium specimens.

[b]Initial O plus that added as K_2O.

in Table 5.6. In this case, the percentage recovered above about 1000 ppm O again decreased, but the decrease was not as large as for the tests with K.

We selected Mo as the container material because it is relatively resistant to oxidation in alkali metals. Indeed, for all tests with Na and for those tests in which the K contained low concentrations of O, there was no indication of any attack on the Mo. However, the surfaces

Table 5.6. Oxygen Recovered from Sodium by Gettering-Vacuum-Fusion Analysis[a]

Total Oxygen[b] (ppm)	Oxygen Content in Zirconium (ppm)	Percent Oxygen Recovered by Zirconium
500	465	93
900	845	94
1250	945	76
1900	1450	76
2100	1900	90

[a]All tests were made at 815°C for 100 hr on 0.04-in.-thick zirconium specimens.

[b]Initial O plus that added as Na_2O.

of the molybdenum end caps that had been in contact with K that had a high concentration of O ($\gtrsim$ 1000 ppm) appeared etched, and metallography showed them to be faceted.

Zirconium specimens that had contacted the alkali metals with low oxygen content appeared unaffected. But zirconium specimens that had contacted the K with high oxygen content had a dull metallic appearance as opposed to their highly polished appearance before test, and specimens that had contacted Na with high oxygen content were covered by a dark-gray nonadherent film. X-ray diffraction showed that surfaces that had contacted the K with high oxygen content contained Mo and an intermetallic compound, Mo_2Zr. Bulk analyses of these zirconium specimens, which contained less than 10 ppm Mo before test, confirmed the presence of Mo:

Concentration (ppm)	
Oxygen in Potassium Before Test	Molybdenum in Zirconium After Test
385	930
625	1580
820	1130
1125	3300
1575	4500
2200	5800
3000	4400

By contrast, the surfaces of Zr exposed to Na with high oxygen content showed ZrO_2 with no evidence of molybdenum transport.

Oxygen had previously been shown to increase the solubility of Mo in K.[13,14] These results apparently reflect this effect and, in turn, suggest that this increased solubility causes significant dissimilar-metal mass transfer of the Mo in the K. The Mo and Mo_2Zr on the

[13] R. E. Cleary, S. S. Blecherman, and J. E. Corliss, Solubility of Refractory Metals in Lithium and Potassium, TIM-850 (October 1965).

[14] E. M. Simmons and J. F. Lagedrost, "Mass Transfer of TZM Alloy by Potassium in Boiling-Refluxing Capsules," pp. 237–271 in AEC-NASA Liquid Metals Information Meeting held in Gatlinburg, Tennessee, April 21–23, 1965, CONF-650411, USAEC Division of Technical Information Extension, Oak Ridge, Tennessee.

zirconium surface apparently act as a barrier to the absorption of O, thereby causing a decrease in the percentage of O recovered at the higher oxygen concentrations.

This interpretation is strengthened by the results of tests with Na. Our own unpublished studies of the comparative oxidation of Nb and Ta in alkali metals suggest that O does not affect the solubility of refractory metals in Na to the same degree as in K. The decrease in the percentage of O recovered from Na that contained > 1000 ppm O appears to be connected with the ZrO_2 formed. Mackay[15] showed that the oxidation of Zr in Na is independent of oxygen concentration in the Na above about 3 ppm O. If Mackay's extrapolated rate constant is used to calculate the amount of O that can be gettered in 100 hr at 815°C, all of the O present should have been recovered even if a ZrO_2 scale formed. The decrease in the percentage recovered in the sodium tests may have resulted from the loss of some of the surface scale when the specimens were prepared for vacuum-fusion analysis.

Table 5.7 shows the results of GVF analyses on K and Na that contained < 100 ppm O. A correction, which will be discussed in a future report, was required to account for O contributed by the Mo of the container. Also shown are results obtained by amalgamation. The two methods of determination agree quite well at these low levels of oxygen content. The concentration of Mo in the Zr did not change (< 10 ppm Mo both before and after exposure).

Corrosion of Refractory Alloys by Lithium

Thermal Convection Loop Tests (J. H. DeVan). — We are continuing our analysis of thermal convection loop TCL-6R, which operated with Li for 3000 hr with a maximum temperature of 1350°C in the hot leg. The loop was constructed of the tantalum alloy T-222 and contained T-222 insert specimens. Initial results[16] showed weight losses over two-thirds

---

[15] T. L. Mackay, Oxidation of Zirconium and Zirconium Alloys in Liquid Sodium, NAA-SR-6674 (February 1962).

[16] J. H. DeVan, Fuels and Materials Development Program Quart. Progr. Rept. Sept. 30, 1968, ORNL-4350, pp. 127–130.

Table 5.7. Comparison of Gettering-Vacuum-Fusion (GVF) and Mercury Amalgamation Techniques for Analysis of Oxygen in Potassium and Sodium

	Oxygen Concentration (ppm)	
	GVF	Mercury Amalgamation
Potassium	70	46
	88	52
	23[a]	28
	31[a]	35
	29[a]	28
	35[a]	43
	30[a]	30
	26[a]	31
Sodium	55	53
	41	35

[a]Potassium purified by vacuum distillation.

of the loop surface and locally high weight gains over the remainder. The weight changes correlated closely with the pattern of the migration of Hf around the loop.

We examined the concentrations of the interstitial impurities in insert specimens and tubing sections after their contact with Li in a thermal gradient. These chemical analyses are presented in Fig. 5.4. Tubing from the heater section of the loop showed a large increase in O. In contrast, tubing specimens from all other regions contained about the same O as before test, and the insert specimens lost O at all positions. Metallographic examination, as discussed below, indicated that the source of the O that contaminated the heater section of the tubing was external rather than associated with the Li.

We have observed a similar contamination problem in other experiments which, like this loop, were radiantly heated by an unalloyed tantalum heating element. Areas directly under the heater in each case were high in O while areas immediately away from the heater, which saw the same internal environment and temperature, were totally unaffected. It is significant that O was picked up even though the system pressure, as measured by a nude ion gage near the loop, was consistently in the

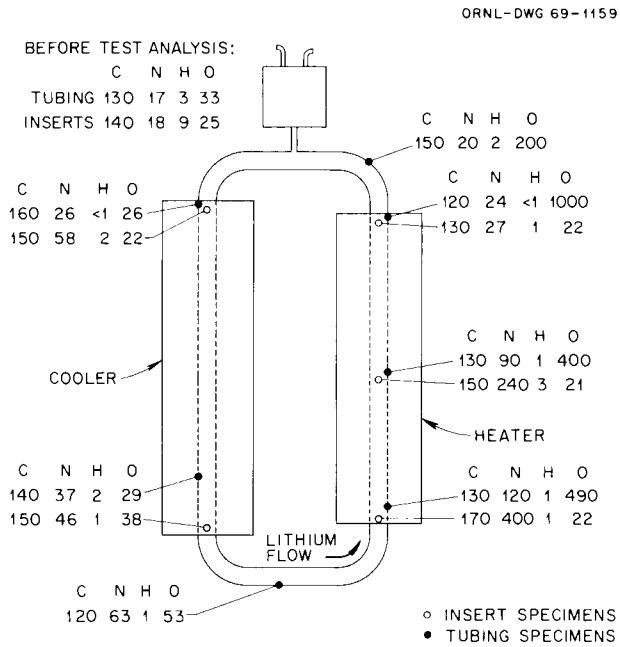

Fig. 5.4. Interstitial Content (ppm) of T-222 Loop Specimens After 3000-hr Test in Flowing Lithium at 1350°C.

range 10^{-8} to 10^{-9} torr. Judging from related test experience,[17] we believe we can circumvent the problem by substituting a tungsten-mesh heater element for the present tantalum assembly.

The nitrogen concentration in tubing and insert specimens increased in the colder regions of the loop and remained essentially unchanged in the hotter regions (Fig. 5.4). Point-to-point variations in carbon content were within the standard deviation of analyses for this element in T-222. The increase in N in colder regions of the loop ties in with the movement of Hf to these regions, as mentioned above, and also with the appearance in this region of a gold-colored film that has been identified by x-ray diffraction as HfN. Metallographic examination of specimens from colder regions revealed a relatively heavy concentration of an extremely fine precipitate evenly dispersed over the cross section of the specimen, as shown in Fig. 5.5(a). In the case of the hotter

[17]J. R. DiStefano, Refluxing Capsule Experiments with Refractory Metals in Boiling Alkali Metals, ORNL-4323 (January 1969), p. 25.

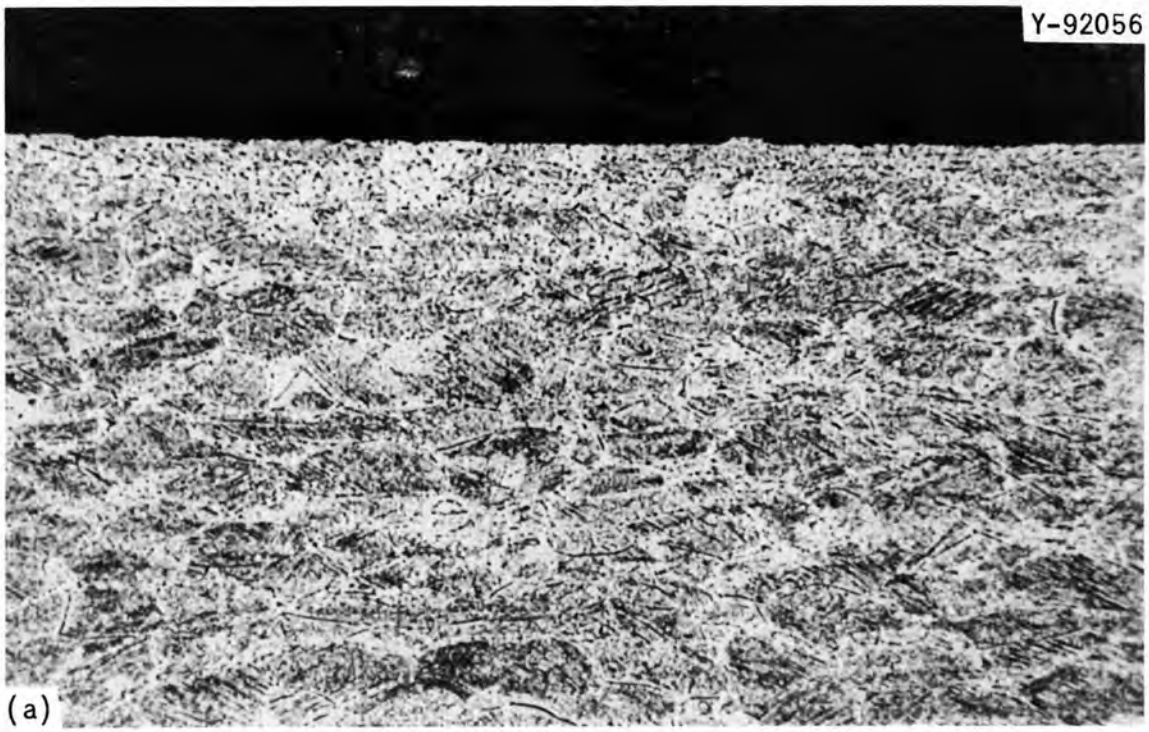

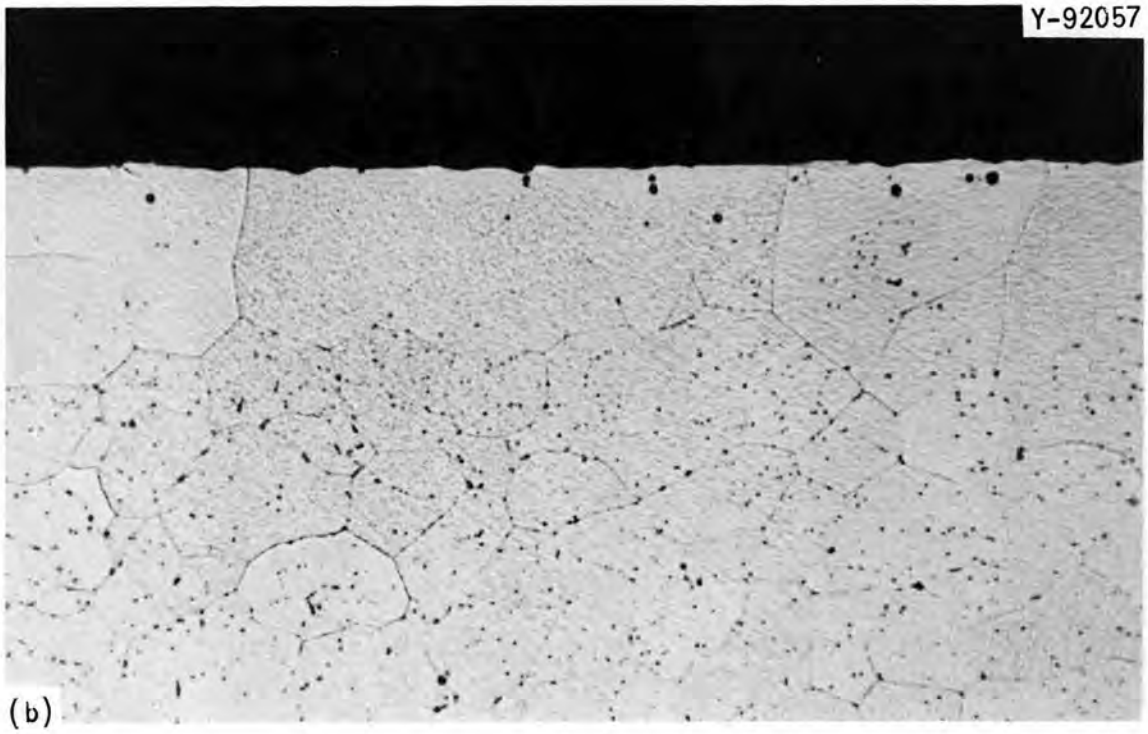

Fig. 5.5. Metallographic Appearance of T-222 Insert Specimens from Loop TCL-6R. Specimens were exposed to lithium for 3000 hr. 500×. (a) Minimum temperature position (1150°C) and (b) maximum temperature position (1350°C).

regions of the loop, we saw no metallographic changes in those insert specimens annealed (2 hr at 1600 °C) before test [Fig. 5.5(b)]. Specimens that were partially cold worked were recrystallized during test but suffered no apparent effects of the exposure to Li.

The inside surfaces of tubing specimens appeared similar to the insert specimens, but external surfaces of tubing from the heater section showed evidence of internal oxidation to a depth of 17 mils and were covered by a very thin external layer that had the characteristics of a carbonitride film.

T-111 Forced Circulation Loop (FCLLL-1) (D. L. Clark, B. Fleischer)

We are constructing a T-111 forced circulation liquid lithium loop that will provide information on the corrosion of materials for cladding and containing fuel elements for lithium-cooled power systems for space. During this report period, we completed a leak check of the vacuum chamber for this facility and assembled the loop into the chamber.

Vacuum Test. — We made a trial evacuation of the vacuum chamber for FCLLL-1 to test the reconditioned triode ion pumps. The trial showed the pumps to be in good working order, and both a helium leak detector and a gas analyzer showed the chamber to be leak-tight against He. During subsequent bakeout, however, a large leak developed in the main flange after the chamber reached about 370 °C. The flange was again leak-tight after the chamber had cooled to 80 °C. In the future we plan to lower the rate of chamber heating to about 0.25 °C/min so that leaks can be detected and eliminated, by tightening the flange, before they become excessive.

The auxiliary pumping system on the vacuum chamber was modified by the addition of a diffusion pump to the rough pumping system and by the installation of an optically baffled trap, cooled by liquid N, in the line between the auxiliary system and the chamber. This conversion makes it easier to detect leaks of He, decreases the likelihood of contaminating the system by back-diffusion of oil vapors, and shortens the period before the ion pumps can be activated. The base pressure attained by the rough pumping system was reduced from about 10^{-3} torr to 6×10^{-8} torr in 24 hr after starting at atmospheric pressure with a baked-out system backfilled with dry N.

Fabrication and Assembly of T-111 Loop Components. — After the annealing treatment,[18] the T-111 loop heater and economizer sections were welded, as shown in Fig. 5.6, and inlet and outlet lines were attached to the pump, as shown in Fig. 5.7. We welded transition joints of Nb–1% Zr and type 316 stainless steel to two lithium sampling lines attached near the pump inlet and outlet (Fig. 5.7) and welded a similar joint to the fill line entering the heater section (Fig. 5.6).

A leak check and penetrant inspection of these final assemblies revealed a leak where 1/16-in.-diam flowmeter wires had been tack welded

[18]B. Fleischer, Fuels and Materials Development Program Quart. Progr. Rept. Sept. 30, 1968, ORNL-4350, pp. 130–131.

Fig. 5.6. Heater and Economizer Sections of FCLLL-1.

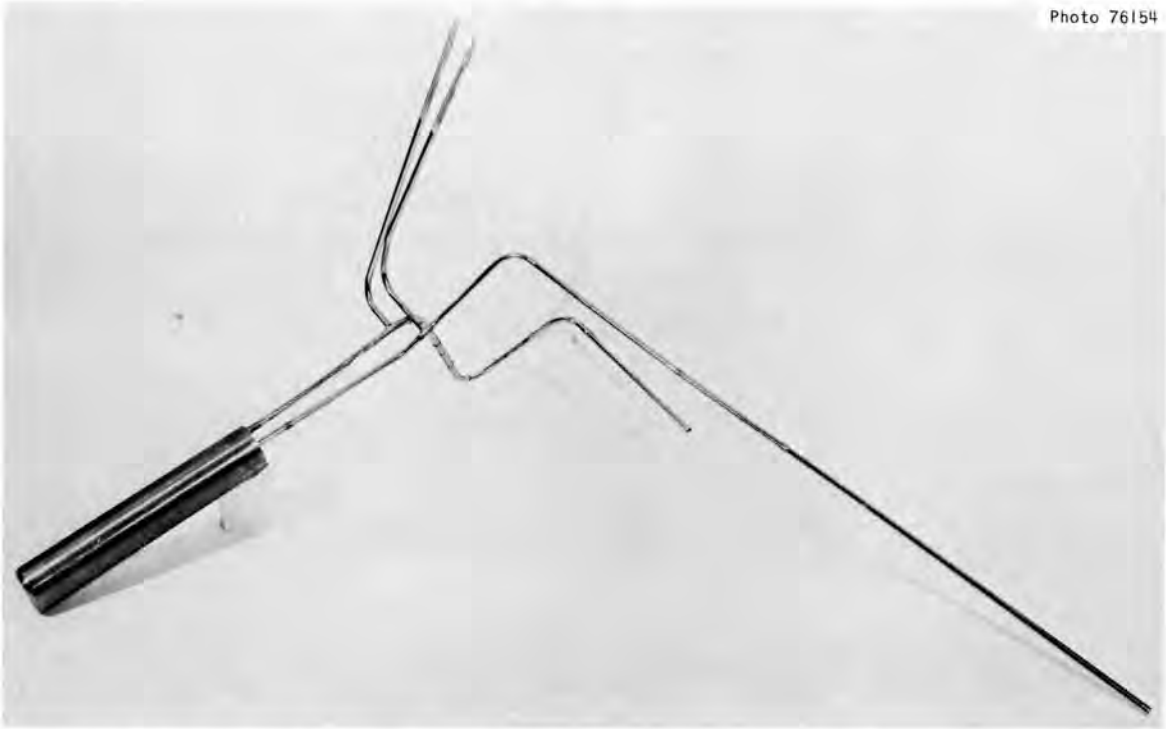

Fig. 5.7. Pump Cell and Associated Inlet and Outlet Lines for FCLLL-1.

to the outer surface of the 1/2-in.-OD × 0.065-in.-wall-thickness tubing of the pump inlet line. Penetrant inspection showed a crack under each tack weld. This area had been rewelded once when one of the wires had broken loose and rewelded again to correct misalignment of the wires. Each time, the welds were difficult to make. We alleviated both the difficulty of welding and the possibility of cracking by replacing the cracked piping with a machined fitting with tab projections that not only moved the weld area away from the piping but also made a self-fixturing, well-balanced weld design for attachment of the wires. This fitting required two more butt welds in the pump section. A picture of the redesigned section before welding is shown in Fig. 5.8.

The T-111 pump cell with its attached tubing was the first subassembly installed into the vacuum vessel. Type 321 stainless steel tubing was welded to the transition joints, and trace heaters were mounted on the stainless steel sections between the transition joints and the vacuum vessel penetrations.

The T-111 radiator section, pictured in Fig. 5.9, and the economizer and heater sections were next assembled on the test stand frame along with

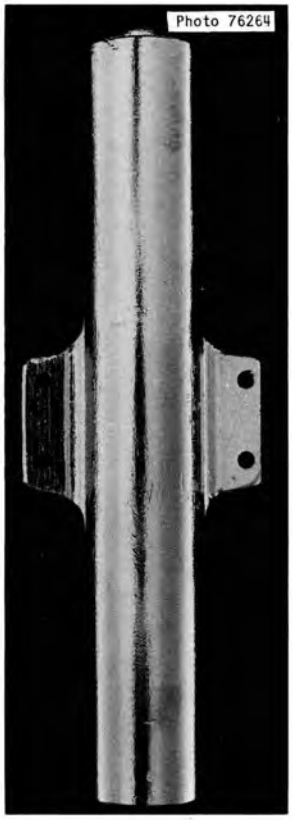

Fig. 5.8. T-111 Fitting for Attachment of Flowmeter Wires.

Fig. 5.9. Radiator Section of FCLLL-1.

the copper bus bar. Only one field bend was needed for proper alignment. The field weld between the economizer and radiator was made before the test stand frame was installed in the vacuum vessel.

Following installation of the test stand frame and T-111 sections, we completed the final fitup of the subassemblies and made the last two field welds. Figure 5.10 shows the assembly for the final field weld with the automatic welder in place.

Weld Corrosion Tests. — It is well known that contaminated welds in refractory alloys exhibit serious intergranular attack when exposed to Li. A solution to the problem is an anneal after welding. Accordingly, we have made corrosion tests for 100 hr at 816°C on weld samples made during the final assembly of the loop to determine if the atmosphere during welding was sufficiently free of contamination to eliminate the necessity of annealing these final welds. One field weld, cut out of the loop for testing, was exposed to Li in a stainless steel capsule, whereas all the other samples were tested in a Nb—1% Zr pot. Because of impurities in the Li used, welds tested in the Nb—1% Zr pot were found to be contaminated by N after their exposure. Despite this effect, neither these samples nor the field weld showed any evidence of intergranular corrosion. Therefore, we concluded that the welds were satisfactory and eliminated the annealing step.

Final Installation of Minor Components of Loop. — The flowmeter magnet assembly, copper bus bar, high-current electrical feedthrough, and flexible connectors for the high-current feedthrough were installed inside the vacuum vessel. All heaters and thermocouples were installed for the fill and drain tank, the sampling glove box was completed, and the units were coupled to the vacuum-vessel feedthrough.

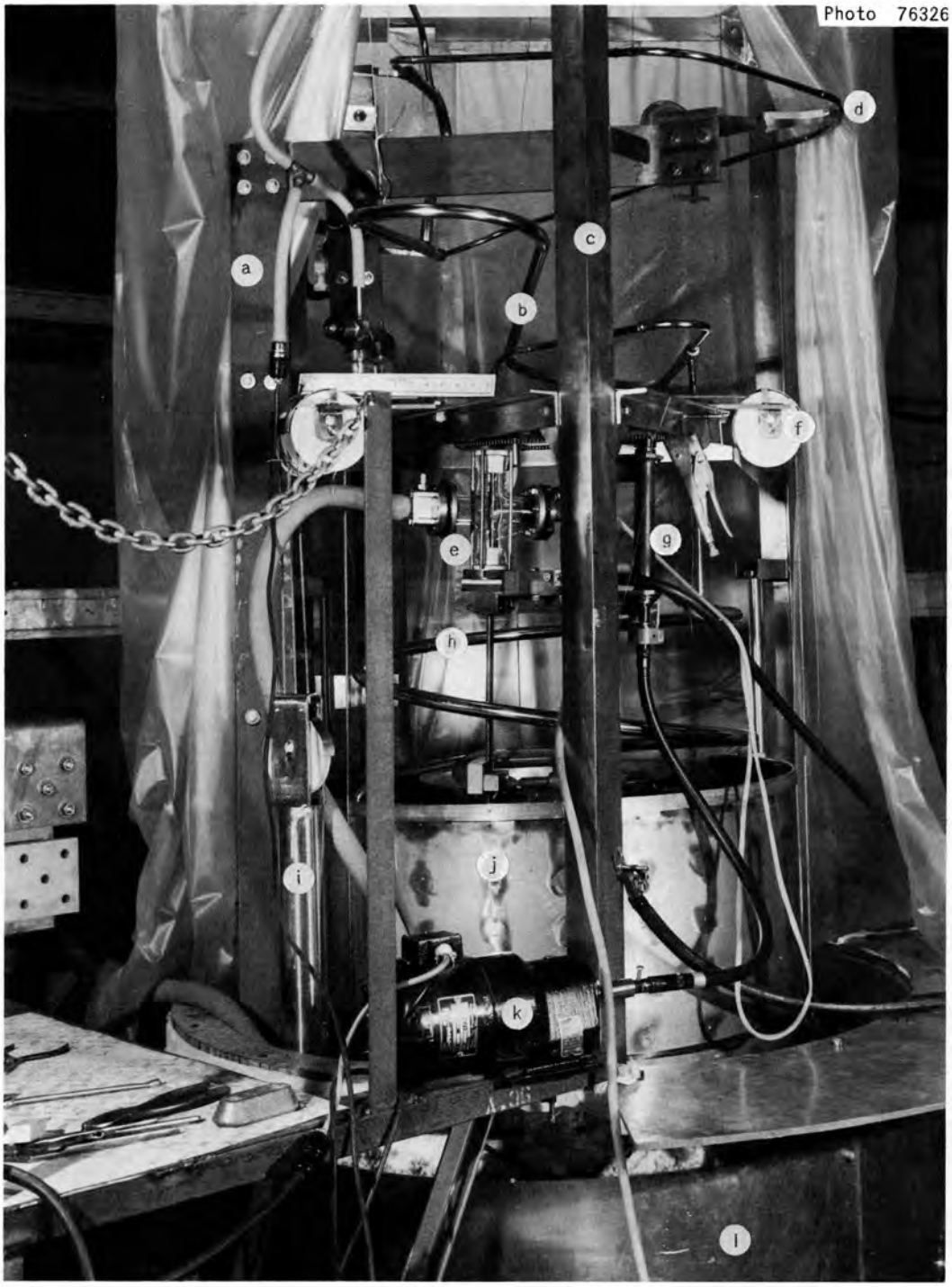

Fig. 5.10. Field Welding Assembly Used to Join Radiator and Economizer Sections After Installation of These Sections in the Vacuum Vessel. (a) Iron titanate coated copper bus, (b) economizer, (c) three-legged test stand frame, (d) resistance heated section, (e) Pyrex cross welding enclosure, (f) alumina sheave, (g) welding jig assembly, (h) radiator, (i) counterweight for shutter, (j) shutter assembly, (k) rotation drive unit, and (l) bottom part of vacuum vessel.

PART III

RADIATION DAMAGE TO STRUCTURAL MATERIALS

6. BEHAVIOR OF REFRACTORY MATERIALS UNDER IRRADIATION

G. W. Keilholtz R. E. Moore D. A. Dyslin[1]

The purpose of this program is to evaluate the effects of high fast-neutron fluences at temperatures from 150 to 1100°C on the properties of refractory nuclear materials for both space and civilian power reactors. While we emphasize nonfissionable ceramic materials such as the carbides, nitrides, and silicides of refractory metals, we have recently included the carbides and nitrides of depleted uranium as an extension of this series of nonfissionable ceramics.

Irradiation Damage to Nonfissionable Refractory Materials

Refractory Metal Carbides

High-Temperature Irradiations. — We have reported observations of gross damage and results of dimensional measurements of carbides of refractory metals (Ti, Zr, Ta, Nb, and W) irradiated at 1000 to 1100°C in the ETR.[2,3] At these temperatures, irradiation damage and volume expansion were less than had been observed[4] at lower temperatures (300 to 700°C).

Results have now been obtained from metallographic and x-ray diffraction examinations. There was no evidence of grain-boundary separation or transgranular fracture of any of the specimens even at the highest neutron fluences (4 to 5 $\times$ 10^{21} neutrons/cm^2 for hot-pressed and slip-cast specimens and about 2.5 $\times$ 10^{21} neutrons/cm^2 for explosion-pressed specimens). No changes in lattice parameters were detected by

---

[1]General Engineering Division.

[2]G. W. Keilholtz, R. E. Moore, and D. A. Dyslin, Fuels and Materials Development Program Quart. Progr. Rept. June 30, 1968, ORNL-4330, pp. 151–158.

[3]G. W. Keilholtz, R. E. Moore, and D. A. Dyslin, Fuels and Materials Development Program Quart. Progr. Rept. Sept. 30, 1968, ORNL-4350, pp. 139–145.

[4]G. W. Keilholtz, R. E. Moore, and M. F. Osborne, Nucl. Appl. 4, 330 (1968).

x-ray diffraction examinations. Small increases had previously been detected in specimens irradiated at 300 to 700°C. The results of the high-temperature irradiations are very encouraging for the applicability of carbides in nuclear devices designed for long-term operation at high temperatures (> 1000°C).

Low-Temperature Irradiations. — Our short-term (one ETR cycle), low-temperature (300 to 700°C) irradiation of explosion-pressed and slip-cast carbides was completed. The purpose of this low-fluence irradiation was to obtain information on dimensional changes for use in the theoretical interpretation of high-fluence data.[3] A nearly identical assembly is being prepared for a short-term irradiation of the same materials at a somewhat lower temperature (150°C). A low-temperature assembly is being fabricated for irradiation in the EBR-II to separate out the effects of slow-neutron absorptions on the property changes of carbides.

Effects of Irradiation on Carbides and Nitrides of Depleted Uranium

Experiments were designed to describe quantitatively the effect of the generation of helium gas in UN through the $^{14}N(n,\alpha)^{11}B$ reaction by comparing the effects of fast neutrons on four types of specimens: UN, UN with ^{15}N enrichment, UC, and U(C,N). The specimens are being prepared, and the first irradiation assembly is nearly complete.

7. FAST-NEUTRON IRRADIATION EFFECTS ON ELECTRICAL INSULATORS

G. W. Keilholtz R. E. Moore
D. A. Dyslin[1] H. E. Robertson

The purpose of this program is to establish the effects of fast neutrons on the mechanical, physical, and electrical properties of materials suitable for use as electrical insulators in thermionic converters and to evaluate the mechanisms of neutron damage in these materials from 150 to 1100°C.

General Survey of Fast-Neutron Effects on Electrical Insulators

The objective of this task is to measure the effects of fast-neutron irradiation on various materials that have physical and electrical properties suitable for use as electrical insulators in thermionic converters. The materials showing greatest promise in these preliminary irradiations will later be investigated more exhaustively.

The irradiation of a low-temperature (150°C) assembly containing large-grained (25 μm) translucent Al_2O_3, sintered MgO, and Si_2ON_2 has been completed. We have made plans to irradiate the same materials and also specimens fabricated from synthetic sapphire and from sintered MgO of high purity in an assembly that will maintain the specimens at various temperatures from 400 to 1200°C. The high-temperature irradiation of this assembly will begin late in FY 1969 or early in FY 1970.

Irradiation of High-Density Commercial Al_2O_3 Products Considered for Thermionic Insulators

Fast-Neutron Damage to Large-Grained Translucent Alumina

Low-temperature (300 to 600°C) results and gross damage and dimensional changes at higher temperatures (700 to 1000°C) for large-grained

[1]General Engineering Division.

(25 μm) alumina[2] were reported previously.[3–5] We found that volume expansion was greater between 600 and 900°C than between 300 and 600°C. There was less expansion at 1000°C than at the "intermediate temperatures" (i.e., 600 to 900°C).

It has now been shown that grain-boundary separation contributes to the increase in volume expansion above 600°C. There is an almost total absence of grain-boundary separation in this material at temperatures below 600°C for fluences less than 2 to 3 × 10^{21} neutrons/cm^2. Figure 7.1 shows severe grain-boundary separation at 700°C as compared with virtually none at 300°C and with a reduced amount at 1000°C. In-reactor thermal annealing probably accounts for the improved microstructure at 1000°C.

An explanation for the increased damage at intermediate temperatures can be found in the recent work of Wilks, Desport, and Smith.[6] These investigators discovered that the growth of the a and c axes of single crystals of Al_2O_3 during irradiation is almost isotropic at 150°C but is highly anisotropic and greater in magnitude at 650°C. This effect would cause an increased volume expansion at intermediate temperatures, and it would also cause grain-boundary separation in polycrystalline specimens at lower neutron fluences than at low temperatures (< 600°C).

The "intermediate temperature effect" seriously limits the usefulness of alumina in thermionic converters. The results suggest, however, that neutron damage can be minimized by operation at high temperatures (> 1000°C). Using alumina of small grain size should increase the neutron fluence at which grain-boundary separation begins.

---

[2]Lucalox, trade name of a proprietary product of General Electric Company, Cleveland, Ohio.

[3]G. W. Keilholtz and R. E. Moore, Nucl. Appl. 3(11), 686–691 (1967).

[4]G. W. Keilholtz and R. E. Moore, Reactor Chem. Div. Ann. Progr. Rept. Dec. 31, 1967, ORNL-4229, pp. 144–145.

[5]G. W. Keilholtz, R. E. Moore, and D. A. Dyslin, Fuels and Materials Development Program Quart. Progr. Rept. June 30, 1968, ORNL-4330, pp. 159–164.

[6]R. S. Wilks, J. A. Desport, and J.A.G. Smith, The Irradiation-Induced Macroscopic Growth of α-Al_2O_3 Single Crystals, AERE-R 5460 (May 1967).

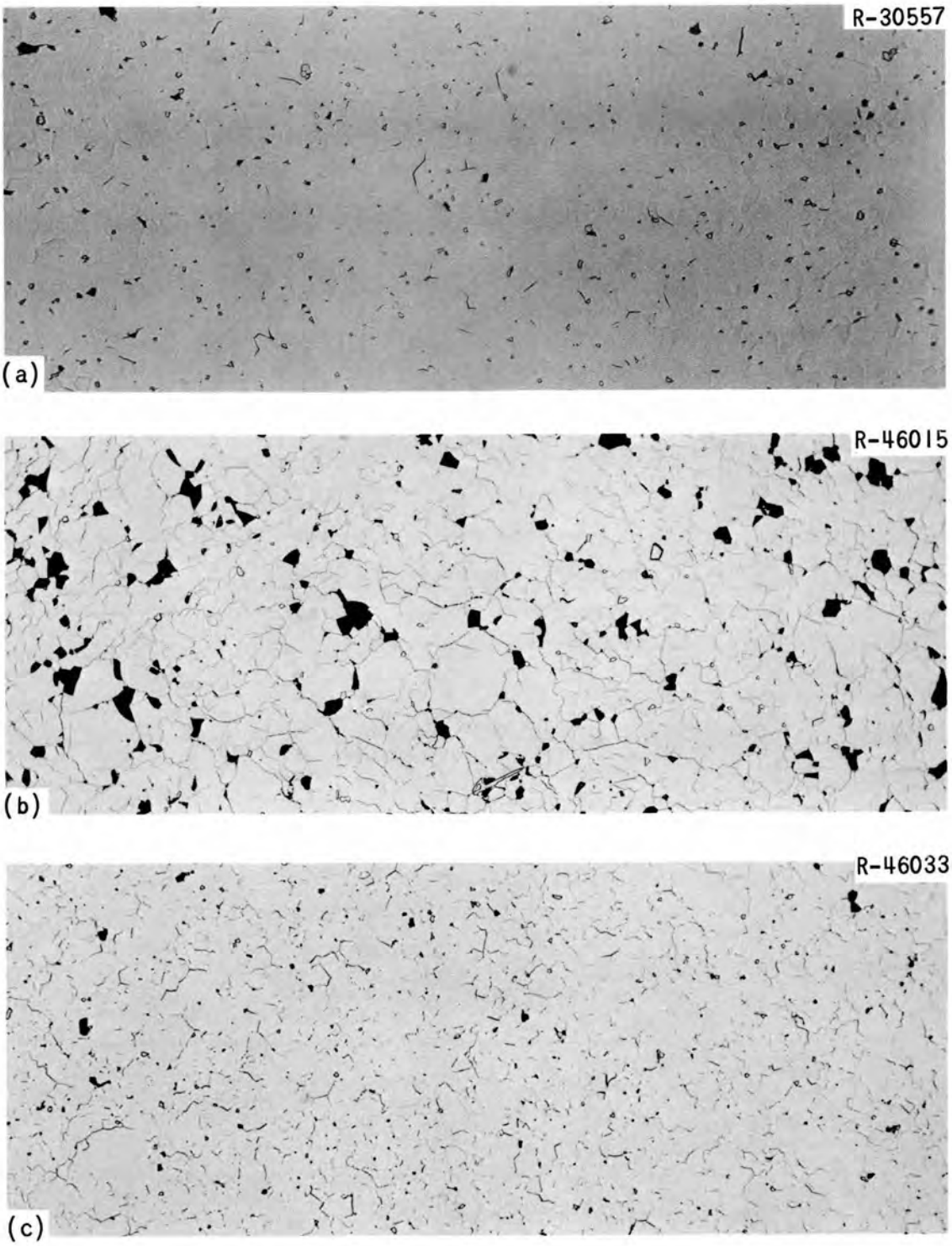

Fig. 7.1. The Effect of Irradiation Temperature on Grain-Boundary Separation in Large-Grained (25 μm) Translucent Alumina. (a) 300 °C, 1.4×10^{21} neutrons/cm^2 (> 1 Mev). (b) 700 °C, 1.1×10^{21} neutrons/cm^2. (c) 1000 °C, 2.7×10^{21} neutrons/cm^2. As-polished, 100×.

Comparison of the Effects of Fast Neutrons on Several Commercial Alumina Products

Irradiations in ETR. — We are evaluating the radiation resistance of three commercial types of small-grained (< 10 μm) alumina as well as one large-grained (25 μm) translucent alumina[2] at 400 to 1230°C. A short-term ETR irradiation in which the specimens received fast-neutron fluences between 0.4 and 3.1×10^{21} neutrons/cm^2 (> 1 Mev) has been completed. Types and numbers of specimens included in this irradiation are given in Table 7.1. Results of spectrographic analysis of the unirradiated specimen types are presented in Table 7.2.

About half of the solid cylinders of the two least pure small-grained types (Types I and II) fractured during irradiation. By comparison, however, all the solid cylinders of the highest purity small-grained type (Type III) and the large-grained alumina (Type IV) survived irradiation without apparent gross damage. There were seven thin-walled cylindrical shells of Types I, II, and III included in the irradiation. The number of each type that fractured was as follows: Type I, 4; Type II, 3; Type III, 2. In general, the impurity content of the specimens appears to be the predominant factor causing fracture.

Table 7.1. Types and Numbers of Alumina Products Irradiated[a]

Type	Trade Name	Grain Size (μm)	Number	
			Solid Cylinders[b]	Cylindrical Shells[c]
I	Coors AD-995	< 10	9	7
II	Wesgo AL-995	< 10	11	7
III	GE Opaque Lucalox	< 10	11	7
IV	GE Translucent Lucalox	25	6	0

[a]Irradiation conditions: fast-neutron fluences from 0.4 to 3.1×10^{21} neutrons/cm^2 (> 1 Mev), temperatures from 400 to 1230°C.

[b]Diameter: 0.493 in.

[c]Diameter: 0.493 in. Wall thickness: 0.020 in.

Table 7.2. Results of Spectrographic Analysis of Commercial Alumina Products[a]

Impurity Element	Limit of Detection (wt %)	Amount of Impurity Present (wt %)			
		Type I[b]	Type II[c]	Type III[d]	Type IV[e]
Be	0.0004	0.004		0.001	
Ca	0.0001	0.007	0.01	0.004	0.001
Cr	0.0004	0.1			
Cu	0.0001	0.06	0.0005	0.005	0.0004
Fe	0.001	0.06	0.03	0.01	0.0025
Ga	0.001	0.004	0.005		
Mg	0.0004	0.1	0.1	0.02	0.08
Mn	0.0004	0.002	0.0004		
Mo	0.001	0.003			
Ni	0.001	0.006		(0.01)[f]	
Si	0.004	0.07	0.1	0.007	0.02
Sr	0.0001	0.0004	0.0004		
Ti	0.0004	0.0025	0.002		0.0006
Zr	0.0004	0.0005	0.0005		0.035

[a]Analysis by C. Feldman and Anna M. Yoakum, ORNL Analyticl Chemistry Division. Accuracies were ±25%.

[b]Coors AD-995, < 10 μm grain size.

[c]Wesgo AL-995, < 10 μm grain size.

[d]GE Opaque Lucalox, < 10 μm grain size.

[e]GE Translucent Lucalox, 25 μm grain size.

[f]Three of four samples analyzed contained less Ni than the detectable limit; one sample contained 0.04% Ni.

Most of the data for volume expansion of specimens irradiated at temperatures between 580 and 1070°C falls within a linear band that lies between 1 and 2% for a fluence of 10^{21} neutrons/cm^2 and between 3 and 4% for a fluence of 3×10^{21} neutrons/cm^2. Large-grained specimens (Type IV) expanded more than small-grained specimens (Types I, II, and III). The average expansion for all specimens irradiated at 580 to 1070°C is about 1.4 times greater than that for specimens of Type IV irradiated at lower temperature (300 to 600°C) (ref. 3) when compared over the range of fluences of 2 to 3×10^{21} neutrons/cm^2.

A group of specimens irradiated at 1100°C (one of each of the four types) expanded less than 1.5% after receiving a fluence of 3.1×10^{21} neutrons/cm^2. This smaller expansion can be explained by in-reactor annealing, but specimens irradiated at an even higher temperature (1230°C) expanded as much or more than those irradiated between 580 and 1070°C. Interpretation of the data for irradiation at 1230°C must await results of metallographic examinations now in progress.

Irradiations in EBR-II. — Assemblies for irradiating commercial alumina products in the EBR-II are being fabricated. In the EBR-II, the neutron flux is nearly all fast. Comparisons of results with those for the same materials irradiated in the ETR, in which the thermal flux is about equal to the fast flux, will provide information on the effect of neutron energy on radiation damage.

8. MECHANICAL PROPERTIES RESEARCH AND LMFBR CLADDING AND STRUCTURAL MATERIALS DEVELOPMENT

J. R. Weir, Jr. H. E. McCoy, Jr.

Work in this program includes studies of the high-temperature irradiation embrittlement and other technologically important aspects of radiation damage to fuel cladding materials at high neutron fluence. The work centers around types 316 and 304 stainless steel, Incoloy 800, and Hastelloy N and the effects of titanium concentration in these alloys on radiation damage.

Radiation Effects in Type 316 and Titanium-Modified Type 316 Stainless Steel

E. E. Bloom

Our investigation of the effects of neutron irradiation on the mechanical properties of type 316 and titanium-modified type 316 stainless steel involves tensile and creep-rupture tests on specimens in three conditions: (1) annealed, (2) annealed and irradiated, and (3) annealed and aged at the irradiation temperature for the irradiation time. Variables under investigation include (1) preirradiation heat treatment, (2) irradiation temperature, and (3) postirradiation test conditions such as test temperature and strain rate.

Results on Standard Types 316 and 316L Stainless Steel

The chemical compositions of the two heats of material being investigated are listed in Table 8.1. The tensile and creep-rupture properties of type 316 stainless steel irradiated at 550, 650 and 750°C and of type 316L stainless steel irradiated at 650°C have been reported.[1,2]

---

[1]E. E. Bloom and J. R. Weir, Jr., Fuels and Materials Development Program Quart. Progr. Rept. June 30, 1968, ORNL-4330, pp. 165–171.

[2]E. E. Bloom, Fuels and Materials Development Program Quart. Progr. Rept. Sept. 30, 1968, ORNL-4350, pp. 152–155.

Table 8.1. Composition of Types 316 and 316L Stainless Steel

Type Stainless Steel	Composition (wt %)										
	C	Cr	Ni	Mo	Mn	Si	P	S	B	N	
										Total	Soluble
316	0.07	17.2	12.5	2.1	1.9	0.5	0.039	0.004	0.0008	0.018	0.011
316L	0.02	16.9	12.7	2.7	2.3	0.6	0.013	0.015	0.0002	0.057	0.014

The uniform and total elongations of irradiated specimens (tested at 550, 650 and 750°C) were significantly lower and the yield strength was slightly higher than those of specimens as annealed. The increased yield strength appears to result from thermal aging rather than the irradiation itself, since specimens of each alloy aged at the irradiation temperature for the irradiation time also increased in yield strength. The reduction in ductility, however, was attributable to the irradiation. The ductility and rupture life at 650°C were significantly lower and the creep rate was higher in irradiated specimens than in specimens as annealed. Results on aged specimens again indicated that the reduced ductility was a result of irradiation, while the increased creep rate was a result of thermal aging effects.

Metallographic examination of several specimens was started. Figure 8.1 shows the area of the fracture in a specimen of type 316 stainless steel annealed 1 hr at 1050°C, irradiated at 650°C for about 2000 hr [9×10^{20} neutrons/cm^2 (thermal) and 7×10^{20} neutrons/cm^2 (> 1 Mev)], and then tested at 650°C and 35,000 psi. The fracture appears to be completely intergranular with little deformation within the matrix. Heavy precipitation has occurred in the vicinity of grain and twin boundaries and to a lesser extent within the matrix.

The fracture in a specimen annealed 1 hr at 1050°C, aged 2000 hr at 650°C, and then tested at 650°C and 30,000 psi is shown in Fig. 8.2. In this case, the fracture was primarily transgranular, and a large amount of plastic deformation had occurred in the necked portion of the specimen. As can be seen from the photomicrograph at the higher magnification, the size and distribution of precipitate particles are essentially the same as in the irradiated specimen. The precipitates have been extracted from the thermal control specimen and identified by x-ray diffraction as being of the $M_{23}C_6$ type. No sigma phase was detected in the extraction.

Results on Titanium-Modified Type 316 Stainless Steel

We are investigating the effects of small additions of up to 0.6% Ti on the mechanical properties of types 316 and 316L stainless steel. The available tensile and creep-rupture properties have been reported.[2] For

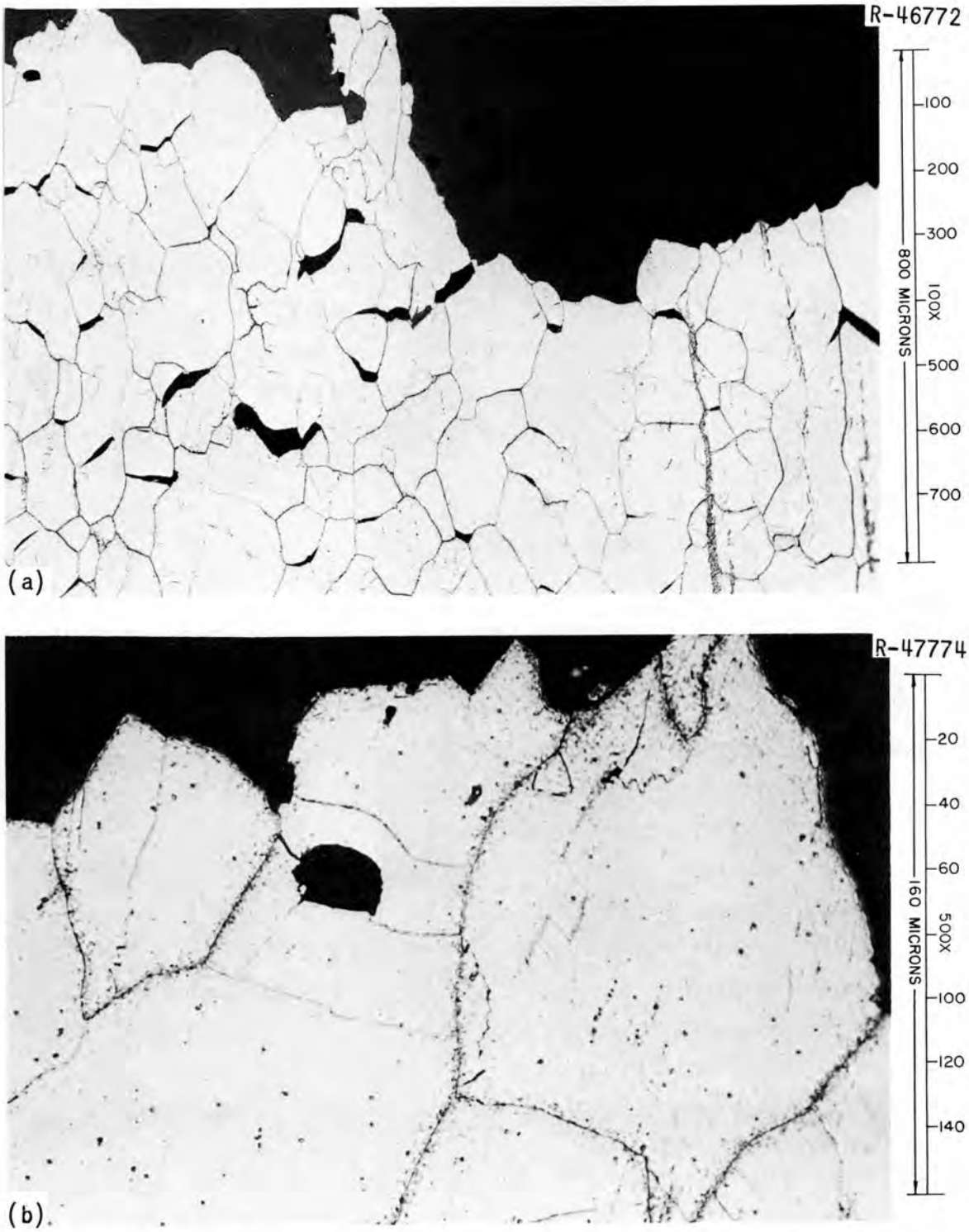

Fig. 8.1. Fracture of Type 316 Stainless Steel Annealed 1 hr at 1050°C, Irradiated at 650°C [9×10^{20} neutrons/cm^2 (Thermal) and 7×10^{20} neutrons/cm^2 (> 1 Mev)], and Tested at 650°C and 30,000 psi. Ruptured after 199 hr, elongated 13.8%. (a) The fracture is entirely intergranular; (b) higher magnification showing precipitation along grain and twin boundaries.

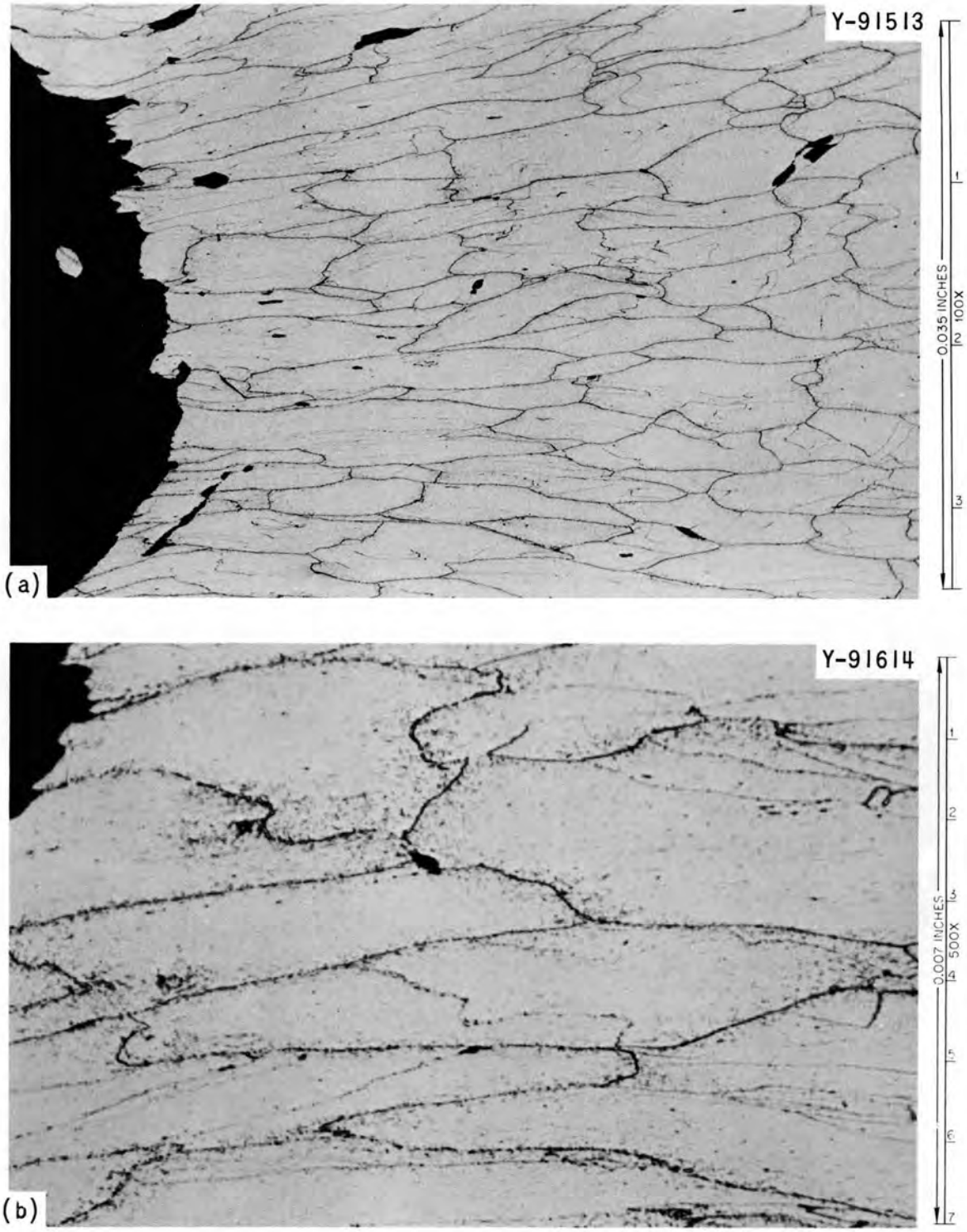

Fig. 8.2. Fracture of Type 316 Stainless Steel Annealed 1 hr at 1050°C, Aged 2000 hr at 650°C, and Tested at 650°C and 30,000 psi. Ruptured after 146 hr, elongated 37.5%. (a) The fracture is transgranular under these conditions, and there is considerable plastic deformation in the matrix. (b) The $M_{23}C_6$ type carbides formed during the aging at 650°C are similar to those present in the irradiated specimen.

both carbon levels, maximum postirradiation ductility at 650°C occurred for titanium contents between 0.15 and 0.25%.

Figure 8.3 shows the fracture of a specimen of type 316 stainless steel containing 0.23% Ti that was annealed 1 hr at 1050°C and irradiated at 650°C to 9×10^{20} neutrons/cm^2 (thermal) and 7×10^{20} neutrons/cm^2 (> 1 Mev) and then tested at 650°C and 30,000 psi. In contrast to the standard type 316 stainless steel, which failed intergranularly after irradiation, the titanium-modified alloy fractured transgranularly. Heavy precipitation similar to that in the standard alloy occurred in regions adjacent to grain boundaries. Examination of a specimen of type 316L stainless steel modified with 0.21% Ti, irradiated and tested under the same conditions, indicates that the fracture is also transgranular in the alloy with low carbon content.

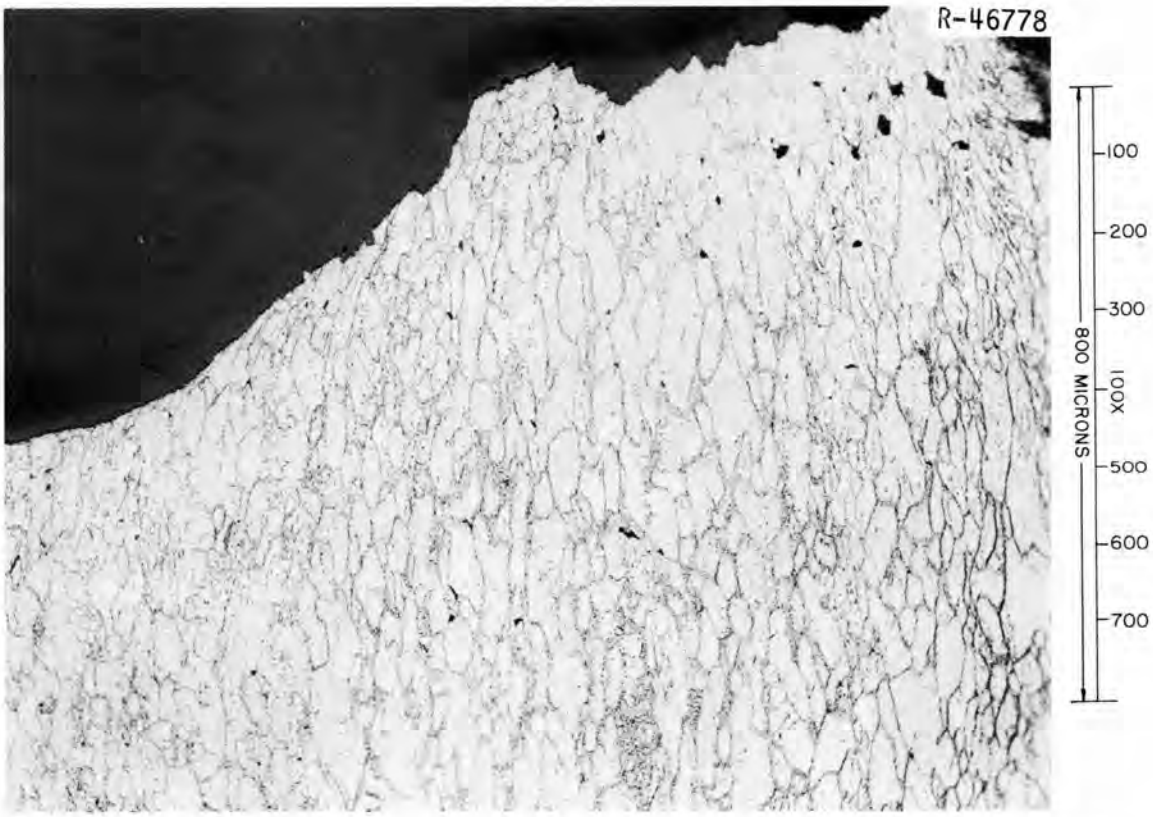

Fig. 8.3. Fracture of a Specimen of Type 316 Stainless Steel Modified with 0.23% Ti, Annealed 1 hr at 1050°C, irradiated at 650°C, and then Tested at 650°C and 30,000 psi. Ruptured after 200.8 hr; elongated 38.6%.

Radiation Damage in Incoloy 800

Mechanical Properties Studies (D. G. Harman)

Our evaluation of vacuum-melted Incoloy 800 is continuing. Our previous work showed enhanced postirradiation creep ductility for those heats containing 0.1% Ti when they were irradiated and tested at 700 and 760°C (ref. 3). We found further improvements in postirradiation ductility by heat treating to a finer grain size or by testing at lower creep stresses (e.g., creep elongations of about 100% at 700°C and 10,000 psi after thermal neutron fluences of 2 to 3×10^{20} neutrons/cm^2).

We are evaluating several heats of material irradiated at 500 or 700°C to thermal and fast neutron fluences of about 0.8×10^{21} neutrons/cm^2. Postirradiation tensile and creep-rupture tests are being conducted at 650°C. We have completed several tests on the heats containing 0.1% Ti and 0.03 or 0.12% C. Calculations show that the neutron fluence experienced would result in the formation of 4 to 6 ppm He in these heats. Specimens from the heat with higher carbon content that were solution annealed at 1150°C and then irradiated at 500°C have been tested and show much lower ductilities than we had expected. The postirradiation tensile elongation at a strain rate of 0.002 min^{-1} was only 3.5% as compared to 7.5% for an identical specimen irradiated at 700°C. The control specimen aged about 2300 hr at 500°C also showed a lower tensile elongation of 21% compared with 47% for the specimen aged at 700°C.

After test, these two control specimens were sectioned and examined metallographically as shown in Fig. 8.4. A comparison shows that a much thicker and more continuous phase is present along the grain boundaries after aging at 500°C than after aging at 700°C.

The postirradiation creep ductility (at 650°C) of the heat containing 0.1% Ti and 0.12% C was affected similarly by the thermal aging during the irradiation at 500°C. A total elongation of only 11% was measured as compared with the 25 to 30% previously exhibited after the irradiations at higher temperatures.

---

[3] D. G. Harman, Fuels and Materials Development Program Quart. Progr. Rept. Sept. 30, 1968, ORNL-4350, pp. 159–162.

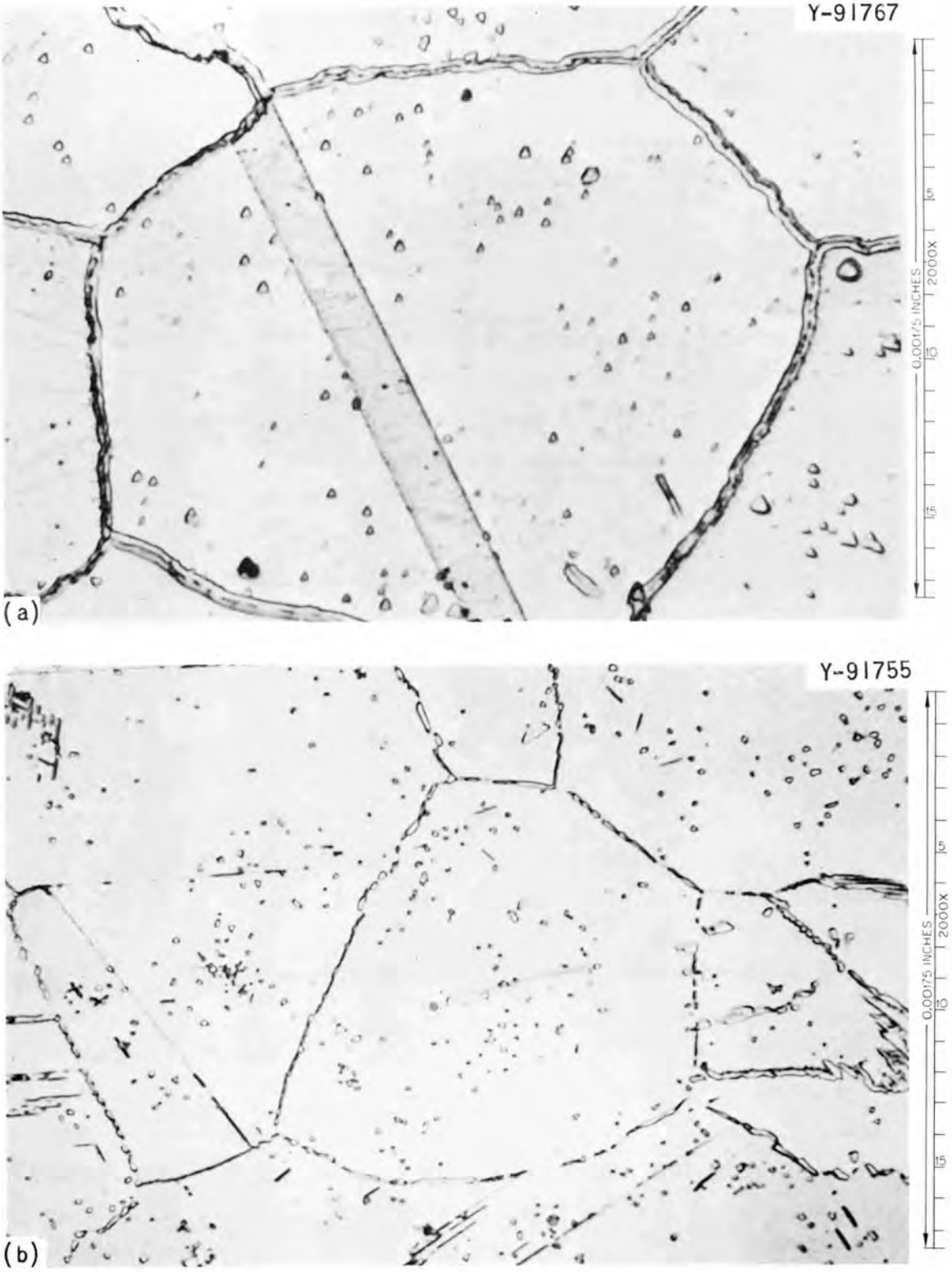

Fig. 8.4. Typical Photomicrographs of Incoloy 800 Containing 0.1% Ti and 0.12% C after Solution Annealing at 1150°C and Aging for 2300 hr at (a) 500 and (b) 700°C.

We tested specimens of the heat containing 0.1% Ti and 0.12% C that were aged 100 hr at 800°C after the 1150°C anneal and then irradiated. After the 500°C irradiation, these specimens showed three times the tensile and creep ductilities of those irradiated without the aging treatment.

The deleterious effect of aging at 500°C can also be circumvented by lowering the temperature at which specimens are solution annealed. Postirradiation ductilities equivalent to those of the preaged specimens were obtained, but the creep strength was lower because of the smaller grain size. Two considerations may be important: first, the lower temperature may not dissolve as many of the carbides formed during solidification from the melt, thus returning less C into solution to precipitate in the more damaging form at 500°C; second, the finer grain size would afford more total grain-boundary area and thus a lower concentration of carbides precipitated at 500°C.

The data for postirradiation ductility for the heat with 0.12% C and 0.1% Ti are summarized in Fig. 8.5, which shows the total plastic elongation as a function of the tensile strain rate or the measured minimum creep rate.

Postirradiation tests of specimens from the heat with 0.1% Ti and only 0.03% C show no susceptibility to the detrimental 500°C aging reaction. Annealed material irradiated at either 500 or 700°C showed elongations equivalent to those of the preaged heat with high carbon content. Control specimens from this heat that were tensile tested showed good ductility (48 to 55% elongations) regardless of the initial heat treatment.

Electron Microscopy Studies (G. T. Newman, W. B. Snyder[4])

Four heats of material used in our studies of irradiation damage have been characterized by electron microscopy in the unirradiated condition. Each heat had the same basic composition, but the titanium and carbon levels varied as shown in Table 8.2. The material was cold-worked in the as-received condition and was annealed or annealed and aged before examination. The heat treatments were identical to those given to

[4]Summer employee.

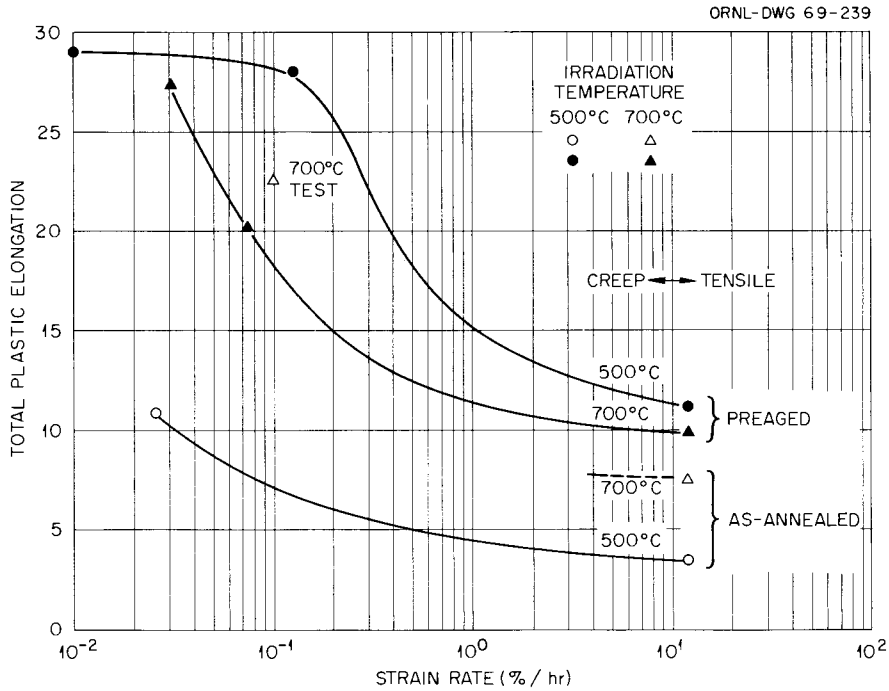

Fig. 8.5. Effect of Preirradiation Aging on Ductility of Incoloy 800 at 650°C. All specimens contained 0.1% Ti and 0.12% C and were annealed at 1150°C. Some specimens were then aged 100 hr at 800°C before being irradiated at the indicated temperature to about 0.8×10^{21} neutrons/cm^2 (thermal and fast).

Table 8.2. Compositions of Heats of Incoloy 800

Heat Code	Composition[a] (wt %) C	Ti	Al	(ppm) B	Ratio Ti:C	Annealing Temperature (°C)	Approximate Grain Diameter (μm)
B	0.03	0.21	0.22	3.0	7	980 1040	15 30
J	0.12	0.26	0.21	4.0	~ 2	1040 1150	10 40
H	0.12	0.10	0.24	6.0	~ 1	1150	40
G	0.10	> 0.02	0.21	3.0	~ 0.2	1150	40

[a]Base composition
Fe–30% Ni–19% Cr–0.7% Mn–0.2% Si–0.02% Cu–0.03% Co– < 0.02% V–0.007% S.

mechanical test specimens used in irradiation experiments. As noted in Table 8.2, the grain size was controlled predominantly by the carbon content and was not influenced detectably by Ti over the range of composition investigated.

The distribution and morphology of the precipitates were studied by transmission and carbon-extraction electron microscopy techniques. We found that a 30-min anneal at the temperatures listed in Table 8.2 was insufficient to dissolve completely all the "primary" precipitates (illustrated in Fig. 8.6) present in the heats as received. The temperatures were, however, sufficient to cause complete recrystallization. Studies by carbon extraction revealed that in all the annealed heats a feathery, dendritic precipitate (illustrated in Fig. 8.7) formed at the grain boundaries in amounts that increased as the annealing temperature increased. It was also evident that, under similar annealing conditions, such precipitation increased as the ratio of Ti:C decreased.

Aging the annealed material for 100 hr at 800°C greatly increased the amount of precipitate and resulted in the formation of precipitates with widely varying shapes in various locations, typically at coherent and incoherent twin boundaries and grain boundaries (see Figs. 8.8–8.10).

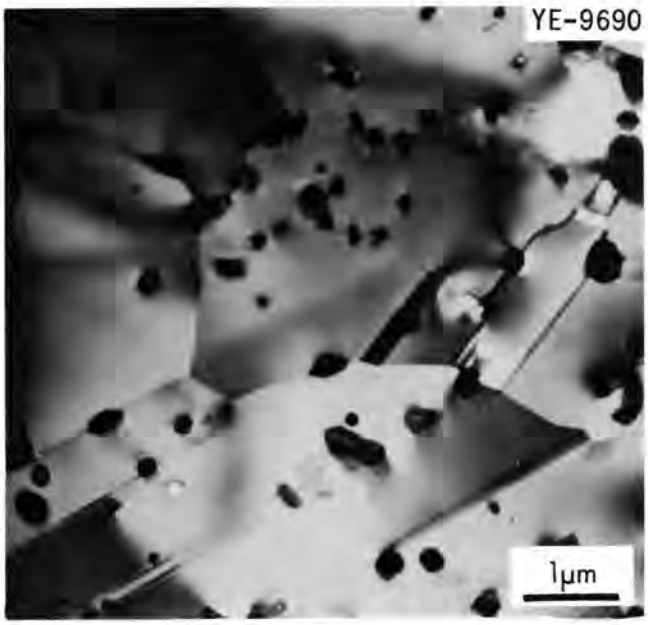

Fig. 8.6. Incoloy 800, Heat J, Annealed 30 min at 1040°C.

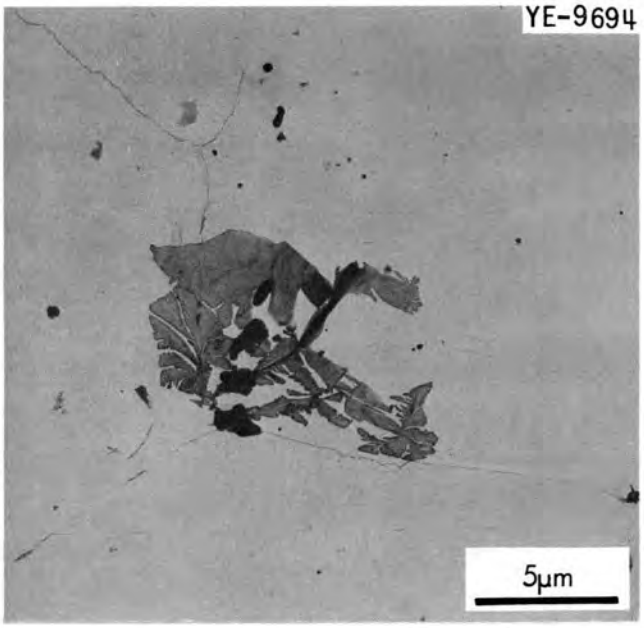

Fig. 8.7. Incoloy 800, Heat J, Annealed 30 min at 1150°C.

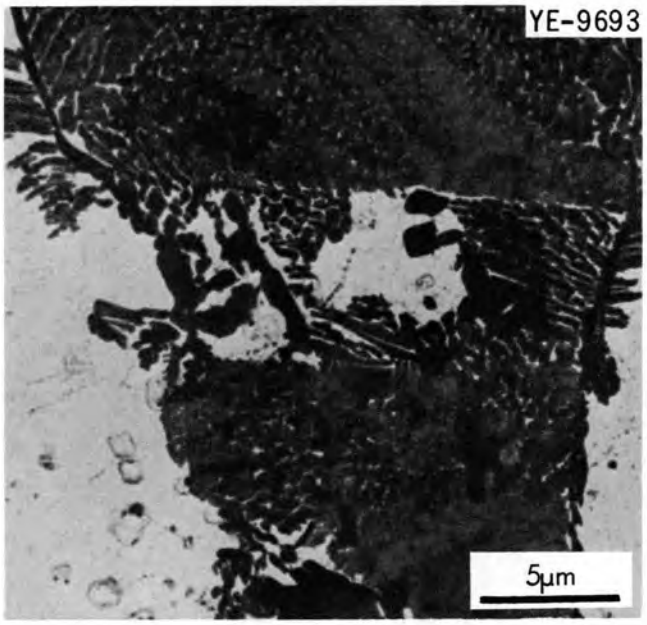

Fig. 8.8. Incoloy 800, Heat J, Annealed 30 min at 1150°C and Aged 100 hr at 800°C.

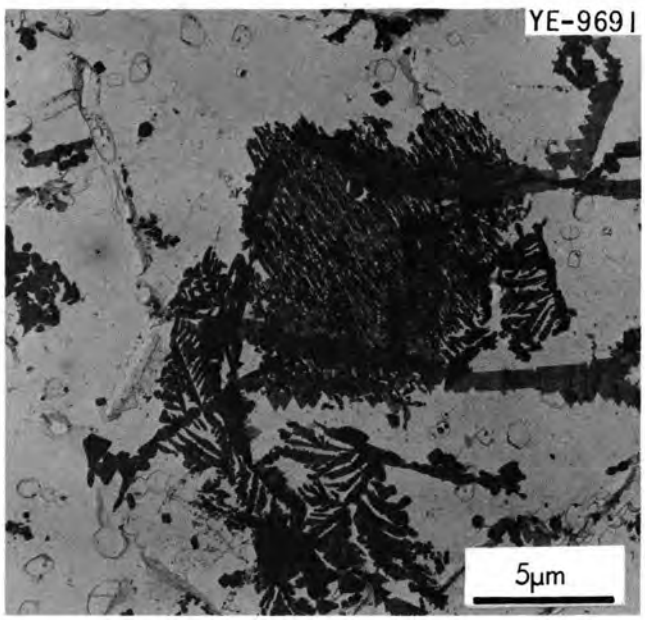

Fig. 8.9. Incoloy 800, Heat J, Annealed 30 min at 1150°C and Aged 100 hr at 800°C.

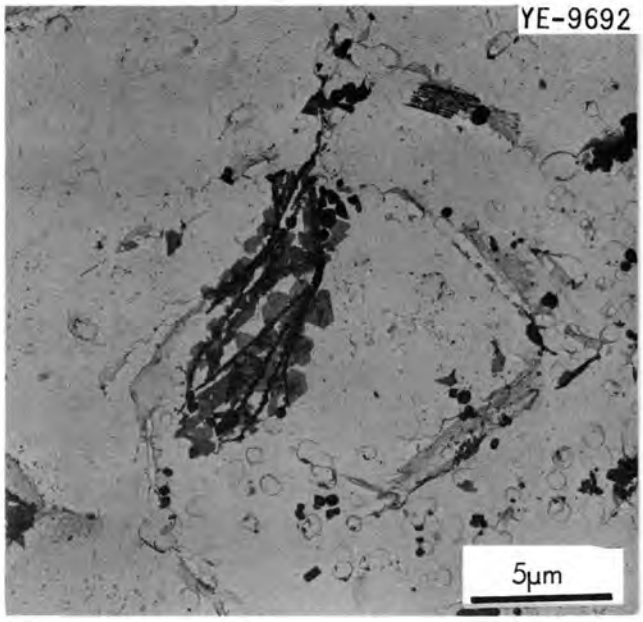

Fig. 8.10. Incoloy 800, Heat J, Annealed 30 min at 1150°C and Aged 100 hr at 800°C.

Again, precipitates were generally more concentrated in heats with lower ratios of Ti:C.

The precipitates in our samples look similar to those reported by other experimenters[5,6] for the complex carbide $M_{23}C_6$. We have not completed an identification of all the shapes of precipitate present, but all the angular precipitate illustrated in Fig. 8.9 is of the $M_{23}C_6$ type.

Utilization of EBR-II

Examination of Stainless Steel and Nickel Irradiated in EBR-II
(E. E. Bloom, J. O. Stiegler)

Specimens of type 304 stainless steel and nickel 270 have been irradiated in row 2 and row 7 positions of the EBR-II to a total exposure of 33.8 Mwd. These specimens were included in the ORNL Gamma Heat Experiment. Figure 8.11 is a schematic drawing of the specimen holder.

---

[5] C. N. Spallaris, Incoloy 800 for Nuclear Fuel Sheaths — A Monograph GEAP-4633 (July 1964).

[6] F. R. Beckitt and B. R. Clark, Acta Met. 15, 113 (1967).

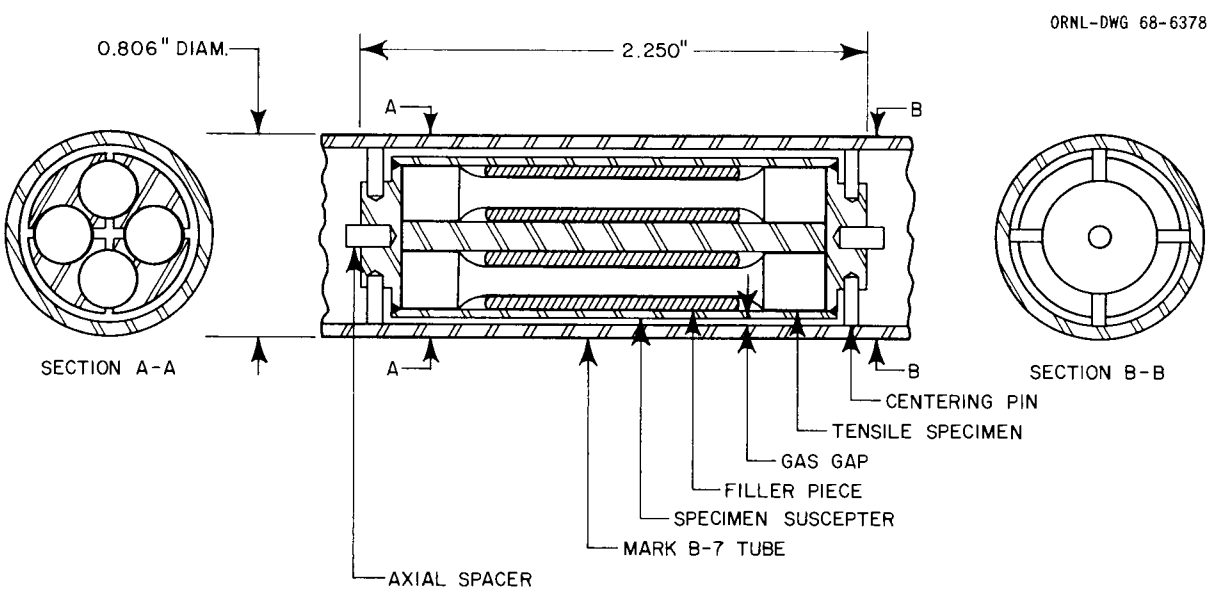

Fig. 8.11. Schematic of EBR-II Specimen Holder.

Two specimens of nickel 270 and two of type 304 stainless steel were placed in each holder to compare directly the behavior of these two materials. Table 8.3 is a complete listing of the irradiation conditions for the specimens in the row 2 experiment. Irradiation temperatures were calculated from measurements of gamma heat, and the neutron fluences were calculated from the data of Moteff.[7]

In type 304 stainless steel, the visible damage was in the form of "black dots" or defect clusters. Figure 8.12 shows the microstructure after irradiation at 384°C to 1.4×10^{20} neutrons/cm^2 (> 0.1 Mev). In

[7]J. Moteff, General Electric Nuclear Materials and Propulsion Operation, Cincinnati, Ohio, personal communication.

Table 8.3. Irradiation Conditions for Specimens of Nickel 270 and Type 304 Stainless Steel Irradiated in EBR-II Gamma Heat Experiment

Irradiation Temperature (°C)	Neutron Fluence (neutrons/cm^2)		
	(> 0.01 Mev)	(> 0.1 Mev)	(> 1 Mev)
370	1.5×10^{18}	5.0×10^{17}	1.4×10^{16}
370	3.7×10^{19}	3.2×10^{19}	5.7×10^{18}
400	3.7×10^{19}	3.2×10^{19}	5.7×10^{18}
420	3.7×10^{19}	3.2×10^{19}	5.7×10^{18}
445	3.7×10^{19}	3.2×10^{19}	5.7×10^{18}
480	3.7×10^{19}	3.2×10^{19}	5.7×10^{18}
503	3.7×10^{19}	3.2×10^{19}	5.7×10^{18}
384	1.6×10^{20}	1.4×10^{20}	2.6×10^{19}
410	1.6×10^{20}	1.4×10^{20}	2.6×10^{19}
438	1.6×10^{20}	1.4×10^{20}	2.6×10^{19}
467	1.6×10^{20}	1.4×10^{20}	2.6×10^{19}
496	1.6×10^{20}	1.4×10^{20}	2.6×10^{19}
524	1.6×10^{20}	1.4×10^{20}	2.6×10^{19}

Fig. 8.12. Type 304 Stainless Steel Irradiated at 384°C to 1.4×10^{20} neutrons/cm^2 (> 0.1 Mev). About 75% of the defect clusters are interstitial loops that have an $\frac{a}{3}$ {111} Burgers vector. Two other types of defect clusters are present: dislocation loops with an $\frac{a}{3}$ {110} Burgers vector and clusters that have a three-dimensional strain field.

this case, the concentration of defect clusters was about 4.5×10^{15} clusters/cm^3. Quantitative measurements of defect concentration are not complete, but the concentration decreases with increasing temperature as expected. The specimen irradiated at 467°C to 1.4×10^{20} neutrons/cm^2 (> 1 Mev) contained about 1.3×10^{14} clusters/cm^3, while no damage was visible in the specimen irradiated at 524°C to the same fluence.

We are studying the nature of the defect clusters by diffraction contrast analysis. In the specimen irradiated at 467°C to 1.4×10^{20} neutrons/cm^2 (> 0.1 Mev), about 75% of the defects are interstitial dislocation loops that have an $\frac{a}{3}$ {111} Burgers vector. Two other types of clusters have been identified: (1) dislocation loops that have an $\frac{a}{2}$ {110} Burgers vector that could be formed from an $\frac{a}{3}$ {111} loop by the dislocation reaction

$$\frac{a}{3}(\bar{1}\bar{1}\bar{1}) + \frac{a}{6}(\bar{2}11) + \frac{a}{6}(1\bar{2}1) \rightarrow \frac{a}{2}(\bar{1}\bar{1}0) , \qquad (8.1)$$

and (2) defects that are spherical or three dimensional and may be vacancy clusters or small voids.

The microstructure shown in Fig. 8.13 is of nickel 270 irradiated at 384°C to 1.4×10^{20} neutrons/cm^2 (> 0.1 Mev) (the same irradiation conditions as for the type 304 stainless steel shown in Fig. 8.12). In the case of nickel 270, the damage takes the form of polyhedral voids, ranging from the smallest observable (about 60A in diameter) to about

Fig. 8.13. Microstructure of Nickel 270 Irradiated at 384°C to 1.4×10^{20} neutrons/cm^2 (> 0.1 Mev). The microstructure contains voids, dislocation lines and dislocation loops.

300A in diameter, and dislocation lines and loops. Quantitative information on void density and size distribution is being obtained. The following qualitative observations have been made: voids are present in all samples irradiated to 1.4×10^{20} neutrons/cm^2 (> 0.1 Mev) at temperatures between 384 and 524°C, and the mean and maximum void sizes increase with increasing irradiation temperature.

Mechanical Properties of Hastelloy N and Related Compositions

Experience with Modified Hastelloy N in the Molten-Salt Reactor Experiment (H. E. McCoy, Jr.)

We have a surveillance facility in the core of the Molten-Salt Reactor Experiment (MSRE) for following the changes that occur in the

mechanical properties of graphite and Hastelloy N, the two materials used in constructing the reactor.[8] We have removed several groups of samples and have installed some samples of modified Hastelloy N to observe their behavior. The environment in this facility consists of a molten fluoride salt (65 LiF-29.1 BeF_2-5 ZrF_4-0.9 UF_4, mole %) at 650°C and a neutron flux of 3.3×10^{13} neutrons cm^{-2} sec^{-1} (thermal) and 8.0×10^{12} neutrons cm^{-2} sec^{-1} (> 1.22 Mev). The samples discussed here were held at temperature for 9789 hr and received a neutron fluence of 5.3×10^{20} neutrons/cm^2 (thermal) and 1.3×10^{20} neutrons/cm^2 (> 1.22 Mev). Control samples were run in a static salt for a comparable time and temperature to allow us to separate the respective effects of aging and neutron damage.

We studied two alloys of modified Hastelloy N that have the nominal compositions Ni–12% Mo–7% Cr–0.2% Mn–0.05% C–2% W–0.5% Ti (heat 67-502) and Ni–12% Mo–7% Cr–0.2% Mn–0.05% C–0.5% Hf (heat 67-504). Previous studies[9] showed that small additions of Ti and Hf improve the post-irradiation properties of Hastelloy N. Both of these alloys were vacuum melted as 100-lb melts and fabricated into 1/2-in.-thick plate. The material was further worked at ORNL into 1/4-in.-diam rod and annealed for 1 hr at 1177°C. Each heat had about 2 ppm B.

These alloys were in excellent physical condition when removed from the surveillance and the control facilities. Metallographic examination revealed a thin deposit on the surface but no indications of corrosion.

Postirradiation tests showed the mechanical properties of the modified alloys superior to those of standard Hastelloy N. Control samples showed that aging for 9789 hr at 650°C caused very slight changes in the strength and doubled the fracture strain under creep conditions at 650°C. The creep properties of the modified alloys at 650°C are compared in Table 8.4 with those of a heat of standard

---

[8]H. E. McCoy, Jr., An Evaluation of the Molten-Salt Reactor Experiment Hastelloy N Surveillance Specimens – First Group, ORNL-TM-1997 (November 1967), p. 2.

[9]H. E. McCoy, Jr., and J. R. Weir, Jr., Materials Development for Molten-Salt Breeder Reactors, ORNL-TM-1854 (June 1967), p. 17.

Table 8.4. Comparison of Creep Properties at 650°C of Standard and Modified Hastelloy N, Unirradiated and After Irradiation to 5.3×10^{20} neutrons/cm^2 (Thermal)

Property	Standard Hastelloy N		Modified Hastelloy N			
	Heat 5085		Heat 67-502		Heat 67-504	
	Unirradiated	Irradiated	Unirradiated	Irradiated	Unirradiated	Irradiated
Stress to produce rupture in 1000 hr, psi	36,000	26,000	41,000	37,000	40,000	36,000
Stress to produce 1% creep in 1000 hr, psi	18,000	18,000	23,000	28,000	22,000	27,000
Minimum fracture strain, %	20	1	~ 30	6	~ 30	6

Hastelloy N irradiated under similar conditions. The stress to produce rupture in 1000 hr for standard Hastelloy N is reduced about 30% by irradiation and for the modified alloys is reduced only about 10%. The stress to produce rupture in 1000 hr after irradiation is about 40% higher for the modified alloys. Based on a minimum creep rate criterion, the allowable stresses after irradiation are about 50% higher for the modified alloy. The fracture strain of irradiated standard Hastelloy N is very dependent on the strain rate at 650°C, with the minimum fracture strain of 0.5 to 1% occurring at a strain rate of about 0.1%/hr. The modified alloys irradiated under the MSRE operating conditions exhibit decreasing fracture strain with strain rate at 650°C to a minimum value of about 6%. Thus, the postirradiation fracture strain of the modified alloys is superior to that of the standard alloy.

Influence of Irradiation Temperature on the Creep Properties of Hastelloy N (H. E. McCoy, Jr.)

We previously reported our observation that the postirradiation creep properties of the titanium-modified Hastelloy N (heat 66-548) were excellent when the irradiation temperature was 650°C or less but deteriorated dramatically at higher irradiation temperature.[10] The specific property changes noted are that the minimum creep rate increases and the fracture strain decreases. These changes are most pronounced in creep tests at 650°C when samples are tested that have been irradiated at various temperatures. Electron microscopy indicated that two carbides were involved: coarse Mo_2C was associated with the poor properties, and a fine carbide with a face-centered cubic structure and a lattice size of 4.24A was associated with good properties. Analyses of extracted residues indicate that Mo and Cr are present in both precipitates, so the changes in the morphology of the precipitate may be more important than the chemical changes.

A further irradiation experiment has been performed in which alloys of various compositions were irradiated at 760°C to a thermal fluence of 2.6×10^{20} neutrons/cm^2 to determine how universal these property

[10] C. E. Sessions, H. E. McCoy, Jr., and R. E. Gehlbach, Fuels and Materials Development Program Quart. Progr. Rept. Sept. 30, 1968, ORNL-4350, pp. 163–173.

changes were for several heats of standard and titanium-modified Hastelloy N and whether strong carbide formers such as Nb, Y, Zr, and Hf would result in improved stability at high temperatures. Some of the results of postirradiation creep tests on these materials at 650°C are shown in Figs. 8.14 and 8.15, and the nominal composition of each alloy is given in Table 8.5. The individual data points in Fig. 8.14 are identified by the heat number and the percentage of fracture strain. The rupture life of heat 66-548 (0.5% Ti) at 650°C is reduced dramatically by irradiation at 760°C compared with that after irradiation at 650°C. The other heats modified with 0.5% Ti (104, 7320, 21545, 67-526) are not affected as drastically by the higher irradiation temperature, but the rupture lives are still less than those observed for standard Hastelloy N melted in air, and the fracture strains are quite low.

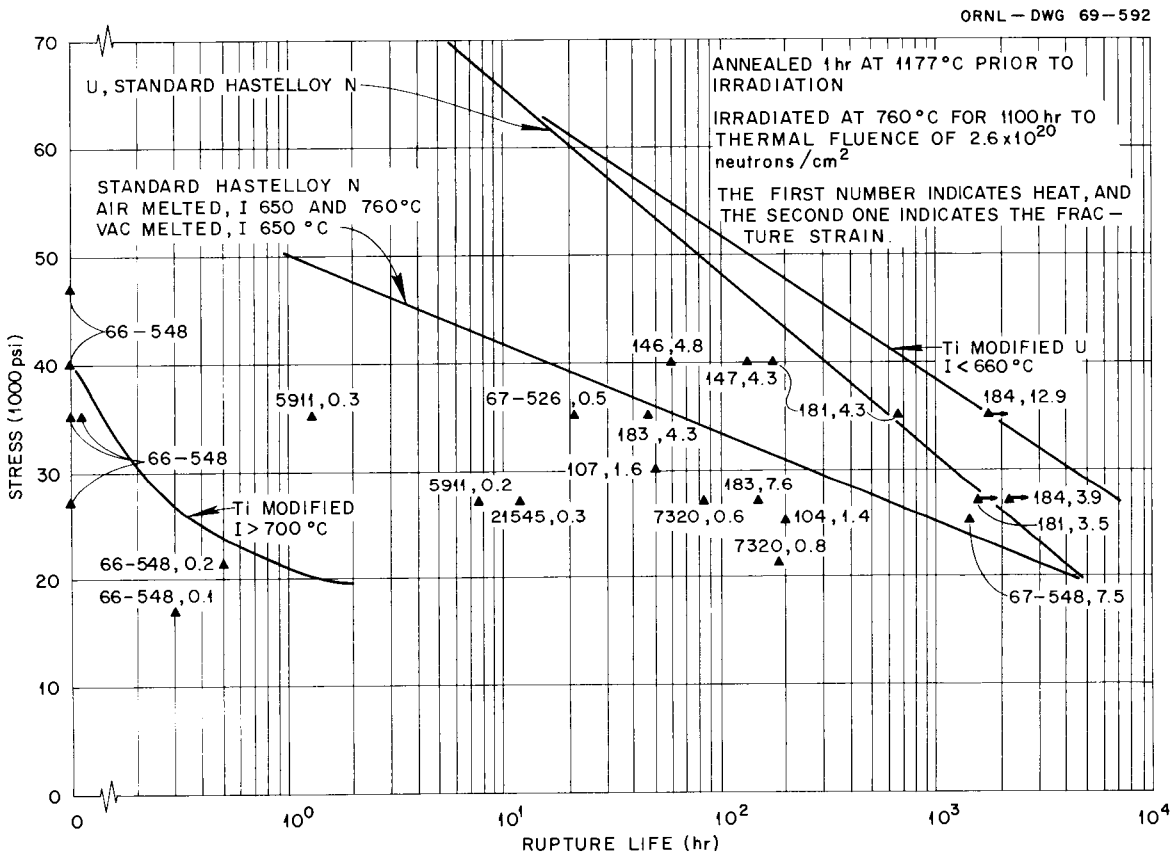

Fig. 8.14. Creep-Rupture Properties of Several Modified Hastelloy N Alloys Measured in Postirradiation Creep Tests at 650°C.

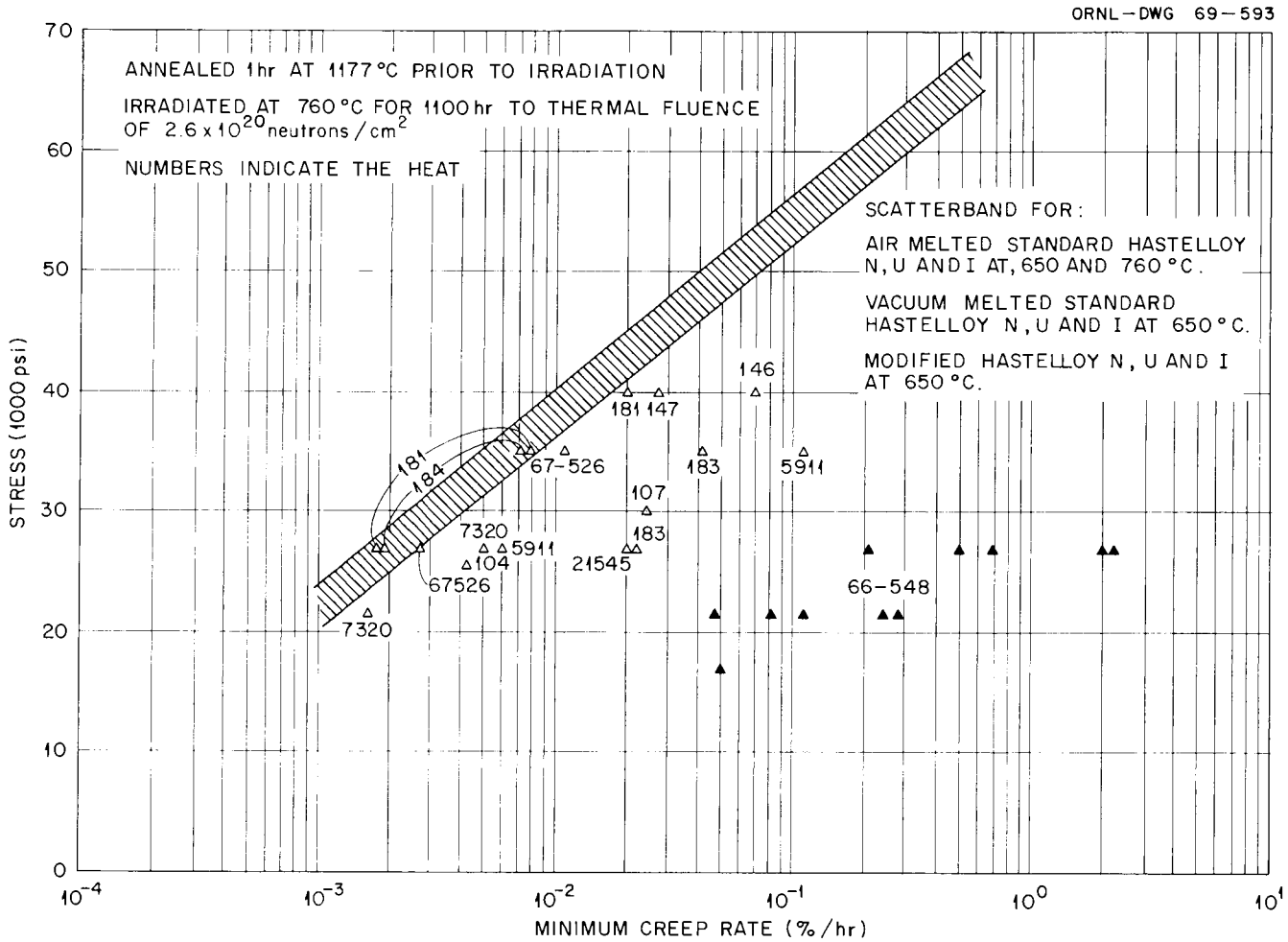

Fig. 8.15. Minimum Creep Rate of Several Modified Hastelloy N Alloys Measured in Postirradiation Creep Tests at 650°C.

Table 8.5. Nominal Compositions of Alloys Studied

Alloy	Composition (wt %)								
	Ni	Mo	Cr	Fe	Si	Mn	Ti	C	Other
Standard Hastelloy N	Bal	16	7	4	0.5	0.5	0	0.05	
5911	Bal	16	7	0	0.1	0.2	0	0.05	
66-548	Bal	12	7	0	0	0.2	0.5	0.05	
21545	Bal	12	7	0	0	0.2	0.5	0.05	
67-526	Bal	16	7	0	0	0.2	0.5	0.05	2 W
104	Bal	12	7	0	0	0.2	0.5	0.05	
107	Bal	12	7	0	0	0.2	1.0	0.05	
7320	Bal	12	7	0.1	0	0.2	0.5	0.05	
67-548	Bal	12	7	0	0	0.2	1.2	0.05	
146	Bal	12	7	0	0	0.2	0	0.05	1 Zr, 0.1 Re
147	Bal	12	7	0	0	0.2	0	0.05	1 Zr, 1 Re
181	Bal	12	7	0	0	0.2	0.5	0.05	2 Cb
183	Bal	12	7	4	0.2	0.5	1	0.05	1 Y
184	Bal	12	7	4	0.2	0.5	1	0.05	1 Hf

Heat 5911 is a commercial vacuum-melted heat of standard Hastelloy N, and the rupture life and fracture strain of this alloy are reduced dramatically by the higher irradiation temperature. Heats 67-548 and 107 contained about 1% Ti, and the datum point for heat 67-548 looks very encouraging; but additional data will be necessary before we can conclude that 1% Ti will give the desired stability. Heat 146 received additions of both Zr and Re and shows good postirradiation properties. Heat 181 contained 2% Nb in addition to 0.5% Ti and has excellent properties. Preliminary extractions show that the carbide in heat 181 is the same after aging at 650 and 760°C, thus supporting our supposition that the carbide stability is a determining factor for the postirradiation properties. Although the rupture life of heat 183 (1% Y and 0.5% Ti) is not extremely good, the fracture strains are quite good. The addition of 1% Hf and 0.5% Ti results in a material (heat 184) that is strong and quite ductile.

The minimum creep rates shown in Fig. 8.15 indicate that for many of these alloys the creep properties are altered and not just the fracture characteristics. Irradiating at 760°C results in a material that creeps faster and fails more quickly and at a lower strain. Heats 181 and 184, which showed good properties in Fig. 8.14, also compare well in Fig. 8.15. Thus, the potential for increasing the stability of these alloys at high temperatures looks very good.

Aging of Modified Hastelloy N (C. E. Sessions)

We are evaluating the tensile and creep properties of four heats of titanium-modified (0.15 to 1.2% Ti) Hastelloy N after aging at temperatures of 650 and 760°C. As reported previously,[11] the tensile property changes after 3000 hr of aging at 650 and 760°C indicated that aging of the modified alloy did result in a reduction in ductility at high temperatures that was more significant after the 760°C treatment. This indication of a thermal instability in the alloy system, however, required assessment for longer aging times and for creep conditions to fully characterize the material.

Table 8.6 shows the effects of aging at 650 and 760°C for 1500 and 3000 hr on the tensile properties measured at 650°C and a strain rate of 0.002 min^{-1} for the four alloys investigated.

Aging at 650°C slightly reduces the ductility at high temperatures after 1500 hr and significantly reduces it after 3000 hr for each heat except 466-548. Aging at 760°C significantly reduces the ductility for all heats after both 1500 and 3000 hr. A corresponding increase in the yield and ultimate tensile strengths is found for most aging conditions.

Thermal-mechanical treatment before testing influences the overall level of strength and ductility as shown in Table 8.6, but the influence of any particular heat treatment before testing differs from heat to heat.

The effects of aging on the creep properties of these modified alloys are being evaluated. Table 8.7 lists the results from the control

---

[11]C. E. Sessions, H. E. McCoy, Jr., and R. E. Gehlbach, Fuels and Materials Development Program Quart. Progr. Rept. Sept. 30, 1968, ORNL-4350, pp. 163–173.

Table 8.6. Comparison of Properties of Modified Hastelloy N Before and After Testing, Measured at 650°C[a]

Heat Number	Titanium Content[b] (%)	Heat Treatment Code	Properties Before Aging		Percent Change in Properties After Aging Indicated Time at 650°C				Percent Change in Properties After Aging Indicated Time at 760°C			
			Uniform Elongation (%)	Yield Strength (psi)	Uniform Elongation		Yield Strength		Uniform Elongation		Yield Strength	
					1500 hr	3000 hr	1500 hr	3000 hr	1500 hr	3000 hr	1500 hr	3000 hr
				$\times 10^3$								
466-535	0.15	121[c]	27.4	28.9	-9	-32	34	36	-42	-51	22	13
		123[d]	30.4	25.3	-31	-60	31	39	-55	-53	30	21
		109[e]	18.9	48.5	-20	-43	19	11	-38	-42	2	-8
466-541	0.30											1
		121	31.4	27.0	12	5	30	28	-43	-51	23	16
		123	30.7	21.4	-47	-66	24	40	-50	-56	46	39
		109	22.6	44.9	-4	-20	7	-2	-51	-57	0	-4
466-548	0.50	121	29.3	24.7	38	35	20	21	20	-31	22	22
		123	30.0	20.4	57	48	19	28	8	-17	33	26
		109	20.0	42.8	36	34	5	3	-26	-27	-3	-5
467-548	1.2	121	34.5	36.6	-18	-24	27	18	-25	-29	14	11
		123	41.3	29.1	-41	-58	47	54	-73	-68	61	53
		109	23.1	68.8	-6	-21	-6	-11	-10	-11	-10	-19

[a]Tensile tested at 650°C and 0.002 min^{-1} strain rate.

[b]All alloys have a nominal composition of Ni-12% Mo-7% Cr-0.2% Mn-0.05% C.

[c]1 hr at 1177°C solution anneal.

[d]1 hr at 1260°C solution anneal.

[e]1 hr at 1177°C solution anneal plus 10% prestrain at room temperature.

Table 8.7. Results of Creep-Rupture Tests on Titanium-Modified Hastelloy N Tested at 40,000 psi and 650°C

Heat Number	Pretest Annealing Code	Aging Time (hr)	Aging Temperature (°C)	Rupture Life (hr)	Fracture Strain (%)	Minimum Creep Rate (%/hr)	Reduction in Area (%)
466-535	121[a]	0		166	9.5	0.013	10.6
	123[b]	0		51	13.6	0.012	24.4
	109[c]	0		194	3.6	0.005	6.4
	121	1500	650				
	121	1500	760	136	11.3	0.049	17.4
	123	3000	650	> 167	> 6.6		
	123	3000	760	26	8.3	0.087	9.5
466-541	121	0		342	15.2	0.006	17.7
	123	0		189	21.5	0.008	26.6
	121	1500	650				
	121	1500	760	217	18.9	0.054	19.5
	123	3000	650	50	9.7	0.072	12.9
	123	3000	760	41	9.9	0.084	7.2
466-548	121	0		358	16.7	0.012	22.3
	123	0		620	11.7	0.006	17.8
	121	1500	650	670	27.2	0.020	30.1
	121	1500	760	42	7.9	0.120	18.3
	(duplicate)			594	42.1	0.025	34.2
	123	3000	650	345	29.1		37.3
	123	3000	760	175	24.1	0.066	37.6
467-548	121	0		1100	41.1		38
	123	0		< 472	21.6		17.6
	109	0		< 149	30.5	0.005	29.0
	121	1500	650				
	121	1500	760	1006	32.4	0.017	47.7
	123	3000	650	> 850	> 5		
	123	3000	760	> 550	> 3		

[a]Solution annealed 1 hr at 1177°C.

[b]Solution annealed 1 hr at 1260°C.

[c]Solution annealed 1 hr at 1177°C plus 10% prestrain.

and aged samples tested so far. The control tests on unaged samples show the greatest strength and the lowest ductility for the unstrained material. The optimum ductility was obtained from the samples solution annealed at 1260°C before creep testing. Tests on the aged samples indicate no deterioration in the creep properties after aging 1500 hr at either 650 or 760°C. However, heats 466-535 (0.15% Ti) and 466-541 (0.30% Ti) lost creep strength and ductility after aging 3000 hr at 760°C. In agreement with the tensile results, heat 466-548 (0.5% Ti) actually showed an increase in strength and ductility after 1500 and 3000 hr at the two aging temperatures. No conclusions can be drawn from the tests on heat 467-548 (1.2% Ti) except that the properties for this heat as annealed are definitely superior to those of the three heats with lower levels of Ti.

The few tests completed indicate that in some heats a deterioration in properties is found at high temperatures after aging, but none of these results account for the gross deterioration in creep strength and ductility that have recently been found for modified Hastelloy N when irradiated at temperatures above 700°C (ref. 11). That is, the effects found under irradiation cannot be accounted for by thermal aging effects alone.

9. RADIATION EFFECTS IN ALLOYS AND STRUCTURAL MATERIALS

M. S. Wechsler

The object of this work is to determine the effect of neutron irradiation on the mechanical properties of reactor pressure-vessel steels and irons that contain controlled amounts of technologically significant alloying additions. For reactor development, the main consequence of irradiation in these materials is radiation embrittlement, manifested by an increase in the ductile-to-brittle transition temperature (DBTT) and a decrease in ductility even in the nominally ductile temperature range. Both effects increase the likelihood of a fast rupture of the pressure vessels of water-cooled reactors. Since such an event could have catastrophic consequences to the public safety, the Advisory Committee on Reactor Safeguards emphasized the need for better understanding of the problem of brittle fracture and of how to cope with it.[1,2]

Much remains to be learned about why neutron irradiation embrittles reactor pressure vessel steels or other body-centered cubic metals. It is known that different steels have varying degrees of sensitivity to the deteriorating effects of neutron irradiation, but this depends on a complex combination of chemical, metallurgical, and radiation variables.[3,4] Also, the embrittlement is probably associated with radiation strengthening, which in turn is due to defect clusters produced by radiation. A recent study of the relationship between radiation embrittlement and radiation strengthening in an ASTM (American Society for Testing and Materials) A 212-B steel indicated that the increase in the DBTT upon

---

[1] J. P. Blakely, Nucl. Safety 8, 277 (1967).

[2] "ACRS Qualms on Possible Vessel Failure Startle Industry," Nucleonics 24(1), 17–18 (1966).

[3] M. S. Wechsler, "Radiation Embrittlement of Metals and Alloys," pp. 296–345 in The Interaction of Radiation with Solids, ed. by R. Strumane et al., North Holland Publishing Company, Amsterdam, 1964.

[4] M. S. Wechsler, Nucl. Safety 8, 461–469 (1967).

irradiation can be accounted for by the increase in yield stress on the basis of a cleavage fracture stress that is independent of temperature.[5] In particular, no decrease in the cleavage fracture stress was suggested by the results, and no change in the mode of fracture was observed by means of optical and electron metallography.

Radiation Effects on Pressure-Vessel Steels

R. G. Berggren W. J. Stelzman

Radiation Hardening and Embrittlement in ASTM A 533-B Class 1 Steel

We obtained data on the changes induced by radiation in the tensile and notch-impact properties of a 12-in.-thick plate of ASTM A 533-B Class 1 steel as a function of irradiation temperature and depth in the plate for neutron fluences between 4.4 and 13.5×10^{18} neutrons/cm^2 (> 1 Mev). Results of tensile tests are presented in Table 9.1, and results of Charpy V-notch impact tests are presented in Table 9.2. To compare the increases induced by radiation in yield strength and DBTT for the several irradiation temperatures and depths in the plate, we normalized the results to a fluence of 9×10^{18} neutrons/cm^2 (> 1 Mev) by assuming the increases to be proportional to the square root of fluence. The normalized increases in yield stress and DBTT are shown in Table 9.3 with the ratios of the property changes at elevated irradiation temperatures to the property changes at the 66°C irradiation temperature. The smaller increases in yield stress would indicate that the surface material is slightly less sensitive to radiation than quarter-thickness or midthickness material. No similar conclusion can be based on transition temperature increases since scatter is inherent in notch-impact test data. The relative effects of elevated irradiation temperatures (compared to irradiation at 66°C) are almost identical for the three levels in the plate.

---

[5]M. S. Wechsler, R. G. Berggren, N. E. Hinkle, and W. J. Stelzman, "Radiation Hardening and Embrittlement in a Reactor Pressure Vessel Steel," to be published by American Society for Testing and Materials in an ASTM Special Technical Publication, 1969.

Table 9.1. Tensile Properties of Irradiated 12-in.-Thick A 533-B Class 1 Steel[a] from Heat A-1008-1, HSST[b] Plate 01

Fluence [neutrons/cm^2 (> 1 Mev)]	Irradiation Temperature (°C)	Strength Properties, psi			Elongation, %	
		Upper Yield	Lower Yield	Ultimate Tensile[c]	Uniform	Total[d]
$\times 10^{18}$		$\times 10^3$	$\times 10^3$	$\times 10^3$		
		Surface Specimens				
0		85.9	82.4	98.4	9.2	18.7
5.4	67	114.1	106.5	107.1	7.3	17.3
5.9	232	105.5	100.7	111.7	10.1	18.5
5.5	291	100.0	94.7	108.5	10.9	20.0
12.5	343	93.6	88.2	102.7	11.2	20.0
		Quarter-Thickness Specimens				
0		69.5	68.3	89.8	9.8	19.5
7.5	64	105.5	101.8	102.9	4.7	13.3
8.8	232	95.5	93.8	108.3	8.9	15.9
11.8	288	90.2	87.6	106.5	9.5	16.8
12.5	343		77.0	97.1	10.1	17.2
		Three-Eights-Thickness Specimens				
0		71.4	69.8	91.6	9.0	17.8
9.8	66	111.5	106.7	106.9		10.7
		Midthickness Specimens				
0		69.0	68.0	90.0	9.3	18.0
7.3	66	107.5	103.3	104.3	4.7	12.1
8.3	232	95.9	95.3	109.8	7.7	14.3
11.0	288	88.2	86.4	106.1	8.5	15.3
11.5	349	77.7	76.7	98.2	10.6	18.1

[a]All specimens are of longitudinal orientation, tested at 21°C.

[b]Heavy Section Steel Technology.

[c]Ultimate tensile strength is here defined as the maximum load after the yield point divided by original area of cross section.

[d]Length-to-diameter ratio: 7.

Table 9.2. Charpy V-Notch Impact Properties of Irradiated 12-in.-Thick ASTM A 533-B Class 1 Steel[a] from Heat A-1008-1, HSST Plate 01

Irradiation Temperature (°C)	Fluence [neutrons/cm^2 (> 1 Mev)]	DBTT[b] (°C)	Change in DBTT[b] (°C)	Shelf Energy (ft-lb)
	$\times 10^{18}$			
	Surface Specimens			
		−98		110
62	4.4	−9	89	95
232	5.5	−12	86	90
290	4.7	−59	39	100
338	11.0	−68	31	105
	Quarter-Thickness Specimens			
		−12		120
68	6.2	82	94	100
232	7.1	79	92	100
293	9.4	41	53	100
349	13.5	2	14	120
	Midthickness Specimens			
		−7		110
63	6.5	96	103	80
235	7.2	91	97	85
293	10.5	66	72	
349	9.8	13	19	110

[a]All specimens of longitudinal orientation.

[b]Energy level: 32 ft-lb.

Table 9.3. Tensile and Charpy V-Notch Impact Properties of Irradiated 12-in.-Thick A 533-B Class 1 Steel[a] from Heat A-1008-1, HSST Plate 01

Irradiation Temperature (°C)	Normalized Increase[b] in Lower Yield Stress	$\frac{\Delta\sigma_{LY}}{\Delta\sigma_{LY_{66°C}}}$ [(c)]	Irradiation Temperature (°C)	Normalized Increase[b] in DBTT at 32 ft-lb	$\frac{\Delta DBTT}{\Delta DBTT_{66°C}}$ [(d)]
		Surface Specimens			
69	31.1	1	63	127	1
232	22.6	0.73	232	110	0.87
290	15.7	0.50	290	54	0.42
343	4.9	0.16	338	28	0.22
		Quarter-Thickness Specimens			
66	36.6	1	69	114	1
232	25.8	0.70	232	103	0.91
288	16.8	0.46	293	52	0.46
343	7.4	0.20	349	11	0.10
		Midthickness Specimens			
66	39.2	1	63	121	1
232	28.4	0.72	235	109	0.90
288	16.6	0.42	293	67	0.55
349	7.7	0.20	349	19	0.16

[a]All specimens are of longitudinal orientation.

[b]Data normalized to a fluence of 9×10^{18} neutrons/cm^2 (> 1 Mev).

[c]$\Delta\sigma_{LY}$ denotes change in lower yield stress.

[d]ΔDBTT denotes change in ductile-to-brittle transition temperature at the 32 ft-lb level.

Investigation of Submerged Arc Weldment in HSST Plate 01

Charpy V-notch impact tests were conducted on weld metal from a full-thickness submerged-arc weld in a portion of the 12-in.-thick Heavy Section Steel Technology (HSST) plate 01. Specimens with notches 1 in. below the weld surface had a DBTT of −57°C at the 32 ft-lb level and a shelf energy of 125 ft-lb. Specimens from the quarter-thickness plane had a DBTT of −51°C at the 32 ft-lb level and a shelf energy of 120 ft-lb.

Charpy V-notch impact specimens from a series of depths through the weld from one weldment surface to the opposite surface (1/2-in. increments) were tested at −51°C to determine the notch-impact properties through the weldment. No significant variation was observed as a function of distance from the surface.

From the data obtained, we infer that the DBTT of the weld metal at the 32 ft-lb energy level (−51°C) is lower than that for the interior of the parent plate and about the same as for the material 1 in. below the surface of the parent plate.

Characterization of HSST Plate 03

We obtained results from Charpy V-notch impact tests for several levels and orientations in HSST plate 03, ASTM A 533-B Class 1 steel. This plate was quenched flat, rather than on edge as plates 01 and 02 were, so that we could determine possible effects of steam binding during quenching. The results presented in Table 9.4 show no significant difference in properties between the two surfaces. Also, DBTT and the ductile energies are almost the same as for corresponding depths in plates 01 and 02. Thus the manner of quenching has no more than minimal effect on notch-impact properties.

Radiation Effects in Iron

N. E. Hinkle

The work on radiation effects on iron is largely associated with the influence of N, which is known to affect the mechanical properties of iron and steel in several important ways. The creep resistance of steels is thought to decrease when N is removed from solid solution. Furthermore, the poorer resistance to creep of aluminum-killed steels as compared to silicon-killed steels may be due to the formation of aluminum nitride, which decreases the concentration of N in solid solution. This is of significance in connection with aluminum-killed reactor pressure-vessel steels, such as the ASTM A 533-B steel now used, since the better notch ductility of aluminum-killed steels may be outweighed by poorer

Table 9.4. Charpy V-Notch Impact Properties of 12-in.-Thick A 533-B Class 1 Steel from Heat C-2702-2, HSST Plate 03

Level in Plate	Orientation[a]	Charpy V-Notch Impact Transition Temperature[b] (°C)	Ductile Shelf Energy (ft-lb)
Top surface	L	−87	118
	T	−67	98
Quarter thickness	L	−1	120
	T	7	93
	P	16	80
Half thickness	L	4	124
	T	10	85
Three-quarter thickness	L	−1	118
	T	2	96
Bottom surface	L	−79	118
	T	−71	84

[a]L: long axis of specimen longitudinal (parallel to plate surface).

T: long axis of specimen transverse to rolling direction and parallel to plate surface.

P: long axis of specimen perpendicular to plate surface.

[b]Transition temperature for 32 ft-lb fracture energy.

resistance to creep. A further consideration is the effect of the neutron irradiation on the disposition of the N. In the case of other body-centered cubic metals, notably Nb (ref. 6), interstitial impurities become trapped at defects produced by radiation and so are effectively removed from solid solution. There is also some evidence — from measurements of internal friction and magnetic disaccommodation[7] — of the trapping of N in irradiated iron.

Therefore, our object is to study the effect of N on the radiation hardening and embrittlement in iron, paying particular attention to the

[6]J. M. Williams, W. E. Brundage, and J. T. Stanley, Metal Sci. J. 2, 100–104 (1968).

[7]M. Wuttig, J. T. Stanley, and H. K. Birnbaum, Phys. Status Solidi 27, 701–712 (1968).

question of the removal of N from solid solution by trapping at defects produced by radiation. The starting material is vacuum-melted Ferrovac-E iron, decarburized and denitrogenized at 800°C in dry H_2. This material contained a maximum of 2 ppm N by weight as determined by vacuum fusion. Nitrogen is then reintroduced into some of the material by treating at 590°C in a hydrogen-ammonia atmosphere. In previous reports[8,9] we described the experimental details and results. To elucidate the results, we prepared iron tensile samples containing 300 ppm N by weight, Fe-300N.

We have completed the postirradiation evaluation of the yield stress and strain-aging response as a function of postirradiation annealing temperature for the Fe-300N material. The irradiation temperature was −75°C to −130°C, and the fluence was 4.5×10^{17} neutrons/cm^2 (> 1 Mev). We have observed the following:

1. The strength of unirradiated Fe-300N material at a test temperature of −36°C is greater than that of the Fe and Fe-20N materials[8] because of the solid solution strengthening due to the higher nitrogen concentration.

2. The effect of the low-temperature irradiation is greater on the Fe-300N material than it is on the Fe-20N material. Also, the increased yield stress of the irradiated Fe-300N material due to anneal hardening between 0 and 100°C is greater than previously observed for the Fe and Fe-20N materials. In fact, when we compare the increases in yield stress — due to both irradiation and anneal hardening — for the two materials that contain N, we find that the Fe-300N material has nearly doubled the change in yield stress of the Fe-20N material.

3. The strain-aging response of the Fe-300N material, as measured by the increase in flow stress due to aging at 40°C for 20 hr after 4%

---

[8]S. M. Ohr, N. E. Hinkle, and M. S. Wechsler, Fuels and Materials Development Program Quart. Progr. Rept. Sept. 30, 1968, ORNL-4350, pp. 202–214.

[9]N. E. Hinkle, J. M. Williams, W. E. Brundage, and J. T. Stanley, Radiation Metallurgy Section Solid State Division Progress Report for Period Ending July 1967, ORNL-4195, pp. 15–21, ORNL-TM- 2020, pp. 133–139.

strain, is two to three times greater than for the Fe-20N material both before and after irradiation. Upon postirradiation annealing up to 100°C, the strain-aging response of the Fe-300N material decreases in the same manner as Fe-20N material. However, the strain-aging response of the irradiated Fe-300N material does not approach zero; this indicates that all of the N is not removed from solid solution, which in turn suggests that the defects produced by radiation have become saturated with nitrogen atoms.

4. The strain-aging response of the irradiated Fe-300N material increases back to the preirradiation value after postirradiation anneals between 150 and 250°C; this indicates an increased concentration of N in solution, as was observed also for the studies on the Fe-20N material.

5. The yield stress of the Fe-300N material decreases at a greater rate when annealed at 150 to 250°C than did the Fe-20N and Fe materials. This is probably closely related to the relative amounts of the N in solution or combined with defects produced by radiation.

6. The yield stress of the irradiated Fe-300N material returns to the preirradiation level after postirradiation annealing at 400°C for 15 min, whereas the Fe and Fe-20N materials retained a significant amount of radiation hardening after the same annealing treatment.

In conclusion, our work on the effect of N on radiation hardening in iron indicates that N is removed from solid solution in irradiated iron at temperatures near 100°C where N is mobile. The removal of N from solid solution is probably due to trapping by defects produced by radiation. An increase in strength is associated with the trapping of N, but the increase is apparently not proportional to the total nitrogen content.

PART IV

TECHNIQUES OF FABRICATION AND TESTING

10. TUNGSTEN METALLURGY

P. Patriarca

The object of this program is to develop economical methods for producing high-quality tungsten and tungsten-alloy tubing with good creep-rupture properties at high temperatures, good microstructural stability, good ductility at low temperatures, and good weldability. We fabricate tubing both by modification of conventional techniques based on extrusion, tube reduction, and warm drawing and by direct chemical vapor deposition (CVD) through the hydrogen reduction of heavy-metal halides. Our program includes complete physical and metallurgical evaluation of both fabrication processes.

Primary and Secondary Working of Tungsten and Tungsten Alloys

W. R. Martin

Extrusion of Tungsten and Tungsten Alloys (R. E. McDonald)

Four powder-metallurgy tungsten duplex billets, previously described, were extruded on the 1250-ton high-speed extrusion press using our base-metal-oxide (BMO) lubrication technique. Table 10.1 is a compilation of the extrusion data. The data show that with a constant reduction ratio and speed, the extrusion constant varied less than 10% from 1750 to 1250°C.

Figure 10.1 shows the tungsten tubes after the TZM alloy cladding was removed by acid etching. The surface improved with decreased extrusion temperature. There is yet no explanation for the extremely coarse surface on the nose end of the 1650°C extrusion.

A 1/2-in.-long sample was cut from the nose of each tube for metallography. Also, several rings (1.054 in. in diameter, 0.020 in. in wall thickness, and 0.25 in. long) were machined from each tube to determine the quality of the machined surfaces and the ease with which rings can be cut without fracture. The remainder of the tubing will be stress relieved for 1 hr at 1100°C, and several more rings will be machined to determine the effect of the heat treatment.

Table 10.1. Duplex Extrusion of Powder-Metallurgy Tungsten Tube Shells

Extrusion Number	Extrusion Conditions[a]					Dimensions of Extrusions (in.)		
	Preheat Billet Temperature (°C)	Reduction Ratio	Ram Force (tons)		Extrusion Constant (psi)	Diameter		Length
			Maximum	Minimum		Outside	Inside	
					$\times 10^3$			
0685	1750	3.73	320	240	73	1.130	0.903	20.5
0686	1650	3.72	315	220	71	1.125	0.906	20.75
0687	1450	3.75	320	220	72	1.115	0.913	20.5
0688	1250	3.61	340	220	79	1.185	0.931	19.75

[a]All extrusions at 15 ips.

Fig. 10.1. Duplex Tubes After Dissolution of TZM Cladding.

Chemical Vapor Deposition of Tungsten Alloys

J. I. Federer

Deposition of Tungsten-Rhenium Sheet

Development of a codeposition process for chemical vapor deposition of W–5% Re alloy sheet material has continued. Alloys deposited on sheet substrates heated by self-resistance have been nonuniform in thickness. Thickness variations result in nonuniformity of temperature, which in turn results in a composition gradient in the deposit. The deposits are typically thicker near the end of the deposition chamber where the gas enters. If the gas flows in only one direction, the thickness of the deposit gradually decreases in the direction of the flow of gas. If the flow is periodically reversed, both ends of the deposit are thicker than the middle. Gas depletion evidently causes this behavior. Possible remedies are to (1) increase gas flow until the amount reacted is a small fraction of the total amount so that all parts of the substrate are exposed to essentially the same environment, (2) decrease the size of the substrate to produce the same effect, (3) dilute the reacting gases with another gas, such as Ar, (4) lower the $H_2:(WF_6+ReF_6)$ ratio in order to decrease the deposition rate, (5) use a baffle in the deposition chamber to change the flow pattern, and (6) vary the pressure. Each of these techniques, except the last lowers or tends to lower the deposition efficiency, which is probably a necessary requirement for producing uniformly thick sheet material.

The suggested ways of overcoming gas depletion and improving the uniformity of the thickness of the deposit have been tested by the experiments shown in Table 10.2. The results are shown in Fig. 10.2. The conditions of the first experiment (180) resulted in nonuniform thickness. Lowering the $H_2:(WF_6+ReF_6)$ ratio from 15 to 12.5 (experiments 181 and 184) and to 10 (experiment 183) did not improve uniformity, nor did doubling the gas flow (experiment 184). The thickness distribution of these deposits was typical of the distribution obtained by periodically reversing the flow of gas. Next, a 3-in.-diam baffle was placed on the end of the substrate in the inlet end of the 4-in.-ID deposition chamber

Table 10.2. Conditions[a] of Tungsten-Rhenium Codeposition Experiments

Experiment Number	Flow Rates (cm^3/min)			H_2:(WF_6+ReF_6) Ratio	Pressure (torr)	Substrate[b]	Efficiency (%)	Remarks
	H_2	WF_6	ReF_6					
180	3000	190	10	15	10	A	86	Flow periodically reversed.
181	2500	190	10	12.5	10	A	89	Flow periodically reversed.
184	5000	380	20	12.5	10	A	73	Flow periodically reversed.
183	2000	150	50	10	10	A		Flow periodically reversed.
185	2500	190	10	12.5	10	B	76	Baffle, unidirectional flow.
186	1500	190	10	7.5	10	B	75	Baffle, unidirectional flow.
187	1500	190	10	7.5	10	B	48	Baffle, unidirectional flow, 1500 cm^3/min Ar.
188	1500	190	10	7.5	~ 200	B	65	Baffle, unidirectional flow.
189	1500	190	10	7.5	~ 200	B	65	Unidirectional flow.
190	1500	190	10	7.5	~ 100	B	54	Unidirectional flow.

[a]Temperature, 750°C.

[b]Substrates: A – 3 1/4 in. wide by 14 in. long, B – 1 7/8 in. wide by 14 in. long.

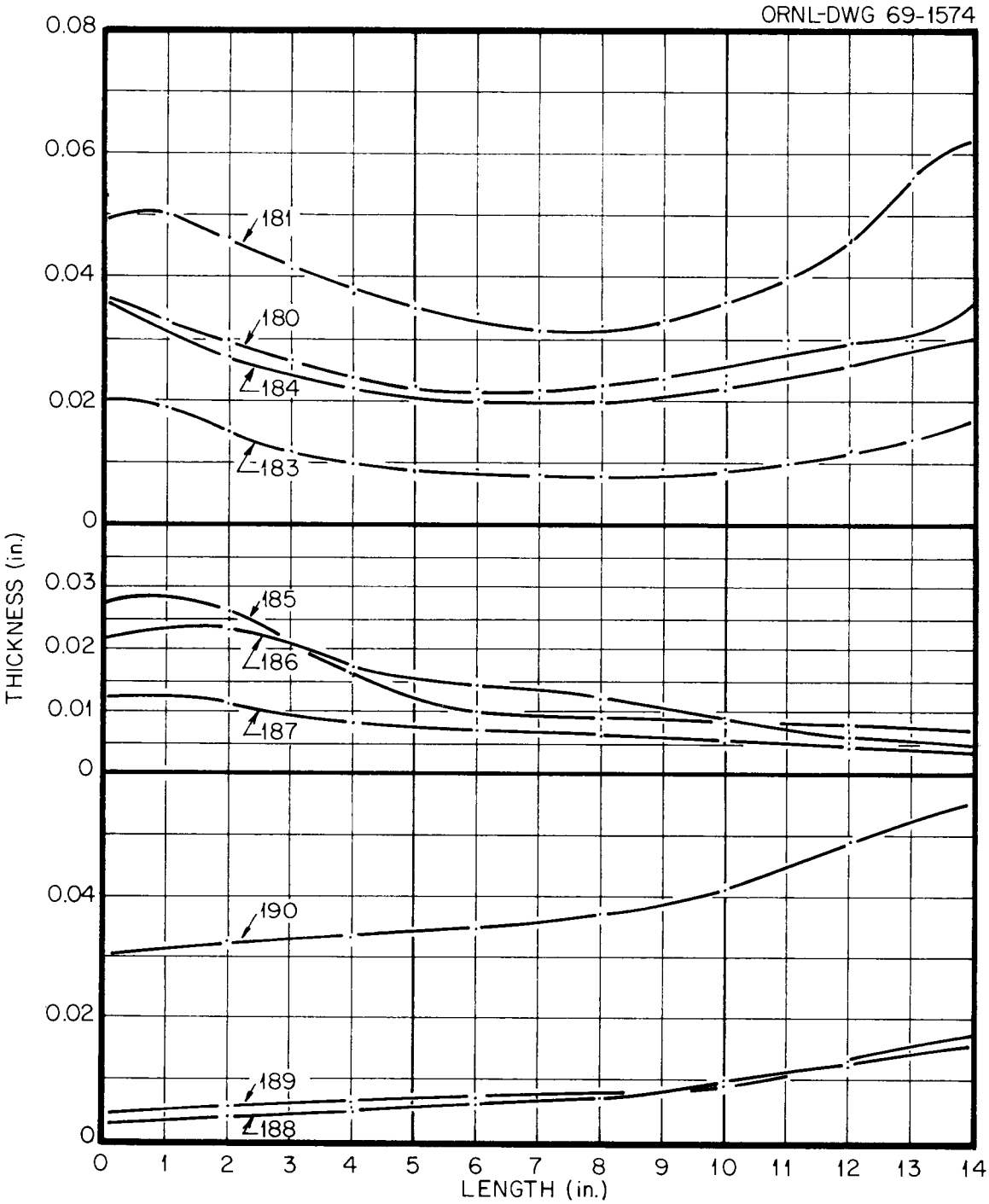

Fig. 10.2. Thickness of Tungsten-Rhenium Deposit as a Function of Length for Experiments 180 to 190. Test variables are shown in Table 10.2.

to form a 1/2-in.-wide annulus so that a larger fraction of the gas could flow unreacted past the inlet end of the substrate. Gas flow was unidirectional in these experiments. The results of experiment 185, however, show that the deposit at the inlet end was about four times thicker than that at the outlet end. The substrate was only 1 7/8 in. wide instead of the 3 1/4-in.-wide substrates used in the first two experiments, which probably accounts for the lower efficiency, 76% compared to 86% in the first experiment. Substantially the same results were obtained in experiment 186, in which the same baffle arrangement was used with a lower H_2:(WF_6+ReF_6) ratio. In experiment 187, the same arrangment and flow rates, except for the addition of 1500 cm^3/min of Ar, resulted in the deposit at the inlet end being about three times thicker than that at the outlet end and in a decrease of efficiency to 48%.

Experiment 188 was conducted under the same conditions as experiment 187 except that the pressure was increased from 10 to about 200 torr. The thickness distribution in this case showed a marked change. The deposit increased in thickness from the gas inlet end towards the outlet end. The same result was obtained without the baffle in experiment 189 and in experiment 190, which was conducted at about 100 torr.

Since the deposits were thicker on the inlet end at a pressure of 10 torr and thicker on the outlet end at a pressure of about 100 torr, the results suggest that thickness might be uniform at some intermediate pressure. We are investigating this possibility.

Parametric Studies of the Tungsten-Rhenium Codeposition Process

A series of experiments were performed to determine the isodeposition temperature (that is, the temperature at which the deposit has the same composition as the metal composition of the reacting fluorides) for W—25% Re alloys. The deposition temperature was varied between 600 and 1200°C in these experiments with other conditions maintained as constant as possible. The gas composition intended was 600, 30, and 10 cm^3/min of H_2, WF_6, and ReF_6, respectively, to produce a W—25% Re deposit. The deposits formed on 1/8-in.-diam by 3-in.-long steel substrates that were contained within a 3 1/2-in.-ID deposition chamber and heated by self-resistance. The 1/2-in.-long central section of each deposit was

analyzed, and the composition was compared to the metal content of the WF_6-ReF_6 mixture used during deposition.

Variations in gas flow caused the rhenium content of the gas mixture to range from about 14 to 22% instead of the intended 25%. The difference between the rhenium content of the deposit and that of the gas mixture (ΔRe) is plotted against deposition temperature in Fig. 10.3. The data show that at 600°C a rhenium-rich deposit was formed but that at 700°C and above the rhenium content of the deposit was about the same as the rhenium content in the gas mixture. Thus, in the temperature range studied, the isodeposition temperature appears to be any temperature between 700 and 1200°C for the conditions of these experiments.

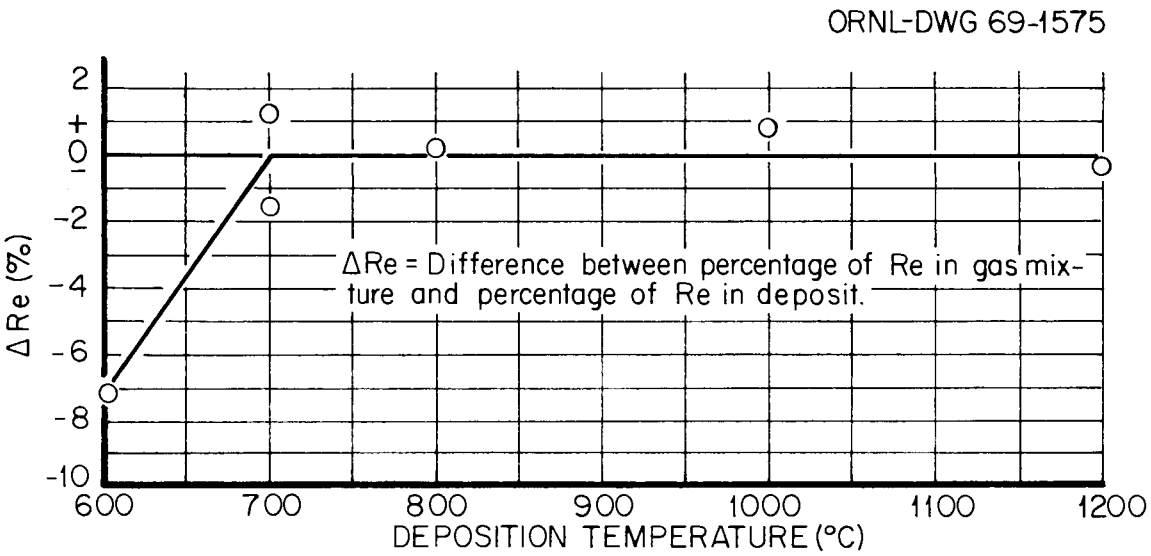

Fig. 10.3. Temperature for Isodeposition of Tungsten and Rhenium from a W–25% Re Gas Mixture.

Effect of HF on Deposit Morphology

Various reasons have been proposed to explain the cause of the nodules that often form in vapor-deposited materials, including tungsten and tungsten-rhenium alloys. One reason frequently mentioned is the concentration of HF at the surface of deposits prepared by hydrogen reduction of metal fluorides. Since HF is a byproduct of the process, it would eventually attain a certain surface concentration during

deposition and could possibly alter the surface chemistry in such a way as to favor growth of nodules.

In order to investigate the effect of HF on deposit morphology, we added HF to the reacting gases for a series of tungsten deposits. The substrate in each case was a 3/4-in.-ID copper tube heated in a furnace that had a heavy-walled metal liner to minimize temperature gradients. The temperature, pressure, time, and flow rates of H_2 and WF_6 were maintained constant in all experiments. Anhydrous HF was added in amounts of 5, 15, and 30 vol %. These experiments produced two unexpected results. Although all of the deposits had rough or nodular surfaces, the deposit prepared without the addition of HF definitely had a rougher texture than the other deposits. And, as shown below, the metal recovery was lowest for the deposit prepared with no added HF:

Hydrogen fluoride added, vol %	0	5	15	30
Recovery, %	78	91	94	93

Since HF is a byproduct of the deposition reaction, added HF would be expected to retard deposition. We are still evaluating the results of these experiments. We are particularly trying to correlate some subtle changes in surface texture with microstructure.

Chemical Vapor Deposition of Vanadium

W. C. Robinson, Jr.

We are continuing our investigation of the possibility of chemically vapor depositing V into tubing or thin coatings on stainless steel tubing. Previous efforts to reduce VCl_3 at 950°C were unsuccessful and resulted in a deposit of solid VCl_2 (ref. 1). Since the temperature limit of our resistance furnace is 950°C, an induction furnace was modified for vanadium deposition. Reaction of entrained VCl_3 and H_2 at 1300°C on an induction-heated graphite substrate for 2 hr resulted in a bright metallic deposit that was identified by x-ray diffraction as vanadium metal

[1]W. C. Robinson, Jr., Fuels and Materials Development Program Quart. Progr. Rept. Sept. 30, 1968, ORNL-4350, p. 233.

with a trace of carbide. A subsequent experiment at 1200°C yielded the same type of deposit. It is therefore possible to deposit vanadium metal, on graphite at least, at temperatures of 1200°C and above.

Metallurgical Properties of Tungsten Alloys

A. C. Schaffhauser

Chemically Vapor Deposited Tungsten-Rhenium Alloys

We began bend tests of chemically vapor deposited W–5% Re sheet material to determine the ductile-to-brittle transition temperature (DBTT) and effects of heat treatment. The sheet was deposited on both sides of a resistance-heated substrate of molybdenum sheet. The deposition conditions, thickness profile, and chemical analysis of the deposit tested (W–Re 181) were previously described.[2] We thought the periodic reversal of the gas flow was helpful in obtaining uniform thickness along the length of the sheet, but it also produced a slightly layered microstructure, grown-in porosity between the layers (Fig. 10.4), and a nonuniform microstructure along the length of the deposit. Even though a small amount of grown-in porosity was present in this material, we decided it would be worthwhile to perform preliminary tests since most of the porosity would be near the center plane of the bend specimen and would not be subjected to high tensile stresses during the initial stages of bending.

Bend specimens, 1 1/2 × 3/8 × 0.030 in., were cut and ground from the sheet. Most of the specimens cut from the sheet as it had been deposited broke during grinding. The remaining specimens were inspected for cracks with dye penetrant and by microscope after electropolishing. Only the specimens that had not been ground on the first deposited surface were suitable for testing. None of these specimens bent at test temperatures as high as 500°C. But specimens annealed at 1200 to 2000°C could be bent at test temperatures as low as 200°C. Although the

[2] J. I. Federer, Fuels and Materials Development Program Quart. Progr. Rept. Sept. 30, 1968, ORNL-4350, pp. 230–232.

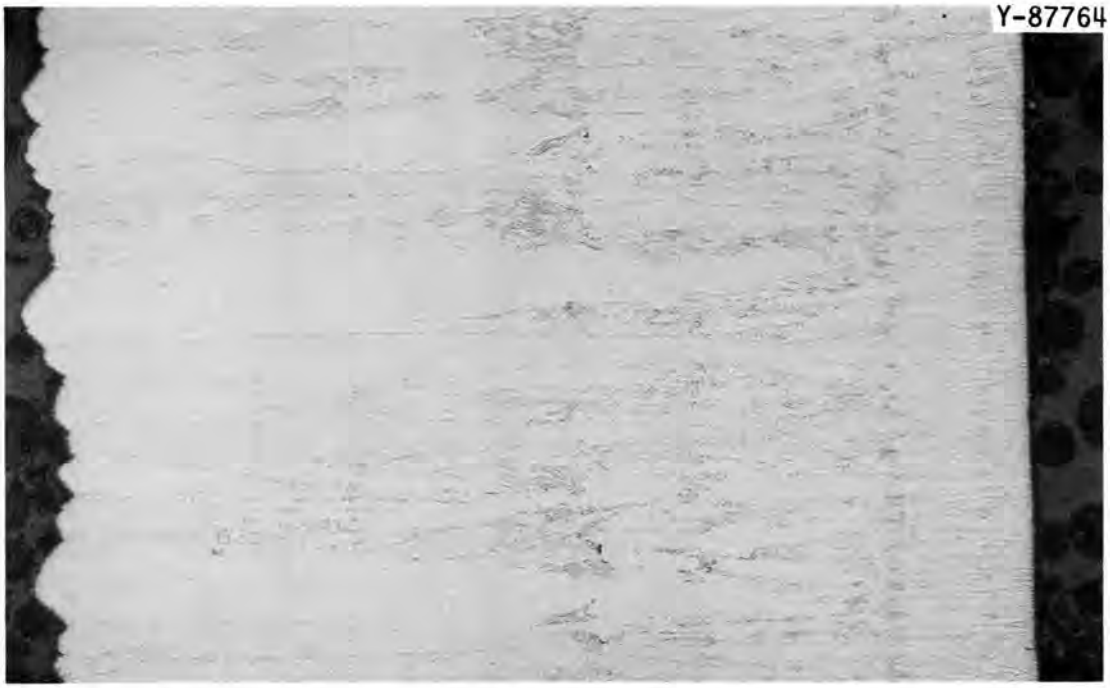

Fig. 10.4. Microstructure of Chemically Vapor Deposited W–5% Re Showing Slightly Layered Structure and Porosity in the Center Layer Produced by Periodic Reversals of Gas Flow During Deposition. 75×.

results were scattered, there was a trend of greater ductility after the higher annealing temperatures (solid data points in Fig. 10.5).

Because of these results, we stress relieved a second group of specimens for 2 hr at 1100°C before grinding them. The specimen yield was increased, and annealing 1 hr at 1600, 2000, and 2200°C produced more consistent bend results. The greatest ductility was observed after the higher annealing temperatures (open data points in Fig. 10.5).

The improved ductility produced by annealing at 2000 and 2200°C is unusual since the lowest DBTT previously reported for unalloyed CVD tungsten was obtained after annealing at 1000 to 1600°C (ref. 3). This behavior suggests that sintering of grown-in porosity or homogenization of the alloy is necessary to produce maximum ductility. A detailed metallographic examination of the specimens is under way to find an

---

[3]A. C. Schaffhauser, "Low-Temperature Ductility and Strength of Thermochemically Deposited Tungsten and Effects of Heat Treatment," pp. 261–276 in Summary of the Eleventh Refractory Composites Working Group Meeting, Tech. Rept. AFML-TR-66-179 (July 1966).

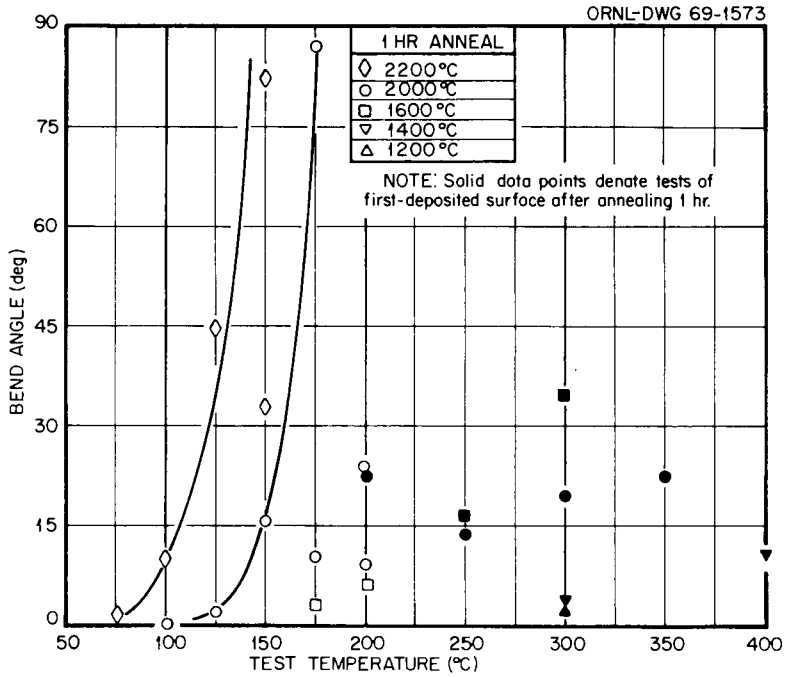

Fig. 10.5. Ductile-to-Brittle Transition Temperature of CVD W–5% Re as a Function of Annealing Temperature. (4T punch radius, 0.1 in./min deflection rate.)

explanation for these results. In either case, these results are encouraging because the DBTT of 150°C is the lowest reported for unworked W or W–5% Re.

Evaluation of Welds and Brazes in Tungsten Alloys

Gas Porosity and Hot Cracking in Welds in Tungsten (K. Farrell)

There appears to be little or no published information on microstructural defects in fusion welds in W, but experience at ORNL has revealed that such welds are prone to porosity and hot cracking. These defects are particularly troublesome in CVD tungsten. This material is made by reducing WF_6 with H_2 over a heated substrate.[4] It is quite pure, for W, but it contains some residual F that is thought to be

[4]R. L. Heestand, J. I. Federer, and C. F. Leitten, Jr., Preparation and Evaluation of Vapor-Deposited Tungsten, ORNL-3662 (August 1964).

connected with the development of gas bubbles (porosity) during annealing at high temperatures.[5] Many of the gas bubbles lie on grain boundaries, and it has been demonstrated that tensile stresses will cause these bubbles to grow at high temperatures.[6] Similarly, creep cracking in powder-metallurgy W has been shown to result from stress-induced linking of cavities at grain boundaries.[7]

In the making of a fusion weld, both stresses and high temperatures are involved, and when cracking is found in the weld metal or in the heat-affected zone in W it is invariably intergranular. It seemed reasonable to suppose, therefore, that the hot cracking observed in the CVD welds might result from stress-induced bubble growth just as it did in creep tests. Moreover other forms of W could possibly be subject to the same phenomenon since gas bubbles have been reported[8–10] in powder-metallurgy W and in arc-cast W. Therefore we made welds in sheets of chemically vapor deposited, powder-metallurgy, and vacuum-arc-melted W and examined them for porosity and cracking.

The sheets were in the wrought condition and were 0.050 to 0.060 in. thick. Full-penetration bead-on-plate welds were made by the tungsten inert-gas (TIG) process. The sheets were clamped on each side of the weld to simulate welding practice and impose stresses across the weld during cooling.

Optical examination of polished and etched sections across the welds showed that easily visible gas porosity (some bubbles up to 0.1 mm in diameter) occurred in all welds except in the arc-melted material.

---

[5]K. Farrell, J. T. Houston, and A. C. Schaffhauser, "The Growth of Grain Boundary Gas Bubbles in Chemically Vapor Deposited Tungsten," pp. 363–390 in Proceedings of the Conference on Chemical Vapor Deposition of Refractory Metals, Alloys and Compounds, Gatlinburg, Tennessee, September 12–14, 1967, ed. by A. C. Schaffhauser, American Nuclear Society, Hinsdale, Illinois.

[6]J. O. Stiegler, K. Farrell, and H. E. McCoy, J. Nucl. Mater. 25(3), 340–343 (1968).

[7]J. O. Stiegler, K. Farrell, B.T.M. Loh, and H. E. McCoy, ASM (Am. Soc. Metals) Trans. Quart. 60(3), 494–503 (September 1967).

[8]A. Wronski and A. Fourdeux, J. Less-Common Metals 8, 149 (1965).

[9]G. Das and S. V. Radcliffe, Trans. Met. Soc. AIME 242, 2191 (1968).

[10]P. A. Blenkinsop and P. H. Morton, J. Inst. Metals 96, 248 (1968).

The largest gas bubbles usually lay along the fusion line but were isolated from one another; finer bubbles were observed within the weld metal, but there was no obvious preference for grain boundaries. Only in the CVD material was porosity observed in the heat-affected zone, notably at grain boundaries. Very narrow cracks were noted at grain boundaries in the heat-affected zone in the CVD material and in the weld metal in the powder-metallurgy and arc-cast materials. These cracks were usually only one or two grain edges in length.

Electron fractography[5–7] confirmed that the large porosity on the fusion line and within the weld metal consisted of isolated gas bubbles that showed no preference for the grain boundary. The bubbles in the heat-affected zone in the CVD material were largest on those grain boundaries nearest the fusion line. The studies also revealed quite clearly that in all cases the cracks at the grain boundaries were caused by the linking of pores. The electron photomicrographs in Figs. 10.6 to 10.8 show some examples of these cracks and demonstrate the probable sequence of events during development of cracks. Figure 10.6(a) illustrates bubbles that have formed on the grain boundaries of CVD tungsten in the heat-affected zone close to the fusion line. Under the effects of stress and high temperature, bubbles on some favorably oriented boundaries grow into one another so that the boundary becomes wormholed or tunneled [Fig. 10.6(b)]. Finally the tunnels merge to form a continuous crack that advances over the face of the grain by consuming the bubbles in its path [Fig. 10.6(c)]. The same behavior seems to occur in powder-metallurgy W, and Fig. 10.7 shows small cracks forming at the grain boundaries in the weld metal. The development of cracks in arc-melted W is demonstrated in Fig. 10.8.

These studies appear to support the supposition that hot cracking in fusion welds in W is caused by stress-induced interconnection of grain-boundary porosity (gas bubbles). It is not known whether these findings are peculiar to W. If not, they may represent a new approach to our understanding of hot cracking in welds.

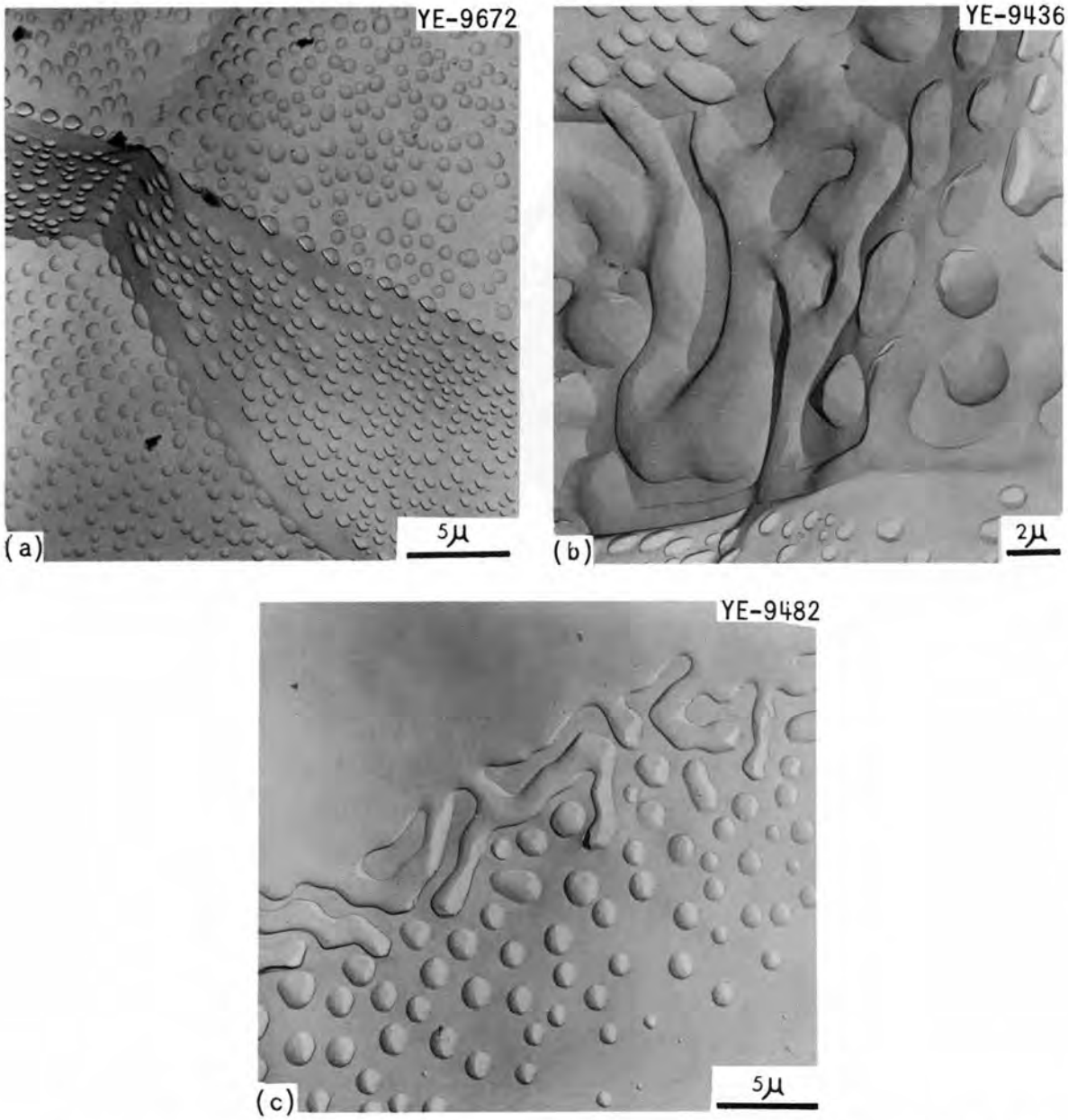

Fig. 10.6. Electron Fractograph Showing Development of Hot Cracking Along a Grain Boundary in the Heat-Affected Zone of Weld in CVD Tungsten. (a) Typical distribution of gas bubbles near fusion line. (b) Linking of bubbles to form tunnels on one grain boundary. Note that bubble coalescence is not apparent on all boundaries. (c) Merging of tunnels to form a narrow crack is complete in the upper half of the photograph. The crack is growing into the surviving bubbles in the lower half of the photograph.

Fig. 10.7. Hot Cracks Maturing on a Grain Boundary in the Weld Metal of Powder-Metallurgy Tungsten.

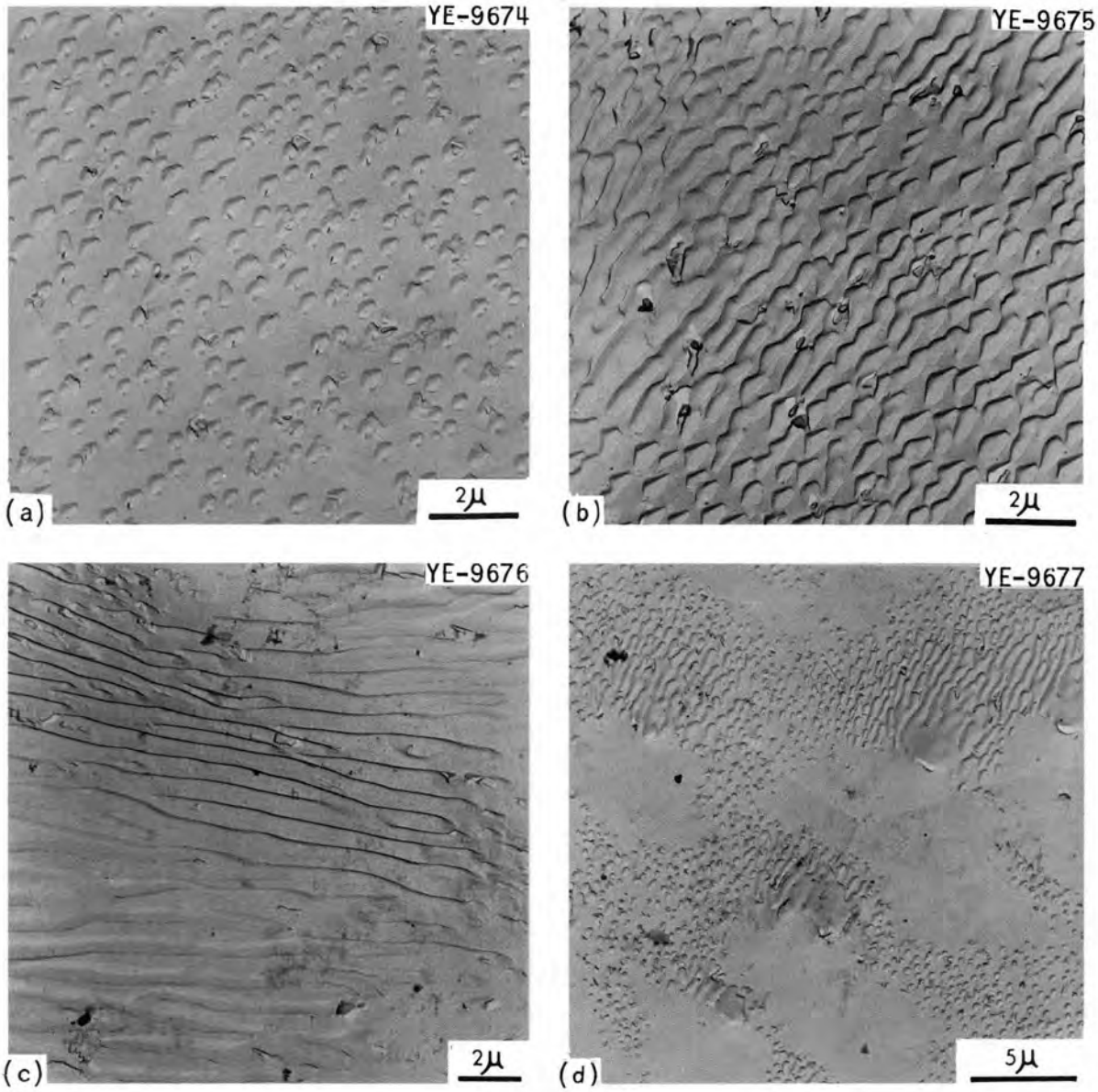

Fig. 10.8. Hot Cracking in Arc-Melted Tungsten Weld Metal. (a) Region of grain boundary showing a cluster of bubbles. (b) Bubbles are beginning to coalesce into tunnels. (c) Tunnel formation is complete. Merging of tunnels will form the crack. (d) Nonuniform distribution of bubbles with associated crack formation.

Long-Time Creep-Rupture Properties of Tungsten Alloys

R. L. Stephenson

We are continuing our comparison of the creep-rupture properties of arc-cast W, W–5% Re, W–26% Re, and W–25% Re–30% Mo. The stress-rupture data obtained for unalloyed W are plotted in Fig. 10.9. A computer program was used to determine the Larson-Miller constant by least-squares fitting. The master curve obtained was used to determine the isotherms shown on Fig. 10.9. At those temperatures where data exist, the computed curves are in good agreement with the data.

Data from the other alloys are being correlated. Preliminary results indicate that the large additions of elements with lower melting points (Re and Mo) decrease strength at longer times and higher temperatures.

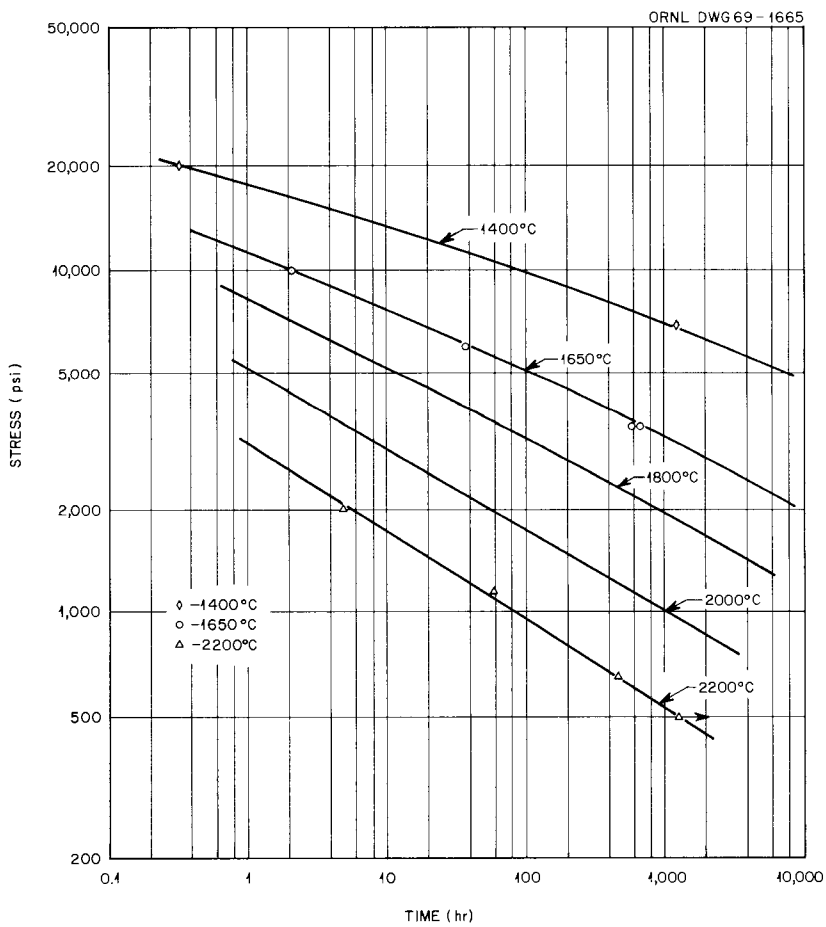

Fig. 10.9. Stress-Rupture Data for Unalloyed Tungsten Compared with Isotherms Derived from Larson-Miller Constant.

11. NONDESTRUCTIVE TEST DEVELOPMENT

W. O. Harms R. W. McClung

Our task is to develop new and improved methods of nondestructively testing reactor materials and components. We are studying various physical phenomena, developing instruments and other equipment, devising techniques, and designing and fabricating reference standards. Among the methods being studied for both normal and remote inspection are electromagnetics (with major emphasis on eddy currents), ultrasonics, penetrating radiation, and holography.

Electromagnetic Inspection Methods (Eddy Currents)

C. V. Dodd J. W. Luquire[1]
W. E. Deeds[1] W. G. Spoeri

We continued research and development on both analytical and empirical bases.

Analytical Studies

In our analytical research we are continuing to derive integral equations for problems of interest and are using our computer programs to provide numerical solutions directly applicable to actual eddy-current tests.

One practical goal is to optimize the design of eddy-current coils for tubing inspection. We began with the case of a coil encircling a tube and calculated the signal due to a defect on the inner surface of the tube directly under the coil. This is the defect farthest from the coil and thus in principle the most difficult to detect. We have varied both the product of frequency, conductivity, and permeability and the wall thickness of the tubing to produce the family of curves shown in Fig. 11.1. This figure shows that for a given wall thickness and type of tubing there is an optimum operating frequency for maximum sensitivity to defects on the inner surface of the tubing. We then selected the minimum thickness and one of the thicker sections and varied the dimensions of

[1]Consultant from the University of Tennessee.

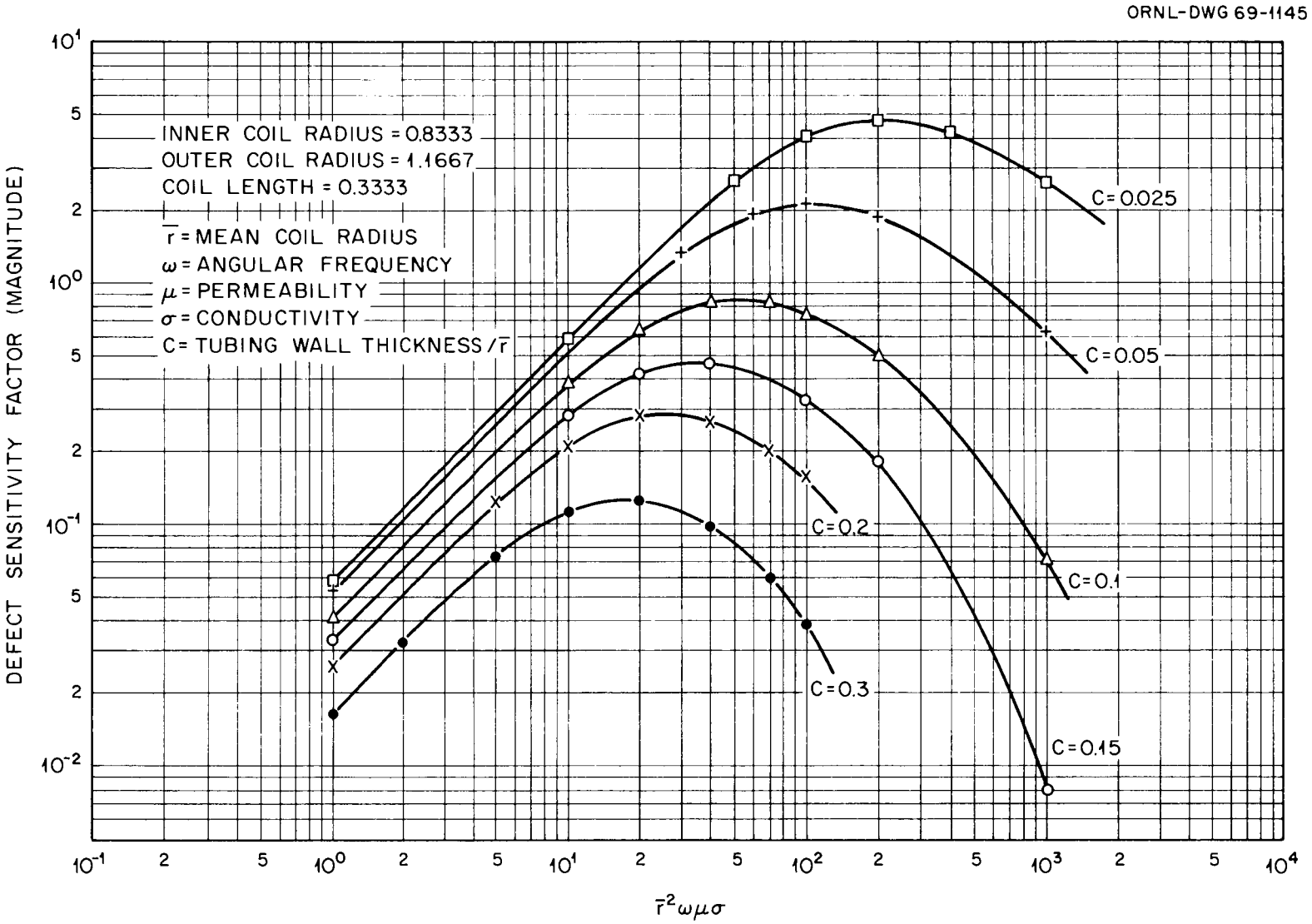

Fig. 11.1. Curves Showing Sensitivity to Defects on the Inner Surface of Tubing as Wall Thickness and Other Test Conditions Vary.

the coil, as shown in Fig. 11.2. While the sensitivity varies with the shape of the coil, the coils still have their maximum sensitivity at the same frequency. We are now studying the effective field size of differential coil systems as a function of intercoil spacing and coil dimensions. These studies should lead to more sensitive eddy-current tests.

Probe Development (C. V. Dodd)

Since the key component in any eddy-current testing device is the probe containing the transmitting and receiving coils, we are developing improved procedures for making precision coils. The effective diameter of the coil is important because of its relation to the ability of the instrument to detect small discontinuities and to resolve the response from a small discontinuity near other discontinuities. Figure 11.3 shows the relative size of three of the coils that are necessary to make a high-resolution probe assembly for our phase-sensitive eddy-current instrument. The two smaller detector coils on the plastic form are 0.016 in. in inner diameter by 0.024 in. in outer diameter by 0.016 in. long; the "large" transmitter coil alongside is 0.028 in. in inner diameter, 0.032 in. in outer diameter, and 0.137 in. long. It will be assembled coaxially around the detector coils and inserted into the shielded probe shown in Fig. 11.4. The wire used for winding the coils is only 0.0006 in. in diameter.

Ultrasonic Inspection Methods

H. L. Whaley K. V. Cook

Optical Visualization of Ultrasound

A new ultrasonic immersion tank with 3/8-in.-thick Pyrex walls was fabricated and installed in the mirror schlieren system to eliminate the problem of bending of the glass walls due to the weight of the water, which occurred in the old tank with 1/8-in.-thick walls. The new tank was designed to allow us to manipulate the specimen into the desired orientation relative to the transducer. Cross-feed parts and a milling attachment from a small lathe were mounted on the tank and altered to

ORNL-DWG 69-1146

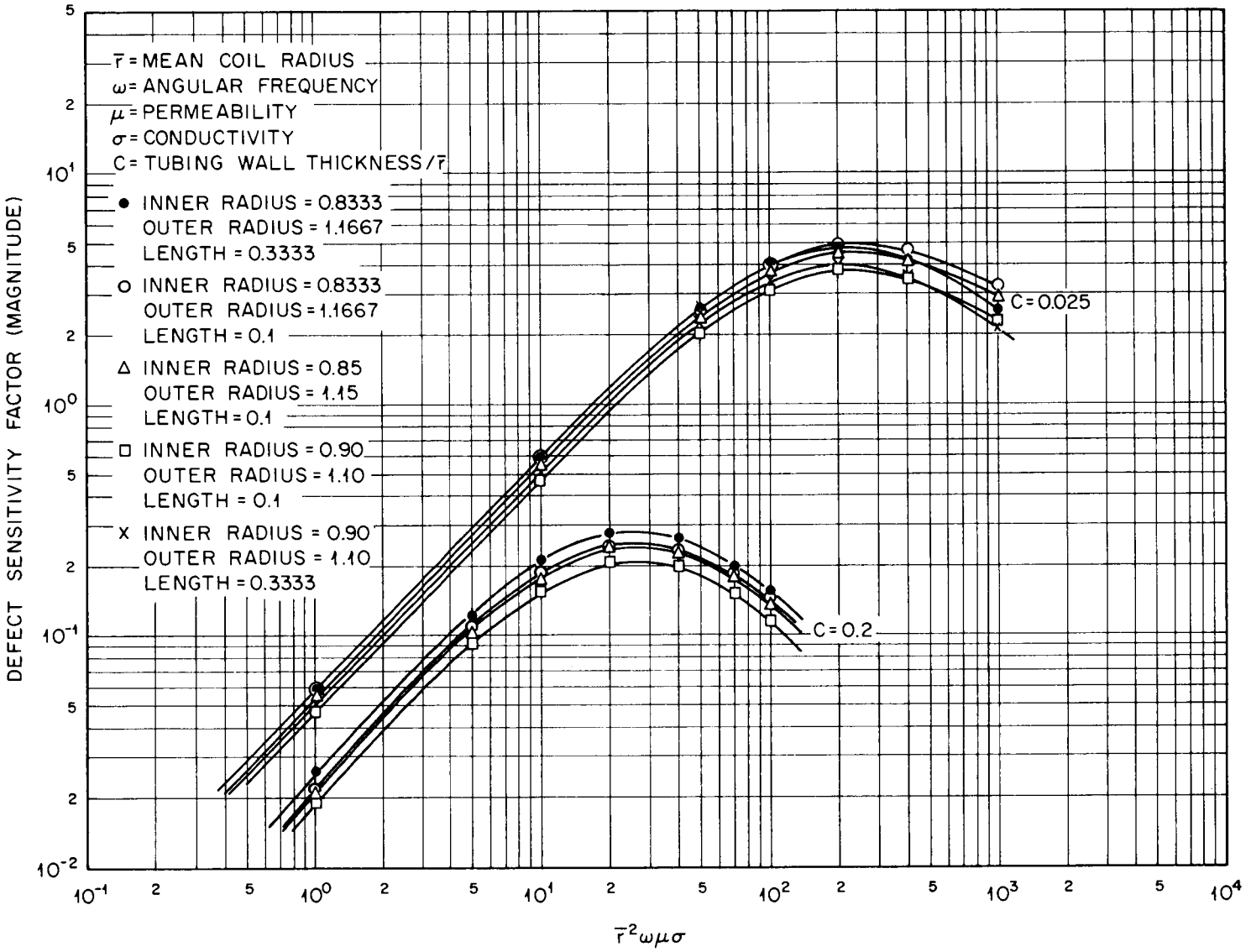

Fig. 11.2. Curves Showing Sensitivity to Defects on the Inner Surface of Tubing for Two Wall Thicknesses and Variable Coil Shapes.

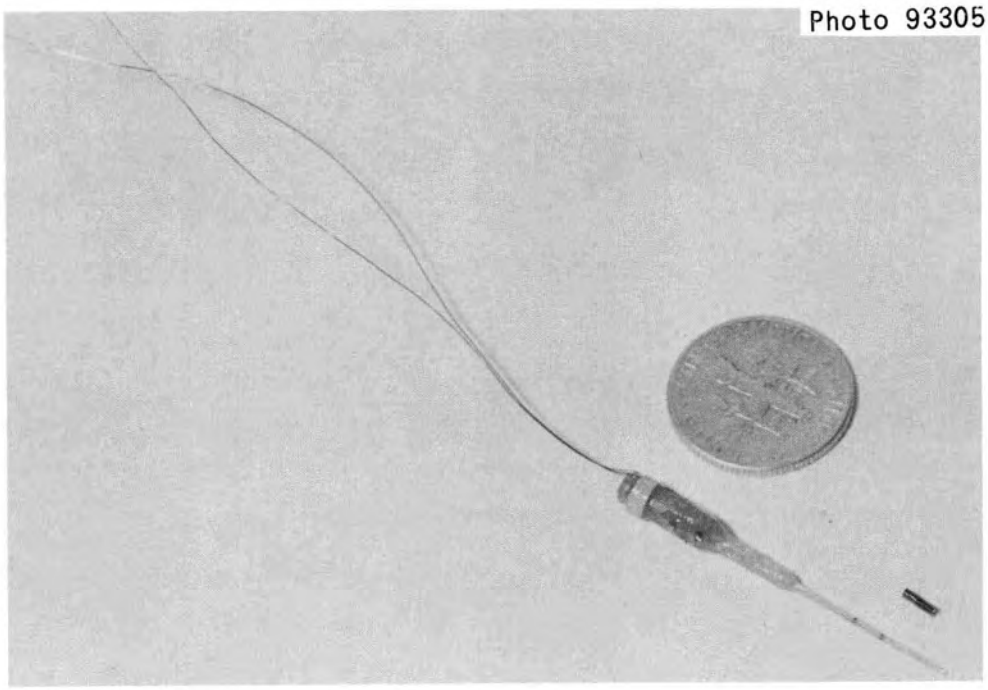

Fig. 11.3. Disassembled View of Three Tiny Coils for a High-Resolution Probe for the Phase-Sensitive Eddy-Current Instrument.

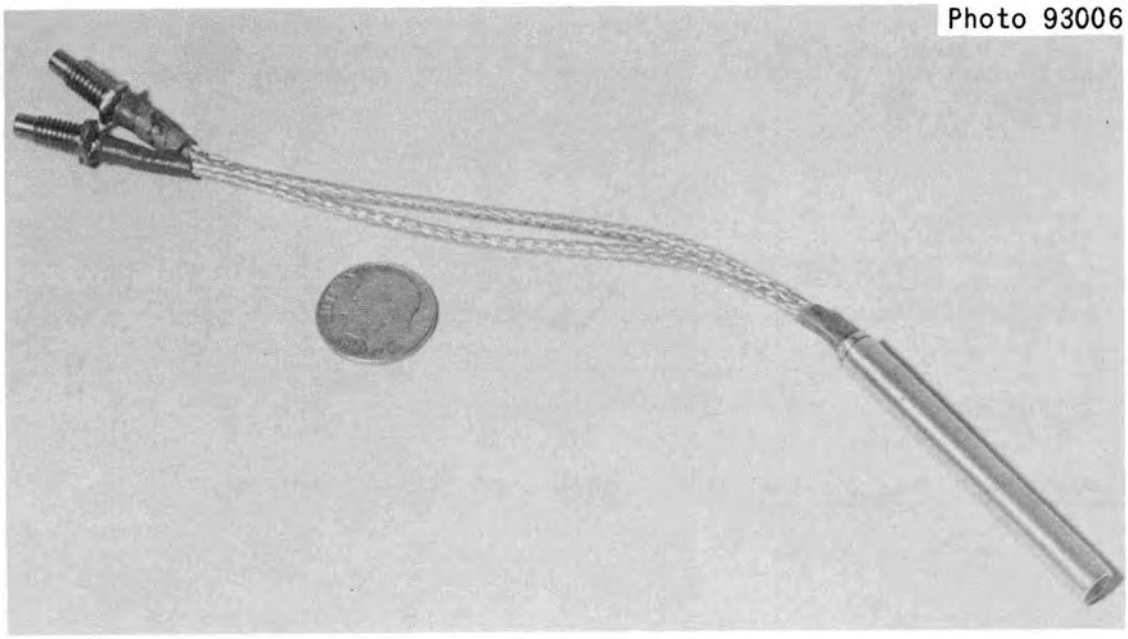

Fig. 11.4. Assembled High-Resolution Probe for the Phase-Sensitive Eddy-Current Instrument.

allow the sample to be moved vertically, angled with respect to the light beam, and rotated with respect to a vertical axis. These improvements now allow reproducible mechanical positioning of specimens.

Frequency Analysis

We have concentrated our investigation in four main areas this period: (1) determining the effects of certain tuning variables in the transducer circuit; (2) determining the effect of the size of a discontinuity in a metal plate on the frequency spectrum of a reflected ultrasonic pulse; (3) developing a method for determining the relative energy in a spectrum between any two frequency limits; and (4) improving the capability of the system for analyzing small signals.

Tuning Variables

It is common to employ various tuning networks (e.g., tunable radio-frequency coils) in the transducer circuit of an ultrasonic test system to improve sensitivity. These coils affect the impedance of the circuit, the shape of the excitation pulse, and thus the frequency spectrum of the transducer. Since these effects are quite complicated, we wanted to be able to observe them directly with the aid of the frequency-analysis system.

We compared the spectra of the electric excitation pulse and the corresponding transmitted ultrasonic pulse for various types of tuning. One type of tuning coil we observed produced broad-banded frequency spectra while another produced narrow-banded spectra with well defined harmonics. By observing the resultant spectrum, we can now tune the system for peak response at the desired frequency.

Spectra Affected by Discontinuities

Attempts to compare directly the spectra reflected from three sizes (8/64-, 5/64-, and 3/64-in. diam) of flat-bottomed holes drilled in an aluminum plate were unsuccessful because the signals were too small for analysis with the existing system. Instead, we analyzed pulses modified by the presence of the flaw and reflected from the rear surface of the plate. The flat, reflecting bottom of the hole was about 1 in. from the

entry surface of the 1.5-in. plate. Since the 5-MHz, 0.75-in.-diam transducer was larger than the holes, the signals from the rear surface at the hole sites were essentially equal in overall amplitude. We noted, however, a reproducible difference in the shapes of the frequency spectra of the three pulses. These spectra were displayed between 1 and 6 MHz, and the greatest differences were between 3 and 5 MHz, where the amplitude of the spectrum decreased with decreasing hole size (see Fig. 11.5). At these frequencies, the ultrasonic wavelength is in the

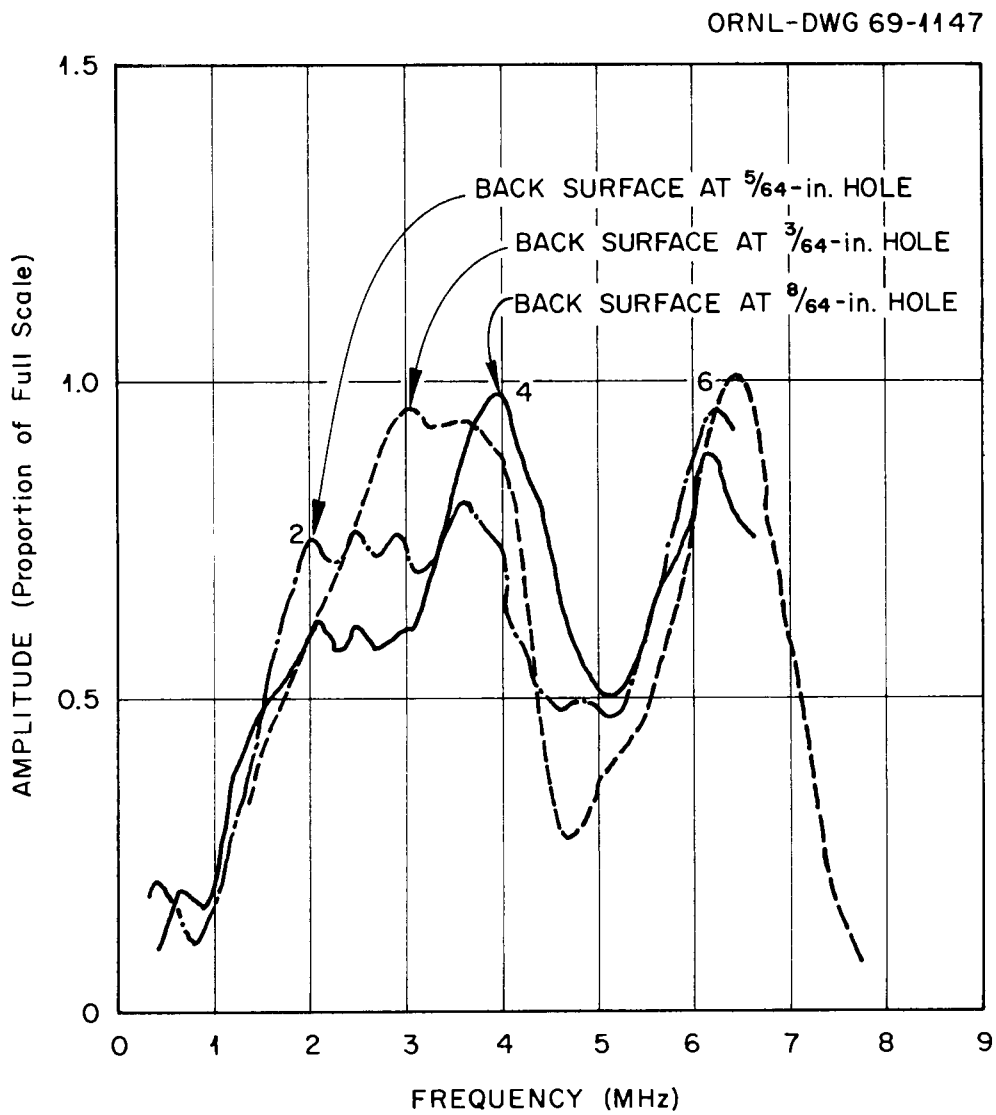

Fig. 11.5. Ultrasonic Frequency Spectral Differences in Rear-Surface Reflections Produced by Internal Flaws of Different Sizes.

same range as the hole diameters. We also used a flat 0.75-in.-diam 15-MHz transducer, and the spectra from about 12 to 18 MHz were displayed for the rear surface as affected by the three holes. These appeared to be identical. At these higher frequencies, the ultrasonic wavelength is only one-fifth as large as the hole diameter. In this case, the reflection from the 8/64-in.-diam hole itself could be analyzed, and it exhibited the same spectra as that from the rear surface.

Integration of Spectral Energies

Since it is difficult to observe several spectra in succession and evaluate their differences, we devised a simple circuit that integrates the output of the analyzer to give a single value (which we can read from a digital voltmeter) that is directly proportional to the area (or average amplitude) under a spectrum envelope. Thus, we can now quickly obtain a single value that contains information about the total intensity between preselected frequencies. This will allow us to compare spectra of different shapes and observe frequency-dependent effects even though identical amplitude may be indicated with conventional instrumentation.

We applied this integrating technique to the situation discussed above, that of examining reflections from the rear surface of a plate at the sites of drilled holes of three sizes. A qualitative difference had been detected by the usual method of observing the spectra, but the integrating technique demonstrated a quantitative difference in the spectra. Table 11.1 illustrates how greater sensitivity and discrimination of flaw size can be obtained by selecting the area of the spectrum with the greatest differences and narrowing the frequency range to this area.

System Improvements

The ability of the frequency-analysis system to work with smaller signals was also very significantly improved this period in two ways. First, circuit changes in the mixers that control the gating of the signal reduced the noise to a level far below that of pulses reflected directly from drilled reference holes. Second, the addition of a second preamplifier further amplified (10×) the small signals of interest. It

Table 11.1. Effect of Different Bandwidths on Integrated Intensity of Ultrasonic Response from Flat-Bottomed Reference Holes

Hole Diameter (in.)	Digital Voltmeter Reading		
	4.5-MHz Center Frequency and 6-MHz Sweep Width	4.5-MHz Center Frequency and 3-MHz Sweep Width	4.27-MHz Center Frequency and 1.05-MHz Sweep Width
8/64	9.46	11.90	10.60
5/64	8.80	10.95	8.50
3/64	8.40	10.35	6.60

was necessary to use a second mixer between the preamplifiers for isolation and to screen out larger pulses. Now, signals 20 db smaller than that from the 3/64-in.-diam hole can be analyzed with the 5-MHz transducer described above. The changes of frequency spectrum that we can now see are a direct function of hole size; all other reflections are screened out and ignored. Figure 11.6 is the current block diagram of the frequency-analysis system.

Penetrating Radiation and Holographic Inspection Methods

B. E. Foster S. D. Snyder T. Eck[2]

Radiation Attenuation Studies[3]

In our development of x-ray attenuation as well as in our studies of radiographic densitometry, it was often quite difficult to fit the correct curve for the many data points. Therefore we developed computer programs for a time-sharing computer to provide representative curves in fifth-degree polynomial form by a least-squares fit. We have developed programs for the following:

1. uranium content versus x-ray attenuation (used for homogeneity calibration curves and data evaluation),
2. fuel concentration versus distance from edge of core (used for evaluation of core loading), and
3. aluminum thickness versus film density (used for radiographic-densitometry calibration curves and evaluations of "dogboning" or excess fuel concentration at the ends of fuel cores).

Radiation Scattering Studies[3] (B. E. Foster, S. D. Snyder)

We have begun preliminary investigations into the use of Compton backscattered radiation for measuring the thickness of the coatings or claddings on reactor components. We built an on-axis unfocused

---

[2] Summer student sponsored by Oak Ridge Associated Universities.

[3] These studies are also of interest to the aluminum technology programs and are partially funded by them.

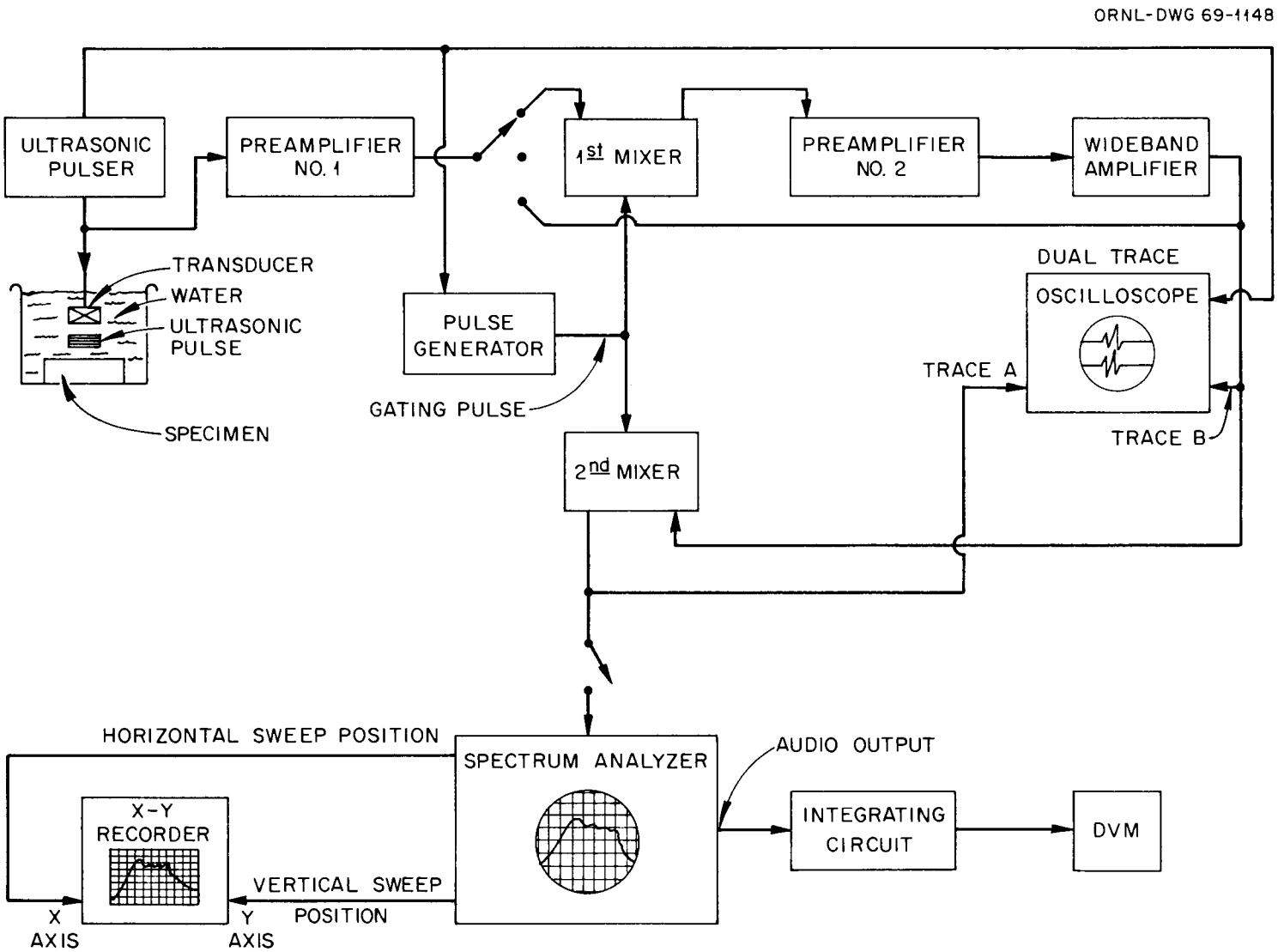

Fig. 11.6. Block Diagram of the Ultrasonic Frequency-Analysis System.

collimator to be used with an isotopic source of radiation and a NaI(Tl) crystal-photomultiplier detector. The important design feature of this collimator is that the angle between the source axis and the detector axis can be varied from about 35 to 45° with the intersection of the two axes always remaining at the same point. This allows us to adjust the scattering angle for maximum intensity at the detector. The detector signal is processed with a 1600 channel analyzer that allows us to determine the intensities of the various energies in the radiation spectra.

12. JOINING RESEARCH ON NUCLEAR MATERIALS

G. M. Adamson, Jr. G. M. Slaughter

The purpose of this program is to gather fundamental and applied data needed for a better understanding of the weldability of materials that are either being considered or now used for nuclear applications. The fundamental aspects of the program are concerned with the effects of minor variations in amount and type of alloying elements and impurities on the behavior of weldments. Special alloys of interest are the austenitic stainless steels and the nickel-rich alloys such as Incoloy 800 and Inconel 600.

Our applied studies emphasize the application of stainless steels in the Fast Flux Test Facility (FFTF). These project-oriented investigations will help define the influence of welding process, variables, and postweld treatments on the microstructure and mechanical properties of irradiated and unirradiated weldments. A modest program concerned with the influence of weld defects will provide base-line results in this much-talked-about but little-investigated field.

We hope this broad-based research will develop the modifications in both chemical analysis and procedures necessary to produce the high-quality weldments needed for the various programs of the Commission. These data will be immediately and directly applicable to such components as the Fast Test Reactor vessel by providing the capability for predicting the effects of chemical composition and welding procedure on overall welding behavior.

The Effect of Minor Variations in Chemical Composition on Weldability

Our continuing investigation of the effect of minor variations in the quantity of those elements usually present in small quantities in structural materials has included Incoloy 800, Inconel 600, and stainless steel.

Effect of Minor Elements on the Hot Ductility of Inconel 600
(D. A. Canonico, W. J. Werner)

Our investigation of the effects of minor quantities of incidental elements on the weldability of Inconel 600 is continuing. We have already discussed the effects of S and P on the hot ductility of specially prepared experimental alloys.[1] As before, the weldability evaluations reported here apply to the heat-affected zone and are based on hot-ductility data obtained with the Duffers Gleeble.[2] We discuss the on-heating results obtained with the alloys contaminated with the maximum amounts used in this program of S, P, and combined S and P. We have also investigated the effect of Mn on alloys nominally containing 0.010% S. For comparison, we have included data for the ternary alloy (600-1) and the nominal Inconel 600 composition (600-2).

Figure 12.1 contains the on-heating data obtained for the alloys contaminated with S, P, and both S and P. The ternary alloy 600-1 maintains a high level of ductility to within 30°C of its zero ductility temperature (ZDT). The presence of those elements (at representative compositional levels) usually found in Inconel 600 did tend to reduce, rather dramatically, the hot-ductility properties. This response (alloy 600-2) can be seen in Fig. 12.1. The presence of 0.012% S (alloy 600-5) caused a sharp reduction in both the hot ductility and ZDT of Inconel 600. It has the most deleterious effect of those elements shown in the data in Fig. 12.1. The presence of P did not have a deleterious effect, and, indeed, the data indicate that it actually improved the hot ductility of Inconel 600 between 1095 and 1260°C. The presence of P and S (alloy 600-11) resulted in an improved alloy (as compared to alloy 600-5); however, this effect may be attributable to the lower content of S (0.006 rather than 0.012%).

Figure 12.2 shows the effect of Mn on the hot ductility of Inconel 600 when it is heated. Again, the ternary alloy (alloy 600-1) and the nominal composition (alloy 600-2), which contains 0.11% Mn, are

---

[1]D. A. Canonico and W. J. Werner, Fuels and Materials Development Program Quart. Progr. Rept. June 30, 1968, ORNL-4330, pp. 307–309.

[2]Duffers Associates, Inc., Troy, New York.

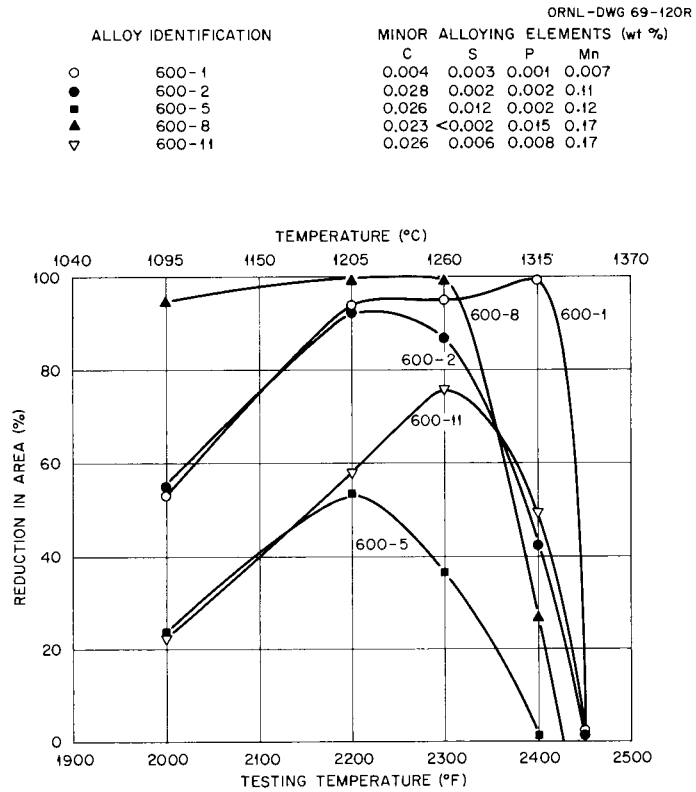

Fig. 12.1. Results of the On-Heating Hot-Ductility Tests of Selected Alloys. The alloying elements shown above were added to the basic composition Ni—15.7 to 16.1% Cr—8.13 to 10.4% Fe. Alloys 600-2, -5, -8, and -11 also nominally contained < 0.05% Al—0.2% Si— < 0.01% Ti—0.26% Cu.

included for comparison. To the nominal alloy that contained about 0.010% S (alloy 600-4 in Fig. 12.2) we added 0.15% Mn. The hot ductility of this alloy is nearly identical to that of alloy 600-5, shown in Fig. 12.1; this undoubtedly can be attributed to their similar sulfur levels (0.010 and 0.012%). Increasing the Mn to 0.32% (alloy 600-12) improved the hot ductility at 1260°C. Higher levels of Mn, 0.48 (alloy 600-13) and 0.84% (alloy 600-14), tended to reduce the hot ductility at 1205°C (from about 55 to 45%) and had little effect on the ductility at 1260°C and, if anything, a deleterious effect on the ZDT.

In summary, the presence of those elements normally found in Inconel 600 decreased the hot ductility of the simulated heat-affected zone as the ZDT was approached. Sulfur had by far the most deleterious effect on both the hot ductility and ZDT of Inconel 600. Adding Mn to an alloy containing S did not significantly improve its high-temperature

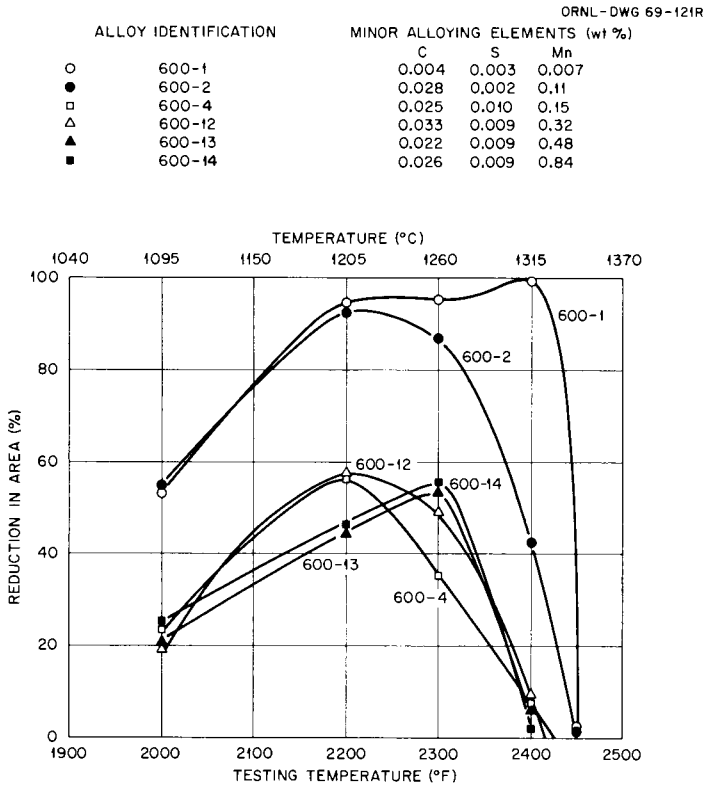

Fig. 12.2. Results of On-Heating Hot-Ductility Test Showing the Effect of Manganese in the Presence of About 0.010% S. The alloying elements shown above were added to the basic composition Ni–15.5 to 16.1% Cr–8.04 to 9.05% Fe–0.001 to 0.002% P. Alloys 600-2, -4, -12, -13, and -14 also nominally contained < 0.05% Al–0.2% Si– < 0.01% Ti–0.26% Cu.

properties or its ZDT. Indeed, a critical review of the data could lead to the conclusion that the presence of Mn is somewhat detrimental. Of the three elements investigated, P proved the least detrimental and, indeed, advantageous, particularly at the lower temperatures used in this study.

Effect of Certain Minor Elements on the Intermediate Temperature Ductility of Incoloy 800 (W. J. Werner)

Our studies to date on the joining of nuclear materials have been directly concerned with the effect of minor elements on the weldability of alloys containing Ni. We have used both the Duffers Gleeble and the VARESTRAINT[3] tests. For the VARESTRAINT test, the metal is

[3]W. F. Savage and C. D. Lundin, Welding J. (N.Y.) 44(10), 433s–442s (1965).

actually melted. It tests the weld-metal in terms of crack length after the weld puddle has been strained a known amount. The Duffers Gleeble evaluates the heat-affected zone of an alloy in terms of loss of ductility (reduction in area) or loss of strength. A specimen is subjected to a thermal excursion simulating that of the heat-affected zone of a weldment and then fractured at high temperatures. Both the ZDT and zero strength temperature (ZST) are measures of weldability.

Another important factor that influences the behavior of a weldment is its intermediate-temperature ductility. It is established that materials rich in Ni lose ductility between 760 and 870°C. Since this loss of ductility can also contribute to the cracking propensity of a weldment rich in Ni, we have begun a study of the effect of exposure at these temperatures.

To complement our studies on Incoloy 800, we began our studies of the ductility of this alloy at intermediate temperatures. The tensile properties of several of the special Incoloy 800 alloys, which had previously been tested by VARESTRAINT and the Duffers Gleeble,[4] were determined as a function of testing temperature at a strain rate of 0.002 min^{-1} with an Instron Universal Testing Machine. The nominal and actual compositions of the special alloys tested to date are shown in Table 12.1. Alloys with various amounts of Al and Ti were chosen for study because of the probable (but undetermined) major influence of these elements on the mechanical properties at intermediate temperatures. Alloys containing the residuals S and P were chosen for study since it had already been shown that these elements can have a major effect on the propensity toward hot cracking in this alloy system. Small button-bead specimens with a 1/8-in.-diam gage section were tested for tensile strength at elevated temperatures in Ar. Before testing, the specimens were given a solution heat treatment at 1150°C for 1 hr in Ar. This is the standard mill

---

[4]D. A. Canonico, W. F. Savage, W. J. Werner, and G. M. Goodwin, "Effects of Minor Additions on the Weldability of Incoloy 800," to be published in a monograph by the Welding Research Council.

Table 12.1. Nominal and Actual Compositions of Experimental Incoloy 800 Alloys

Alloy Designation		Composition (wt %)														Composition (ppm)	
		Ni	Cr	Fe	C	H	N	O	S	P	Si	Al	Mn	Cu	Ti	B	Pb
CVO 53	Nominal	32.5	21.0	bal													
	Actual	32.9	21.2	46.3	0.007	0.0004	0.0026	0.013	0.004	0.002	0.03	< 0.05	0.02	< 0.01	< 0.01	4	< 0.2
CVO 176	Nominal	32.5	21.0	bal								0.38			0.38		
	Actual	33.8	21.2	43.9	0.007	0.0005	0.0008	0.018	0.002	0.001	0.02	0.43	0.03	< 0.01	0.44	< 0.2	< 0.2
CVO 185	Nominal	32.5	21.0						0.015			0.38			0.38		
	Actual	32.0	21.3	44.9	0.006	0.0014	0.019	0.022	0.010	0.001	< 0.1	0.30	< 0.005	< 0.01	0.33	0.3	< 0.2
CVO 188	Nominal	32.5	21.0							0.015		0.38			0.38		
	Actual	32.5	21.3	45.4	0.007	0.0002	0.0009	0.0083	0.002	0.010	0.05	0.34	0.07	< 0.01	0.38	0.2	< 0.2
CVO 191	Nominal	32.5	21.0						0.015	0.015		0.38			0.38		
	Actual	32.5	21.6	44.8	0.006	0.0003	0.0018	0.020	0.010	0.013	< 0.01	0.40	< 0.005	0.015	0.40	< 0.2	< 0.2
CVO 208	Nominal	32.5	21.0												0.38		
	Actual	34.0	20.6	44.4	0.010	0.0001	0.0018	0.0065	0.002	0.004	0.01	< 0.03	0.01	0.002	0.30	< 0.2	< 0.2
CVO 209	Nominal	32.5	21.0									0.38					
	Actual	32.4	21.8	45.4	0.005	0.0004	0.0018	0.0018	< 0.002	0.004	< 0.01	0.33	0.001	0.0005	< 0.01	< 0.2	< 0.2
CVO 235	Nominal	32.5	21.0						0.015								
	Actual	36.2	20.8	43.3	0.003	0.0003	0.0037	0.023	0.016	0.005	0.01	< 0.03	0.0003	0.0005	< 0.01	< 0.2	< 0.2
CVO 236	Nominal	32.5	21.0							0.015							
	Actual	37.3	20.2	42.7	0.004	0.0003	0.0038	0.021	0.005	0.017	0.02	< 0.03	0.01	0.002	0.03	< 0.2	< 0.2

anneal for Incoloy 800 as designated in the ASME Boiler and Pressure Vessel Code.[5]

The ductility of the special Incoloy 800 alloys as a function of test temperature is shown in Fig. 12.3. The figure also contains, as a reference, data on a commercial heat of Incoloy 800. Values for reduction in area were plotted as a measure of ductility, since they tend to be least affected by crack propagation and enlargement. Inspection of Fig. 12.3 shows that the special alloys can be separated immediately into two classes: (1) those that exhibit a ductility minimum at an intermediate temperature and then recover ductility at elevated temperatures, and (2) those that exhibit a continuous decrease in ductility with increasing test temperature. All of the special alloys that recovered ductility at elevated temperatures contained about 0.40 wt % Ti.

We tested commercial Incoloy 800 at a strain rate of 0.05 min^{-1} as compared to 0.002 min^{-1} for the special alloys. The faster strain rate tended to diminish the ductility minimum at intermediate temperature and shift the entire curve up the temperature scale. Although this particular commercial heat of alloy exhibited a ductility minimum, the material still had more than adequate ductility for application at intermediate and elevated temperatures (greater than 30% reduction in area at the minimum).

Load-extension curves typical of the two classes of special alloys are shown in Figs. 12.4 and 12.5. Close inspection of the data shows that the engineering uniform strain and elongation follow the same pattern of minimum ductility at an intermediate temperature minimum as do the data for reduction in area. This was true for all of the alloys tested, including the commercial material.

Figure 12.6 shows the ultimate tensile strength of the materials tested dependent on temperature. As expected, the more complex special alloys tend to have higher strengths. The great difference between the strengths of the commercial material and the special alloys is probably

---

[5]Case 1325-4, pp. 257–260 in 1968 ASME Boiler and Pressure Vessel Code Case Interpretations, The American Society of Mechanical Engineers, New York, 1968.

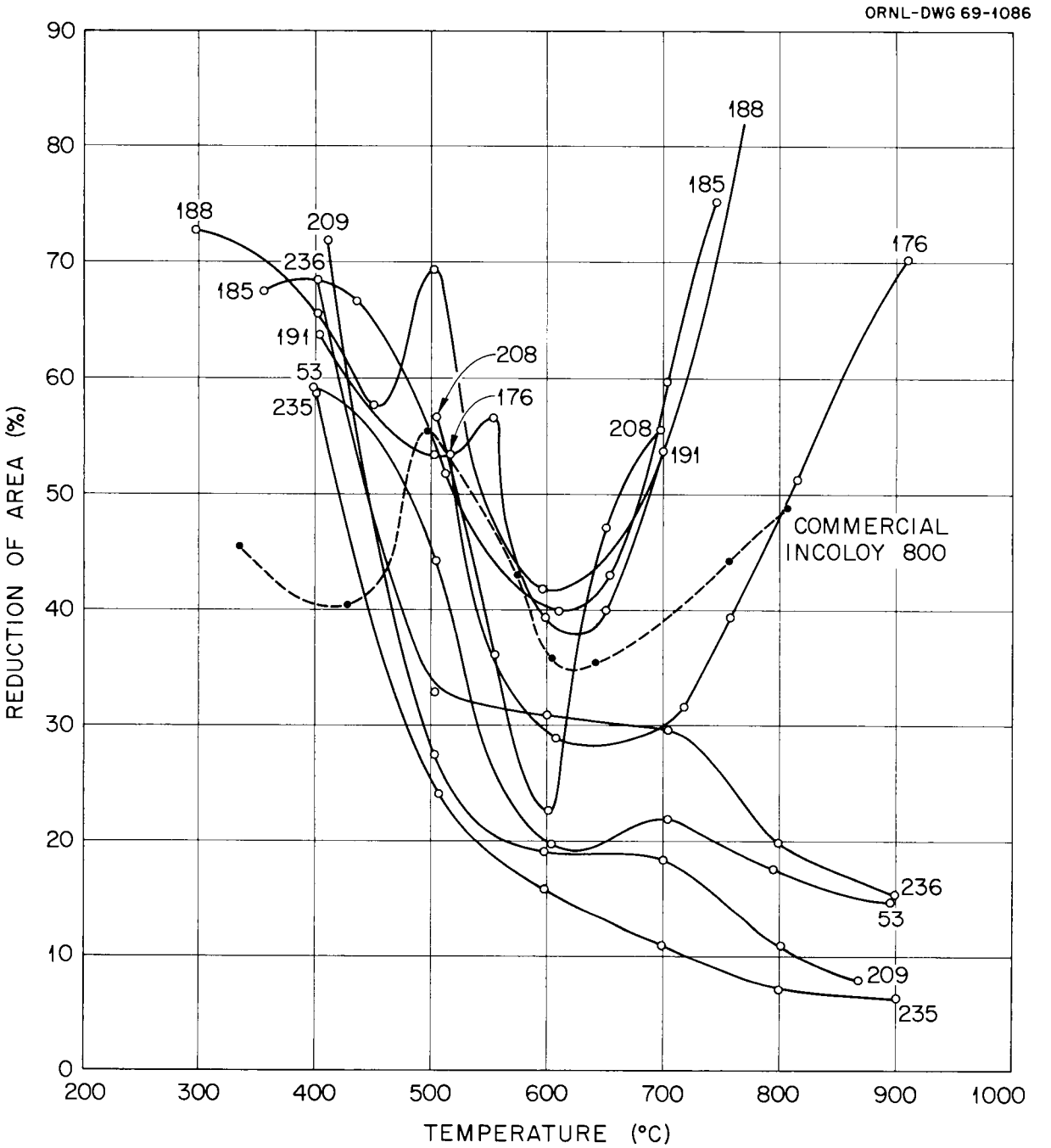

Fig. 12.3. Ductility of the Special Incoloy 800 Alloys and a Commercial Heat of Incoloy 800 as a Function of Testing Temperature.

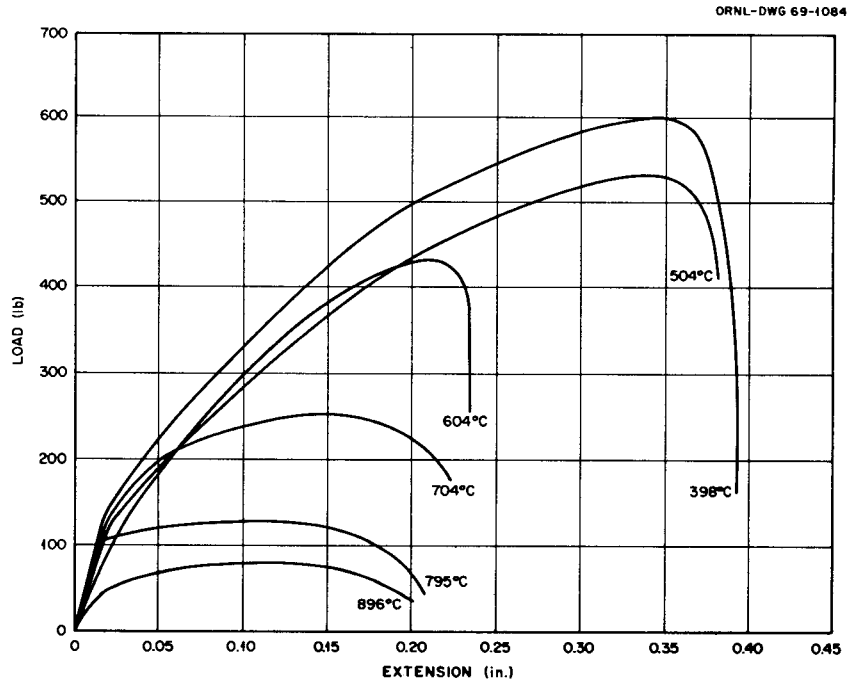

Fig. 12.4. Typical Load-Versus-Extension Curves for a Titanium-Free Alloy.

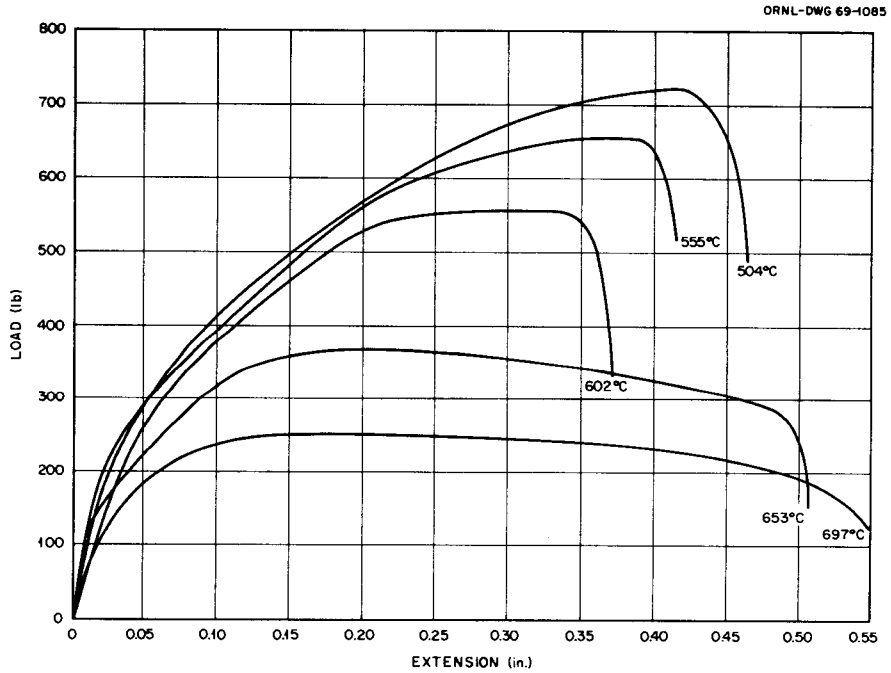

Fig. 12.5. Typical Load-Versus-Extension Curves for a Titanium-Bearing Alloy.

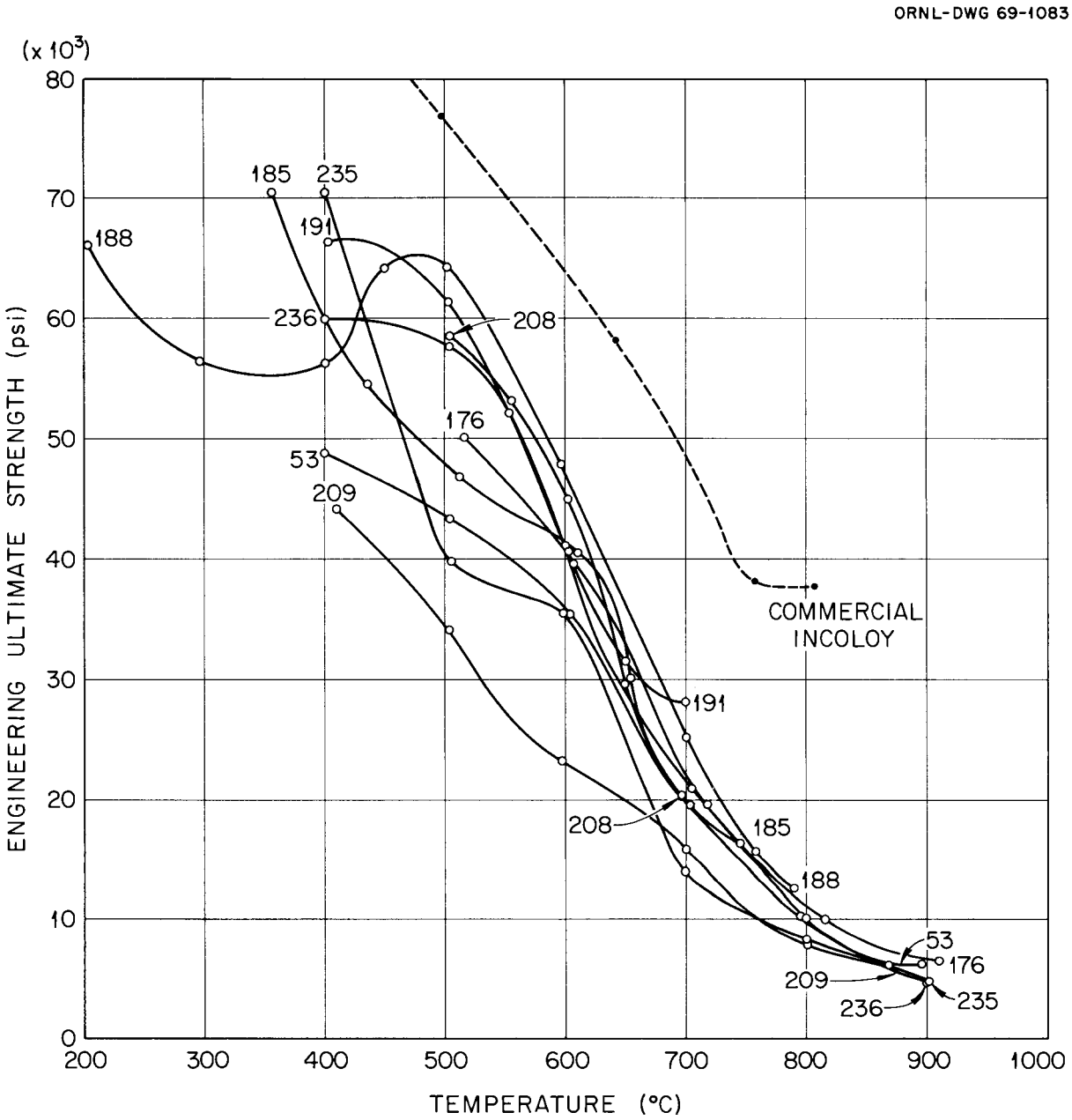

Fig. 12.6. Temperature Dependence of the Ultimate Tensile Strength of the Special Incoloy 800 Alloys and a Commercial Heat of Incoloy 800.

due to a combination of purity, melting practice, and fabrication practice.

We are trying to relate microstructural characteristics to these differences in mechanical properties.

Weldability of 18% Cr–8% Ni Class Stainless Steels (W. J. Werner, D. A. Canonico)

The eight special alloys of type 308L stainless steel that were mentioned in the last report[6] have been melted and made into plate. Samples of each heat (as rolled) have been submitted for chemical and metallographic analyses.

Development of Welding Procedures for Commercial and Modified Alloys

Our objective is to develop welding information that can be directly applied to the fabrication of a particular component. We are now gathering data required in support of the FFTF primary containment vessel, information about welding *per se* and the properties of both unirradiated and irradiated weldments.

Joining Development in Support of Fast Flux Test Facility (G. M. Goodwin)

Representatives from ORNL, Battelle Northwest, and the Division of Reactor Development and Technology met at ORNL on October 1, 1968. This group selected for investigation the following combinations of welding processes and filler wires:

1. submerged-arc welding with type 308 stainless steel filler metal,
2. gas metal-arc (GMA) welding with type 308L stainless steel filler metal,
3. shielded metal-arc (SMA) welding with 16% Cr–8% Ni–2% Mo filler metal.

---

[6]W. J. Werner and D. A. Canonico, Fuels and Materials Development Program Quart. Progr. Rept. Sept. 30, 1968, ORNL-4350, pp. 253–254.

It was decided that ORNL would prepare 125 specimens from each of these combinations and that Battelle Northwest would study the irradiation behavior and mechanical properties of these specimens.

The first shipment of specimens was sent to Battelle Northwest on December 12, 1968. The 130 specimens were all prepared by submerged-arc welding with type 308 stainless steel filler metal by the procedure outlined below:

1. The 1-in.-thick plate of type 304 stainless steel received from Battelle Northwest was sectioned, as shown in Fig. 12.7, by the plasma-arc process, which produces a heat-affected zone less than 1/8-in. deep on either side of the cutting plane. In the subsequent preparation for the joint, we removed at least 1/8 in. of material from these cut surfaces.

2. We machined the 23 3/4-in. edges of each of the six pieces to the shape shown in Fig. 12.8. We were careful to minimize heating of the joint surfaces and, after machining them, to remove all traces of lubricant, crayon marks, et cetera.

3. After we thoroughly cleaned and degreased the surfaces, we made two submerged-arc welds:

   a. Two of the plate sections were clamped to a 1-in.-thick strongback of type 304 stainless steel and carefully aligned with a 1/8-in. root opening.

   b. The root pass and each of the subsequent passes were made under the following welding conditions:

Current, ac	600 amp
Voltage	35 to 37
Travel speed, in./min	18
Wire stickout, in.	1 1/2
Wire	5/32-in.-diam type 308 stainless steel, Arcos heat No. E9470F308
Flux	Arcosite S-4, Lot 8H5F
Power supply	Linde type CAC-1500

c. After the root pass, we removed the clamps holding the weld pieces to the strongback to minimize residual stresses in the resulting weldment. We removed flux between passes by chipping and wire brushing. About 14 passes were required to complete each of the two welds at an interpass temperature < 177° C.

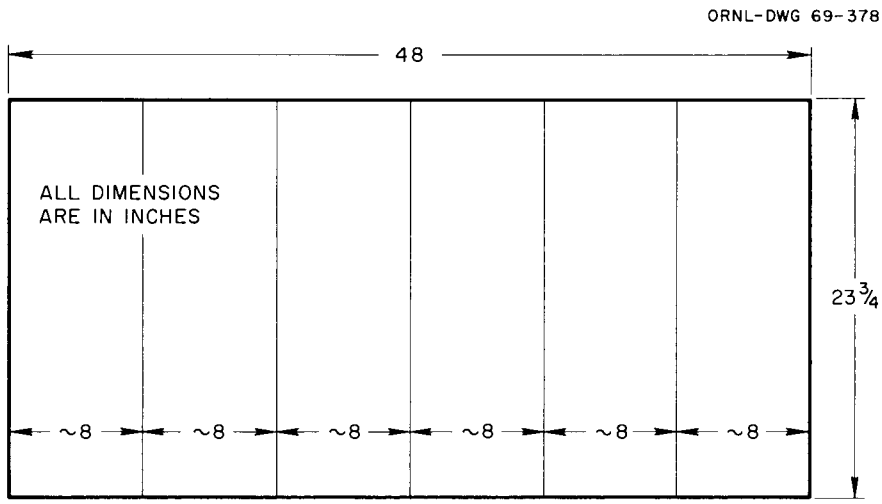

Fig. 12.7. One-Inch-Thick Type 304 Stainless Steel Plate – Initial Cuts.

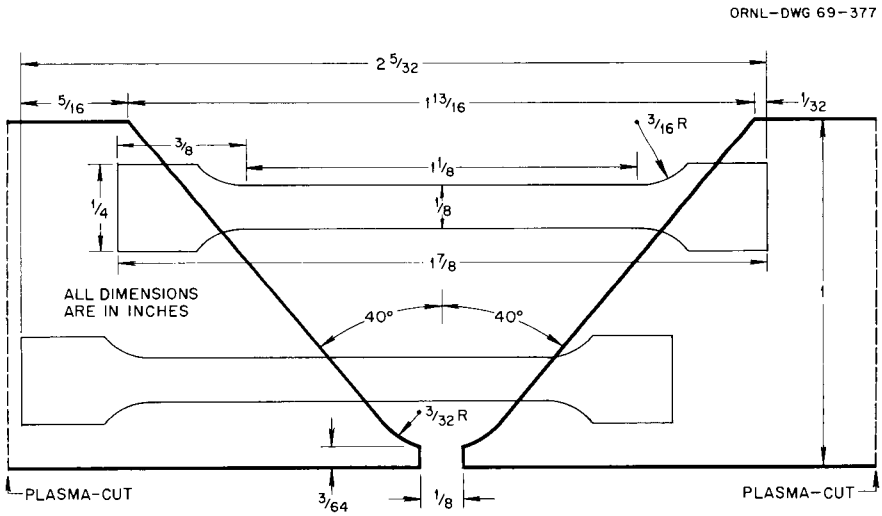

Fig. 12.8. ORNL Joint Design for GMA, SMA, and Submerged-Arc FFTF Welds.

The vendor's analysis of the wire, along with an ORNL analysis of the resulting weld deposit, is shown in Table 12.2. Note from the table that the only significant change in the chemistry of the weld deposit was a pickup of Si from the flux.

Table 12.2. Analyses of Type 308 Stainless Steel Filler Wire and Resulting Weld Deposit

	Certified Wire Analysis (wt %)	ORNL Weld Deposit Analysis (wt %)
C	0.042	0.046–0.049
Mn	1.67	1.53–1.59
Si	0.43	0.72–0.75
S	0.011	0.010
P	0.016	0.013–0.015
Cr	20.95	20.7–20.8
Ni	10.38	10.0–10.1

4. A strip about 2 1/2-in. wide, containing the fusion zone of the weld, was plasma-arc cut from the resulting weldment as shown in Fig. 12.8. We then radiographed these strips through their 1-in. thicknesses.

5. Since no gross defects appeared in the radiographs, we sawed the welds into 1/4-in. wafers in planes parallel to the view shown in Fig. 12.8. We radiographed each wafer through its 1/4-in. thickness. We found very few indications, but we rejected those wafers containing even minor indications.

6. We macroetched the wafers to reveal the exact location of the fusion boundaries and machined the specimens from the locations shown in Fig. 12.8.

7. We labeled each specimen.

8. We then radiographed each specimen to further insure integrity in the 1/8-in.-thick gage section.

The plate stubs from which the weldments had been cut will be remachined and used for subsequent welds. We now have the necessary

supplies for producing the manual metal arc and gas-metal arc welds; barring unforeseen difficulties, the remainder of the weld specimens should be delivered to Battelle Northwest on schedule.

The Effect of Defects on the Mechanical Properties of Weldments

C. D. Lundin[7]

It is a known and accepted fact that discontinuities generally exist in the structural components. To determine when a discontinuity becomes unacceptable, we are trying to characterize various discontinuities and establish their effects on the mechanical properties of the materials being joined.

Our emphasis this quarter was on (1) evaluating the discontinuities previously produced by both metallographic and nondestructive testing methods, and (2) determining the effect of electron-beam and gas tungsten-arc welding conditions on the occurrence of discontinuities.

Visual, ultrasonic, magnetic, and eddy-current nondestructive testing techniques were used on the specimens with the as-welded surface intact and on those with the surfaces of the welds machined to a 15-RMS finish. The results of the nondestructive testing program will determine our ability to locate the discontinuities within production welds with both machined and as-welded surfaces. The results will also show if it is possible to suitably map the discontinuities before mechanical testing. The success of the mechanical testing program in evaluating the effects of the weld discontinuities will depend upon the ability of the nondestructive testing program to locate and characterize the discontinuities.

We made a series of electron-beam and gas tungsten-arc welds in the material for this program to determine the effect of welding conditions on the occurrence of discontinuities. A metallographic investigation was begun to evaluate the effect of the welding conditions.

---

[7]Consultant from the University of Tennessee.

13. DEVELOPMENT OF LMFBR TUBING FABRICATION

G. M. Adamson, Jr.

The tubing fabrication program involves development of fabrication techniques for the manufacture of high-quality type 316 and modified type 304 stainless steel tubing in sizes of interest to the liquid-metal fast breeder reactor (LMFBR) program.

The general scope includes using fabrication techniques that may be transferred to commercial vendors and sufficient nondestructive and destructive testing of the intermediate and final products to assure and demonstrate the quality. The initial studies used titanium-modified type 304 stainless steel, and recently work has begun on type 316 stainless steel.

Fabrication Studies on Type 316 Stainless Steel

W. R. Martin

Drawing of Type 316 Stainless Steel Tubing (R. E. McDonald, T. M. Nilsson, G. A. Reimann)

Preliminary studies involving mandrel drawing of type 316 stainless steel are under way, and a small quantity of 0.375-in.-OD by 0.035-in.-wall-thickness tubing was purchased for this purpose. While only eight draws are required to achieve 0.250-in. outside diameter by 0.016-in. wall thickness, these should be enough to let us determine workability and study the effect of cold work and various annealing temperatures on hardness, grain size, and mechanical properties.

Sections of the type 316 stainless steel were mandrel drawn to 5, 10, 20, 30, 40, and 50% cold work with anneals of 1 hr at 925°C between passes. Samples of the cold-worked sections were annealed at 925 and 1050°C for 1 hr. We found that grain size decreased with increasing cold work at 925°C but not at 1050°C. Other cold-worked samples are now being annealed at 700 and 800°C. The room temperature hardness and tube-burst strength of these tubes are also being determined. Tube-burst

samples could not be ruptured at room temperature if they contained more than 20% cold work because their burst strength was beyond the capacity of our pressure apparatus. The test results obtained thus far for a given amount and type of reduction are consistent. All results will be completed shortly and reported in the next progress report.

Fabrication Studies on Titanium-Modified Type 304 Stainless Steel

W. R. Martin

Drawing of Titanium-Modified Type 304 Stainless Steel Tubing
(G. A. Reimann)

The titanium-modified type 304 stainless steel tubing (Latrobe heat 60508) was fabricated, and 0.250-in.-OD by 0.016-in.-wall-thickness tubing is being nondestructively tested and metallographically examined. The last tube shell of this material was mandrel drawn on a 25-pass schedule with hydrogen anneals after each 30% reduction. While previous tube shells drawn with this schedule were subjected to 1/2-hr 1200°C anneals, the last tube shell was annealed 1 hr at 1050°C for passes 10 through 16 and 1 hr at 925°C for passes 17 through 25.

The first 20 passes were made by conventional mandrel drawing, and two different methods were used for the last five passes: conventional mandrel drawing as a control and plantetary swaging by the same reduction schedule. The 925°C anneals between passes were arranged so that samples of tubing of the final size contained 6, 27, or 46% cold work. All of the tubing fabricated by conventional mandrel drawing was satisfactory, but most of that fabricated by planetary swaging was unsatisfactory. Planetary swaging requires further study with respect to reduction per pass, rate of feeds, and speeds.

Evaluation of Drawn Titanium-Modified Type 304 Stainless Steel Tubing
(T. M. Nilsson)

Last quarter we determined the texture of several tubes of titanium-modified type 304L stainless steel during the last steps of fabrication

and reported grain sizes.[1] The tubing was about 1/4 in. in outside diameter by 0.015 in. in wall thickness. The tubes were machined from the outside to 0.010-in. wall thickness. The tubes were then thinned chemically to about 0.001-in. thickness from both inside and outside as described previously.[1] This means that the texture measured on the resulting foil corresponds to the texture in a layer about 5 mils from the inner wall. The elastically flattened foils were mounted on a holder for the x-ray texture goniometer. A conventional Schultz's technique was used with an iron tube as the radiation source, and the measured intensities were recorded on both an X-Y recorder and a paper tape. By means of a computer program written by Love,[2] conventional pole figures were drawn directly with the intensities on the paper tape as input. We tried to measure the texture using three reflections, (111), (200), and (220), but the (220) intensities were low compared to the background scatter and did not give meaningful pole figures. The sample intensities were nomalized by comparison with the intensities of a random sample produced by cold pressing type 304L stainless steel powder (−100 + 325 mesh).

The resulting pole figures look like conventional pole figures from rolling studies, but the rolling direction now corresponds to the axial direction (A.D.) of the tube, and the transverse direction now corresponds to the tangential direction (T.D.) of the tube. The radial direction is perpendicular to the plane of the pole figure. Figure 13.1 shows the texture in a tube cold worked about 30% by mandrel drawing. The texture is composed of two components, about equally strong. These are the analogs of (011) $[\bar{1}00]$ and (322) $[\bar{4}33]$ rolling textures. Figure 13.2 shows the texture of the same tube after annealing 1 hr at 925°C. The texture still consists of mainly the same two components as before, but the degree of preferred orientation is much smaller and the peaks are

---

[1]G. A. Reimann and T. M. Nilsson, Fuels and Materials Development Quart. Progr. Rept. Sept. 30, 1968, ORNL-4350, pp. 148–149.

[2]G. R. Love, Calcomp Plotting of X-Ray Pole Figures, ORNL-TM-2018 (January 1968).

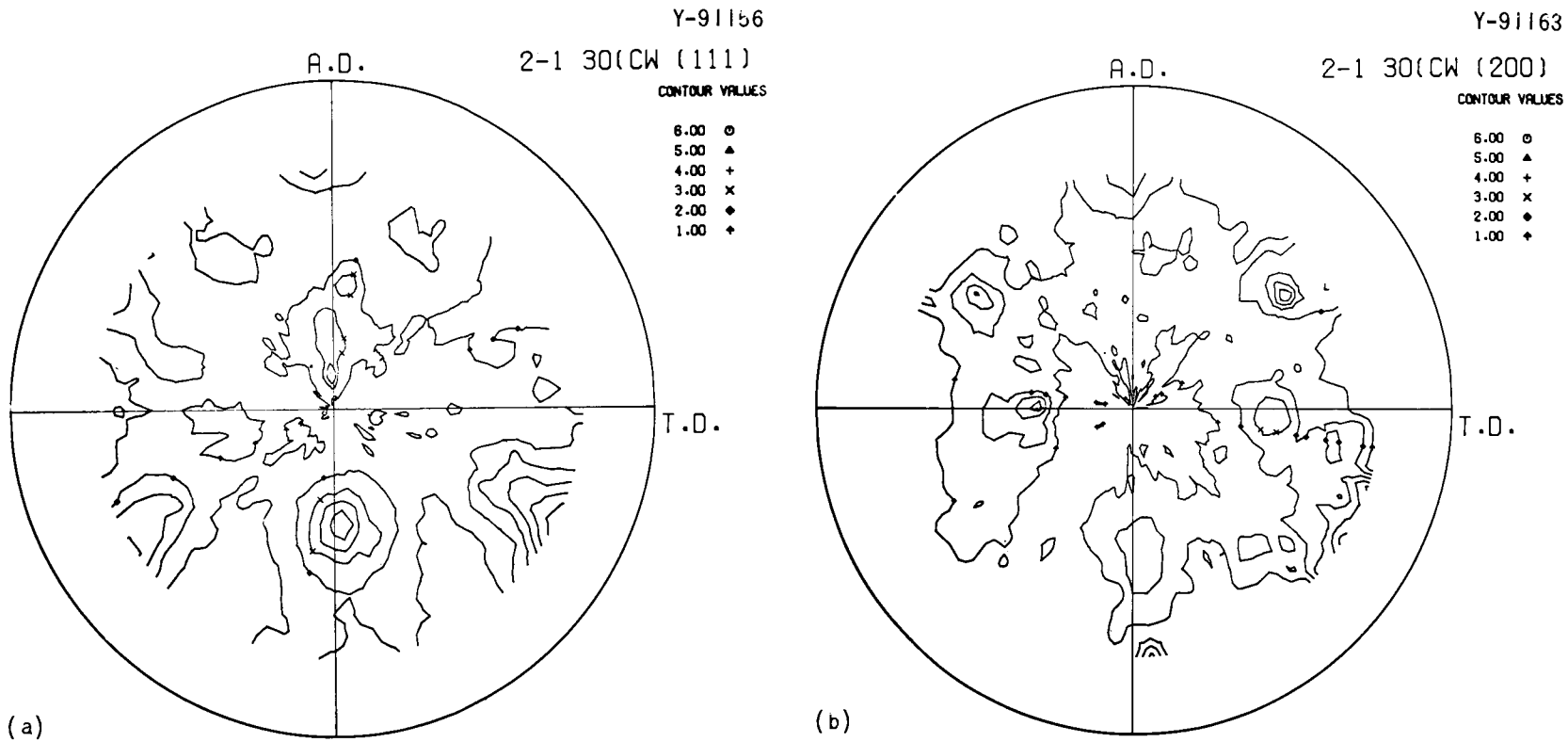

Fig. 13.1. Pole Figures of Titanium-Modified Type 304L Stainless Steel Tubing, Cold Worked 30% by Mandrel Drawing. (a) Crystal plane (111) and (b) crystal plane (200).

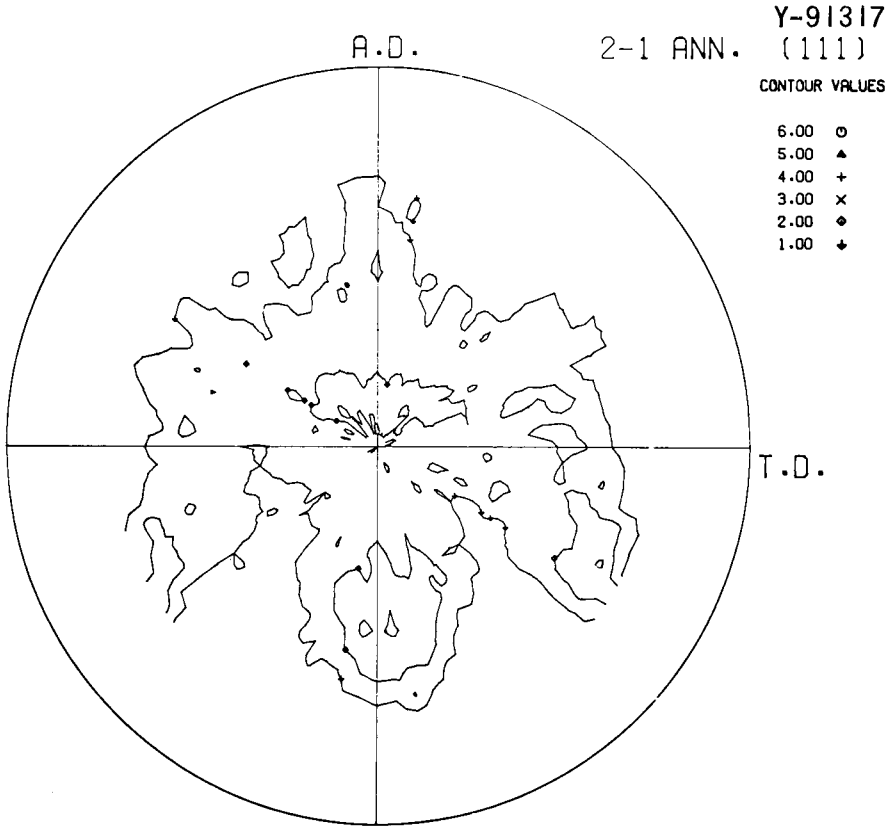

Fig. 13.2. Pole Figure of Titanium-Modified Type 304L Stainless Steel Tubing Cold Worked 30% and Recrystallized by Annealing 1 hr at 925°C. Crystal plane (111).

broader. After an additional 5% cold work by plug drawing, the (011) [$\bar{1}$00] component has increased somewhat (see Fig. 13.3), but there is still little preferred orientation.

The slower development of the (322) [$\bar{4}$33] texture component at low levels of cold work is confirmed by examination of another series of titanium-modified type 304L stainless steel. The tubes in this series were only mandrel drawn about 15% between anneals. The pole figure obtained after about 15% cold drawing is shown in Fig. 13.4. This texture consists primarily of the (011) [$\bar{1}$00] component. In general, this series with lower amounts of cold work showed less preferred orientation as compared to the first series. This is illustrated in Table 13.1, where we have listed maximum intensities as a measure of the degree of texture.

We have also measured the texture of another batch of titanium-modified type 304L stainless steel tubing during the last steps of

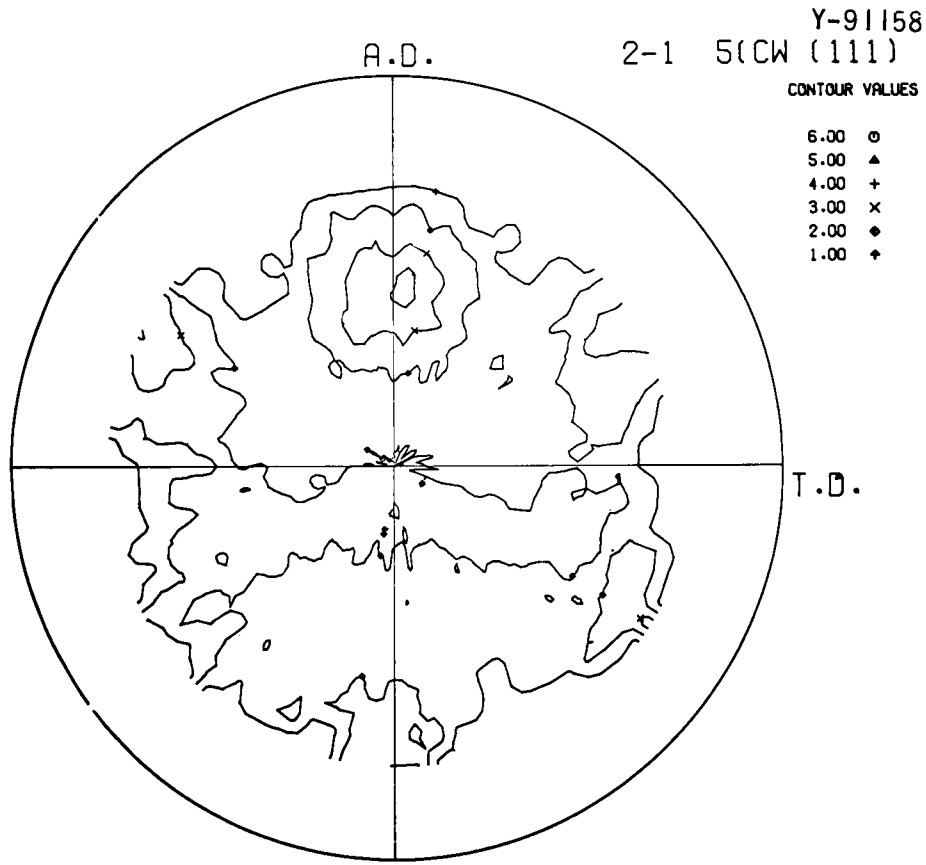

Fig. 13.3. Pole Figure of Titanium-Modified Type 304L Stainless Steel Tubing, Cold Worked 5% by Plug Drawing. Crystal plane (111).

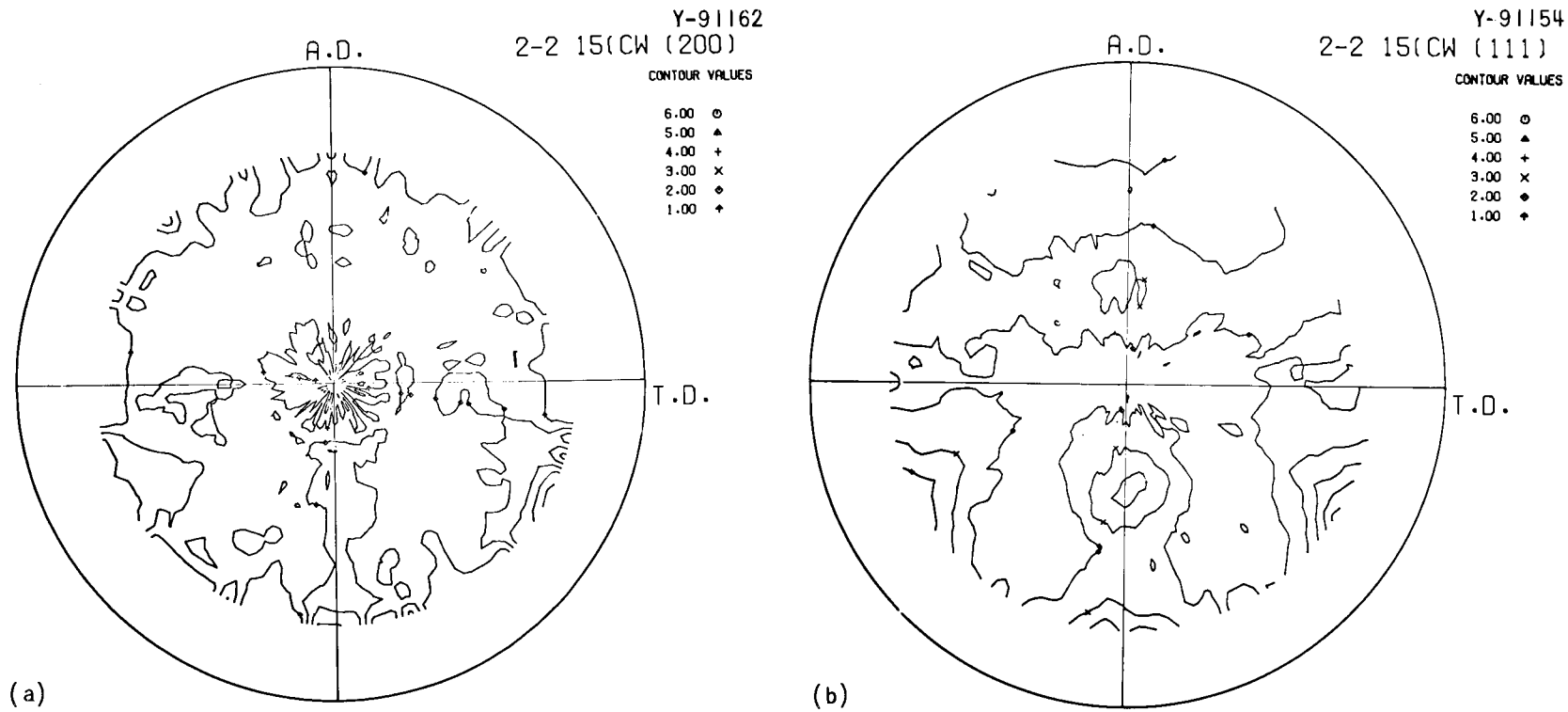

Fig. 13.4. Pole Figures of Titanium-Modified Type 304L Stainless Steel Tubing, Cold Worked 15% by Mandrel Drawing. (a) Crystal plane (111) and (b) crystal plane (220).

Table 13.1. Degree of Texture in Titanium-Modified Type 304L Stainless Steel Tubing During Last Steps of Fabrication

Batch Number	Condition	Maximum Intensity	
		(111)	(200)
2-1	Last 30% cold work[a]	5	4
	plus 925°C 1-hr anneal	3	3
	plus 5% cold work[b]	4	
2-2	Last 15% cold work	4	3
	plus 925°C 1-hr anneal	(c)	(c)
	plus 5% cold work[b]	3	2

[a]Mandrel drawing

[b]Plug drawing

[c]Large degree of scatter due to large grain size and slight preferred orientation.

fabrication. This batch was annealed at 1200°C during processing and had a correspondingly large grain size.[3] This gave a large degree of scatter in the measurements, and it was only possible to obtain meaningful pole figures for cold-worked tubes. The scatter could have been reduced by scanning a larger area, but the small size of the tubing did not allow this. The texture components in the cold-worked samples were the same as found above, and there was good correspondence between the position and the size of the intensity peaks.

A transmission electron micrograph of the type 304 stainless steel tubing after the final 5% cold work by plug drawing is shown in Fig. 13.5. The figure shows the characteristic features that develop during cold working of type 304L stainless steel: dislocation networks and secondary phases. The formation of two new phases has been reported.[4] The hexagonal close-packed phase ϵ forms on the (111) planes. This phase appears

[3]G. A. Reimann and T. M. Nilsson, Fuels and Materials Development Quart. Progr. Rept. Sept. 30, 1968, ORNL-4350, pp. 148–149.

[4]R. Lagneborg, Acta Met. 12(7), 823 (1964).

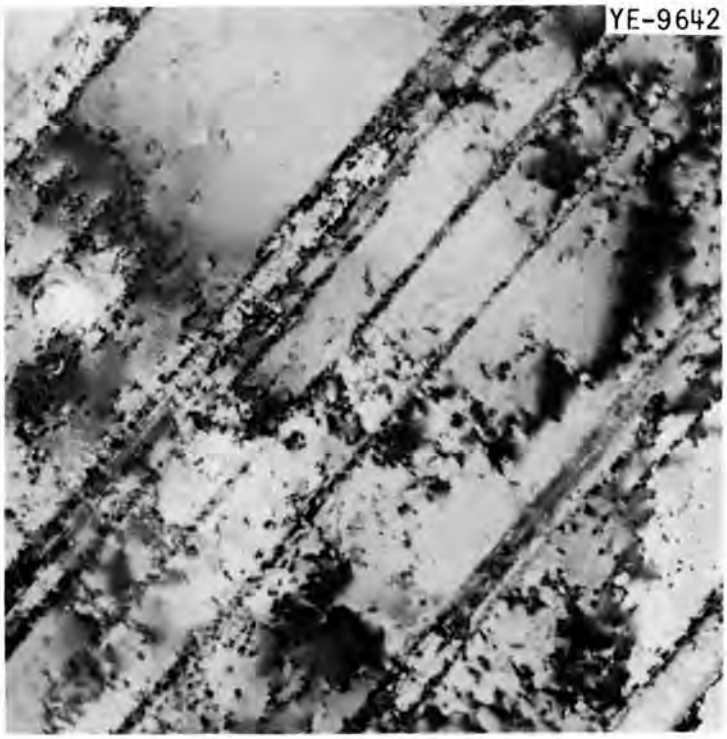

Fig. 13.5. Structure of Titanium-Modified Type 304L Stainless Steel Tubing After 5% Cold Work by Plug Drawing. 25,000×.

in Fig. 13.5 as long thin needles. We were not able to determine the dimensions perpendicular to the thin foil because the wall thickness was only 0.015 in. The other new phase, termed martensitic ferrite α', usually develops inside the ϵ-phase. The α'-phase is formed by a shear mechanism like ordinary martensite, but it contains so little C that it is essentially ferrite. We are presently investigating the new phases more closely.

An electron photomicrograph of a tube of type 304L stainless steel cold worked 43% by mandrel drawing is shown in Fig. 13.6. The density of both the new phases and dislocations has increased considerably. The tubes at this stage have become strongly magnetic due to the ferrite, but there was insufficient intensity to obtain x-ray measurements of the ferrite phase texture. The distribution of the ϵ- and transformed ϵ-phase is quite heterogeneous. Figure 13.6 shows a high density, but other grains do not contain any ϵ at all even at this high level of cold work. The density of dislocations, however, appears to be quite homogeneous and increases with increasing amount of cold work.

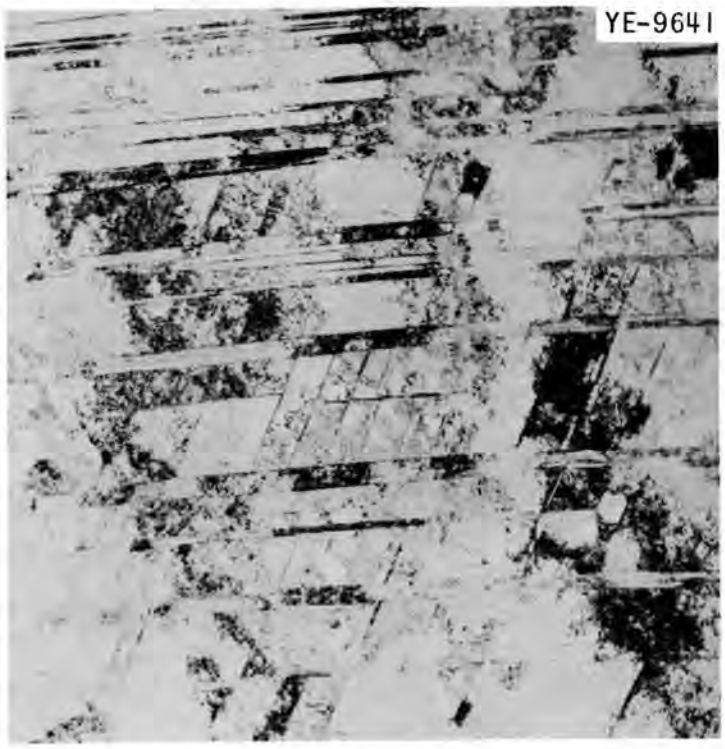

Fig. 13.6. Structure of Titanium-Modified Type 304L Stainless Steel Tubing After 43% Cold Work by Mandrel Drawing. 25,000×.

Both of our standard anneals of 1 hr at 925 and 1200°C caused recrystallization of the cold-worked structures. After annealing at 1200°C for 40 min, the density of small precipitates (likely, carbides and nitrides) is relatively low. Also, grain growth has occurred to give large stable grains containing well-developed annealing twins. After the 925°C anneal for 1 hr, there are more small precipitates, and small-angle boundaries can still be found (Fig. 13.7).

Biaxial Stress-Rupture of Titanium-Modified Type 304 Stainless Steel Tubing (R. T. King)

The development of titanium-modified stainless steels with improved resistance to irradiation damage has been in progress for several years. Martin and Weir,[5] Bloom,[6] Weir,[7] Bloom and Weir,[8] and Stiegler and Weir,[9]

---

[5]W. R. Martin and J. R. Weir, Solutions to the Problems of High-Temperature Irradiation Embrittlement, ORNL-TM-1544 (June 1966).

[6]E. E. Bloom, Effect of Titanium Additions on the Stress-Rupture Properties of Type 304 Stainless Steel, ORNL-TM-1807 (June 1967).

Fig. 13.7. Structure of Titanium-Modified Type 304L Stainless Steel Tubing After 30% Cold-Work and a 1-hr Anneal at 925°C. 5000×.

described the effects of small additions of titanium on the properties of unirradiated and irradiated stainless steel. King and Weir[10,11] reported that titanium additions improve the resistance of type 304L stainless steel to the loss of ductility at high temperatures after the cyclotron injection of uniform concentrations of He. More recently, Reimann[12,13]

---

[7]J. R. Weir, Science 156, 3783 (1967).

[8]E. E. Bloom and J. R. Weir, Development of Austenitic Stainless Steels with Improved Resistance to Elevated-Temperature Irradiation Embrittlement, ORNL-TM-2328 (December 1968).

[9]J. O. Stiegler and J. R. Weir, "Effects of Irradiation on Ductility," pp. 311–342 in Ductility, Seminar ASM, October 14 and 15, 1967, American Society for Metals, Metals Park, Ohio, 1968.

[10]J. R. Weir and R. T. King, "The Effect of Cyclotron-Injected Helium on the Mechanical Properties of Stainless Steel," (summary) Trans. Am. Nucl. Soc. 10(1), 130–131.

[11]R. T. King and J. R. Weir, "The Effects of Cyclotron-Injected Helium on the Creep-Rupture Properties of Type 304 and 0.2% Ti-Type 304 Stainless Steel," (abstract) J. Metals 20(8), 64A (1968).

[12]G. A. Reimann, Fuels and Materials Development Program Quart. Progr. Rept. June 30, 1968, ORNL-4330, p. 175–176.

[13]G. A. Reimann and T. M. Nilsson, Fuels and Materials Development Program Quart. Progr. Rept. Sept. 30, 1968, ORNL-4350, p. 148–149.

fabricated tubing with an outside diameter of 0.25 in. and a nominal wall thickness of 0.016 in. from an ingot of the same heat (Allvac heat 3756) of titanium-modified type 304L stainless steel that was used in several of the investigations mentioned above. Preliminary data and tentative interpretations of some biaxial stress-rupture tests on unirradiated tubes are presented here.

The specimens were from the first batch of tubing produced by mandrel drawing of material from heat 3756. All tubes were annealed in H_2 for 40 min at 1200°C between drawing steps. The three lots of tubes had been cold-drawn 12, 24, or 43% between successive annealing treatments during the final drawing passes to ASTM grain sizes of ASTM 5 to 6, 5 1/2, and 7, respectively.[12]

Each tube was ultrasonically inspected by pulse-echo techniques for longitudinal and transverse discontinuities whose signal responses were greater than those from standard spark-machined notches 0.0015 in. deep by 0.030 in. long. The locations of such discontinuities were recorded.

Test specimens 4 in. long were lathe-cut from each tube, tight-fitting end caps were machined individually for each tube, and the bottom end caps were tungsten-arc welded to the specimens. (This procedure was adopted because loose-fitting end caps could not be satisfactorily welded to the tubes for test purposes.) The wall thickness variations along a helical path around the tubes were than recorded by an ultrasonic resonance technique. The top end caps, which were fitted with capillary tubes for pressurizing the specimens, were then welded into place.

The entire length of the cold-worked specimens was heated to either 600 ± 2°C or 700 ± 2°C at a pressure selected to cause rupture after about 0.1 to 100 hr. The pressurizing gas was He–1% O_2, and the external environment was 1 atm He. Other tubes were annealed in either air or Ar for 1 hr before testing, since this optimizes the ductility of rod and sheet stock that has been cold-worked 50% before annealing. The pressures and temperatures for tests on annealed specimens were selected to duplicate the conditions for certain tests on unannealed specimens.

The percentage of increase in the circumference of the tubing at fracture is plotted in Figs. 13.8 and 13.9 as a function of the tangential stress calculated at the thinnest region of the tube wall. Because of

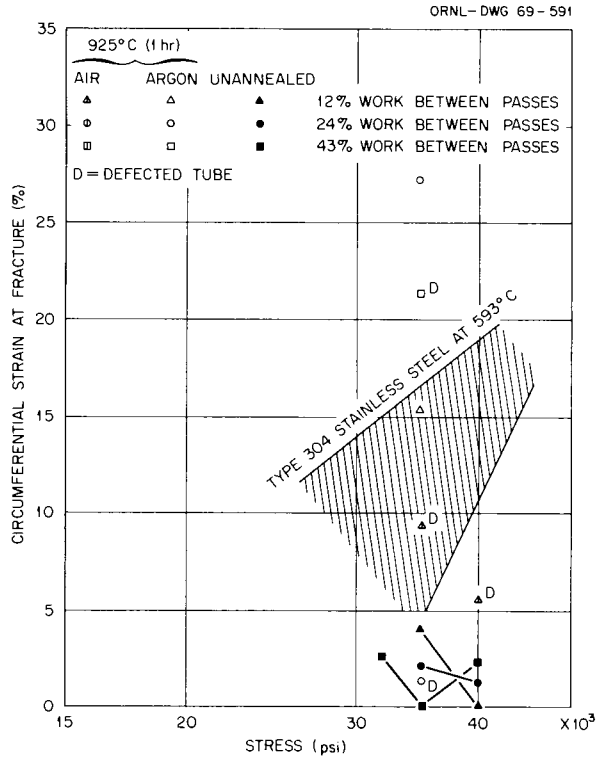

Fig. 13.8. Ductility of Titanium-Modified Type 304L Stainless Steel Tubing From First Batch Drawn From Heat 3756 at 600°C.

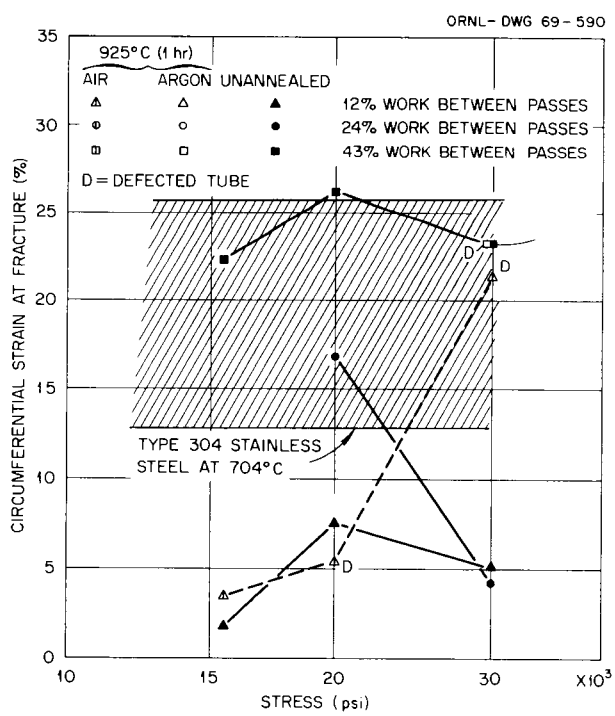

Fig. 13.9. Ductility of Titanium-Modified Type 304L Stainless Steel Tubing From First Batch Drawn From Heat 3756 at 700°C.

the difficulties inherent in making such measurements, these results are at best accurate to ±4% strain for tubes that ruptured explosively. Because the average variation in wall thickness from the thick to the thin side of the tubes was 0.001 in., the circumferential strain was probably not uniform around the tubes. The times to rupture are plotted versus maximum tangential stress in Fig. 13.10 and 13.11. Tubes that failed after less than 0.1 hr are shown separately. In all figures, specimens with pulse-echo signals for longitudinal discontinuities greater than that from the standard notch are indicated by the letter D and are referred to as defective. No specimens yet tested had signals for transverse discontinuities greater than the standard. Stress-rupture data[14] for type 304 stainless steel tubing tested at 593 and 704°C are also shown on the figures.

Unannealed Tubing Specimens. — At 600°C, all tubes tested in the cold-drawn condition had ductilities below 5%. None of these tubes were defective. At any given stress over the range investigated, the 24% cold-worked specimens ruptured after the longest times, and the 40% cold-worked specimens ruptured after the shortest times.

The inner surface of all these tubes contained broad, shallow, longitudinal bore defects (scratches) that were introduced during fabrication. In all cases where the failure point could be found by borescope or macrographic techniques, the failure of cold-worked tubes at 600°C appeared to initiate at a scratch located near the thin side of the tube wall. It is important that these scratches, which do play a role in failure, are not detectable by the nondestructive testing techniques now used.

At 700°C over the range of stresses investigated, the specimens cold drawn 12 and 24% had longer rupture times than the specimens cold drawn 43%. These tube specimens were not defective. None of the specimens cold drawn 12% deformed more than 7.5% before rupturing; these specimens all failed at scratches. The specimens cold drawn 24% had low

[14] J. T. Venard, Stress-Rupture Properties of Type 304 Stainless Steel Tubing, ORNL-TM-535 (June 1963).

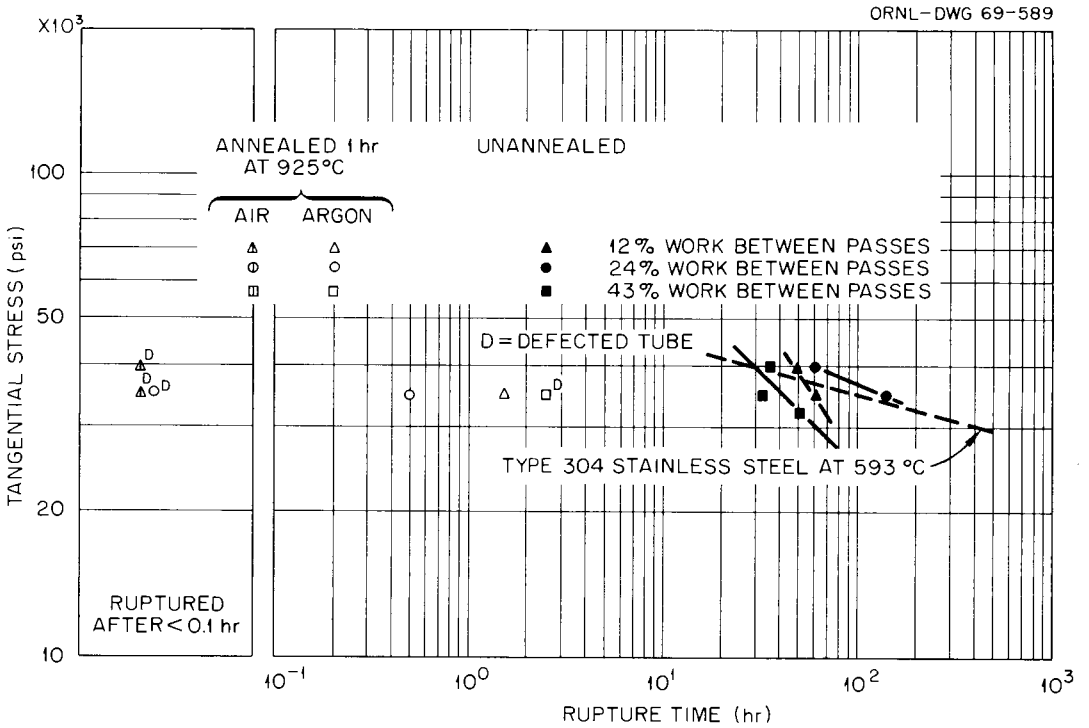

Fig. 13.10. Biaxial Stress-Rupture Properties of Titanium-Modified Type 304L Stainless Steel Tubing From First Batch Drawn From Heat 3756 at 600°C.

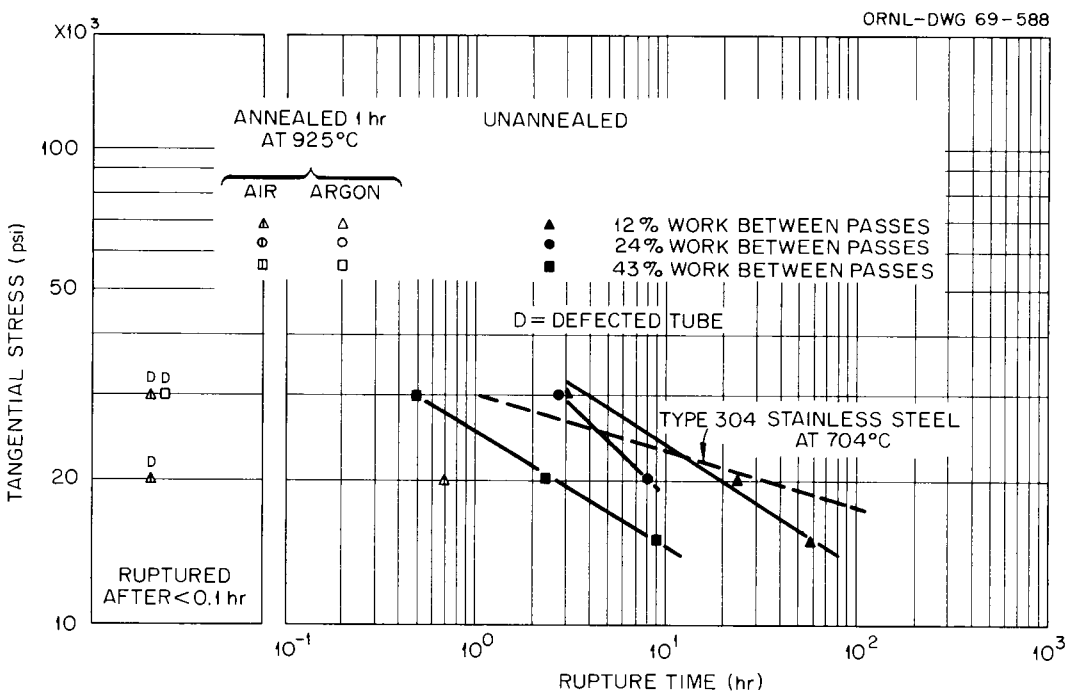

Fig. 13.11. Biaxial Stress-Rupture Properties of Titanium-Modified Type 304L Stainless Steel Tubing From First Batch Drawn From Heat 3756 at 700°C.

ductility (4.2%) at high stress (30,000 psi) but relatively high ductility (16.8%) at low stress (20,000 psi), while the ductility of all specimens cold worked 43% exceeded 20%. We tentatively conclude from these results that the specimens more heavily cold worked either recrystallize or recover substantially while being heated to or tested at 700°C. Although scratches were present in all of these specimens, only one specimen exhibiting high ductility failed at a scratch.

Figure 13.12 shows the failure of a 12% cold-worked tube tested at 700°C and 30,000 psi tangential stress. Extensive intergranular cracks were found to follow the fabrication scratches, which varied in width from 0.001 to 0.004 in. Even when the intergranular separations were not visible at scratches by macroscopic examination, metallography showed that extensive intergranular separation had occurred under the scratches. Both the primary failure and secondary failures (regions with macroscopically visible cracks that nearly penetrated the tube wall) were clearly intergranular. In Fig. 13.13, the primary failure of this specimen is shown to follow a scratch about 0.0003 in. deep by 0.004 in. wide. The morphology of the scratch is shown at several sections along the length of the tube. About 0.1 in. away from the end of the failure, an intergranular separation was found just under the scratch. Although the bulk of the tube did not recrystallize during the test, the severely cold-worked metal just under the scratch did recrystallize, forming a very fine-grained structure. Nearly all of the newly recrystallized grains separated from their neighboring grains.

Annealed Tubing Specimens. — The circumferential strains of 15.4% and 27.3% measured for the two nondefective, argon-annealed specimens drawn 12 and 24% and tested at 600°C and 35,000 psi stress are much higher than the ductilities of comparable unannealed specimens. However, the rupture times were much shorter than those of the annealed specimens.

Two defective, air-annealed specimens drawn 12% strained 9.4 and 5.1% before failing at 600°C under 35,000 and 40,000 psi stresses. These ductilities are higher than those for unannealed, nondefective tubes but lower than the ductility of comparably annealed, nondefective tubing.

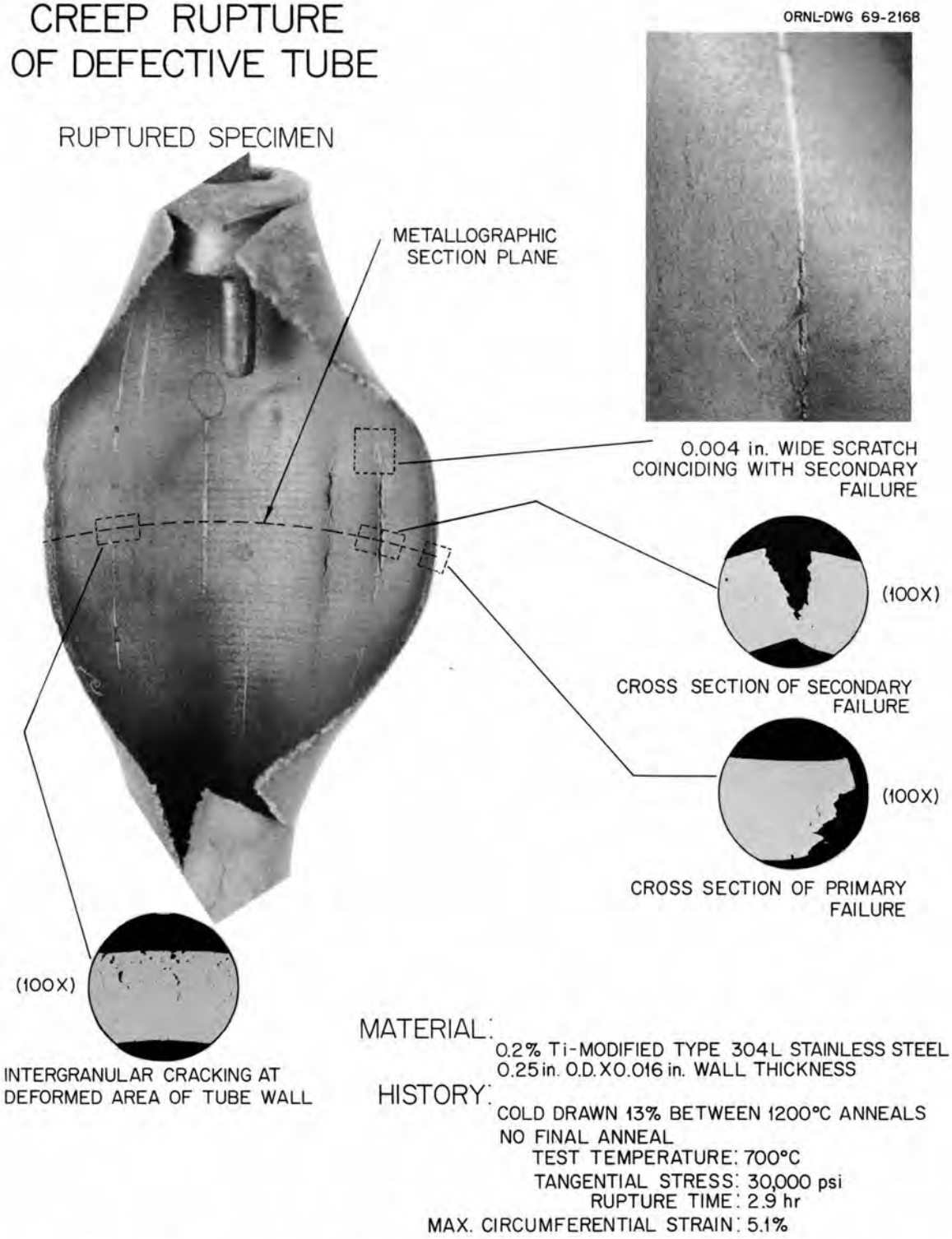

MATERIAL:
0.2% Ti-MODIFIED TYPE 304L STAINLESS STEEL
0.25 in. O.D. X 0.016 in. WALL THICKNESS

HISTORY:
COLD DRAWN 13% BETWEEN 1200°C ANNEALS
NO FINAL ANNEAL
TEST TEMPERATURE: 700°C
TANGENTIAL STRESS: 30,000 psi
RUPTURE TIME: 2.9 hr
MAX. CIRCUMFERENTIAL STRAIN: 5.1%

Fig. 13.12. Failures Coinciding with Scratches in Unannealed Tubing Specimen.

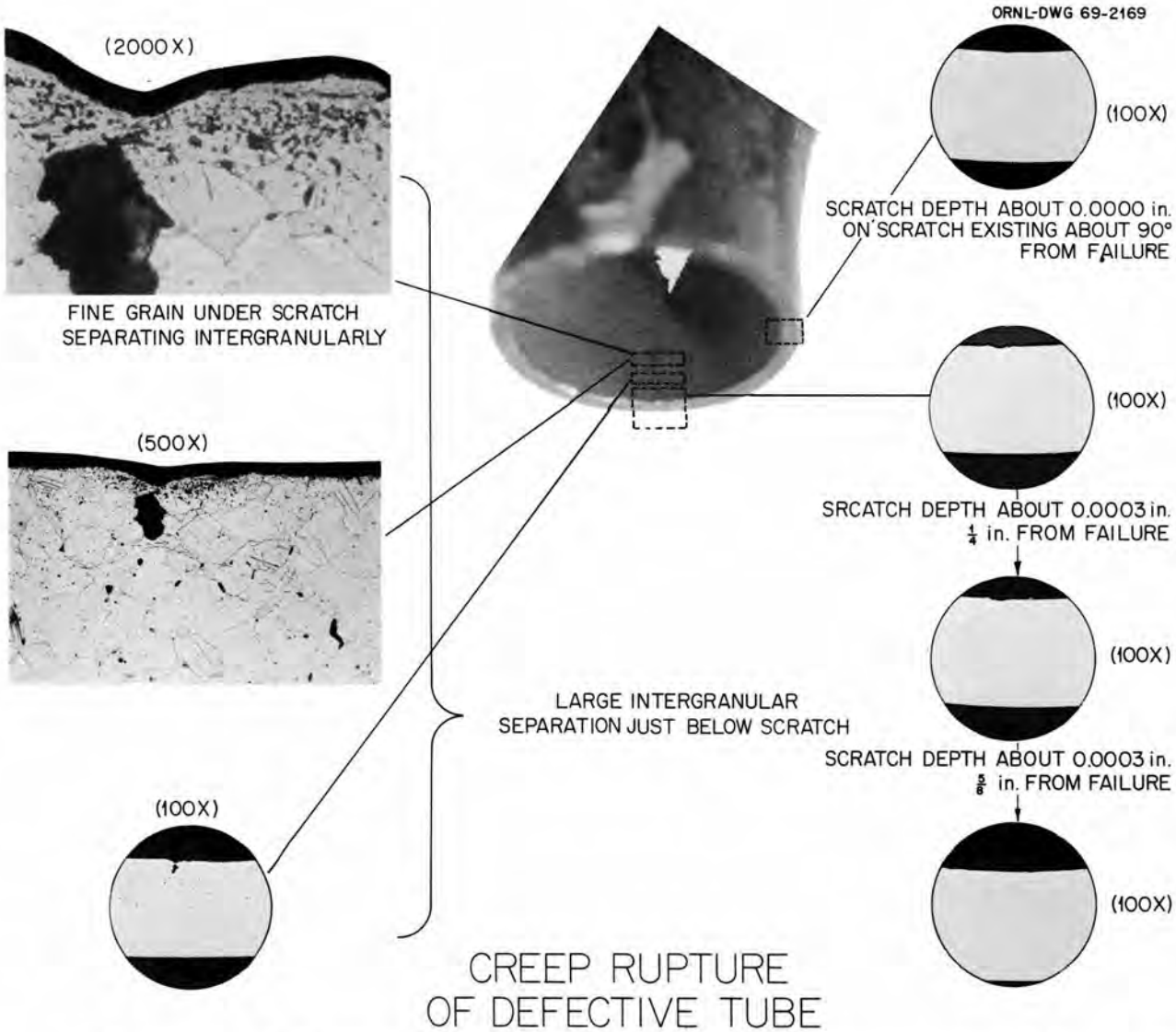

Fig. 13.13. Morphology of Scratch and Associated Intergranular Failure of Unannealed Tubing Specimen.

The very short rupture times and darkened interior surface of these tubes suggest that some contamination of the tubing occurred during annealing.

One defective, argon-annealed tube drawn 43% exhibited 21.4% strain and a relatively long rupture life at 600°C under 35,000 psi stress. However, another defective, argon-annealed tube drawn 24% deformed only 1.4% and failed after less than 0.1 hr, while the comparable nondefective tube ruptured after 0.5 hr and deformed 27.3%. Since the defective tube failed in the vicinity of the defect, it seems highly likely that under certain circumstances the defects found by nondestructive testing techniques can cause drastic reductions in the rupture life and apparent ductility of annealed tubing.

The air-annealed specimens drawn 12% and tested at 700°C decreased in ductility with decreasing stress, falling from 21.4% at 30,000 psi to 3.5% at 15,000 psi. However, there is a high probability that these specimens were accidentally contaminated chemically during the annealing process, so that the significance of these results is uncertain.

The defective, argon-annealed specimen drawn 43% and tested at 30,000 psi stress at 700°C had the same ductility as the comparable nondefective, unannealed tube but had a much shorter rupture time. We have not yet determined whether the defect played any role in this failure.

14. DEVELOPMENT OF FUEL ELEMENT FABRICATION

G. M. Adamson, Jr.

The purpose of this program is to devise new combinations of materials or new fabrication techniques to advance the technology for fabricating fuel elements and components for research reactors. We are attempting to improve the performance of advanced research reactors, such as HFIR and ATR, by developing fuel elements with lower production cost, longer lives, increased safety or reliability, or all three. The studies include factors affecting both fabrication and irradiation performance. We must also develop sufficient knowledge of the processes used for fabricating aluminum-based dispersion fuel elements so that we can adequately assist commercial fabricators, purchasers, specification writers, and technical inspectors. Other studies are aimed at improving the reliability and reducing the cost of the required nondestructive inspection techniques.

Fabrication Studies of Fuel Dispersion Plates

W. R. Martin

Investigations of Nonuniform Deformation in Simulated Fuel Plates
(J. H. Erwin, W. R. Martin, R. W. Knight)

We used high-speed motion pictures in our investigation of the mechanism by which a "dogbone" shape is formed in the core section of composite fuel plates.

We assembled composite billets with simulated fuel cores and then machined coordinate networks at 0.050-in. intervals on the side of the billet (Fig. 14.1). Alloy 6061 simulated the core material since the frames and covers were made of X8001 alloy. The billet was assembled with one edge of the core exposed; thus, part of the side restraint of the frame that would normally have been present during rolling was absent during this test. The billets were rolled at 500°C with a reduction of 0.150 in./pass through the first six passes. A high-speed motion picture

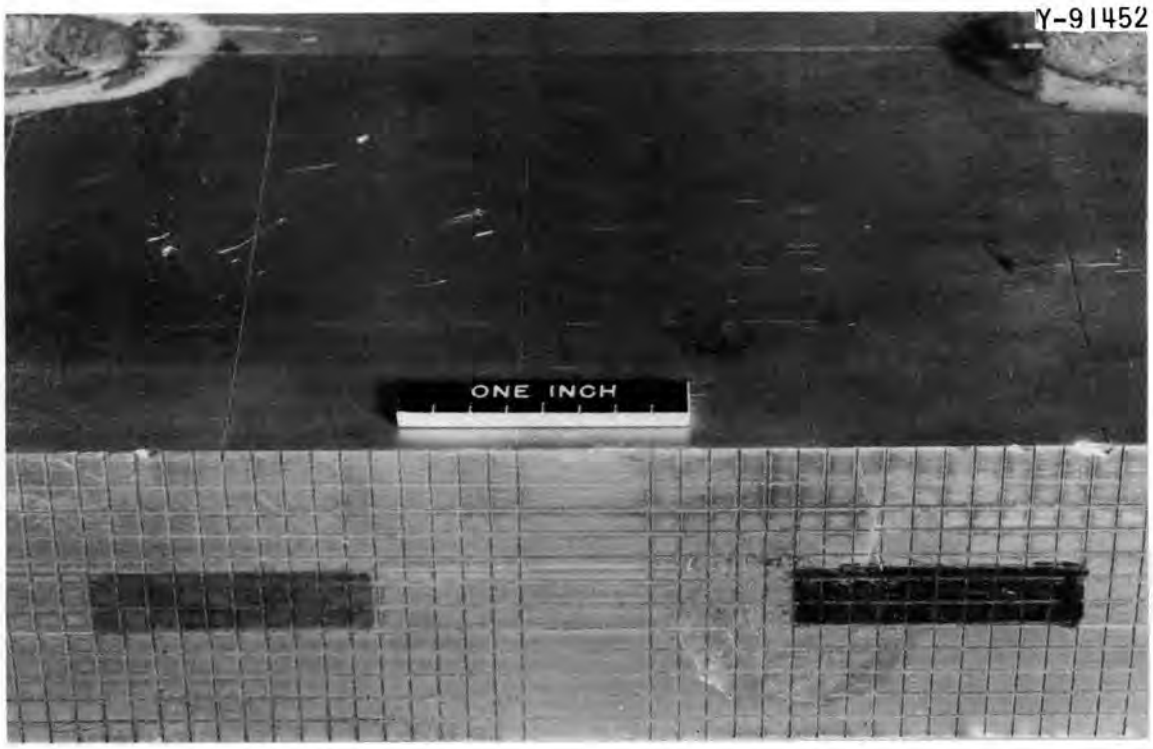

Fig. 14.1. Oblique View of Simulated Fuel Plate Showing Two Cores with Grids Machined on the Side of the Billet.

camera was positioned to view the side of the rolls and the billet as it passed through the rolls. The film speed was adjusted to 500 frames/sec; the surface speed of the rolls was 16.6 in./sec; the simulated core within the billet was 1 in. long. Thus, about 28 frames were obtained per pass, giving 28 positions of the core as it passed through the rolls. Selected frames from the first pass are shown in Fig. 14.2. The hard core resists deformation as it passes through the mill until the nose of the core is about to leave the mill; then the middle zone of the core begins to deform. Generally, for billets of this size, the nose of the core begins to deform as it starts to leave the mill, but since the metal surrounding the nose of the core is very much weaker, the weakest metal (frame and cover plate at the interface of core and frame) deforms instead of the hard core (as shown in Fig. 14.3). This gives the thick part of the dogbone. As the nose of the core moves out of deformation zone, the middle zone of the core approaches the no-slip line; it begins to deform as it should, since there is no weak metal in front of it to

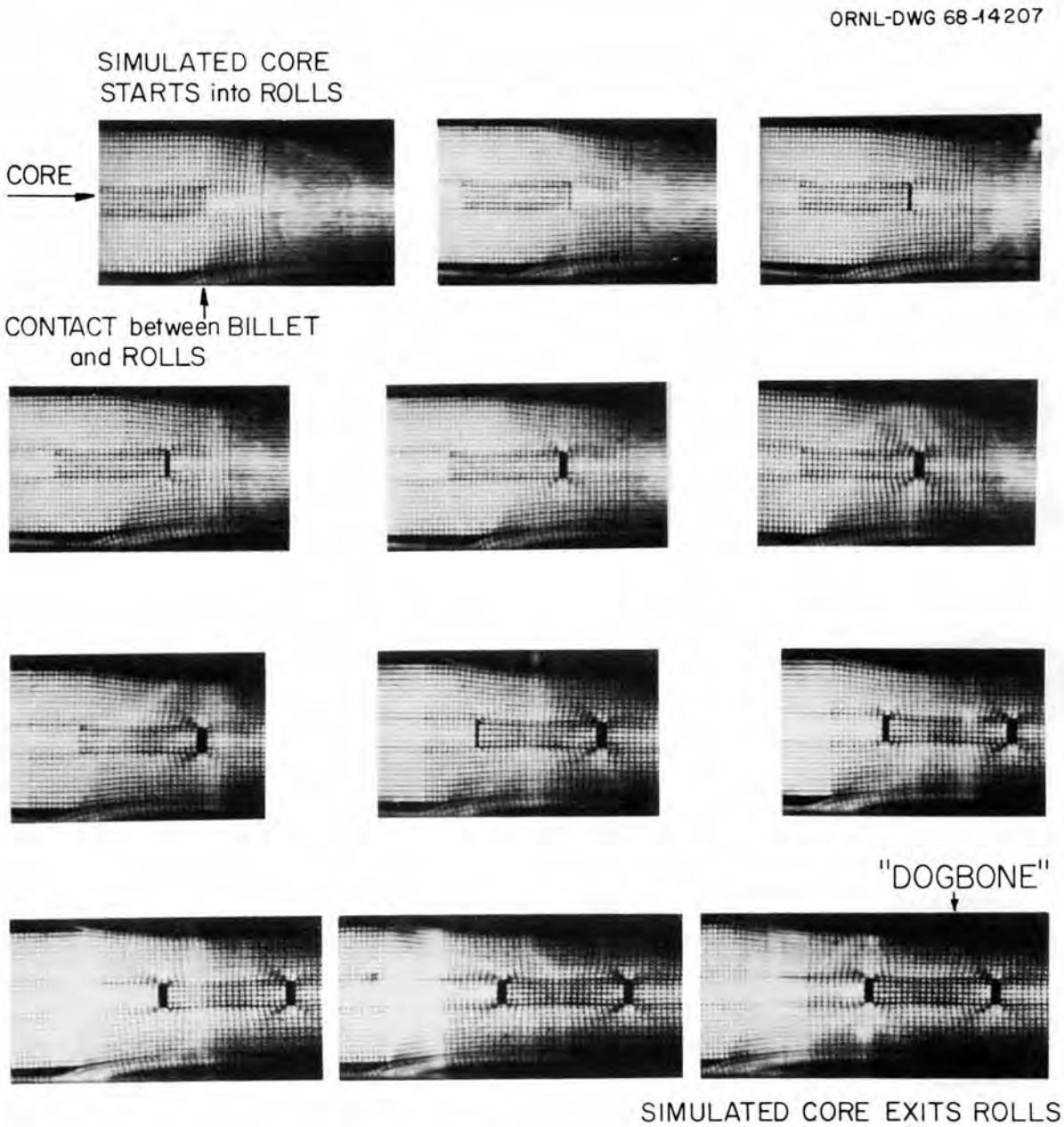

Fig. 14.2. Formation of Dogbone During Rolling (0.138 sec) of Simulated Fuel Element at 500°C.

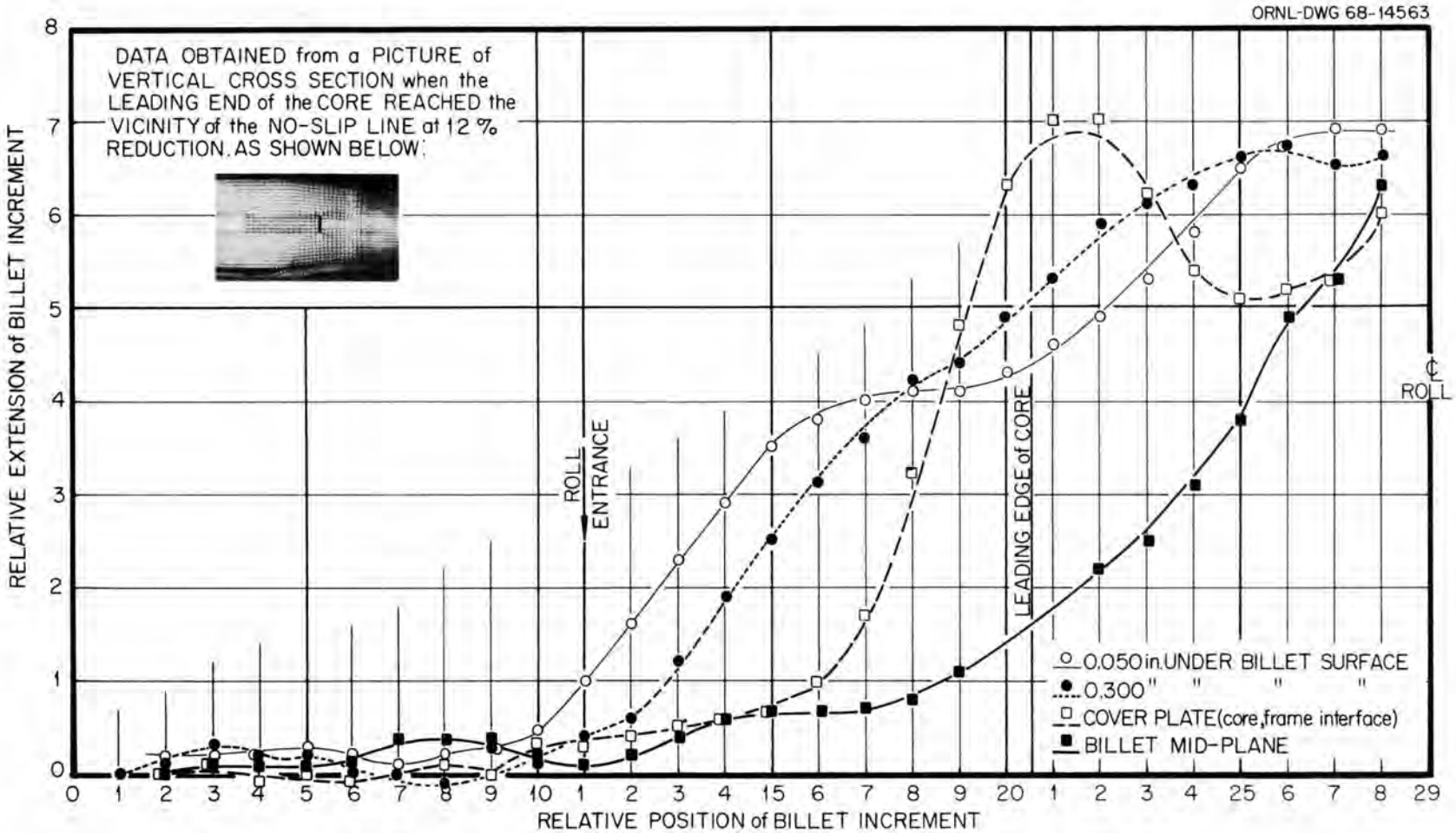

Fig. 14.3. Relative Extension of 0.050-in.-Long Segments in a 1 1/4-in.-Thick Type X8001 Alloy Billet Containing a 0.255-in.-Thick Simulated Core of Type 6061 Aluminum.

be deformed. This gives the dogbone shape on the front of the core. The relative deformation of core and total reduction of billet thickness are given in Fig. 14.4. The same process is repeated as the tail of the core moves through the deformation zone to give a dogbone on the rear of the core. The position of the no-slip line on the first pass is shown in Fig. 14.5, and a comparison of Fig. 14.4 with Fig. 14.5 indicates no relationship between the slip line and the start of dogboning.

The motion picture frames were analyzed for additional information concerning dogboning during the rolling schedule, and these data are given in Table 14.1. Note that the degree of dogboning begins to diminish after the fifth pass. This corresponds to a shape factor of about two. Shape factor is defined as ℓ/H_{mean}, where ℓ is the length of deformation zone and H_{mean} is the mean of initial and final billet thicknesses. When the shape factor is low (< 1.5), the midplane of the billet resists deformation in the first section of the deformation zone but begins to deform as it nears the exit point. This is due to stress variations across the thickness of the billet. But when the shape factor is high (> 1.5), the stress is more uniform across the billet, and the midplane of the billet deforms at about the same rate as the billet surface. This phenomenon is illustrated in Fig. 14.6. In this figure, the billet has been sectioned into horizontal layers (m layers) from the surface to the midplane of the billet. In the bottom two graphs in Fig. 14.6, curve 1 represents the deformation of the surface layer from the time it enters the mill at 0 until it leaves the mill at x. The other curves, numbered from 2 to 5, represent succeeding layers, with the fifth layer representing the deformation along the midplane of the billet. In the graph illustrating the deformation of layers within a billet for a shape factor of less than 1.5, the middle layer of the billet (curve 5) is compressed during the period beginning just before the billet enters the mill and ending a short time after the billet has entered the mill. We confirmed this by inserting a strain gage into the middle of a billet and then rolling the billet on a small, hand-driven mill to a very small reduction. The output of the strain gage, as recorded with a rapid response recorder, is shown in Fig. 14.7.

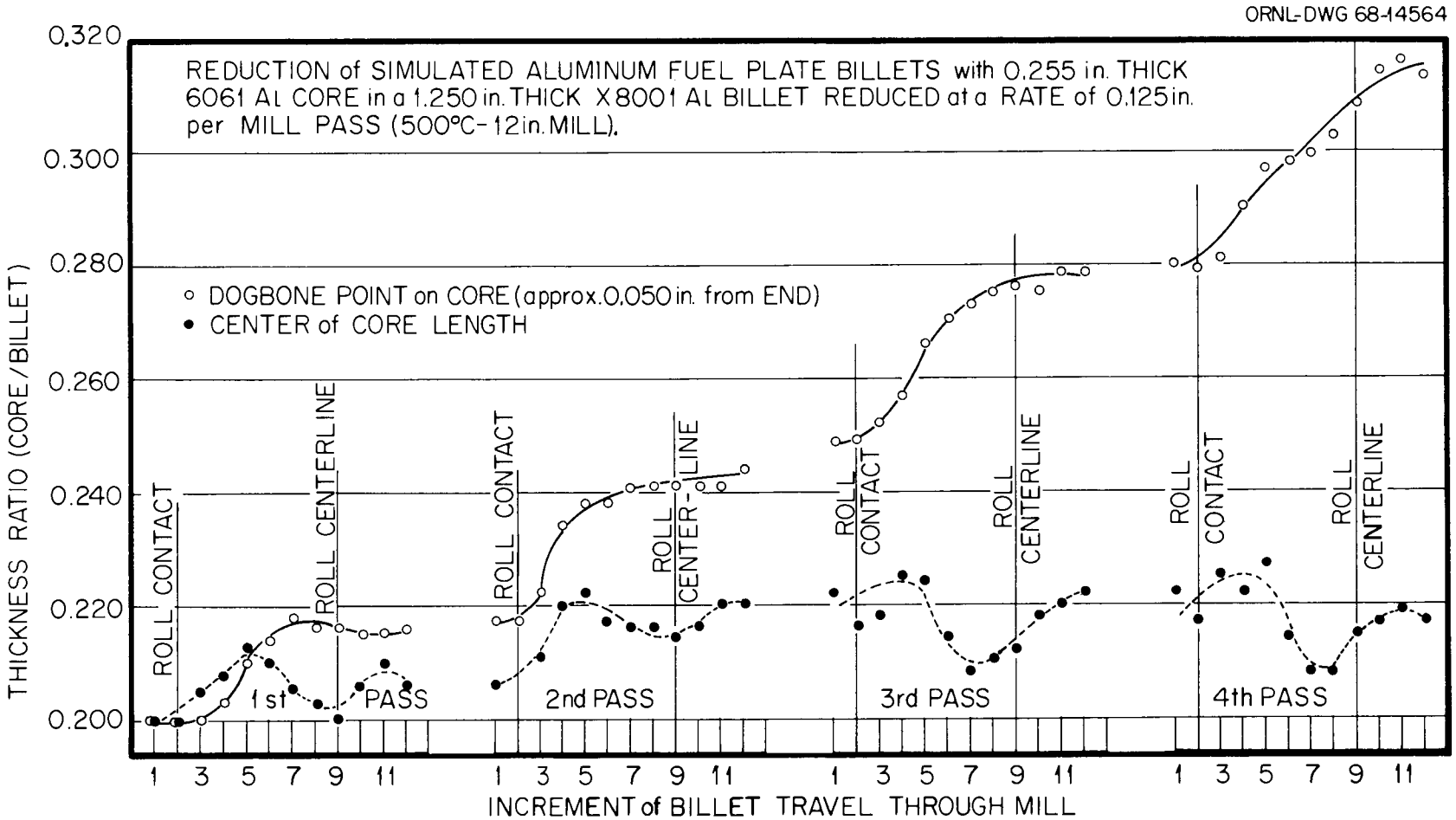

Fig. 14.4. Development of Dogbone End.

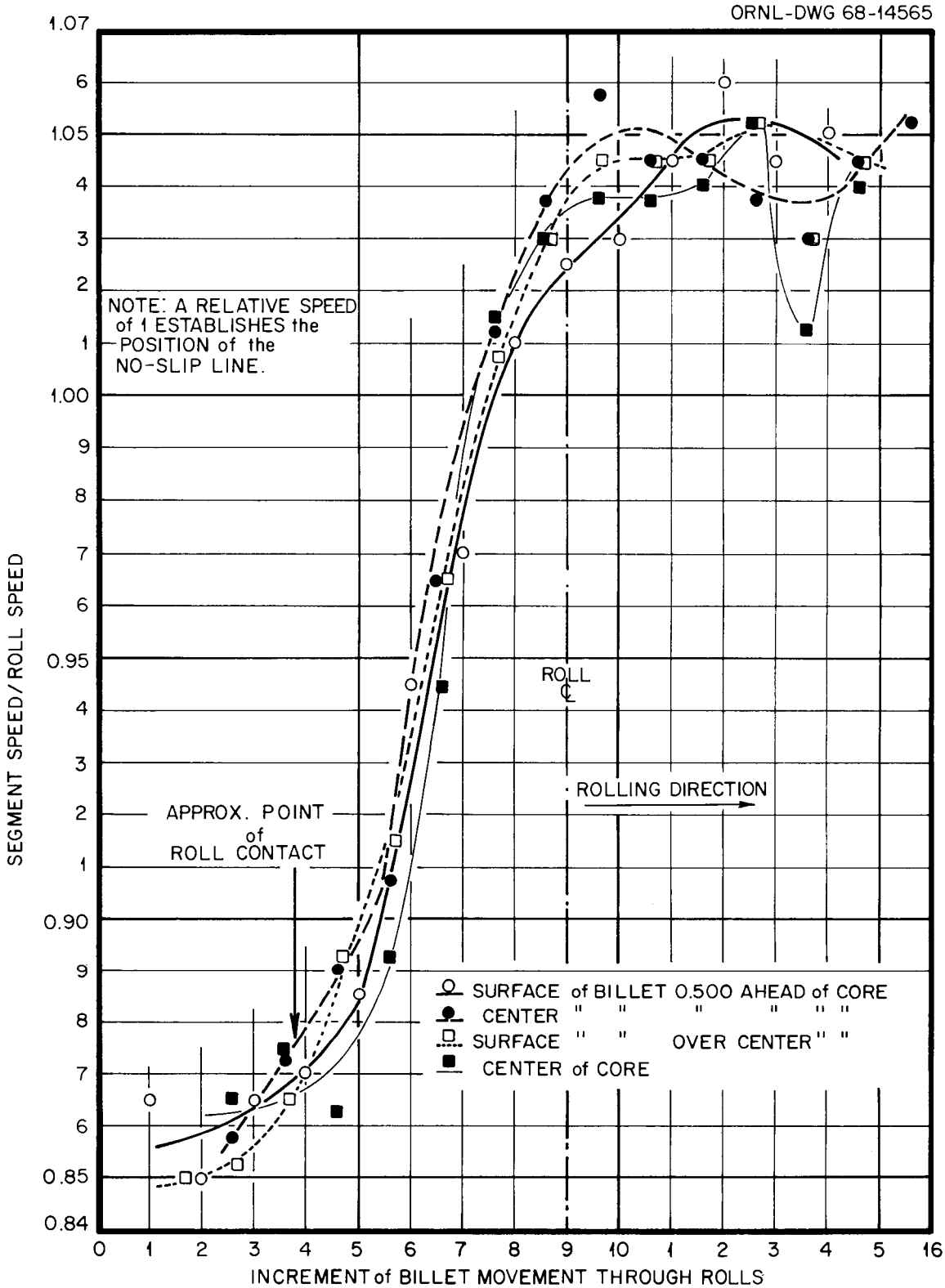

Fig. 14.5. Typical Speeds at Which Composite Billets Progress Through Rolls.

Table 14.1. Results of Analyses of High-Speed Motion Picture Study of the Rolling of Simulated Fuel Plates

Pass Number	Billet Size[a] (in.)		Bite (in.)	Total Reduction Per Pass (%)	Billet Speed (in./sec)[b]			Shape Factor[e]	Core Thickness After Pass (in.)		Dogbone (in.)	
	Entrance	Exit			Entrance[c]	Exit[c]	Exit[d]		Nose	Average	Per Pass	Total
1	1.250	1.100	0.150	12	15.6	17.9	17.8	0.87	0.233	0.221	+0.012	0.012
2	1.100	0.950	0.150	13.6	16.9	20.6	19.6	0.99	0.232	0.214	+0.008	0.020
3	0.950	0.800	0.150	15.8	16.6	19.7	19.8	1.17	0.221	0.182	+0.019	0.039
4	0.800	0.650	0.150	18.8	16.3	19.7	19.9	1.41	0.205	0.144	+0.022	0.061
5	0.650	0.500	0.150	23.1	15.8	19.6	20.5	1.78	0.179	0.109	+0.009	0.070
6	0.500	0.350	0.150	30.0	14.9	20.2	21.3	2.41	0.149	0.091	−0.012	0.058
7	0.350	0.225	0.125	36.0	13.9	19.7	21.4	3.60	0.104	0.059	−0.013	0.045

[a] Core thickness 0.250 in., cladding thickness 0.500 in.

[b] United Mill roll speed: 16.6 in./sec.

[c] Measured.

[d] Calculated

[e] Length of deformation zone is 1.02 in. for passes 1 through 6.

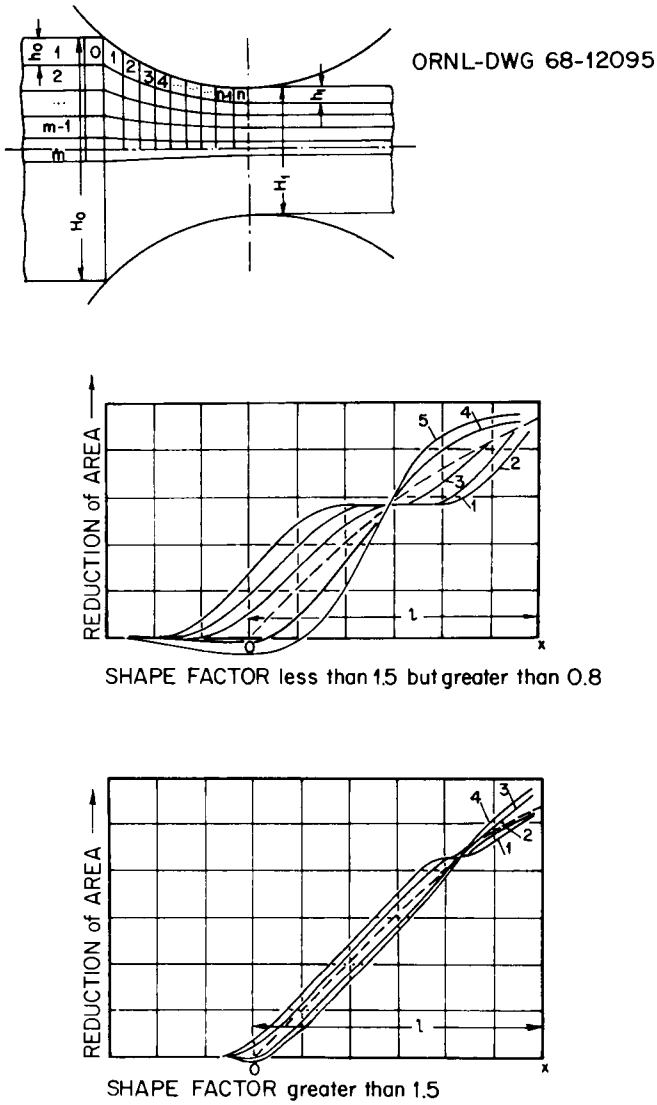

Fig. 14.6. Effect of Shape Factor on the Internal Inhomogeneity of Deformation During Hot Rolling of Aluminum. (Data by I. Ya. Tarnovski, A. A. Pozdeyev, and V. B. Lyashkov, Deformation of Metals During Rolling, pp. 78, 83, Pergamon Press, London, 1965.)

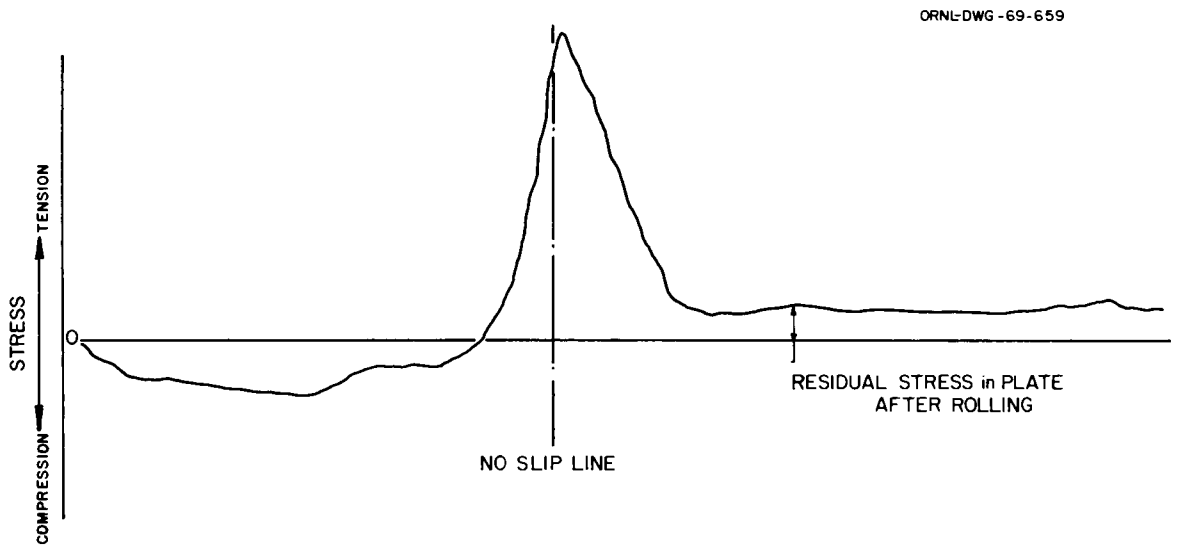

Fig. 14.7. Stress Along the Midplane of a 1/4-in.-Thick Plate During Rolling with a Very Low Shape Factor.

Thus, for composite fuel plates that have geometries that give low shape factors during rolling, the higher strength cores compound the problem of nonuniform deformation along the midplane of the billet. It appears reasonable to expect that, in addition to matching the strengths of the components of composite fuel plates, we need to select rolling conditions — namely, a high shape factor — that give more uniform deformation. High shape factors result from greater reduction per pass, thinner billets, and larger roll diameters.

We now have the knowledge that should make it possible to match the strengths of composite fuel plate components to prevent dogboning. Work by Erwin and Martin[1] has shown the strengths of the fuel core materials as a function of fuel content and type of fuel. Figure 14.8 shows that the aluminum alloy 2219 is considerably stronger than alloy 6061 or 101 aluminum powder compacts.

Previously, Erwin and Martin[2] demonstrated that the fit of fuel compact to frame cavity affected dogboning, illustrating the effect of side restraint imposed by the frame on the deformation of the core.

---

[1]J. H. Erwin and W. R. Martin, Fuels and Materials Development Program Quart. Progr. Rept. June 30, 1968, ORNL-4330, pp. 320–321.

[2]J. H. Erwin and M. M. Martin, Fuels and Materials Development Program Quart. Progr. Rept. Sept. 30, 1968, ORNL-4350, pp. 265–270.

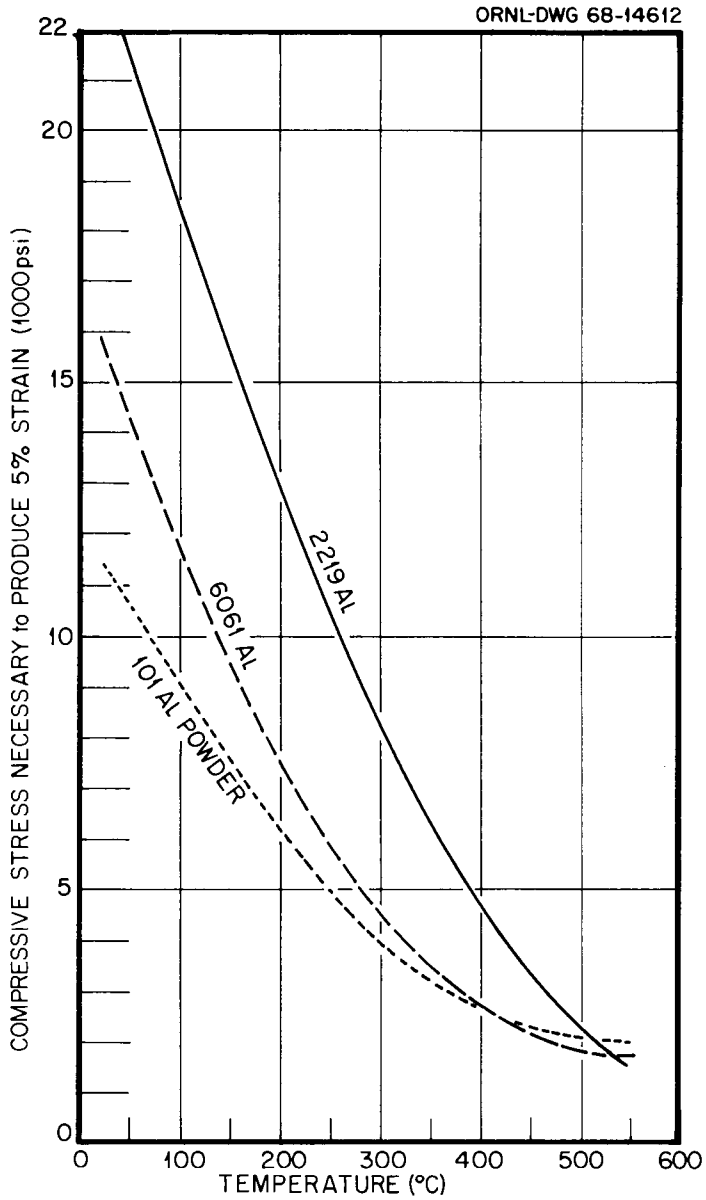

Fig. 14.8. Compressive Strength of Aluminum Cladding, Frame, and Core Filler Materials at Elevated Temperatures.

From these studies, we can summarize the various factors affecting dogboning; these are shown in Table 14.2. Lubricant experiments have not yet been completed, but the effect of friction between the rolls and the billet will affect the stress distribution across the billet, and we have used this well-known fact to predict the effect of friction on dogboning.

Table 14.2. Factors Influencing Dogboning

Factor	Comments
Strength of core, frame, and cover plates	Core must not be stronger than frame or cover plates
Billet thickness	Thinner billets should give less dogboning
Relative thickness of cover plate and core frame	Thinner cover plates relative to a given core thickness should reduce dogboning
Roll diameter	Larger roll diameter should increase shape factor and reduce dogboning if the amount of reduction per pass is not reduced
Reduction per pass	Larger reductions per pass should decrease dogboning
Roll surface, billet surface; coefficient of friction between the two	Friction should be low to minimize dogboning, but a lower limit is set by the bite angle
Spread and elongation of unrestrained cores	Misfit between core and frame cavity that allows the core to deform before contacting the frame will decrease dogboning.

Fabrication of ATR-Type Fuel Plates (M. M. Martin, J. H. Erwin, R. W. Knight, B. E. Foster, S. D. Snyder)

Fuel plates of ATR types 8 and 19 were fabricated to illustrate the effects of several different variables on dogboning. The variations for this study from standard ATR core specifications are shown in Table 14.3. All fuel plates were hot bonded at a 20% reduction per pass and cold rolled 20%.

Plates containing cores 975-1 and 976-1 were rolled conventionally for the first two passes and cross rolled for the third and fourth passes and were intended as process references. Neither of these plates was rolled to specification, but since they did show the rolling procedure to be sound, the rest of the plates were rolled.

The type 8 plates proved well suited to rolling: four plates were within specification limits. The type 19 plates, however, did not fare

Table 14.3. Modifications to Reference Fabrication Process for ATR Fuel Plates

ATR Plate Type Number	Core Number	Modification
8	975-1	No change
8	975-2	No change
8	973-1	6061 alloy cover plates one-half of normal thickness
8	975-3	0.203 × 2.060 × 0.206-in. inserts at the ends of the core 2219 alloy stock
8	975-3	2219 alloy cover plates
19	974-1	No change
19	976-1	No change
19	976-2	No change
19	977-1	Core twice normal thickness
19	976-3	0.279 × 0.250 × 2.071-in. inserts at the ends of core 2219 alloy stock
19	976-4	2219 alloy cover plates

as well. The heavy reduction in the first pass (about 0.300 in.) caused the plates to slip sideways in the rolls; this resulted in a modified cross roll that produced wide cores (see Table 14.4). None of the type 19 plates met the width specification, but since the primary purpose for rolling these plates was to evaluate dogboning, the type 19 plates were considered acceptable.

Results of measurements of the dogboning in sections from several of the rolled plates are shown in Table 14.5. Further evaluation must be done to the remaining plates before they can be sectioned. From these data it appears that the best solution to reducing dogbone is to add Al to the core to reduce its strength. The thicker cores in the type 19 plate reduced dogboning. The addition of the 2219 alloy insert gave a reduction in dogbone that may be beneficial, particularly on the type 19 plate. The effect of inserts on the type 8 plate may be insignificant.

Table 14.4. Core Dimensions[a] of ATR Types 8 and 19 Fuel Plates After Rolling

Plate Number	Width (in.)			Length (in.)
	Top	Middle	Bottom	
975-2-8	2.473	2.492	2.459	48 5/8
973-1-8	2.439	2.441	2.422	48
975-3-8	2.464	2.472	2.447	48
975-4-8	2.462	2.468	2.463	48 1/8
974-1-19	3.671	3.590	3.546	46 9/16
976-2-19	3.590	3.609	3.623	47 5/32
977-1-19	3.504	3.520	3.520	48 9/32
976-3-19	3.423	3.490	3.706	48 17/32
976-4-19	3.684	3.698	3.706	45 1/4

[a]Specification limits for ATR type 8 plate: width — 2.542 in. max, 2.392 in. min; ATR type 19 plate: width — 3.468 in. max, 3.318 in. min, and length — 48.76 in. max, 47.26 in. min.

The use of inserts also reduced the average core thickness, though we do not understand this effect. The use of 2219 alloy cover plates did little to reduce dogboning in the type 8 plate but appears to have reduced dogboning in the type 19 plate. Figure 14.9 shows sections taken from the middle of each end of each plate evaluated. Note the extended flash (or fishtail shape) associated with plates that have the 2219 alloy cover plates. No flaking, by ORNL's definition, was found. In plate 973-1-8, with cover plates of 6061 alloy that were half the normal thickness, and plate 975-4-8, with 2219 alloy cover plates, the flash occurred on both ends of the plates.

Note that the data presented here are from a limited number of fuel plates (only one plate representing each set of variables). Further investigations should be made by commercial fabricators to determine the suitability of other rolling processes.

Table 14.5. Comparison of Core End Thickness with Average Core Thickness

Plate Number	Average Thickness (in.)	Maximum Thickening of Core (in.)	Maximum Thickening of Core (%)	Average Core End Thickness (in.)	Plate Characteristic
Sample 3	0.0192	0.0301	157		Reference type 8 plate
973-1-8	0.0194	0.0268	138	0.0253	Cover plates one-half of normal thickness
975-3-8	0.0178	0.0268	155	0.0220	2219 alloy inserts
975-4-8	0.0206	0.0304	148	0.0265	2219 alloy cover plates
Sample 3	0.0201	0.0404	201		Reference type 19 plate
977-1-19	0.0337	0.0365	108	0.0349	Core twice normal thickness
976-3-19	0.0169	0.0212	125	0.0196	2219 alloy inserts
976-4-19	0.0202	0.0268	133	0.0238	2219 alloy inserts

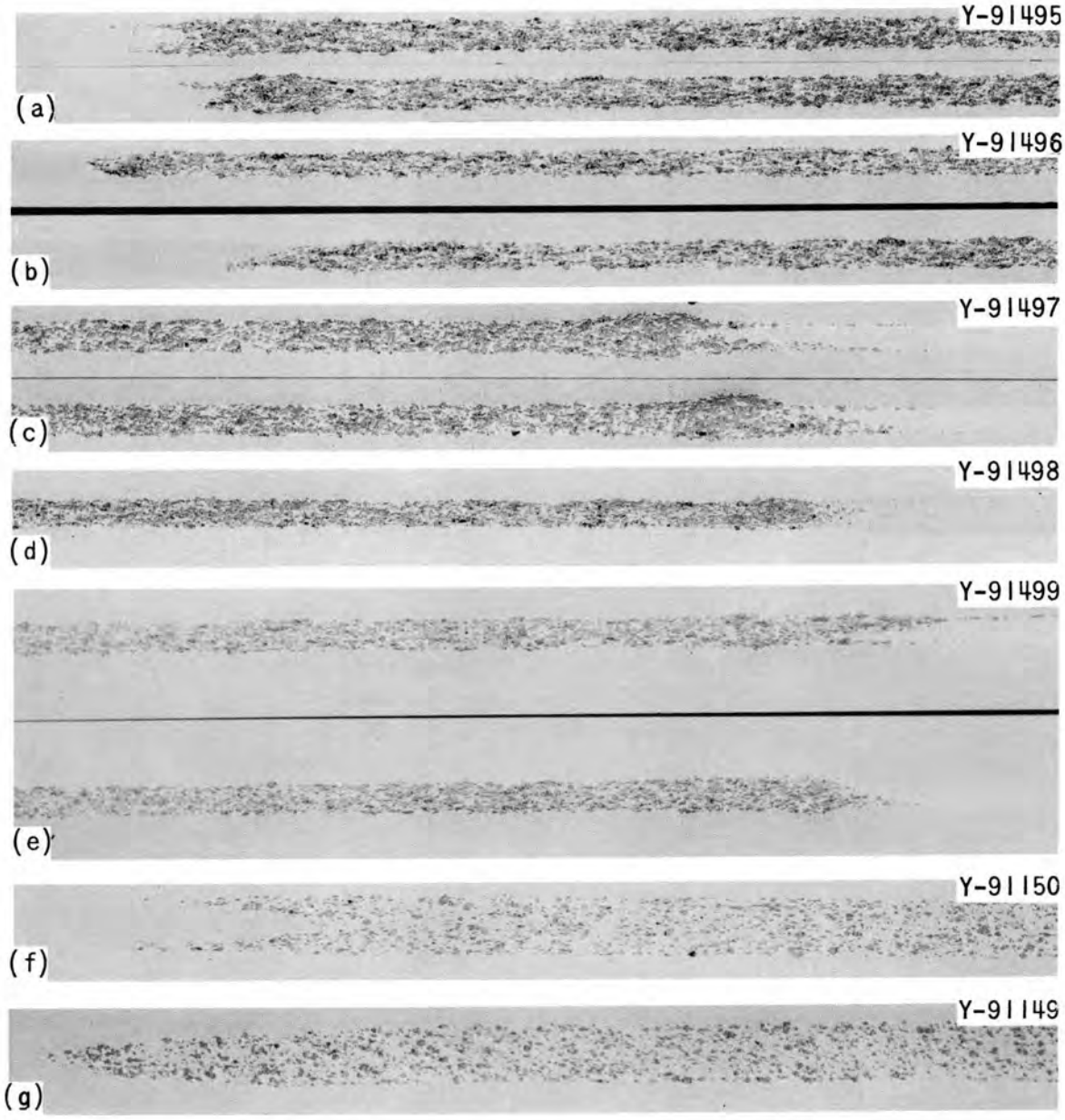

Fig. 14.9. Sections of Fuel Plates Showing End Effects Using Different Billet Parameters: (a) Plate 973-1-9, (b) Plate 975-3-8, (c) Plate 975-4-8, (d) Plate 976-3-19, (e) Plate 976-4-19, (f) and (g) Plate 977-1-19.

Fabrication of Plates Containing Burned U_3O_8 (M. M. Martin, J. H. Erwin)

Our fabrication and irradiation experience indicates burned U_3O_8 to be an inexpensive fuel that performs satisfactorily in a reactor under conditions similar to those of HFIR of advanced loading. To further define its fabrication characteristics, we are investigating the chemical compatibility of burned U_3O_8 with Alcoa 101 aluminum at fabrication temperatures of 500, 525, 550, 575, and 600°C. Individual blends of 49.43 wt % U_3O_8-Al powders were pressed at 30 tsi to 91%-dense compacts that were then degassed for 2 hr at their designed fabrication temperatures. The degassing operation caused less than 2% growth in any of the pressed compacts. The treatments at 525 and 600°C produced maximal and minimal changes of 1.7 and 1.1 vol %, respectively.

After the degassing operation, the compacts were hermetically sealed in type 1100 aluminum alloy by roll bonding to a total reduction in thickness of 87.5% at the degassing temperature (the last 20% at room temperature). We chose the type 1100 aluminum alloy so that we could examine the compatibility at 550 and 600°C without having the eutectic melting that occurs in type 6061 alloys. With these data for higher temperatures, we can compare the burned oxide with the high-fired oxide that was tested several years ago. For ease of fabrication, we chose core geometry and cladding thickness identical to those in our miniature plates for irradiation testing. The two final heat treatments, at the same temperature at which each compact was degassed, were for 3 and 93 hr in air. Surprisingly, this fabrication scheme did not cause the compacts to densify. The void volume retained by the core (10.9 vol %) was also independent of the fabrication temperature and duration of the final anneal. Fabrication temperature is probably an insignificant variable because, in the temperature range of these tests, the strength of the type 1100 alloy is very low and does not vary much with temperature and because there is apparently little or no problem of incompatibility between the fuel and Al.

The plates fabricated for the investigation of compatibility appeared sound and showed no evidence of blistering. But ultrasonic inspection, in reference to a 1/8-in.-diam flat-bottom hole in the HFIR

standard, indicated gross nonbonds over the entire area of the core. For this inspection, we feel that the HFIR standard is a poor reference for plates clad with Al and containing burned U_3O_8. Further, the difference in core void volume between these experimental plates clad with type 1100 aluminum alloy and the HFIR standard — a difference of about 7 vol % — may account for a significant portion of the increased level of sound attenuation. We shall examine this more thoroughly. Sections of the plates are now being polished for visual evidence of nonbonds or reaction products between the fuel and matrix and/or cladding.

Cores of 49.43 wt % burned U_3O_8-Al, to be rolled into miniature plates for our irradiation and compatibility investigations, were clad and framed with the aluminum alloys 2219, 6061, and 1100. As one would expect, these material combinations respond differently to fabrication. We found that the type of cladding greatly affects the degree of dogboning and void concentration in the fuel core. Average values for these important effects are shown in Table 14.6 for plates clad with alloy types 6061, 2219, and 1100, all fabricated at 500°C. As noted before,[3] the compressive strength of the cladding (shown in the last column of Table 14.6) is related to dogboning. We estimate that the compressive

[3]J. H. Erwin and W. R. Martin, Fuels and Materials Development Program Quart. Progr. Rept. June 30, 1968, ORNL-4330, pp. 320–321.

Table 14.6. Effect of Type of Cladding on Fabrication Voids and Dogboning in Sample Plates Containing 49.43 wt % Burned U_3O_8-101 Aluminum Cores

Number of Plates	Aluminum Cladding Alloy	Fabrication Voids (vol %)	Maximum Dogboning[a] (%)	Compressive Strength of Cladding at 500°C for 5% Deformation (psi)
2	1100	10.9	130	1000
10	6061	7.9	113	1900
5	2219	6.0	104	2300

[a]Determined from measurements of x-ray attenuation.

strength of the core is between 2500 and 3100 psi. Dogboning and void concentration follow the same trend; that is, their values increase when weaker cladding materials are used. Thus, replacing type 6061 alloy with type 2219 alloy on a fuel plate for the ATR, for example, would decrease the degree of dogboning at the core ends. The permissible burnup level may be reduced, however, since less space is available for the accumulation of irradiation-induced growth from gaseous fusion products and solid fission fragments.

Grinding and Crushing of UAl_x Fuel (G. L. Copeland)

A major problem in the preparation of UAl_x fuel is the crushing of the arc-melted buttons to particles of usable size without excessive production of particles below the 325 mesh size. Present specifications for the ATR require −100 mesh particles, with a maximum of 25 wt % being −325 mesh, and a uranium content of 69 ± 3 wt % (we generally refer to this composition as hyperstoichiometric UAl_3 in our development work). While most of the commonly used crushing devices produce about 50% fines (−325 mesh) in −100 mesh material, we previously showed that using a roll crusher greatly improved yields with both the hyperstoichiometric and the hypostoichiometric (≥ 74 wt % U) compositions.[4] The −100 mesh fraction of hyperstoichiometric UAl_3, as cast and as annealed, contained, respectively, 15.9 and 24.1 wt % of −325 mesh material. Neither product would require recycling fines to meet the ATR specifications. However, both materials contained particles that tended to roll into flakes rather than be crushed. These remained +100 mesh and accounted for 14.8 wt % of the annealed material and 35.1 wt % of the as-cast material.

During this reporting period, we repeated this experiment with 100-g batches of the material, both as annealed and as cast, with essentially identical results. Because of the decrease in flaking after the anneal, we concluded that areas rich in Al were primarily responsible for the deformation. This is confirmed by the variation in uranium content shown in Table 14.7. The hypostoichiometric UAl_3 included in

[4]G. L. Copeland and M. M. Martin, Fuels and Materials Development Program Quart. Progr. Rept. Sept. 30, 1968, ORNL-4350, pp. 270–275.

Table 14.7. Uranium Concentration in UAl_x After Roll Crushing

U.S. Standard Mesh Size	Uranium Concentration (wt %)		
	Hyperstoichiometric UAl_x As Cast	Hyperstoichiometric UAl_x As Annealed	Hypostoichiometric UAl_x As Cast
+100	68.17	69.04	74.82
−100 +325	70.01	69.10	73.67
−325	69.75	69.30	70.85

Table 14.7 also shows a variation in uranium content for the various size fractions. For hypostoichiometric fuels, however, the large particles are rich in U rather than Al. Each batch of alloy was turned and remelted five times during preparation, but there was still segregation in the ingots. This indicates that the as-cast material must be annealed for product homogeneity.

The +100 mesh flake material from the roll crushing of hyperstoichiometric UAl_3 was passed through a high-speed hammer mill in an attempt to break up the flakes. Roughly 33% of the flake material was broken into usable size range. This decreased the amount of material for recycle to about 23 wt % for the as-cast material and about 10 wt % for the annealed material. Improved yields could probably be obtained by further crushing of the flakes, but we are now attempting to improve the yield directly from the roll crusher.

We attempted to reduce flaking by making a larger reduction in the first pass through the roll crusher. Instead of the usual practice of passing the material through three roll spacings at 0.010, 0.006, and 0.003 in., we passed −10 mesh hyperstoichiometric material directly through the 0.006-in. (about 100 mesh) roll spacing and then through the 0.003-in. spacing. The amount of flaking (+100 mesh material) was increased to 47% for the as-cast material but was decreased to 9.7% for the annealed material. In each case, however, the −100 mesh fraction contained more fines − 22.2% for the as-cast material and 27.7% for the annealed material.

We next increased the uranium content to 71 wt % and annealed the material 72 hr at 600°C to decrease the amount of aluminum-rich area. We found that this material had to be crushed in an inert atmosphere to prevent burning (whereas the material with 69 wt % U could be crushed slowly in air without ignition). We hand crushed 1100 g of this material with 71 wt % U in an inert atmosphere to about 1/4-in. diameter and then passed it through successively smaller roll spacings down to 0.010 in. The −100 mesh fraction was removed at this point, and the remainder of the material was passed through a 0.006-in. roll spacing. The −100 mesh fraction was again removed, and the remainder was passed through a 0.003-in. roll spacing. The separated distribution after roll crushing is shown below:

U.S. Standard Mesh Size	Grams	Weight Percent
+60	11.690	1.07
−60 +100	16.565	1.51
−100 +140	256.055	23.41
−140 +200	230.995	21.12
−200 +270	96.393	8.81
−270 +325	81.917	7.49
−325	399.970	36.57
TOTAL	1093.585	99.98

The flaking was almost eliminated: there was only 1.07% flaking that could not be crushed further in the roll crusher. The amount of fines generated increased, however, especially in the final pass. The percentage of fines in −100 mesh material was about 33% before the final pass. A summary analysis of the size distribution is given below:

	Grams	Percent of Starting Weight
Usable material for ATR (−100 mesh with 25% fines)	887.147	79.92
Returned for further crushing (−60 +100)	16.565	1.49
Recycle		
Flake (+60)	11.690	1.05
Excess fines	178.183	16.05
Loss	16	1.44

From these results one can conclude that even a variation of 2 wt % in the uranium content (69 vs 71 wt % U in UAl_x) can affect grinding and crushing behavior. The 69 wt % U hyperstoichiometric fuel gave an approximate total yield of 90% compared to 80% for the alloy containing 71 wt % U fuel. The unusable portion of the 69 wt % U fuel was oversize flakes, and the unusable portion of the 71 wt % U fuel was fines (< 325 mesh). Clearly, these two hyperstoichiometric alloys behaved differently during powder preparation. Further work is in progress on the effect of uranium concentration on the yield of usable material.

Roll Bonding of Unclad Type 6061 Aluminum (J. H. Erwin)

Fuel plates are normally fabricated of alclad plate (base alloy with type 1100 aluminum alloy cladding) to ensure that a reliable metallurgical bond can be developed during roll bonding. The prime disadvantage of the unclad technique is the difficulty of procuring thick sheet, the type normally used for frame material. By substituting a sheet of unclad type 6061 alloy for the alclad frame and by using chemical cleaning techniques, satisfactory bonding can be achieved during rolling as reported.[5] However, a similar investigation of the interface between two surfaces of type 6061 aluminum alloy has not been reported. While Beaver *et al.*[6] have reported extensive blistering of roll-bonded type 6061 aluminum fuel plates produced from scratch-brushed surfaces, little has been reported on the roll bonding of type 6061 alloy after chemical cleaning.

We are investigating the degree of grain growth that develops at the interface between chemically cleaned pieces of unclad type 6061 aluminum alloy when they are roll bonded at 500°C to various reductions. The fabrication variables of interest are (1) surface preparation, (2) temperature, (3) reduction per pass in the rolling mill, and (4) total billet reduction; all can affect the quality of the metallurgical bond.

---

[5] J. H. Erwin, Metals and Ceramics Div. Ann. Progr. Rept. June 30, 1967, ORNL-4170, pp. 179–181.

[6] R. J. Beaver, J. W. Tackett, J. H. Erwin, G. M. Slaughter, and W. J. Kucera, Initial Development of HFIR Fuel Assemblies, ORNL-4108 (October 1967).

Each type 6061 aluminum alloy plate, 5 in. wide by 8 1/2 in. long, was treated for 2 min in an Oakite 160 solution and then rinsed in 42% HNO_3 in water. All plates were given a final rinse in cold water.

Five plates of type 6061 aluminum were chemically cleaned, stacked together, and welded to form a billet that could be rolled. All parts of each billet were handled as a unit. Five such billets were rolled to reductions of 4:1, 6:1, 10:1, 14:1, and 18:1. The relative interfacial grain growth in the rolled plate was established by measurement of both transverse and longitudinal metallographical samples 1 in. long. These data are summarized in Table 14.8. It is apparent that superior bonds were achieved with the higher reduction ratios. In general, both the upper and lower limits of interfacial grain growth increased with

Table 14.8. Interfacial Grain Growth in Five-Ply Billets of Type 6061 Aluminum Rolled[a] to Five Different Reduction Ratios

	Interfacial Grain Growth (%)				
	4:1	6:1	10:1	14:1	18:1
Transverse view of interfaces[b]					
	84.6	91.4	91.9	99.3	96.2
	79.4	86.8	89.4	98.3	96.1
	67.3	73.2	85.8	90.8	95.5
	59.9	69.4	84.0	88.7	60.0
Longitudinal view of interfaces[b]					
	80.6	88.7	93.3	97.9	98.1
	75.8	88.5	90.6	97.2	94.8
	45.7	88.1	78.8	95.9	93.4
	43.4	70.5	77.8	93.7	62.9

[a]All billets were reduced 25% per mill pass at 500°C.

[b]Percentages for the four interfaces in each five-ply billet are arranged in vertically descending order, from maximum to minimum values.

increasing reduction of area at 500°C. However, the 60 to 63% grain growth shown for the sample reduced 18:1 is inconsistent with the other results. This datum point is real and most likely represents an insufficient control over the cleaning process due to our lack of knowledge of what is causing the problem. Cleaning procedures will have to be studied further, and operational procedures will have to be established to improve the reliability of the bond.

Irradiation Studies of Dispersion Plates

Preparation and Characterization of Test Plates (M. M. Martin, J. H. Erwin, A. E. Richt, B. E. Foster, S. D. Snyder, K. V. Cook, C. V. Dodd)

Our experiment in the ETR continues the investigation of the effect of powder fines on the irradiation performance of burned and high-fired U_3O_8 dispersed in Al. As scheduled,[7] ORNL's eight miniature fuel plates containing the two types of oxide with 10, 25, and 50% fines were fabricated and inserted into the G-12 loop for the start of ETR cycle 99. The plates are performing satisfactorily after an exposure of 3666 Mwd. We plan to expose the plates through the remainder of cycle 99 and all of cycle 100.

We fabricated both sample and instrumented miniature fuel plates for another G-12 loop experiment in ETR cycle 101. Our goal is to reduce the temperature drop that occurs across the 1- to 2-mil-thick oxide film on aluminum-clad fuel plates. In this test, we will investigate the performance in the reactor of a new electroless nickel coating technique for fuel plates clad with both types 6061 and 2219 alloys. The innovation in this new technique is in the procedure for initial cleaning of the Al that permits the electroless deposition of a tightly adhering coating of 7 to 8 wt % P-Ni alloy without a precoating of Zn or Cu (Union Carbide procedure K-L-3088 as developed by R. R. Wright, G. S. Petit, and C. C. Wright). Figure 14.10 shows the as-plated

[7] M. M. Martin, J. H. Erwin, A. E. Richt, W. R. Martin, and K. V. Cook, Fuels and Materials Development Program Quart. Progr. Rept. Sept. 30, 1968, ORNL-4350, pp. 260–265.

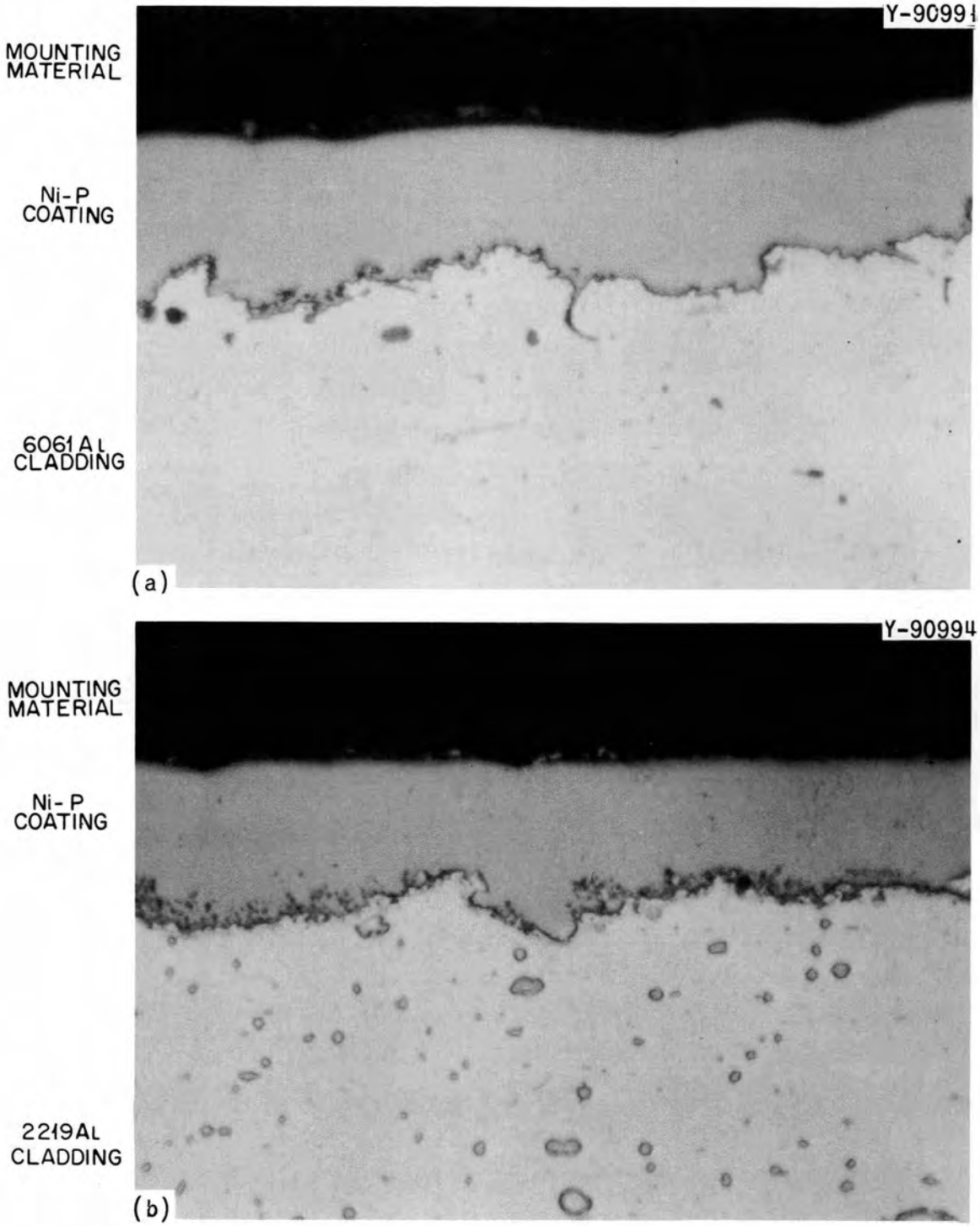

Fig. 14.10. Photographs of Electrolessly Deposited Nickel-Phosphorus Alloy on Types (a) 6061 and (b) 2219 Aluminum Alloys. As polished. 1000×.

deposit on the two aluminum alloys. In a recent test out of reactor, this coating on type 1100 aluminum alloy withstood a heat flux of 470 w/cm^2 for 500 hr in flowing deionized water at 238°C without spalling.[8] This is quite encouraging since the earlier coating completely spalled from over the fuel-core region under similar conditions of heat flux and temperature[9] in the reactor. The high heat-flux test out of reactor was not run.

Table 14.9 describes the plates to be irradiated in ETR cycle 101. The fuel composition is 49.43 wt % burned U_3O_8 dispersed in Alcoa 101 aluminum alloy. In terms of fissile material, this dispersion contains 1.42 g $^{235}U/cm^3$ of fabricated core volume and represents a 25% increase over the present concentrations for HFIR plates. Characteristics of the

[8]John C. Griess, personal communication, October 1968.

[9]W. C. Francis and R. A. Moen, Annual Progress Report for FY 1966. Reactor Fuels and Materials Development, IDO-17218, pp. 105–108.

Table 14.9. Miniature Test Plates for ETR G-12 Loop Irradiations in Cycle 101

Plate Reference Number	Cladding	Average Thickness of Nickel Coating[a] (mils)	Loading of ^{235}U (g)	Location in G-12 Loop	
				Tier	Slot
0-68-1628	6061 Al, Ni coated	0.62	2.446	3	1[b]
0-68-1636	6061 Al, Ni coated	0.60	2.452	3	2
0-68-1643	2219 Al, Ni coated	0.59	2.453	3	3
0-68-1635	6061 Al		2.451	3	4
0-68-1630	6061 Al, Ni coated	0.65	2.451	4	1[b]
0-68-1638	6061 Al, Ni coated	0.62	2.452	4	2
0-68-1642	2219 Al, Ni coated	0.59	2.450	4	3
0-68-1633	6061 Al		2.454	4	4

[a]Calculated from weight and density changes after plating.

[b]Instrumented plates.

U_3O_8, designated PB5, and of the matrix Al have been reported.[10] Two wrought aluminum-base cladding alloys are used: types 6061 and 2219. The latter material is stronger than the former[11] and should reduce dog-boning during fabrication.

We used an eddy-current test to measure the thickness of the Ni-P coating on the aluminum-clad irradiation test plates. A commercial eddy-current instrument, the Dermitron, measured essentially the spacing between the test coil and the aluminum cladding, since the electroless nickel deposit has a lower electrical conductivity than either type 6061 or type 2219 aluminum alloy. If care is taken in positioning the coil, the spacing can be related to the thickness of the coating. We obtained the eddy-current response on a series of standard, unfueled plates of both the 6061 and 2219 alloys that were prepared with various thicknesses of the Ni-P coating. Metallographic measurements of coating thickness were then correlated to the eddy-current response.

Thirty eddy-current measurements were made on each of the nickel-coated fuel plates described above. Table 14.10 summarizes these data and permits comparison with calculated values based on weight and density changes before and after plating. The two techniques differ in the worst case, for plate 0-68-1642, by only 0.09 mil. The eddy-current measurements are reproducible to ±0.01 mil and are preferred. However, each determination represents the coating thickness averaged over an area 100 mils in diameter. On the coated, all-aluminum plates examined optically, point variation in coating thicknesses were seen to be about ±10% from the value for the averaged area.

The fabrication of the miniature test plates proceeded smoothly. As indicated in Table 14.11, eight plates, or 40% of the production, were rejected. The surface defects appeared after plating and probably resulted from improper handling of the fully annealed fuel plates. The small, permissible variations in core dimensions and location within the

---

[10]M. M. Martin, J. H. Erwin, A. E. Richt, W. R. Martin, and K. V. Cook, Fuels and Materials Development Program Quart. Progr. Rept. Sept. 30, 1968, ORNL-4350, pp. 260–265.

[11]See J. H. Erwin, W. R. Martin, and R. W. Knight, "Investigations of Nonuniform Deformation in Simulated Fuel Plates," pp. 223–234, this report.

Table 14.10. Summary of Measurements, by Eddy-Current Techniques, of Coating on Miniature Test Plates

Plate Reference Number	Coating Thickness (mils)			Calculated Average Thickness (mils)
	Maximum	Minimum	Average	
0-68-1628[a]	0.650	0.572	0.612	0.62
0-68-1630[a]	0.770	0.677	0.719	0.65
0-68-1636	0.715	0.585	0.644	0.60
0-68-1638	0.730	0.622	0.672	0.62
0-68-1642	0.720	0.654	0.676	0.59
0-68-1643	0.720	0.629	0.664	0.59

[a]Instrumented plates.

Table 14.11. Summary of Fuel Plate Yield

Reason for Rejection	Number of Plates Rejected[a]	Percentage
Surface	2	10
Plate dimensions	1	5
Core dimensions	1	5
Core location	2	10
Visually detected nonbonds	0	0
Ultrasonic nonbonds	2	10
Uranium homogeneity	0	0
TOTAL rejected	8	40

[a]Total of 20 plates fabricated.

aluminum envelope place rigorous demands on our ability for plate rolling and core marking, and some rejections for these requirements are expected. Ultrasonic indications of nonbond, based on a 1/8-in.-diam flat-bottom hole in the HFIR standard containing high-fired oxide, continues to be a problem for plates containing the highly fragmented burned fuel. New ultrasonic references that are being fabricated from plates bearing burned U_3O_8 will undoubtedly lower these spurious rejections.

Postirradiation Examination of Miniature Fuel Plates (A. E. Richt, M. M. Martin)

Six miniature fuel plates that were irradiated in the G-12 loop of the ETR are being examined in the Oak Ridge Research Reactor hot cells to evaluate their irradiation behavior. These plates contained fuel loadings of 100 and 125% of that now used in the outer annulus of HFIR fuel elements (actual values are shown in Table 14.12). The fuel was incorporated in the test plates as dispersions of either U_3O_8 or UAl_3 in Al.

Examinations showed all six plates to be in excellent physical condition. No blistering or gross damage was visible. Table 14.12 and Fig. 14.11 confirm previous results, that swelling induced by irradiation was significantly less in the U_3O_8 dispersions than in the UAl_3 dispersions.

Metallographic examination of sections of the irradiated fuel plates showed no cracking of the matrix, blistering, or other indications of actual or incipient failure. We did, however, find considerable differences in the extent of reaction between the fuel particles and the aluminum matrix in the specimens fueled with U_3O_8. As shown in Fig. 14.12, there was only a minimal reaction in the microstructure of the plate (0-56-899) fueled with the high-fired or HFIR-grade of U_3O_8. The fuel particles in the plates fueled with the burned grade of U_3O_8 (0-3-893 and 0-56-894) had completely reacted with the matrix; this resulted in a fuel core composed almost entirely of reaction products (Fig. 14.13). We tentatively attribute the greater extent of reaction in plates fueled with the burned grade of U_3O_8 to the smaller particle size of U_3O_8 in these plates (i.e., greater ratio of surface to volume) and to their more

Table 14.12. Summary of Data for Swelling of Fuel Cores in Miniature Aluminum-Based Fuel Plates

Plate Reference Number	Fuel Dispersoid		Initial Fuel Core Density (% of theoretical)	Measured Specimen Burnup (fissions/cm^3)	Fuel Core Volume Change (%)
	Type	Core Concentration (wt %)			
				$\times 10^{20}$	
0-3-893	Burned U_3O_8	44.8	91.1	15.5	+2.0
0-56-894	Burned U_3O_8	52.8	89.1	13.6	−1.4
0-56-899	High-fired U_3O_8	50.2	96.7	11.7	+1.4
0-24-959	Hydride UAl_3	48.6	97.9	16.9	+6.7
0-24-964	Arc-cast UAl_x	48.6	97.7	15.7	+4.8
0-24-965	Arc-cast UAl_x	48.6	97.7	17.7	+6.0

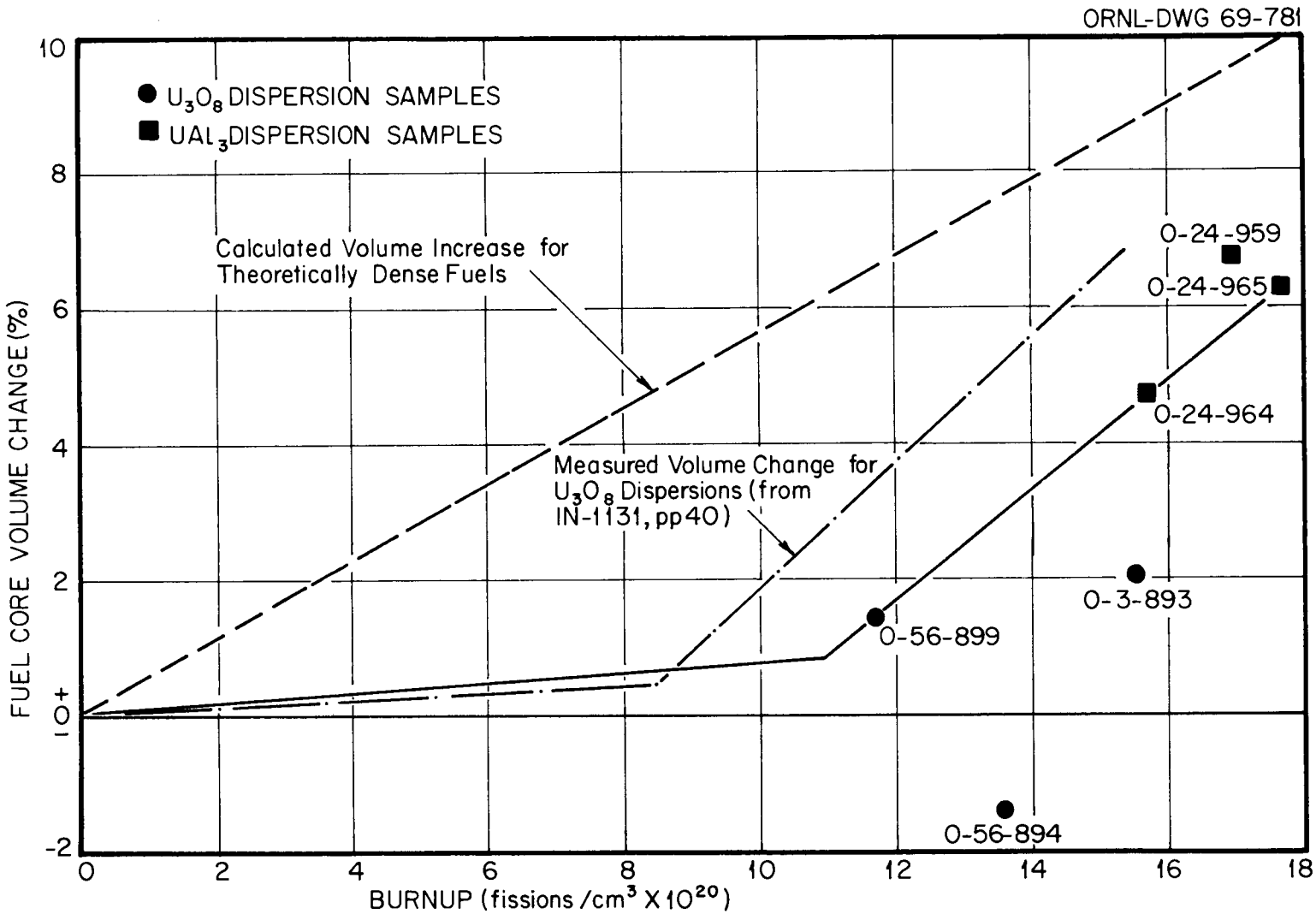

Fig. 14.11. Core Swelling in Miniature Aluminum-Based Fuel Plates. Data reported by Idaho Nuclear Corporation are shown for comparison purposes. [Ref. V. A. Walker, M. J. Graber, and G. W. Gibson, ATR Fuel Materials Development Irradiation Results - Part II, IDO-17157 (June 1966), p. 40.]

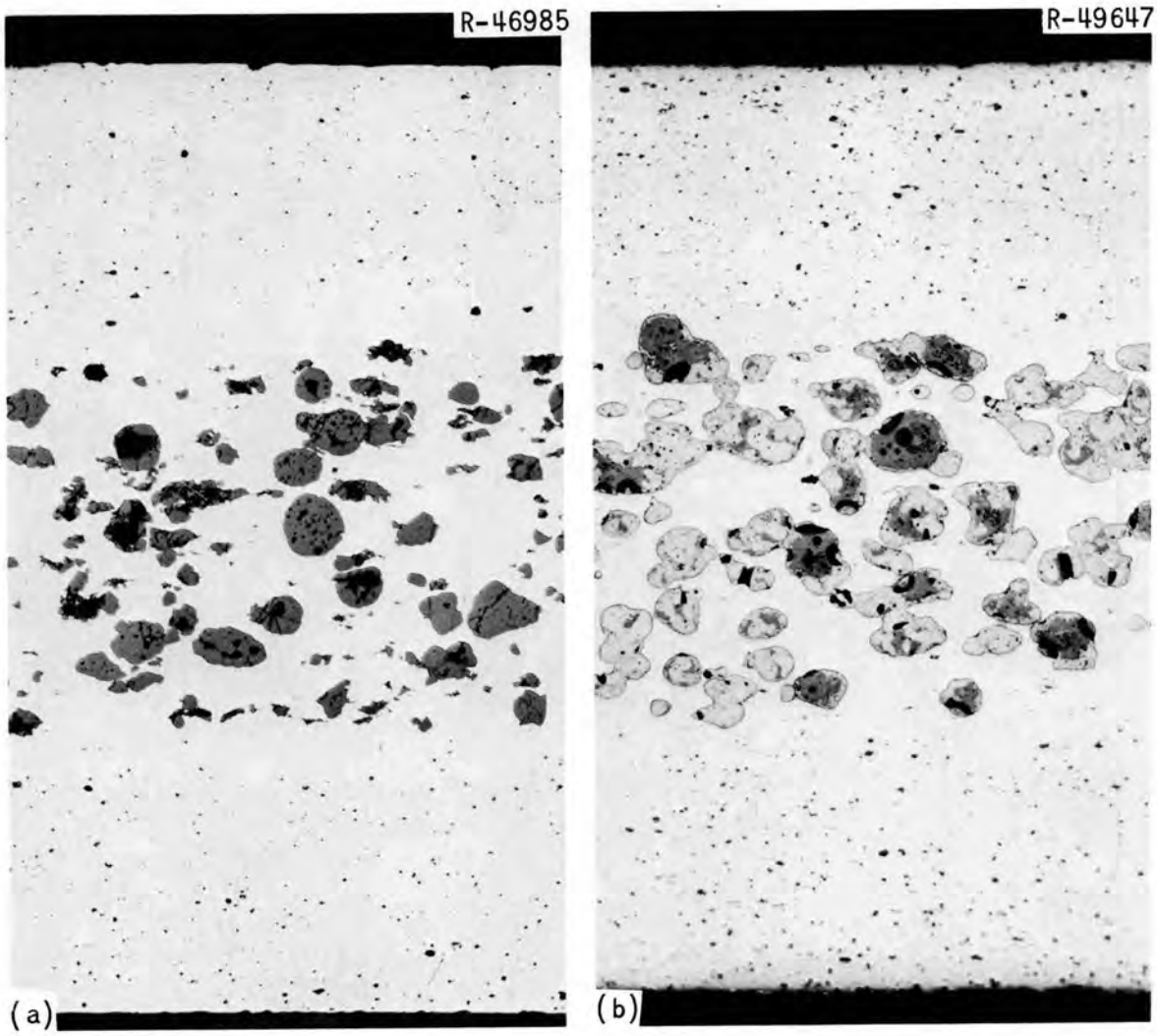

Fig. 14.12. Typical Microstructure of a Miniature Test Plate Fueled with 50 wt % High-Fired U_3O_8. (a) Before irradiation. (b) After 11.7×10^{20} fissions/cm^3. As polished. 100×.

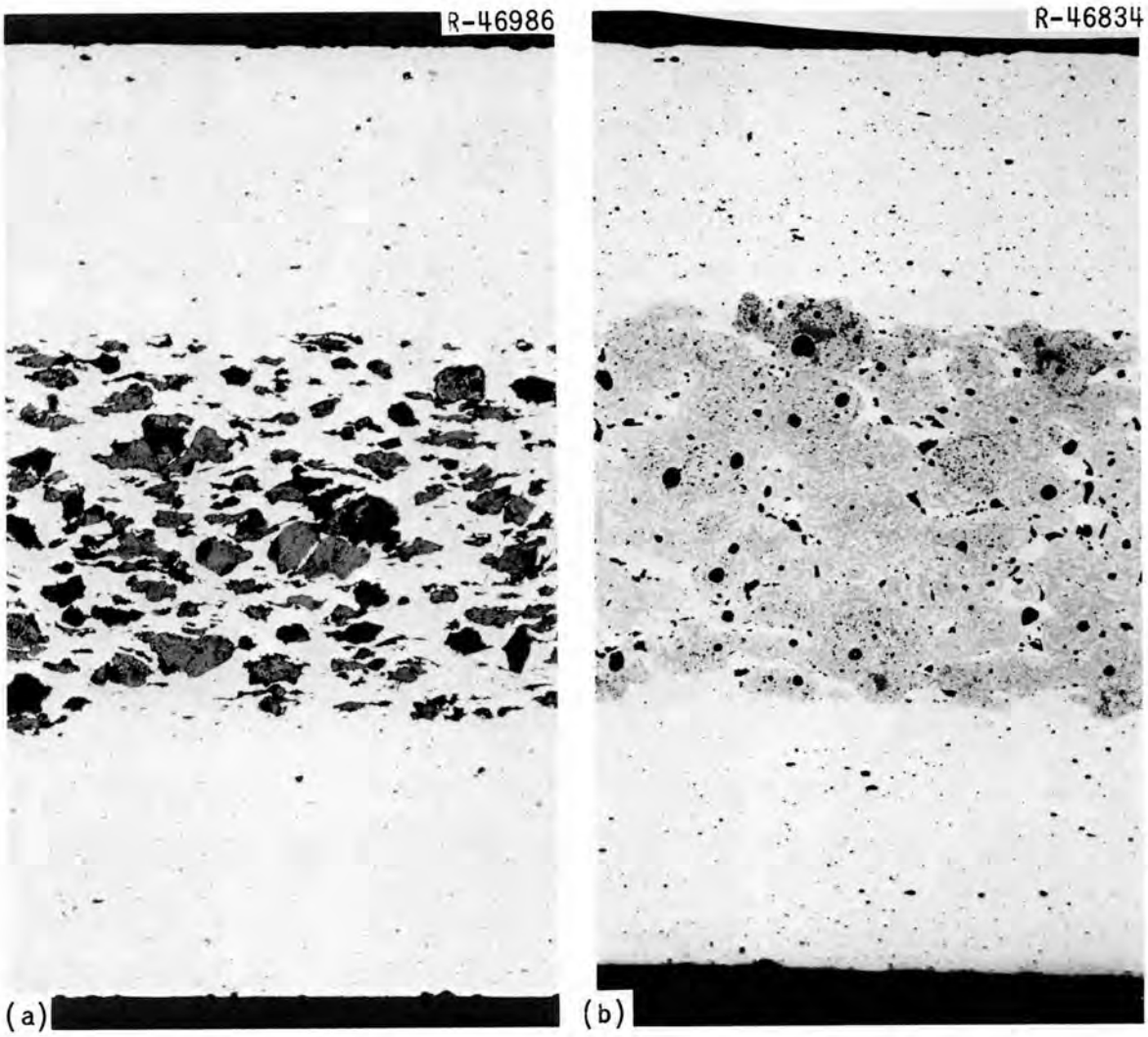

Fig. 14.13. Typical Microstructure of a Miniature Test Plate Fueled with 53 wt % Burned U_3O_8. (a) Before irradiation. (b) After 13.6×10^{20} fissions/cm^3. As polished. 250×.

reactive surfaces. A microstructure typical of one of the plates fueled with UAl_3 is shown in Fig. 14.14 for comparison.

Sections of the six fuel plates were heat treated after irradiation to determine the breakaway swelling or blistering temperature of the various types of fuels. All six specimens survived a 1-hr exposure at 550°C with no visual indications of blistering. This blistering temperature is significantly higher than that reported for other U_3O_8 or UAl_3 dispersion fuels.[12,13] The reasons for this are not yet understood.

As mentioned previously, results of these examinations showed swelling induced by irradiation of the U_3O_8 dispersions to be less than that of the UAl_3 dispersions. However, as indicated by the data for core density in fabricated plates (Table 14.12), the U_3O_8 dispersions also contained significantly more voids than the UAl_3 dispersions. Voids are thought to be beneficial in dispersion fuels by serving as reservoirs that partially accommodate the expected swelling induced by irradiation. Thus, the lesser swelling of the plates fueled with U_3O_8 could be a result of their higher void content. To check this theory, we calculated the amount of swelling that should have occurred in these plates by assuming that the fuel cores swelled at a rate of 6.3% per 10^{21} fissions/cm^3 and that the initial void volumes were 100% effective in accommodating this swelling. As shown in Fig. 14.15, the calculated values agree relatively well with the measured values. Consequently, it appears that the lesser swelling of the U_3O_8 dispersions in these tests can be attributed to the higher content of voids in the fabricated fuels. More importantly, these data indicate that one can calculate with reasonable accuracy the amount of swelling that will occur during irradiation if he knows the total exposure and the void content of the plates as fabricated. Additional tests should be made, however, to establish more conclusively that this relationship holds true.

---

[12]M. M. Martin, A. E. Richt, and W. R. Martin, Fuels and Materials Development Program Quart. Progr. Rept. June 30, 1968, ORNL-4330, pp. 310–311.

[13]G. W. Gibson and M. J. Graber, Idaho Nuclear Corporation, Ann. Progr. Rept. on Reactor Fuels and Materials Development for FY 1967 (Feb. 1968) IN-1131, p. 45.

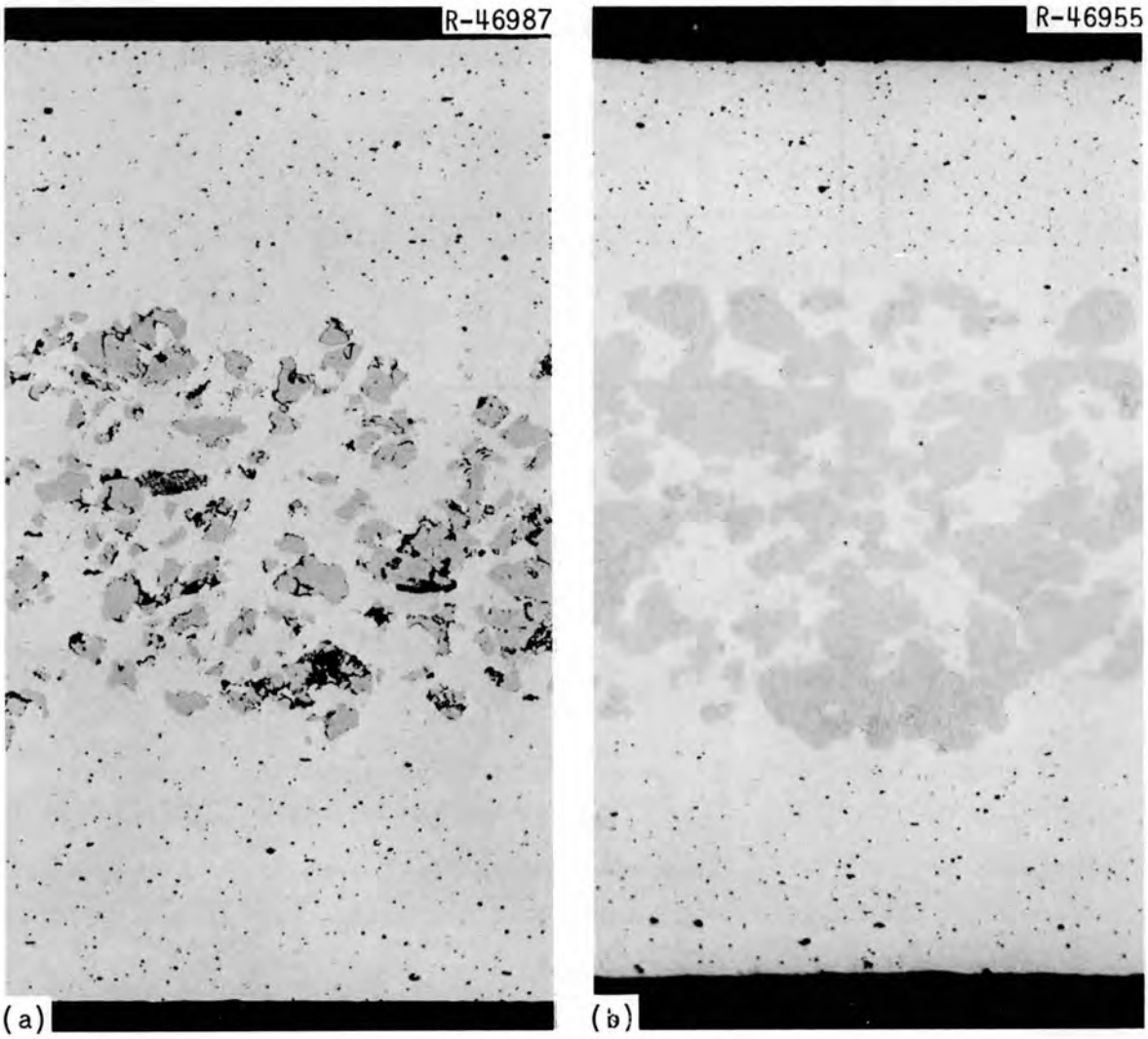

Fig. 14.14. Typical Microstructure of a Miniature Test Plate Fueled with 49 wt % Arc-Cast UAl_3. (a) Before irradiation. (b) After 17.7×10^{20} fissions/cm^3. As polished. 100×.

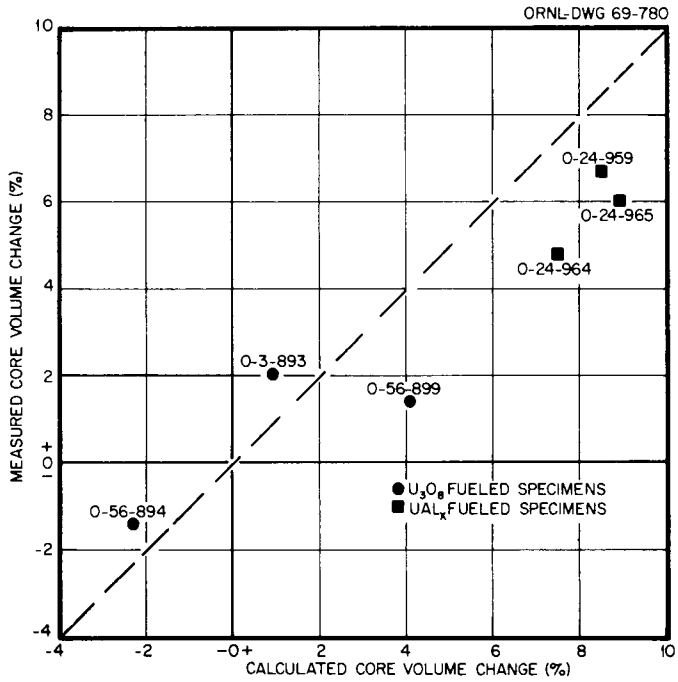

Fig. 14.15. Comparison Between Calculated and Measured Volume Changes in the Cores of Irradiated Aluminum-Based Miniature Fuel Plates.

Studies of Fuel Plate Surfaces

J. V. Cathcart

We continued efforts to develop a protective coating for alclad fuel elements. In our previous work we demonstrated that anodic films formed either in dilute oxalic acid solutions or in a bath containing $TiO(KC_2O_2)_2$, citric acid, and oxalic acid prevented corrosion in static, isothermal tests in water at 200°C. We also showed that the degree of protectiveness of the films formed in oxalic acid was significantly increased when the temperature of the anodizing bath was reduced to 4 to 6°C. Such coatings completely protected specimens of 99.999% Al in tests lasting 1000 hr.

Unfortunately, these films have not effectively inhibited corrosion in test systems that simulate the high heat flux during reactor operations. Last quarter, we prepared two loop sections for testing in the

high heat flux flowing loop designed and operated by John Griess.[14] Both loop sections were fabricated from type 1100 alloy. The interior of the first was coated with an anodic film, about 0.0005 in. thick, formed in an oxalic acid solution; the second loop section was anodized to the same thickness in the $TiO(KC_2O_2)_2$-citric acid-oxalic acid solution. Since films formed in this bath may be tougher and more elastic than those formed in oxalic acid alone, we hoped that they would better withstand the stresses associated with the high heat flux in the loop test.

Both loops were operated for about five days at a water-interface temperature of 200°C. The corrosion rates for both specimens were essentially the same and indistinguishable from the corrosion rate of an uncoated specimen. When the test sections from the loop were examined in cross section by electron microscopy, only the dense, essentially featureless layer of corrosion product formed during loop operation could be seen. No remnant of the original anodic film was detected. This fact and the observation that the corrosion rate during the test matched that for uncoated loops even in the early stages of the test lead one to speculate that the thermal shock accompanying the heating of the loop may have caused the anodic film to spall off early in the test. It is clear, however, that the detailed reasons for the breakdown of the anodic films are still not fully understood.

Our work on the coating program will now return to the study of metallic coatings such as Ni and Zr.

Determination of Fuel-Plate Homogeneity

B. E. Foster S. D. Snyder R. W. McClung

Scanner Calibration Studies

We completed the scanning, at x-ray energies of 50 and 55 kilovolts constant potential (kvcp), of the 32 enriched U_3O_8 fuel plates[15]

---

[14] J. C. Griess, H. C. Savage, and J. L. English, Effect of Heat Flux on the Corrosion of Aluminum by Water. Part IV, ORNL-3541 (February 1964).

[15] B. E. Foster and S. D. Snyder, Fuels and Materials Development Program Quart. Progr. Rept. Sept. 30, 1968, ORNL-4350, p. 288.

fabricated with fuel loadings from nominal to 125% of nominal. These plates were made to determine the effects of particle size on the calibration of the x-ray attenuation system. We have deferred selecting one inner- and one outer-annulus plate of nominal loading and one each of 125% of nominal loading from each group for sample scanning, machining, and chemical analysis for establishing the calibration curves. Instead, we chose to repeat checks on machining accuracy and chemical analysis with the scrap pieces from some earlier plates that had been sampled. We used four plates fueled with U_3O_8 and four plates fueled with UAl_3 for area scanning, area scribing, and subsequent machining. These eight plates produced 128 samples — 15 samples from each of four plates and 17 samples from each of four plates. In two of the 15-sample plates there were no dimensional errors. However, in the remaining six plates (a total of 98 samples), 58 samples were displaced dimensionally from as little as 0.003 in. to as much as 0.024 in. We learned in a subsequent meeting that machine shop personnel had centered their attention on sample dimensions and had overlooked the requirement for precision of sample location. They also proposed a small program that would let them experiment with gang cutting rather than step indexing a single cutter. Preliminary results from ganging four cutters look very favorable, and the machine shop is waiting to receive the rest of the cutters necessary to machine all the samples from a plate with one cut.

The machined samples from the nominally loaded outer-annulus scrap plate fueled with U_3O_8 were sent for determinations of uranium content by chemical analysis. Again we experienced considerable variations (−2% to +35%) between uranium content determined chemically and that determined by attenuation when compared with long-standing calibration. Good correlation was noted between the attenuation data and both the known total fuel content and the desired profile of the tapered fuel core. For another test in progress, we scanned two irradiation test plates fueled with U_3O_8 for determination of total uranium content. We then sent these two plates for total dissolution and determination of uranium content by chemical methods. We are awaiting the results of that chemical analysis.

Radiographic Densitometry

We are continuing our extensive study on the use of radiography and densitometry to determine the qualitative and quantitative capabilities and limitations of these techniques for detecting and measuring fuel inhomogeneity in fuel plates with dispersion cores. Much of our effort has been devoted to evaluating the many variables that can affect the density of radiographic film: x-ray energy, exposure times, distance from film to focal spot, x-ray scattering, film processing, fog factor, densitometer aperture size, and repeatibility.

An ATR-type fuel plate with a flat core of U_3O_8 was used throughout this study. All radiographs were made with a Norelco MG 150 x-ray console with a type C x-ray tube and a large focal spot. All density measurements were made with a Model 12A McBeth-Ansco densitometer with an accuracy of ±0.02 film density. Eastman Kodak Type M x-ray film was used and processed according to the manufacturer's recommendations.

An aluminum step wedge with 26 steps varying in thickness from 0.099 to 0.710 in. in increments of 0.025 in. was used throughout the experiments as a means of standardization as well as calibration. The step wedge was radiographed simultaneously with the fuel plate to give us a calibration curve of film density versus aluminum thickness. A typical calibration curve is shown in Fig. 14.16.

Ten thicknesses (0.011 to 0.137 in.) of type 6061T6 aluminum alloy in four diameters (0.078, 0.125, 0.250, and 0.500 in.) were machined with edges tapered 10°. These were mounted to a 0.005-in.-thick plastic overlay about 3 in. wide × 16 in. long as shown in Fig. 14.17. This overlay was on the fuel plate during radiography to simulate spots that contained excess fuel. The density of the radiograph at each specimen location was obtained at a 0.078-in. aperture on the densitometer because of the large bias introduced with small fuel spots and a larger (1/8 in.) aperture.[15]

The radiographs were made using x-ray energy of both 100 and 50 kvcp; the exposure time (in milliampere minutes) was adjusted to give an overall film density of about 1.0.

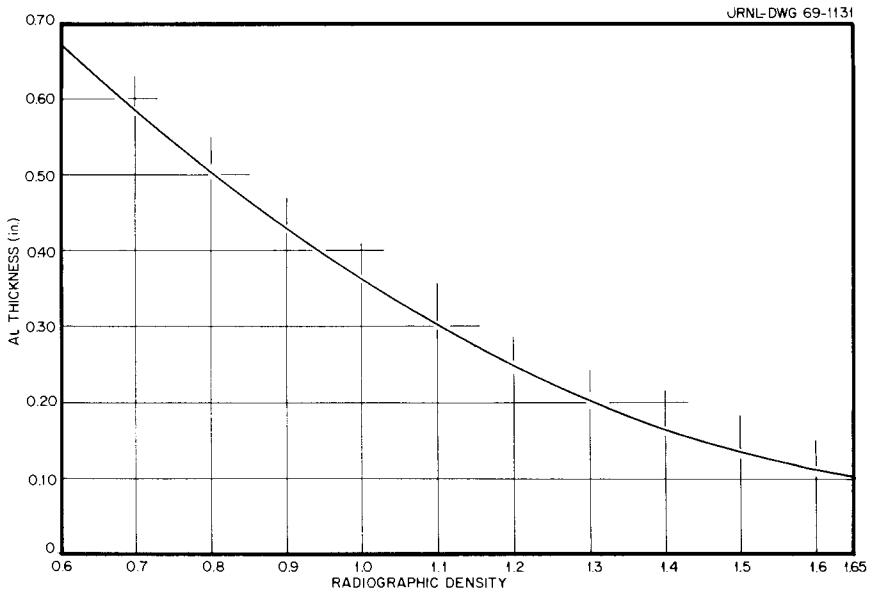

Fig. 14.16. Typical Calibration Curve Relating Aluminum Thickness to Radiographic Density at X-Ray Energy of 100 kvcp.

The average film density over the fueled core was obtained by averaging 25 random density measurements. From the calibration curve of film density versus aluminum thickness, we determined the effective aluminum thickness of the fueled core. The aluminum specimens represented excess material above this effective average value. The values listed in Table 14.13 are the percentage of actual thickness of extra material. The measured percentage shown in this table was obtained by measuring the film density at each specimen location, converting the result to aluminum thickness by means of the step-wedge calibration curve, and calculating the percentage in excess of the effective aluminum thickness of the fueled core. The percentage range shown in this table is due to the ±0.02 tolerance in the accuracy of the densitometer.

It is rather obvious in the table that a 0.078-in. aperture is too large for evaluation of areas of higher density only 0.078 in. in diameter. This may be caused by x-ray scattering and the specimen shape.

We find rather good agreement between the actual and measured percentages when we use a 0.078-in. aperture on 0.125-, 0.250-, and 0.500-in.-diam high-density regions with a radiograph exposed with 100-kvcp energy. The agreement is fairly good on the 50-kvcp radiographs

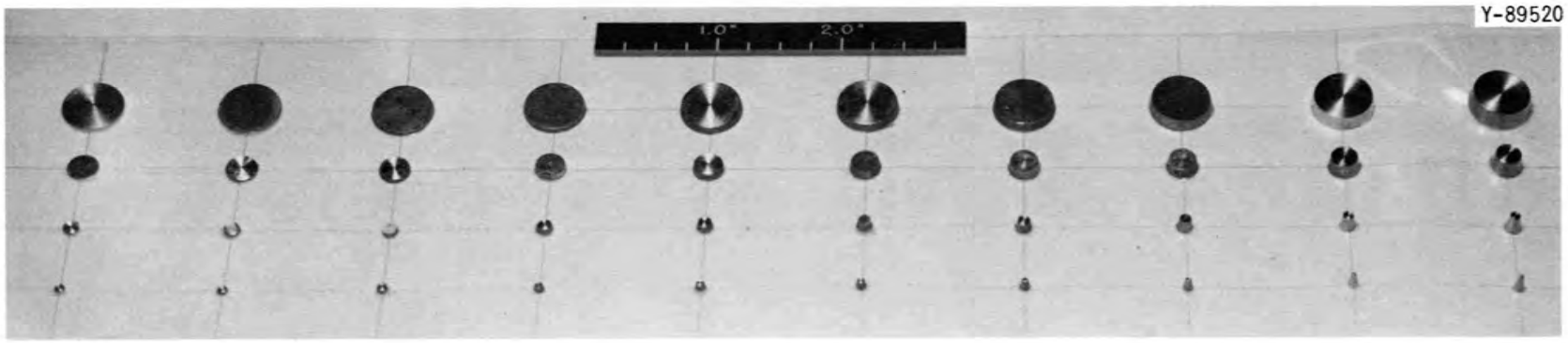

Fig. 14.17. Array of Aluminum Disks Simulating Localized Increase in Fuel Content in a Fuel Plate.

Table 14.13. Actual and Radiographically Determined Value of Increased Material Thickness

Specimen Thickness (in.)	Percentage of Excess Material[a]			
	100-kvcp x rays		50-kvcp x rays	
	Actual, Related to Step Wedge	Measured on Disk	Actual, Related to Step Wedge	Measured on Disk
	0.078-in.-Diam Specimens			
0.0116	3.5	0–5.5	4.0	4.0–7.5
0.0246	7.5	3.6–10.9	8.4	5.8–9.6
0.0370	11.2	7.3–14.6	12.6	14.0–18.8
0.0492	15.0	10.9–17.9	16.8	14.0–18.8
0.0620	18.8	13.1–19.8	21.2	18.8–22.5
0.0742	22.6	16.1–24.0	25.3	19.5–23.9
0.0862	26.2	19.8–28.0	29.4	23.9–28.0
0.0987	30.0	19.8–28.0	33.7	20.5–24.6
0.1202	36.5	22.1–29.8	41.0	22.5–27.0
0.1374	41.8	24.0–31.9	46.9	23.9–28.0
	0.125-in.-Diam Specimens			
0.0117	3.5	0–5.5	4.0	5.8–9.6
0.0245	7.5	3.6–10.9	8.4	9.6–13.3
0.0368	11.2	7.3–14.6	12.6	10.6–14.3
0.0491	15.0	9.1–16.1	16.8	14.0–18.8
0.0614	18.7	14.6–22.2	21.0	19.5–23.9
0.0738	22.4	19.8–28.0	25.2	22.5–27.0
0.0860	26.2	24.0–31.9	29.4	25.6–30.4
0.0985	30.0	28.0–36.5	33.7	30.7–35.5
0.1199	36.4	34.3–43.2	40.9	35.5–40.6
0.1374	41.8	36.5–45.3	46.9	38.2–43.3
	0.250-in.-Diam Specimens			
0.0132	4.0	1.8–9.4	4.5	9.6–13.3
0.0250	7.6	3.6–10.9	8.5	11.7–15.0
0.0369	11.2	7.3–14.6	12.6	14.0–18.8
0.0495	15.0	14.6–22.2	16.9	16.0–20.5
0.0618	18.8	16.1–24.0	21.2	19.5–23.9
0.0742	22.6	19.8–28.0	25.3	22.5–27.0
0.0863	26.2	22.2–29.8	29.4	28.0–32.8
0.0988	30.0	26.1–34.3	33.7	31.7–36.9
0.1202	36.5	34.3–43.2	41.0	36.9–42.0
0.1373	41.8	38.6–47.4	46.9	43.3–49.5

Table 14.13. (continued)

Specimen Thickness (in.)	Percentage of Excess Material[a]			
	100-kvcp x rays		50-kvcp x rays	
	Actual, Related to Step Wedge	Measured on Disk	Actual, Related to Step Wedge	Measured on Disk
	0.500-in.-Diam Specimens			
0.0125	3.8	0.3–7.3	4.3	5.1–8.9
0.0251	7.6	3.6–10.9	8.5	7.5–11.9
0.0373	11.3	7.3–14.6	12.7	9.6–13.3
0.0495	15.0	13.1–19.8	16.9	13.3–17.4
0.0619	18.8	16.1–24.0	21.2	21.5–28.0
0.0742	22.6	19.8–28.0	25.3	24.6–29.4
0.0864	26.2	24.0–31.9	29.4	29.4–34.1
0.0990	30.1	28.0–36.5	33.8	32.8–38.2
0.1203	36.5	34.3–43.2	38.2	38.2–43.3
0.1374	41.8	40.4–50.2	46.9	45.1–51.2

[a]Radiographic density was obtained using a 0.078-in. aperture.

at the higher percentage of excess material but is not as good at the lower percentage.

We would thus conclude that for accurate measurements the aperture size of the densitometer should be somewhat smaller than the region of excess fuel that is of interest. Also, we observed a bias when we radiographed regions of relatively low excess material with 50-kvcp energy.

We are also using the step-wedge standardizing technique in studying the other variables. The use of safelights instead of total darkness during loading of the cassette and film processing merely shifted the overall film density; there was no change (within the ±0.02 density accuracy of the densitometer) in the slope of the calibration curve in the region of interest. Further experiments are needed to evaluate localized variations. The same was true when the film was processed as if the solutions were 2.22°C warmer or colder.

We have found it very difficult to control these many variables and obtain reproducible film densities of the precision required for good quantitative evaluation of fuel inhomogeneity. The use of the step wedge with a separate calibration on each radiograph relieves the requirement

of close control of the many variables. But it must be emphasized that even with the step-wedge calibration, the inaccuracy of ±0.02 in film density due to the inherent limitations of the densitometer is still present and will produce about ±5% uncertainty in the resultant percentage data, as shown in Table 14.13.

This uncertainty may increase when similar measurements are obtained without use of the step-wedge calibration. We attribute this increase in error to variations in energy, film, and processing. We are gathering more quantitative information about these variables.

Development of Ductile Dispersion-Strengthened Aluminum

G. L. Copeland

The objective of this work is to improve the high-temperature ductility of dispersion-strengthened Al through alloy modifications. We have produced alloys containing the solid-solution strengthener Mg and the compound-forming elements Fe, Mo, Zr, Ti, and Cr. When atomized into water from the melt, the latter elements form small, well-dispersed compounds that contribute to the high-temperature strength. Several alloys were fabricated by ball milling atomized powders to increase the oxide content, consolidating the powder by hot pressing, and then hot forming this into rods by extrusion at 30:1 reduction in area. The oxide content varied from < 0.5 wt % for the atomized powders up to about 12 wt % after ball milling for several hours. Where the strength of the alloy prevented extrusion at 30:1, the alloys were extruded at 10:1 and then hot swaged to the total 30:1 reduction in area.

The tensile properties of the alloys consolidated from the atomized powders with no ball milling are presented in Table 14.14. The addition of Mg increases the strength markedly below about 200°C. Above this temperature, there is a slight increase in strength and also in elongation. The alloys containing Fe, Mo, Zr, Ti, and Cr exhibit appreciably greater strengths even up to 450°C while maintaining good ductility. For instance, these alloys are about three times as strong at 300°C as the wrought alloy 6061 in the T6 condition (see footnote to Table 14.14).

Table 14.14. Tensile Properties[a] of Aluminum Alloys Produced from Atomized Powders

	Alloy							
	Al-0	A440-0	A602-0	A204-0	A222-0	M-7-0	M-2-0	M-6-0
Chemical composition,[b] wt %								
Fe		4.1			1.7			
Mo		4.1	3.8	2.1	4.4			
Zr		0.2	0.7	2.4	1.4			
Mg						2.0	4.3	6.2
Ultimate tensile strength,[c] 1000 psi								
Room temperature	14.7	37.0	25.1	32.1	30.2	32.2	44.2	52.6
200°C		26.4	15.8	19.6	20.4	19.1	24.1	24.4
300°C	6.09	18.6	11.6	14.6	15.1	9.91	9.36	7.87
400°C		11.9		8.20	9.70	4.90	4.22	
450°C	2.59	6.85	5.22	5.71	8.20	3.71	3.06	2.77
Uniform elongation, %								
Room temperature	15.1	7.84	8.63	8.64	8.11	11.0	12.9	14.1
200°C		3.10	3.55	3.15	2.34	3.63	4.28	0.22
300°C	0.84	3.16	1.84	2.66	1.77	0.73	0.95	0.41
400°C		2.34		1.53	2.07	2.34	3.42	
450°C	4.75	3.98	2.16	2.12	3.44	4.32	9.02	9.92
Total elongation,[c] %								
Room temperature	27.5	15.6	18.4	16.7	19.2	16.6	14.5	19.7
200°C		13.7	12.7	17.9	16.1	38.0	51.2	44.8
300°C	23.7	14.3	17.4	18.7	17.3	53.8	100.5	98.4
400°C		24.0		37.1	22.0	49.3	75.7	
450°C	40.0	31.0	52.0	41.5	31.0	68.7	83.0	50.2

[a] 0.02 min^{-1} strain rate.

[b] As atomized powders — no ball milling. Oxide contents are between 0.3 and 0.5 wt %. The remainder is Al except for alloys A440, A602, A204, and A222, which contain 0.2% Ti and 0.2% Cr.

[c] For comparison, wrought alloy 6061-T6 has tensile strengths of 45,000, 19,000, and 5,000 psi at room temperature, 200, and 300°C, respectively. Total elongations at these temperatures are 15, 28, and about 80%.

Data from a series of alloys consolidated from powder ball milled for 2 hr are presented in Table 14.15. Although the oxide contents are not yet available, they are probably between 2 and 4 wt %. The magnesium additions increase the strength at temperatures up to about 2200°C; above this temperature, both the strength and elongations are reduced somewhat. The alloys containing Fe, Mo, Zr, Ti, and Cr show increased strengths at all temperatures. The ductility is also improved at the higher temperatures. Both strength and total elongation at 450°C are about 50% higher for these alloys than for unalloyed Al of the same oxide content.

Representative data from alloys of comparable oxide contents around 8.5 wt % are shown in Table 14.16. The trends are the same as those shown by the alloys with lower oxide content. The strength and ductility increases due to the alloying elements are less dramatic at this strength level.

For applications below about 200°C, the tensile strength of dispersion-strengthened Al can be enhanced by the solid-solution strengthening of magnesium additions. The room- and high-temperature strengths of Al-Al_2O_3 dispersions can be improved by using atomized alloy powders containing Fe, Mo, Zr, Ti, and Cr. The ductility for a given strength level is improved by these latter additions.

Table 14.15. Tensile Properties[a] of Dispersion-Strengthened Aluminum Alloys Ball Milled 2 hr[b]

	Alloy						
	A1-2	A440-2	A602-2	A204-2	A222-2	M-7-2	M-6-2
Ultimate tensile strength, 1000 psi							
Room temperature	25.8	37.8	33.3	33.8	30.6	27.7	52.9
200°C	16.5	26.2	21.3	21.0		21.1	24.9
300°C	12.0	18.6	16.0	16.2	14.6	12.5	9.59
400°C	8.77	12.4	11.9	10.4	10.4	8.73	6.57
450°C	6.04	9.54	9.61	8.14	8.40	6.13	6.40
Uniform elongation, %							
Room temperature	7.63	5.98	6.29	7.63	5.98	5.20	5.88
200°C	3.09	5.01	2.36	2.29		1.02	1.44
300°C	1.18	1.82	1.04	1.33	1.31	0.60	0.50
400°C	0.57	0.81	0.82	0.96	0.69	0.69	0.85
450°C	0.49	1.04	1.09	1.45	0.49	0.77	0.69
Total plastic elongation, %							
Room temperature	13.9	10.4	9.14	12.1	9.18	6.98	6.24
200°C	17.6	10.1	8.05	6.51		21.7	23.1
300°C	11.2	8.57	2.70	7.55	14.5	15.2	35.6
400°C	4.75	8.82	3.20	14.8	8.15	1.58	2.36
450°C	4.05	7.72	3.13	7.05	6.00	5.2	2.20

[a] 0.02 min^{-1} strain rate.

[b] Chemical compositions are the same as the alloy types given in Table 14.14 except that the oxide content of these alloys is higher. The oxide contents are not available yet, but they should be between 2 and 4 wt %.

Table 14.16. Chemical Composition and Tensile Properties[a] of Dispersion Strengthened Aluminum Alloys[b]

	Alloy							
	A1-12	A440-8	A602-8	A204-10	A222-8	M-7-8	M-2-12	M-6-12
Oxide content, wt %	8.64	8.37	8.13	7.52	10.07	7.52	8.39	8.73
Ultimate tensile strength, 1000 psi								
Room temperature	51.2	63.5	52.0	53.3	59.0	46.4	67.0	70.8
200°C	36.1	47.5	38.2	38.5	46.4	25.1	33.3	
300°C	25.6	35.4	30.1	29.5	32.9	14.6	23.2	20.5
400°C		26.2	23.8	22.3	21.7	9.38		
450°C	17.8	21.2	20.5	18.2	16.8	7.15	12.8	14.6
Uniform elongation, %								
Room temperature	5.97	2.87	4.86	1.53	0.70	4.20	0.87	0.82
200°C	3.14	1.89	1.97	1.29	1.12	0.60	0.54	
300°C	1.48	1.14	1.34	0.88	1.25	0.34	0.32	0.33
400°C		0.64	0.64	0.56	0.98	0.67		
450°C	0.60	1.02	0.69	0.66	2.26	0.63	0.48	0.34
Total plastic elongation, %								
Room temperature	5.97	2.87	6.15	1.53	0.70	7.49	2.11	1.00
200°C	5.54	2.25	2.99	3.43	2.81	11.6	1.16	
300°C	5.15	2.17	3.05	2.21	1.46	10.1	1.85	2.20
400°C		1.74	1.62	0.93	3.08	5.86		
450°C	1.24	1.50	1.05	1.05	2.47	6.54	1.12	0.48

[a] 0.02 min^{-1} strain rate.

[b] Chemical composition same as in Table 14.14 except oxide content.

PART V

ENGINEERING PROPERTIES OF REACTOR MATERIALS

15. PHYSICAL AND MECHANICAL METALLURGY OF REFRACTORY ALLOYS

P. Patriarca

The purpose of this program is to provide a broad, base-technology evaluation of high-temperature alloys for use in high-performance nuclear reactors and isotopic heat sources for advanced space, terrestrial, and civilian power applications. Principal emphasis is placed on materials problems involving tantalum-, niobium-, molybdenum-, and vanadium-base alloys for systems that use alkali metals as thermodynamic working fluids and heat-transfer media.

Basic Physical Metallurgy Studies

H. Inouye

Solubility, Diffusivity, and Permeability of Interstitials in Refractory Metals (R. L. Wagner)

We are measuring the solubility and the diffusivity of N in W because there is serious disagreement reported in the literature concerning the temperature coefficient of the solubility. We measure with a mass spectrometer the rate at which N is degassed from a resistively heated tungsten wire previously engassed with N at pressures between 1 and 25 torr.

Our solubility, S, and diffusivity, D, data listed in Table 15.1 indicate a positive temperature coefficient of solubility. The results may be summarized in Arrhenius form by
$D = 1.29 \times 10^{-2} \exp(-42{,}300/RT)\,cm^2/sec$ (R is the gas constant and T is absolute temperature) and
$S = 7.5 \times 10^{-2} \exp(-14{,}850/RT)$ torr liter cm^{-3} $torr^{-\frac{1}{2}}$. Table 15.2 gives values for D, S, and K (the permeability, K, is calculated from the relationship K = DS) at 1200 and 1800°C calculated from the expressions given above and those found in the literature.

At 1800°C, our value for D is lower and our value for S is about an order of magnitude greater than the published values. Our values

Table 15.1. Summary of Data on the Diffusivity and Solubility of Nitrogen in Tungsten

Temperature (°C)	Diffusivity (cm^2/sec)	Solubility (torr liter cm^{-3} $torr^{-\frac{1}{2}}$)
1200	8.8×10^{-9}	2.7×10^{-4}
1400	1.8×10^{-8}	9.1×10^{-4}
1400	3.2×10^{-8}	7.2×10^{-4}
1500	1.9×10^{-7}	3.4×10^{-3}
1525	5.8×10^{-8}	1.8×10^{-3}
1600	2.4×10^{-7}	5.7×10^{-4}
1600	1.2×10^{-7}	5.2×10^{-4}
1700	2.5×10^{-7}	3.6×10^{-3}
1800	4.2×10^{-7}	1.9×10^{-3}

for K remain within a factor of two greater than the reported values. We believe the discrepancy in the value for S to be due to the difficulty in measuring solubilities of less than 10 ppm. We are conducting further experiments to determine the reproducibility of our results.

Development of Age-Hardening Refractory Alloys (C. T. Liu, R. W. Carpenter)

The goal of this task is to strengthen refractory metals at high temperatures through precipitation mechanisms that produce fine particles distributed uniformly throughout the matrix. We are studying 12 binary alloys in the Nb-Hf, Nb-Zr, Ta-Hf, and Ta-Zr systems.

The aging characteristics of Nb–53% Hf, Ta–50% Hf, and Ta–65% Hf alloys after oil quenching were reported.[1] Optical metallography showed that the fine, hafnium-rich precipitates were uniformly distributed and had no distinctive shape, but electron micrographs obtained from a two-stage replica method indicate disk-shaped precipitates lying on three mutually perpendicular directions (i.e., [100], [010], and [001])

[1]C. T. Liu, Fuels and Materials Development Program Quart. Progr. Rept. June 30, 1968, ORNL-4330, pp. 345–349.

Table 15.2. Values for Diffusivity, Solubility, and Permeability of Nitrogen in Tungsten at 1200 and 1800°C

Temperature (°C)	Diffusivity (cm^2/sec)	Solubility (torr liter cm^{-3} $torr^{-\frac{1}{2}}$)	Solubility at 1 atm N_2 (ppm)	Permeability (torr liter cm^{-1} sec^{-1} $torr^{-\frac{1}{2}}$)
1200	3.4×10^{-9}	9.1×10^{-4}	2.1	3.1×10^{-12} [a,b]
		5.4×10^{-6}	0.01	
				5.2×10^{-13} [c]
	6.0×10^{-9}	2.5×10^{-4}	0.6	1.5×10^{-12} this study
1800	1.6×10^{-6}	3.4×10^{-4}	0.8	5.5×10^{-10} [a,b]
		2.1×10^{-4}	0.5	
				5.3×10^{-10} [c]
	3.8×10^{-7}	2.8×10^{-3}	6.6	1.0×10^{-9} this study

[a] R. Frauenfelder, Permeation, Diffusion, and Solution of Nitrogen in Tungsten and Molybdenum, WERL-2823-28 (June 30, 1967).

[b] F. J. Norton and A. L. Marshall, Trans. AIME 156, 351 (1944); see also S. Dushman, Scientific Foundations of Vacuum Technique, p. 562, Wiley, New York, 1962.

[c] P. K. Conn, E. C. Duderstadt, and R. E. Fryxell, Measurement of the Permeability of Tungsten to Nitrogen, NASA Cr-72238 (June 1967); also in Trans. Met. Soc. AIME 242, 626 (1968).

of niobium-rich matrix (Fig. 15.1). Rapidly quenched (i.e., oil-quenched) Nb-Hf specimens aged rapidly, and slowly quenched (i.e., inductively heated specimens cooled by radiation) alloys aged much more slowly.[2] In the latter case, the precipitates appeared as coarse rosettes [Fig. 15.2(a) and (b)]. At intermediate quenching rates, the uniform and rosette modes were both present, the uniform mode becoming dominant at higher quenching rates. We explain this behavior as being due to the formation of a far greater number of vacancies by quenching than by slow cooling; these vacancies govern the precipitation process. A calculation based on the vacancy theory[3] revealed that the rate of precipitation in a rapidly quenched specimen may be 10,000 times higher than that in one cooled slowly.

A zone free of precipitates is generally observed near grain and subgrain boundaries in Nb-Hf and Ta-Hf alloys. Occasionally there are small amounts of discontinuous precipitates on the boundaries. A comparison of the aging characteristics of alloys containing different amounts of Hf revealed that the precipitation characteristics described above become less prominent as the concentration of Hf in the alloys increases. For example, no precipitate-free zone is apparent in the Nb—70% Hf alloy aged 3 hr at 1000°C (Fig. 15.3).

The tensile properties of the Nb—53% Hf alloy at room temperature are summarized in Table 15.3. The ultimate tensile strength varied from 108 ksi for the quenched alloy to 70.7 ksi for the overaged alloy. The uniform strain varied from 0.6 to 12.1%. The observed rate of work hardening was low in all cases. The fracture mode was predominantly separation at the grain boundary [Fig. 15.4(a)] with little transgranular fracture [Fig. 15.4(b)], even though grains were obviously severely deformed throughout the gage section.

---

[2]C. T. Liu, Fuels and Materials Development Program Quart. Progr. Rept. Sept. 30, 1968, ORNL-4350, pp. 296—298.

[3]A. Kelly and R. B. Nicolson, Progr. Mater. Sci. 10(3), 172—176 (1963).

Fig. 15.1. Electron Photomicrograph of Nb–40% Hf Alloy Oil-Quenched and Aged 6 hr at 1000° C. 8000×.

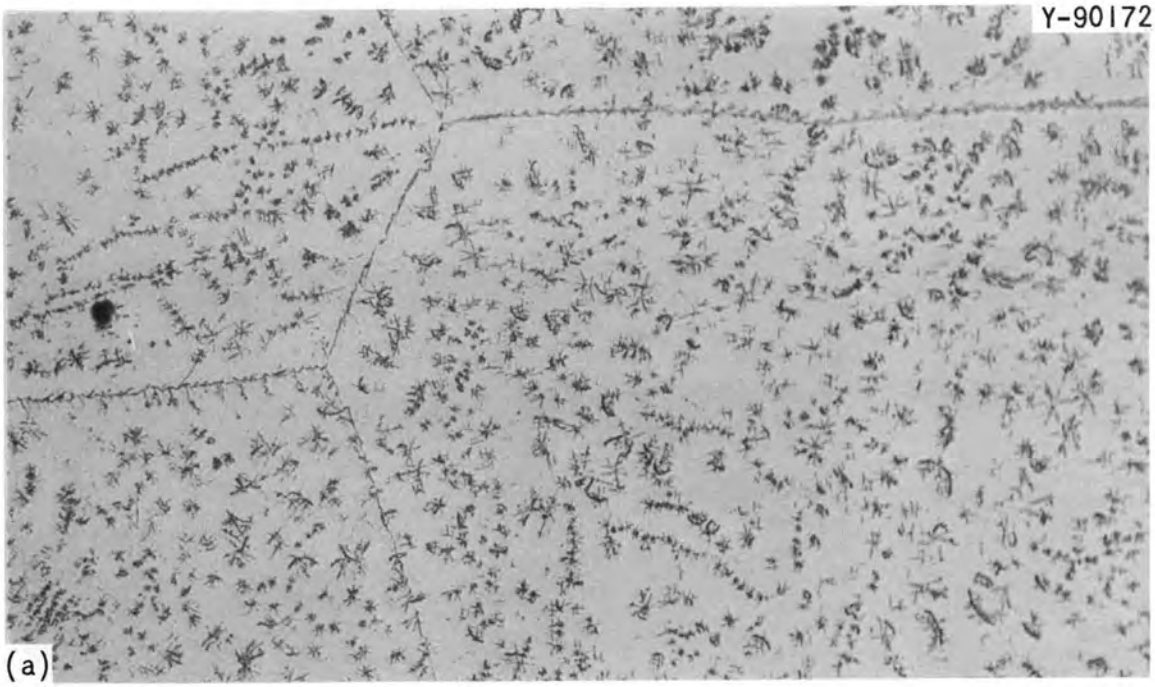

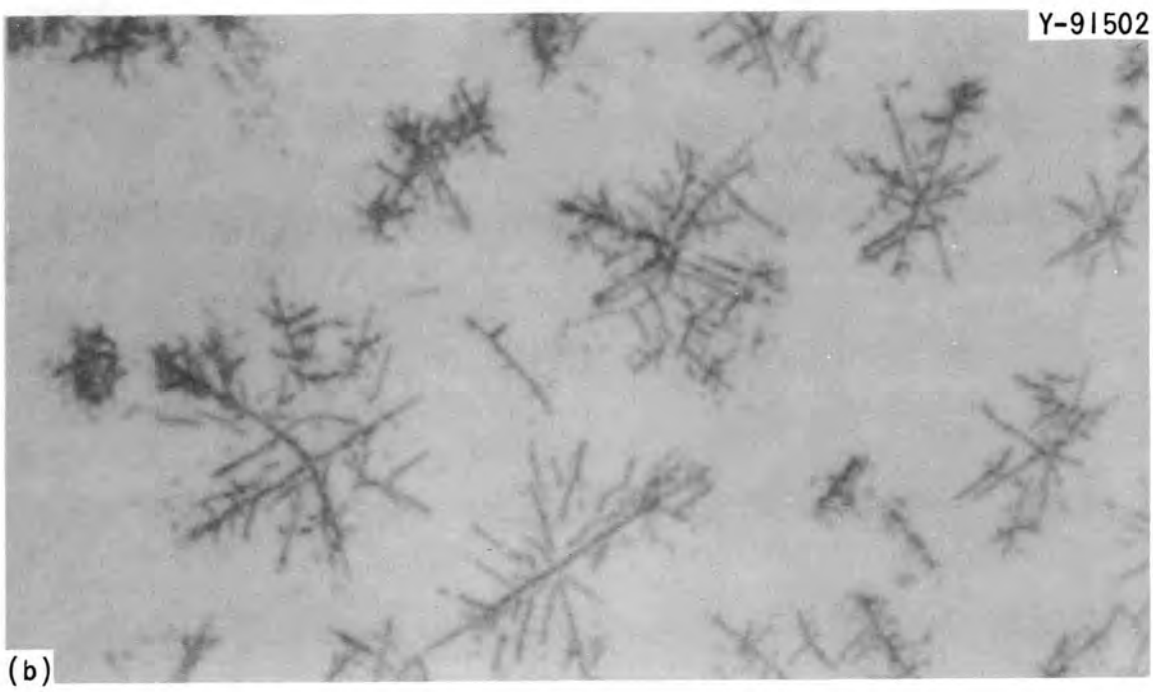

Fig. 15.2. Optical Photomicrographs of Nb–53% Hf Alloy. (a) Cooled from 1820 to 1100°C in 25 sec and then aged 3 hr at 1100°C. 200×. (b) Cooled from 1820 to 1000°C in 40 sec and then aged 6 hr at 1000°C. 1500×.

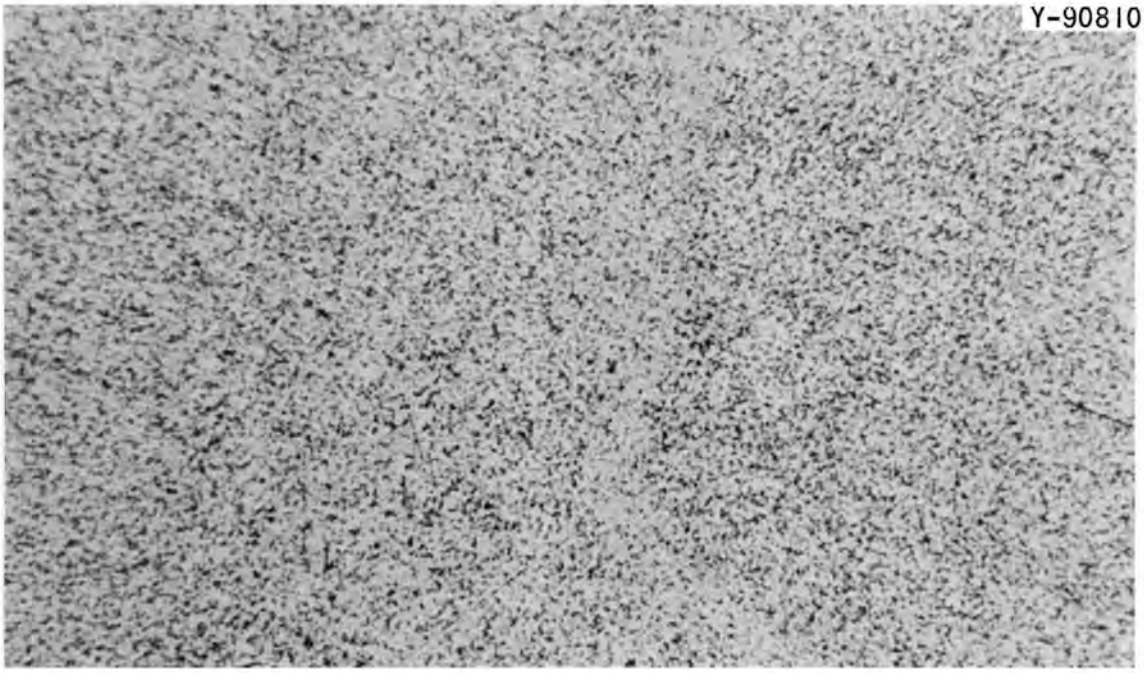

Fig. 15.3. Optical Photomicrograph of Nb–70% Hf Alloy Oil-Quenched and Aged 3 hr at 1000°C. There is no apparent precipitation-free zone near grain boundary. 500×.

Table 15.3. The Effect of Aging on the Tensile Properties of Nb–53% Hf Alloy at Room Temperature

Specimen Number	Aging Treatment		Ultimate Tensile Strength (ksi)	Uniform Strain at Ultimate Tensile Strength (%)
	Temperature (°C)	Time (hr)		
N(47)-1-26[a]			108	0.6
N(47)-1-30-a	900	3	93.5	4.9
N(47)-1-36-a	900	22	70.7	6.3
N(47)-1-27-a	1000	3	92.1	5.5
N(47)-1-35-a	1000	6	77.7	8.8
N(47)-1-32-a	1100	6	93.4	8.2
N(47)-1-33-a	1200	3	93.1	12.1
N(47)-1-34-a	1300	6	93.6	Test discontinued at 3.5%
N(47)-1-39-a	1300	13	88.3	3.4

[a] Oil-quenched specimen.

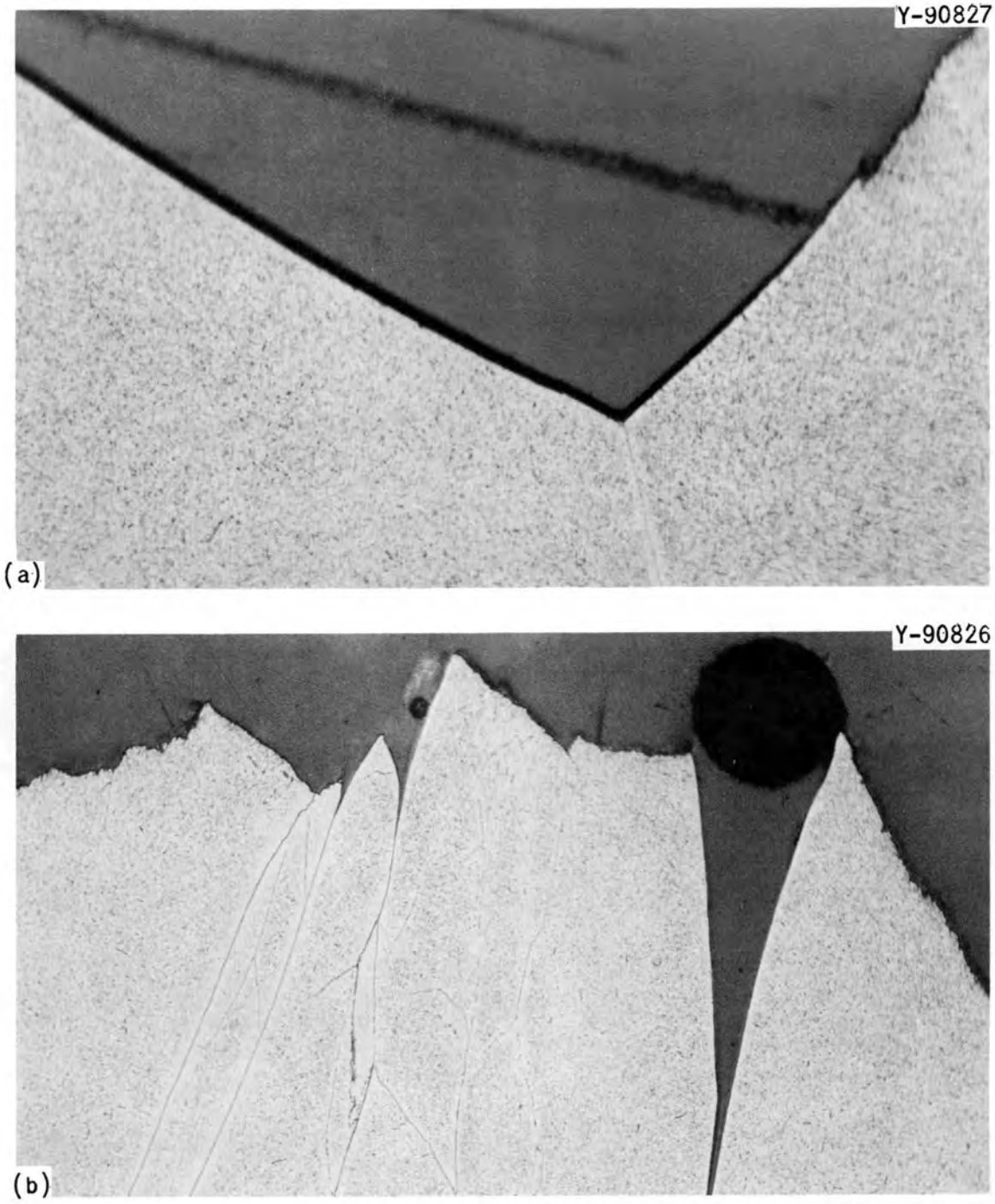

Fig. 15.4. Microstructure and Tensile Fracture Surface of Nb–53% Hf Alloy. (a) Aged 22 hr at 900° C. 500×. (b) Aged 6 hr at 1000° C. 200×.

Thermodynamics of Spinodally Decomposed Alloys (C. T. Liu, B. T. Loh)

By considering the interactions of the first and second nearest neighbor bonds in pairs, we derived[4] an equation for the free energy of mixing of N_A atoms of type A and N_B atoms of type B. Analytical expressions for the solubility limit and chemical spinodal curve can be found by applying the conditions $d\Delta G_m/dc = 0$ and $d^2\Delta G_m/dc^2 = 0$, respectively. The terms of $d\Delta G_m/dc$ and $d^2\Delta G_m/dc^2$ can be calculated from the derivative of the expression for ΔG_m; that is

$$\frac{d\Delta G_m}{dc} = -TNk \left\{ (Z_1 + Z_2 - 1)[\ln c - \ln (1 - c)] - \frac{Z_1}{2}\left[\ln\left(c - \frac{2c(1-c)}{\sqrt{f_1} + 1}\right) - \ln\left(1 - c - \frac{2c(1-c)}{\sqrt{f_1} + 1}\right)\right] - \frac{Z_2}{2}\left[\ln\left(c - \frac{2c(1-c)}{\sqrt{f_2} + 1}\right) - \ln\left(1 - c - \frac{2c(1-c)}{\sqrt{f_2} + 1}\right)\right]\right\} , \quad (15.1)$$

and

$$\frac{d^2\Delta G_m}{dc^2} = \frac{TNk}{c(1-c)}\left[1 - \frac{Z_1}{2}\left(1 - \frac{1}{\sqrt{f_1}}\right) - \frac{Z_2}{2}\left(1 - \frac{1}{\sqrt{f_2}}\right)\right] , \quad (15.2)$$

where

c = concentration,

T = absolute temperature,

N = number of N_A and N_B atoms,

k = Boltzmann's constant,

V = bond energies,

Z = coordination number,

$f = 1 + 4c(1 - c)(e^{2V/kT} - 1)$, and subscripts 1 and 2 = first and second nearest neighbor bonds.

---

[4]C. T. Liu and B. T. Loh, Fuels and Materials Development Program Quart. Progr. Rept. Sept. 30, 1968, ORNL-4350, pp. 298–302.

If V_1 and V_2 are given for a solution, Eqs. (15.1) and (15.2) could be used to calculate the solubility limit and the chemical spinodal curve as functions of concentration and temperature. In practice, V_1 and V_2 can be determined either from the phase diagram of the spinodal alloy or from the measurement of short-range order parameters by x-ray diffraction technique.[5]

In order to compare this model with the model for a regular solution, we assume hypothetical body-centered cubic solid solutions with the same critical temperature, T_c, equal to 1800°K. The results of calculations based on arbitrarily assigning V_2 = +100 k, 0, and −100 k (for these values of V_2, the corresponding values of V_1 have values of 424 k, 517.8 k, and 623.7 k, respectively) for hypothetical solutions are shown in Fig. 15.5, from which some important conclusions can be drawn:

1. All the curves for solubility and spinodal decomposition are symmetrical about the axis of $c = 1/2$.

2. Since the solubility varies with the value of V_2, V_2 can be used to adjust the range of solubility for a given alloy. A plot of solubility for hypothetical solutions at 1500°K as a function of V_2 is shown in Fig. 15.6. The maximum solubility occurs at the value of 270 k, which is about half the sum of V_2 and V_1 for the solution $V_2 = 0$, $V_1 = 517.8$ k. As indicated in Fig. 15.5, the solubility predicted from this model is always less than that predicted by a regular solution.

3. The range of concentrations over which spinodal decomposition can occur, as predicted by Eqs. (15.1) and (15.2), is always wider than that predicted by a regular solution. It may be proper to emphasize here that the physical model underlying Eqs. (15.1) and (15.2) is much more appropriate than the one for a regular solution.

---

[5] J. M. Cowley, Phys. Rev. 11, 669 (1950).

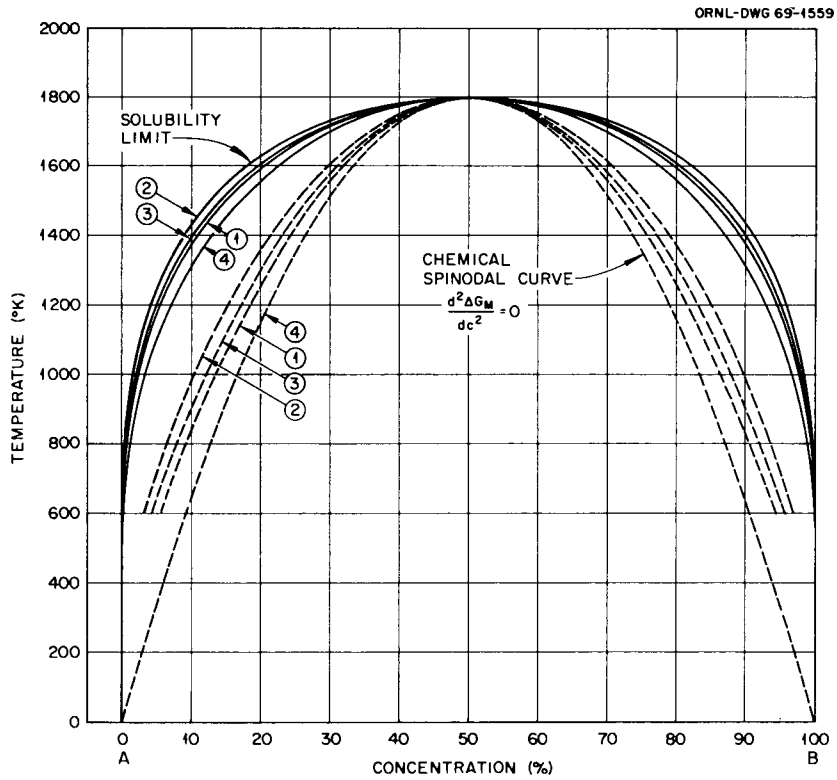

Fig. 15.5. Comparison of the Solubility Limit and Chemical Spinodal Curves Calculated from Eqs. (15.1) and (15.2), and Regular Solution Model. Curve (1): $V_2 = 100$ k, $V_1 = 424$ k; curve (2): $V_2 = -100$ k, $V_1 = 623.7$ k; curve (3): $V_2 = 0$, $V_1 = 517.8$ k; curve (4) regular solution: $V_1 = 450$ k.

Long-Time, High-Temperature Mechanical Properties of Commercial Refractory Alloys

H. E. McCoy, Jr.

The object of this program is to evaluate the creep-rupture properties of promising refractory metal alloys at high temperatures. In order to provide an adequate evaluation, we determine stress-rupture curves from 10 to 1000 hr at several temperatures from 1000 to 1650°C. In addition, we study the effects of annealing treatment and fabrication variables in an effort to improve and better understand the most promising alloys.

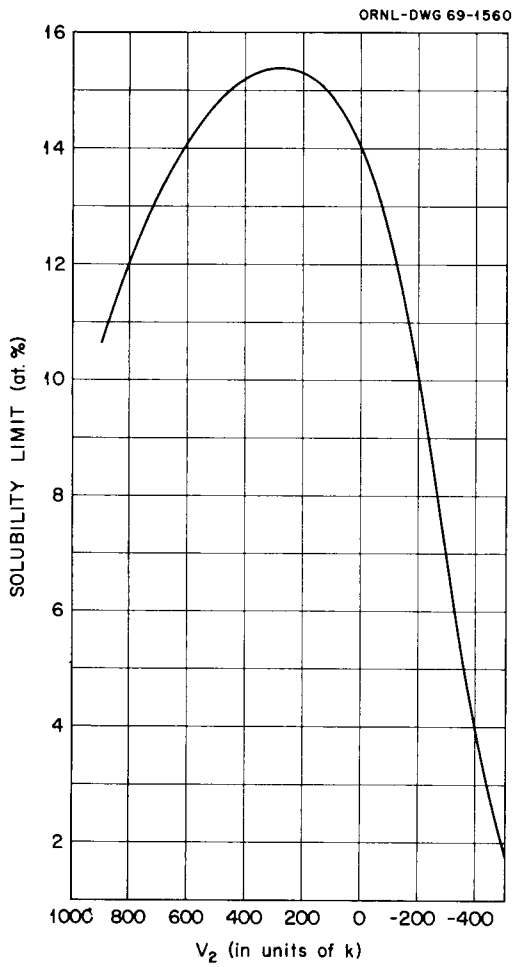

Fig. 15.6. Variation of Solubility Limit for Hypothetical Solutions (T_c = 1800°K) at 1500°K. Calculated from Eqs. (15.1) and (15.2) as a function of V_2.

Molybdenum and Niobium Alloys (R. L. Stephenson)

The creep testing of molybdenum alloys is essentially complete.[6] Electron and optical microscopy are being used in an effort to understand the observed effects in terms of microstructure.

The three niobium-based alloys, SU-16 (Nb–11% W–3% Mo–2% Hf–0.08% C), SU-31 (Nb–17% W–3.5% Hf–0.12% C), and C-129Y (Nb–10% W–10% Hf–0.1% Y), are currently receiving attention. The creep testing of SU-16 is nearly complete. Figure 15.7 shows stress-rupture curves at 980, 1095, and

[6]R. L. Stephenson, Fuels and Materials Development Program Quart. Progr. Rept. June 30, 1968, ORNL-4330, pp. 350–351.

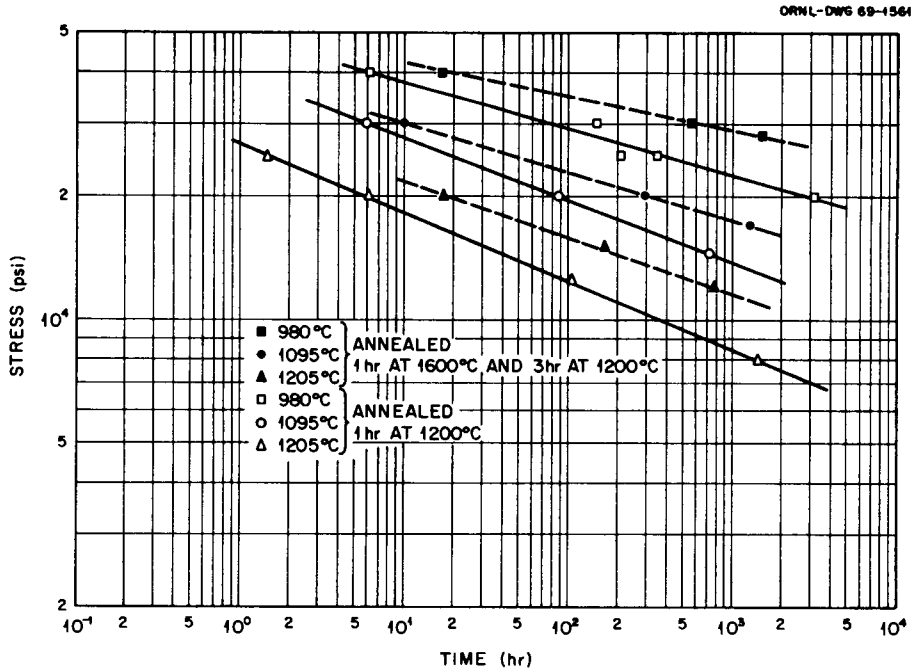

Fig. 15.7. Creep-Rupture Properties of SU-16 Alloy.

1205°C for the same heat of SU-16 in two conditions. The effect of annealing temperature on the creep-rupture properties of this alloy is being studied.

Welding and Brazing Development

Brazing Alloy Development (Nancy C. Cole, D. A. Canonico)

We are examining ternary brazing alloy systems that have exceptional ability to join refractory metals, ceramics, and graphite to themselves and to each other. Previously,[7] we discussed the Ti-Zr-Ge system, pointing out the outstanding ability of alloy 8H (Ti–20% Zr–15% Ge) to flow on graphite. This alloy also joins refractory metals to graphite since the alloy wets both very well (Fig. 15.8).

Another brazing filler-metal system (Ti-V-Cr) is even more outstanding. Compositions have been developed within this system that will join all combinations of graphite, Al_2O_3, and refractory metals. Joints

[7]D. A. Canonico and N. C. Cole, Fuels and Materials Development Program Quart. Progr. Rept. June 30, 1968, ORNL-4330, pp. 352–354.

Fig. 15.8. Tantalum Brazed to Graphite with T-Joint of Ti–20% Zr–15% Ge Alloy. Excellent flow is evident.

of Al_2O_3 to Al_2O_3, Ta to Ta, and graphite to graphite have been reported.[8] Figure 15.9(a) shows T-joints of graphite brazed to Ta–10% W with Ti–21% V–25% Cr. The unusual ability of Ti–17% V–40.5% Cr to braze Al_2O_3 to graphite is shown in Fig. 15.9(b).

The Ti-V-Cr system has shown an interesting flowability pattern on Al_2O_3 and graphite. If the ratio of Ti to V is kept constant and the content of Cr is increased from 5 to 55%, the brazing behavior on Al_2O_3 and graphite appears to be quite different. As shown in Fig. 15.10, those brazing alloys with 25 to 47.5% Cr produce excellent joints with Al_2O_3, whereas those alloys with 5 to 20% Cr wet the ceramic but do not flow. If the brazing temperature is raised as much as 50°C, flowability of the filler metal is drastically inhibited.

When graphite is selected as the base material (Fig. 15.11), those compositions with 5 to 25% Cr have excellent flowability; those with

---

[8]D. A. Canonico and N. C. Cole, Metals and Ceramics Div. Ann. Progr. Rept. June 30, 1968, ORNL-4370, pp. 64–66.

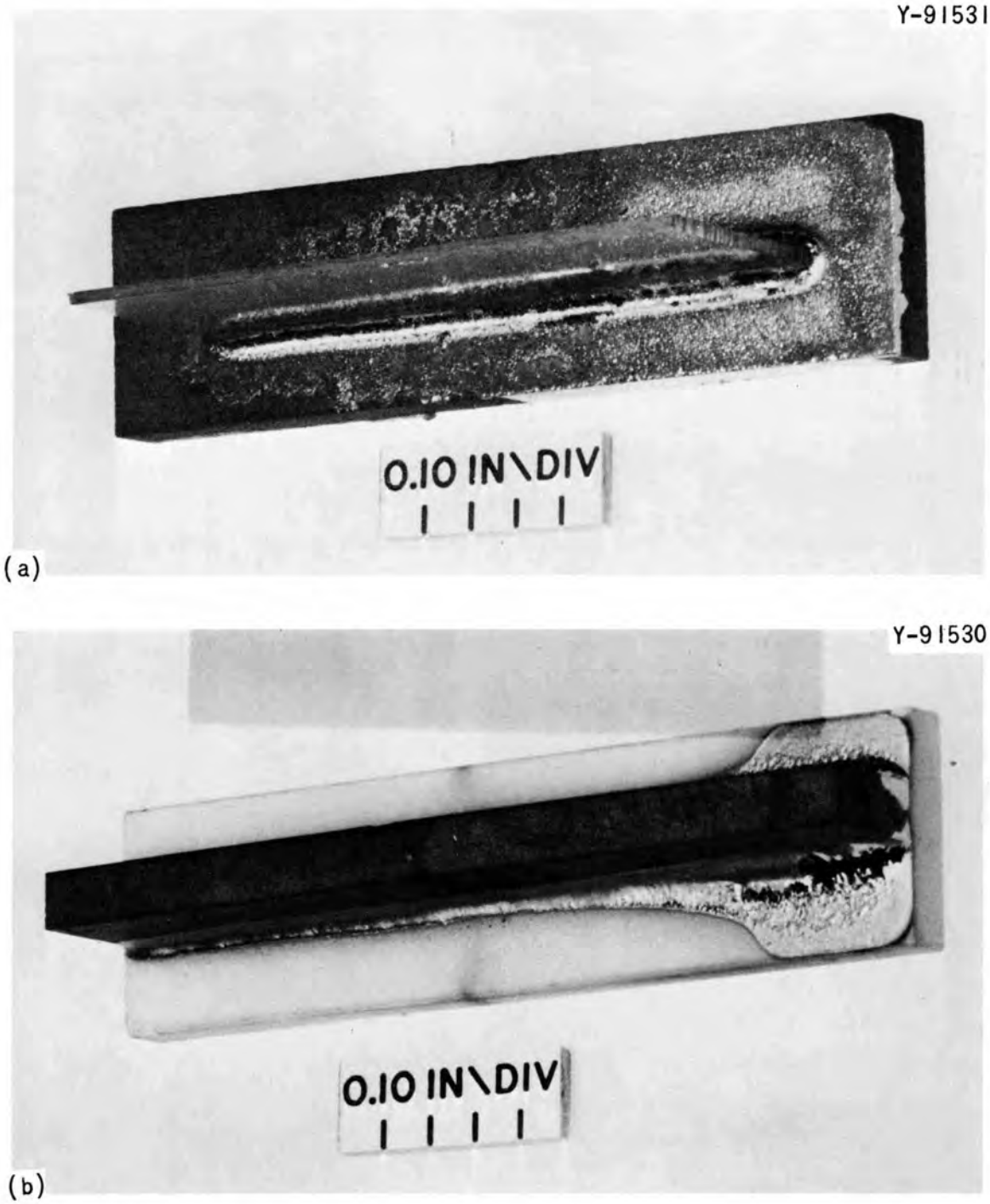

Fig. 15.9. Brazed T-Joints Showing Unusual Versatility of Filler Metals in Ti-V-Cr System. (a) Graphite brazed to Ta–10% W with Ti–21% V–25% Cr. (b) Graphite brazed to Al_2O_3 with Ti–17% V–40.5% Cr.

Y-91538

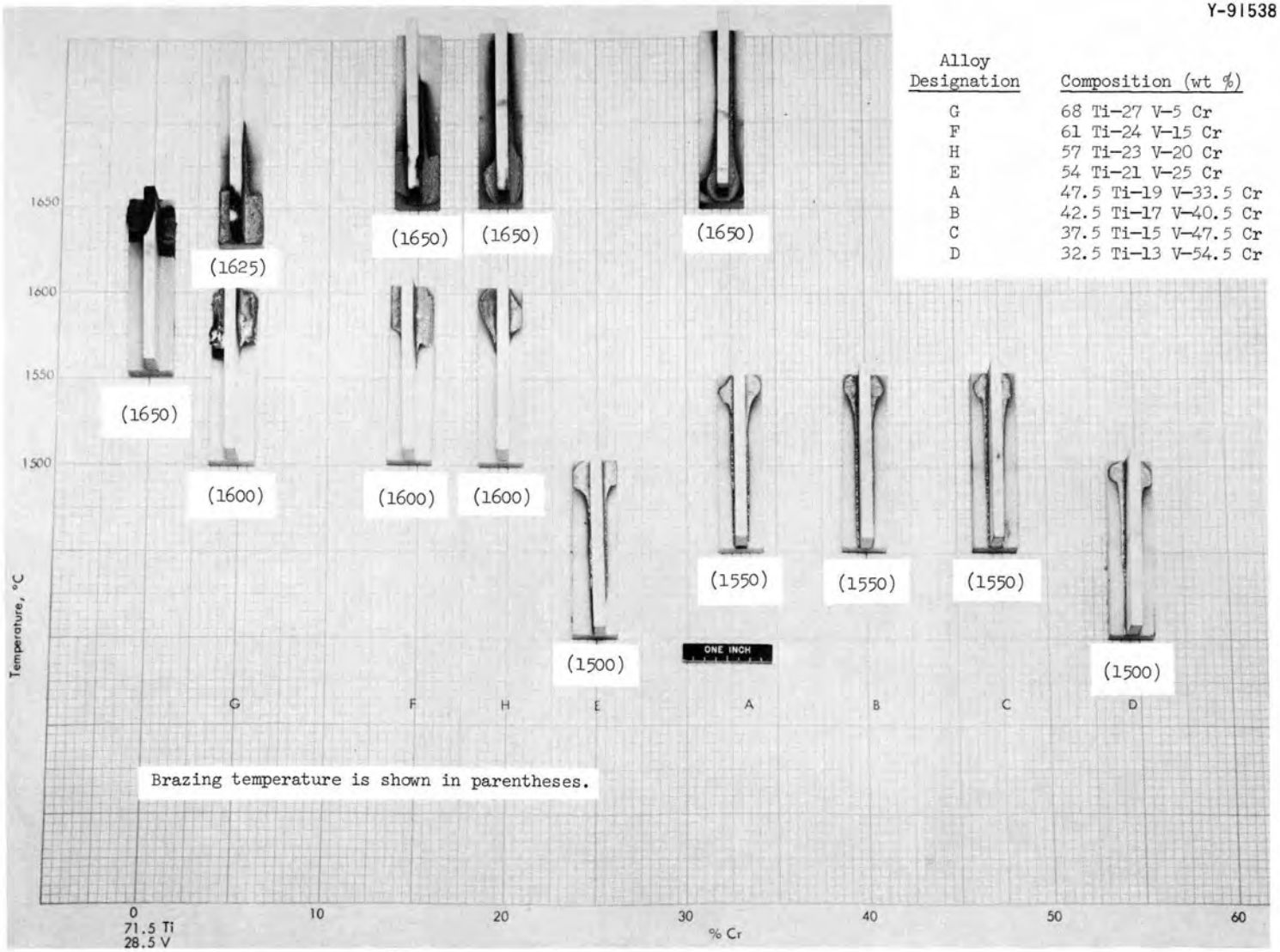

Fig. 15.10. The Effect of Chromium Content and Temperature on the Flowability of Brazing Alloys from the Ti-V-Cr System on Al_2O_3. The ratio of Ti to V is maintained at 3:1 and Cr is added as the third element.

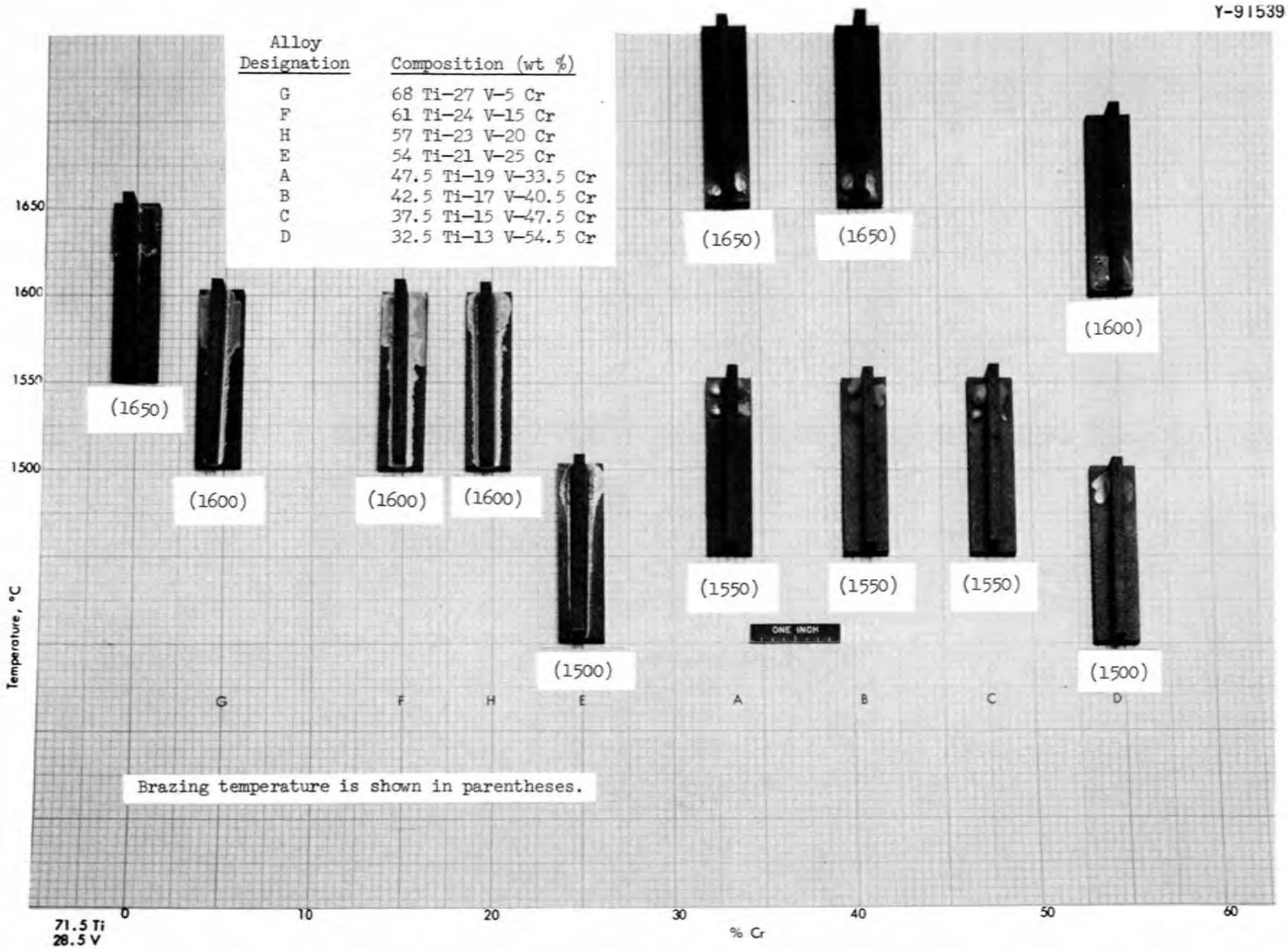

Fig. 15.11. The Effect of Chromium Content and Temperature on the Flowability of Brazing Alloys from the Ti-V-Cr System on Graphite. The ratio of Ti to V is maintained at 3:1 and Cr is added as the third element.

more Cr wet but do not flow. The alloys with lower content of Cr have an additional advantage in that they can be rolled into sheet for preplacement. For comparison, we have included the binary Ti–28.5% V composition in this brazing study. It can be seen in both Figs. 15.10 and 15.11 that this alloy did not flow on either Al_2O_3 or graphite.

Welding of T-111 Alloy Forced Circulation Loop (FCLLL-1) (L. C. Williams)

All the T-111 (Ta–8% W–2% Hf) components of FCLLL-1 were successfully welded. This is by far the most complex structure of T-111 ever constructed at ORNL. It incorporated about 80 gas tungsten-arc welds, with all of the joints in the primary piping being of the multipass, full-penetration type. All components were welded in a vacuum-purged argon-atmosphere chamber. The purity of the Ar before and during welding was constantly monitored by analyzers for O_2 and water vapor and also by making sample welds for subsequent chemical analysis.

Figures 15.12 and 15.13 show the principal parts of the loop before final assembly within its operation chamber. The final three closure welds were made in place with the portable, rotating, inert-atmosphere welding device developed at ORNL (Fig. 15.14).

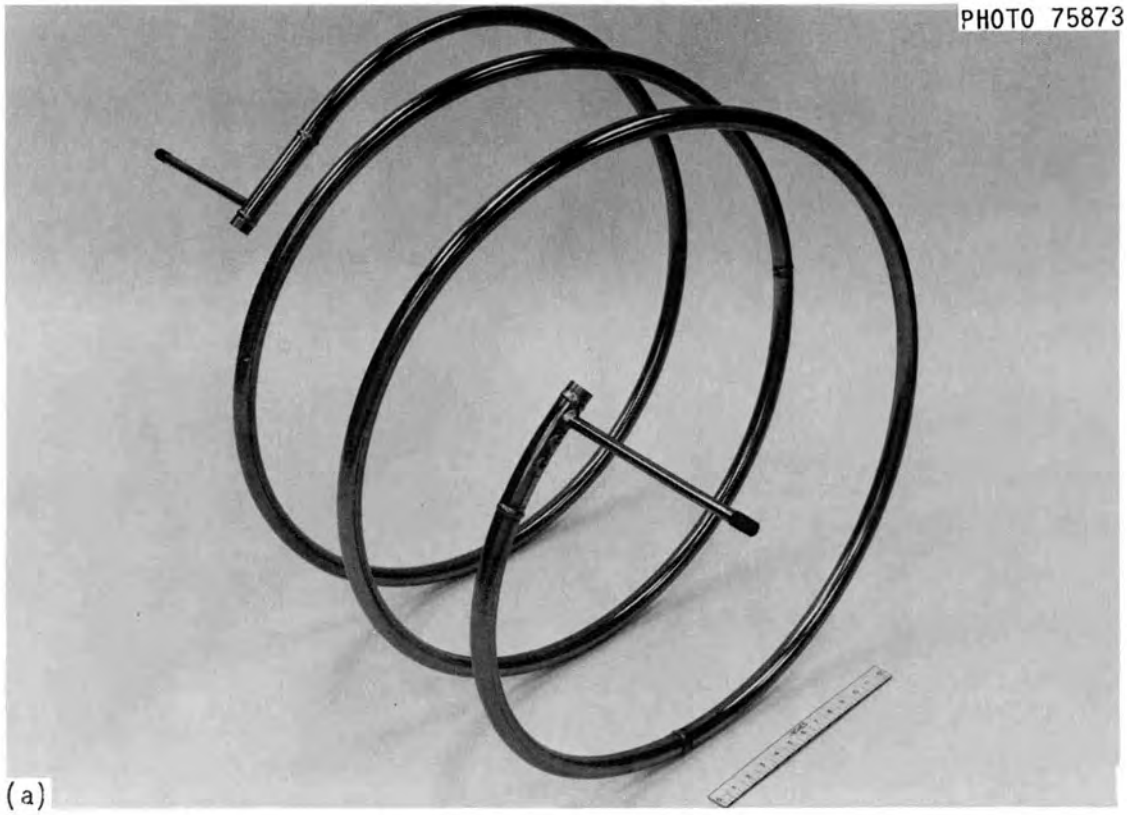

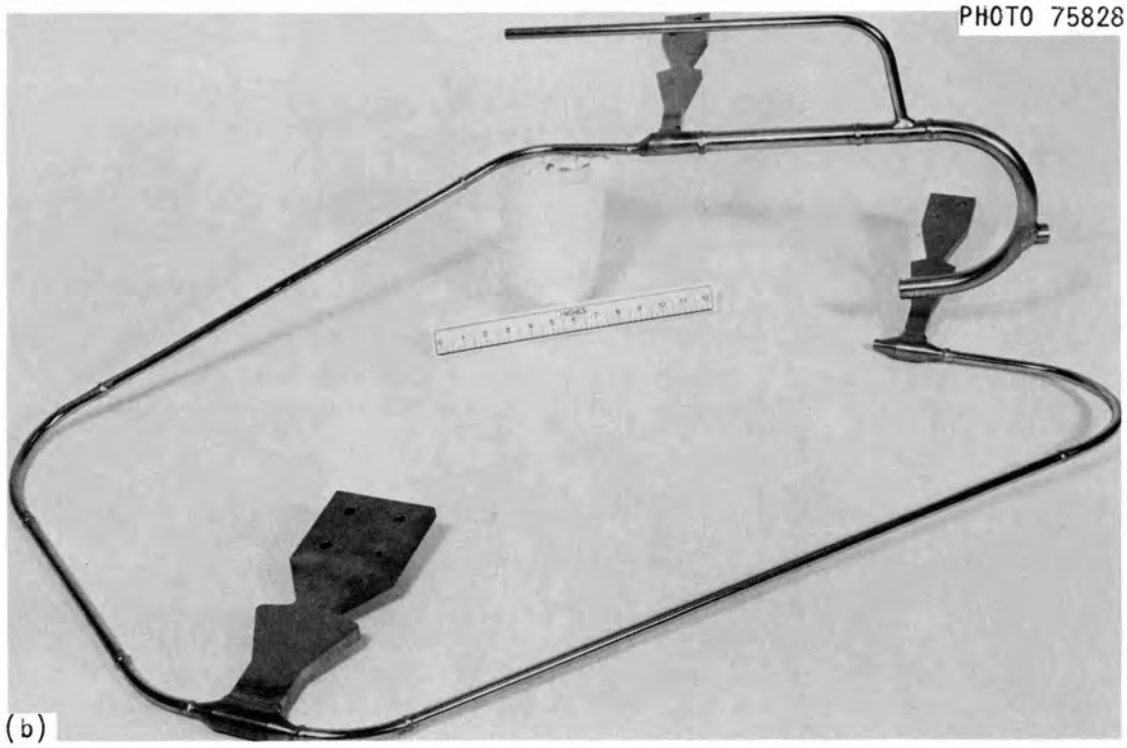

Fig. 15.12. Components of T-111 for Forced Circulation Liquid Lithium Loop (FCLLL-1). (a) Radiator section. (b) I^2R heated section.

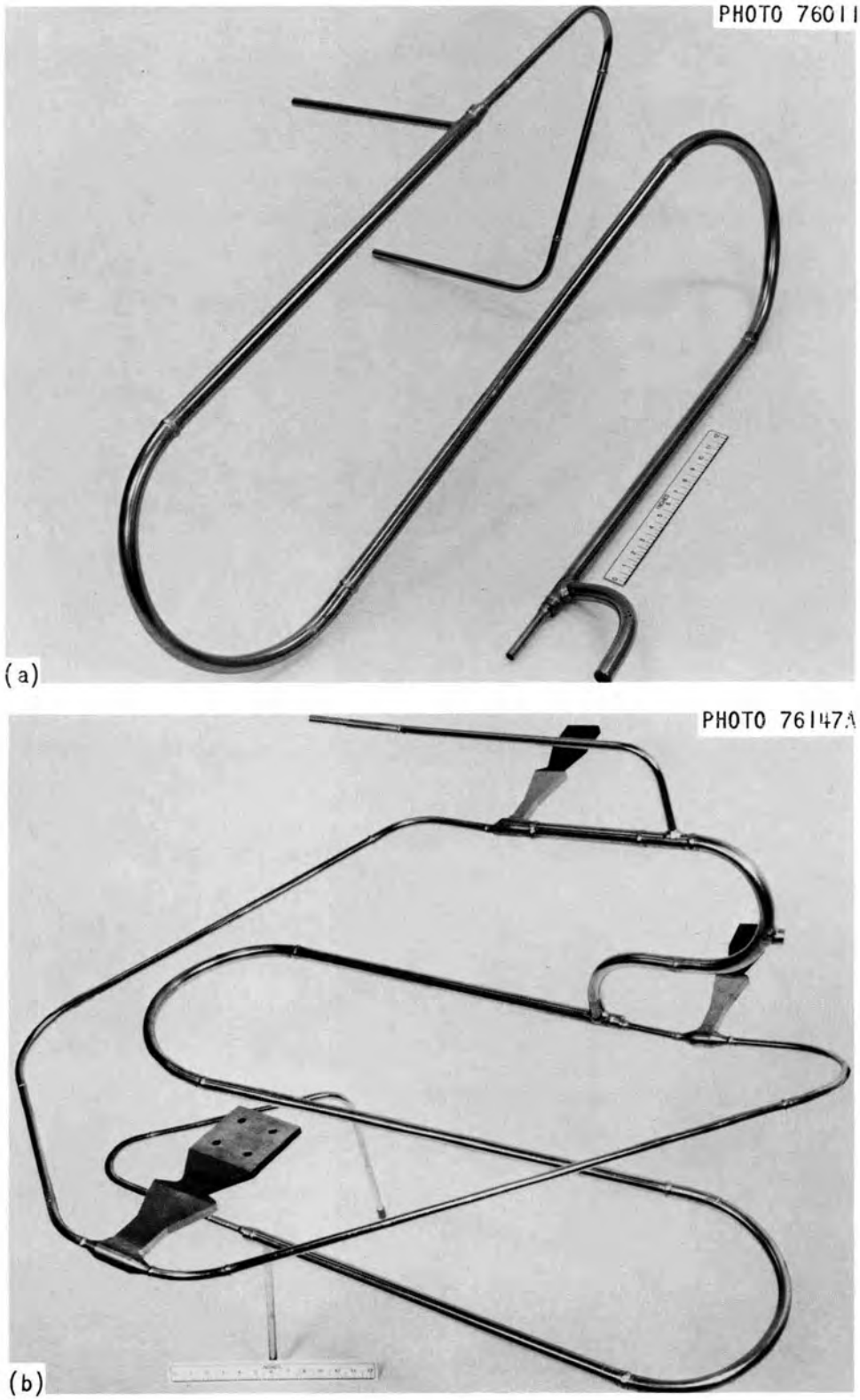

Fig. 15.13. Components of T-111 for Forced Circulation Liquid Lithium Loop (FCLLL-1). (a) Economizer section. (b) I^2R heated section after welding to economizer.

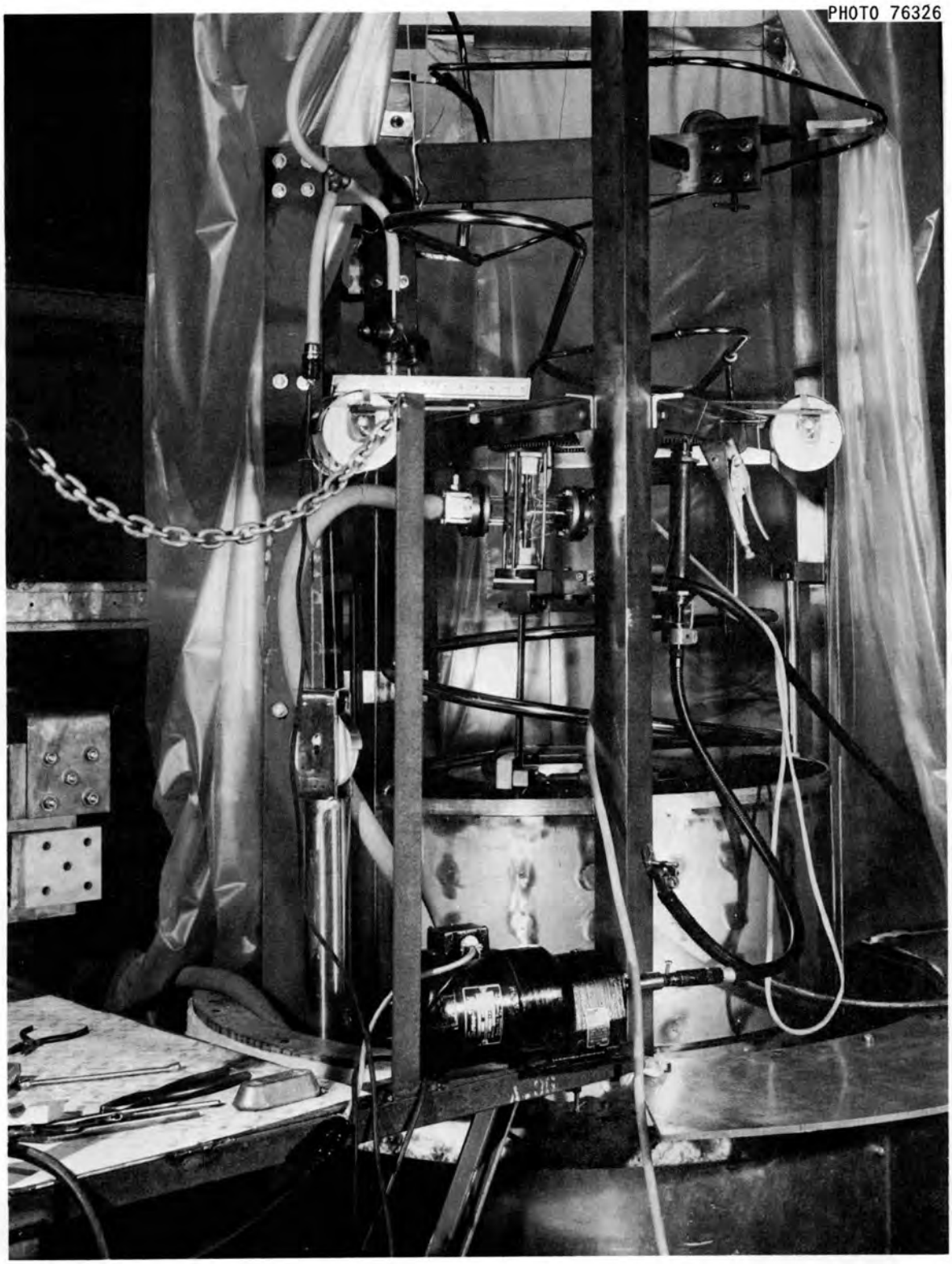

Fig. 15.14. Portable, Rotating, Inert-Atmosphere Welding Device in Operating Position for Welding Refractory Alloy Tubing. Welding head is enclosed in Pyrex Cross.

16. CLADDING MATERIALS FOR SPACE ISOTOPIC HEAT SOURCES

P. Patriarca R. G. Donnelly

The immediate tasks of this program are (1) to evaluate the more promising superalloys that are available commercially and (2) to develop improved alloys and eventually qualify those that show greatest promise for containment of radioisotopes in space power systems. The superalloy studies include evaluation of embrittling aging reactions, determination of their evaporation characteristics, and studies of the interaction of stress and vacuum on properties at elevated temperatures. In the alloy development portion of the program, the strength and air-oxidation properties will be determined as well as the aging and evaporation properties.

Studies of Commercial Superalloys

Interaction of Stress and Vacuum on Properties of Superalloys at Elevated Temperatures (D. T. Bourgette)

The effect of evaporation losses on the creep properties of Haynes alloy No. 25 (Co–20% Cr–15% W–10% Ni) in high vacuum at 800°C for specimen thicknesses of 0.007, 0.012, and 0.030 in. has been reported.[1,2] The results indicate that the thinner the specimen, the greater the degradation of the creep strength. Because the creep data from 0.030-in.-thick specimens tested in vacuum and Ar are fairly close but deviate after 1000 hr of testing, we believe that the critical thickness above which evaporation losses at 800°C are insufficient to alter the creep properties is greater than 0.030 in. Therefore, specimens 0.060 in. thick are being tested beyond 1000 hr to determine when evaporation losses degrade creep properties. We are also testing the alloy in air at 800°C.

The second phase of this study involves determining the effect of stress on the evaporation kinetics of Haynes alloy No. 25. Initial

---

[1] D. T. Bourgette, Fuels and Materials Development Program Quart. Progr. Rept. June 30, 1968, ORNL-4330, pp. 344–345.

[2] D. T. Bourgette, Fuels and Materials Development Program Quart. Progr. Rept. Sept. 30, 1968, ORNL-4350, pp. 294–296.

results showed that stress increased the surface area and, therefore, increased the evaporation losses. We are installing new equipment for studying this dependence in greater detail.

Development of Improved Alloys

C. T. Liu H. Inouye

In our efforts to develop improved alloys for space applications, we are investigating ordered alloy systems because of their superior strength properties. The alloying elements have been chosen for their low vapor pressures, thus eliminating Cr. In some cases Pt is used to provide resistance to vaporization and oxidation.

Alloys S-1 through S-6 in Table 16.1 were electron-beam melted, drop cast into 1/2-in.-diam. by 5-in.-long bars, canned in stainless steel, and extruded successfully at 1200°C at ratios of 8:1 and 16:1.

Table 16.1. Experimental Cladding Alloys Selected for Preliminary Evaluation

Alloy Number	Nominal Composition (wt %)	Equilibrium State	Critical Temperature[a] (°C)
S-1	Ni–25 Co	Ordered $CoNi_3$	~ 800
S-2	Ni–20.2 Co–4.4 V	Ordered $(N,Co)Ni_3$	850[b]
S-3	Ni–46.4 Co–7 V	Disordered	c
S-4	Ni–38.8 Co–22.5 V	Ordered $V(Ni,Co)_3$	1050
S-5	Pt–23.2 Co	Ordered CoPt	825
S-6	Pt–46.2 Fe	Ordered Fe_3Pt	835
S-11	Co–27 Pt[d]	Disordered	c
S-12	Ni–27 Pt[d]	Disordered	c
S-13	Fe–28 Pt[d]	Disordered	c

[a]The temperature above which the alloy is disordered.

[b]Estimated.

[c]Not applicable.

[d]These compositions correspond to 10 at. % Pt.

The extruded rods are being heat treated and machined into button specimens (1-in. gage length, 0.070-in. gage diameter) for tensile and creep testing. Preliminary evaluation indicates that the alloys are single phased as cast and very close to the nominal composition. Alloys S-11, S-12, and S-13 were arc-cast into 3/16 × 7/8 × 1 1/4-in. slabs and will be rolled to sheet to provide information regarding the principles governing the vaporization and oxidation processes.

Alloys S-1, S-2, and S-3 were cold forged and rolled without difficulty to 0.02 in. with a few intermediate annealings. Alloy S-4 in the ordered state is too hard [Rockwell "C" Hardness (R_C) 43] to cold work, but in the disordered condition obtained by quenching in water from 1150°C it is much softer (R_C 24) and can be fabricated at room temperature without difficulty. The effect of heat treatment on the microstructure and related physical and mechanical properties of alloys S-1 through S-6 is being studied. The heat treatments of tensile and creep specimens will be based on these data.

The aging kinetics of experimental cladding alloys S-1 through S-4 (Table 16.2) have been determined by measuring the room-temperature hardness as a function of aging temperature and time. The alloys were first heated above their critical temperatures (1000°C for S-1 and S-2; 1150°C for S-3 and S-4) in an argon atmosphere and then quenched in ice water. The specimens were aged up to 1050 min between 600 and 900°C. The data summarized in Table 16.2 indicate the following:

1. The ternary ordered alloy S-4 is very age hardenable, and its rate of ordering is largely dependent on the aging temperature. The hardness increases sharply from the quenched value, approximately R_C 10, to a constant value, which depends on the temperature. The highest hardness value obtained from aging 240 min at 800°C was R_C 49.4, but the hardness of the specimen aged at 600°C for 700 min was only R_C 22.

2. Comparison of the hardness data for alloys S-1 to S-3 with those obtained from S-4 indicates that the formation of long-range order in alloy S-4 between V, Ni, and Co atoms [i.e., $V(Ni,Co)_3$] is a very effective strengthening mechanism in this ternary alloy system.

Table 16.2. Effect of Aging Treatment on Room-Temperature Hardness of Experimental Cladding Alloys[a] S-1 Through S-4

Aging Temperature (°C)	Treatment Time (min)	Rockwell Hardness[b]			
		R_A			R_C
		S-1	S-2	S-3	S-4
600	0	20.7[c]	34.0[c]	41.0[c]	10.0[c]
	5	23.8	37.3	41.5	13.4
	20	24.3	39.3	42.2	15.7
	60	24.9	39.9	42.5	17.5
	240	24.7	41.0	43.7	19.0
	700	24.7	41.6	43.8	22.0
700	5	24.0	35.7	41.6	21.5
	20	25.1	38.2	42.7	30.0
	60	25.7	39.3	44.2	34.1
	240	25.5	40.7	47.0	35.3
	700	26.2	40.7	49.2	37.7
800	5	21.0	38.4	42.2	36.2
	20	22.2	39.4	44.7	40.3
	60	22.4	40.2	47.5	48.5
	240	22.3	41.8	49.3	49.4
	700	21.0	38.5	48.0	49.3
900	5	d	d	43.3	44.0
	20	d	d	44.0	44.5
	240	d	d	47.0	44.6

[a]Analysis, wt %:
S-1 Ni–26% Co
S-2 Ni–22% Co–4.7% V
S-3 Ni–46% Co–9% V
S-4 Ni–32.5% Co–24% V

[b]Rockwell "C" Scale readings indicate much harder material than "A" Scale readings (R_C/R_A = about 3).

[c]Quenched hardness.

[d]Not measured.

The high-temperature strength can be estimated from the measurement of hot hardness. Preliminary hardness data from room temperature to 1000°C are given in Table 16.3. In general, the hot hardness decreases slowly with increasing temperature, but the hot hardness for the ordered S-4 alloy is still about 300 DPH between 600 and 800°C, which should indicate good elevated-temperature strength for this alloy.

The preparation of tensile and creep specimens is in progress, and their heat treatment will be based on the data above.

Table 16.3. Hot-Hardness Data for the Experimental Cladding Alloys S-1 Through S-4

Testing Temperature (°C)	Hot Hardness (DPH)			
	S-1	S-2	S-3	S-4
24[a]	90	115	155	415
200	85	106	150	387
400	80	75	145	330
600	50	75	105	325
800	30	50	60	270
1000	15	20	33	150

[a]Room temperature.

Previous reports in this series:

ORNL 4330 Period Ending June 30, 1968

ORNL 4350 Period Ending September 30, 1968

ORNL-4390
UC-25 — Metals, Ceramics, and Materials

INTERNAL DISTRIBUTION

1–3. Central Research Library
4–5. ORNL — Y-12 Technical Library
Document Reference Section
6–20. Laboratory Records Department
21. Laboratory Records, ORNL R.C.
22. ORNL Patent Office
23. G. M. Adamson, Jr.
24. T. E. Banks
25. S. E. Beall
26. R. L. Beatty
27. R. J. Beaver
28. M. Bender
29. R. G. Berggren
30. D. S. Billington
31. E. E. Bloom
32. A. L. Boch
33. E. S. Bomar
34. C. D. Bopp
35. B. S. Borie
36. D. T. Bourgette
37. G. E. Boyd
38. R. A. Bradley
39. R. J. Breeding
40. R. B. Briggs
41. R. E. Brooksbank
42. W. E. Brundage
43. D. A. Canonico
44. R. W. Carpenter
45. R. M. Carroll
46. J. V. Cathcart
47. A. K. Chakraborty
48. Ji Young Chang
49. D. L. Clark
50. G. W. Clark
51. N. C. Cole
52. K. V. Cook
53. W. H. Cook
54. G. L. Copeland
55. W. B. Cottrell
56. C. M. Cox
57. F. L. Culler
58. C. W. Cunningham
59. J. E. Cunningham
60. H. L. Davis
61. V. A. DeCarlo
62. W. E. Deeds
63. J. H. DeVan
64. J. R. DiStefano
65. C. V. Dodd
66. R. G. Donnelly
67. D. A. Dyslin
68. T. Eck
69. W. S. Ernst
70. J. H. Erwin
71. R. B. Evans III
72. K. Farrell
73. J. I. Federer
74. D. E. Ferguson
75. R. B. Fitts
76. B. Fleischer
77. B. E. Foster
78. A. P. Fraas
79. J. H Frye, Jr.
80. W. Fulkerson
81. L. C. Fuller
82. T. G. Godfrey, Jr.
83. G. M. Goodwin
84. J. M. Googan (Y-12)
85. R. J. Gray
86. W. R. Grimes
87. A. G. Grindell
88. H. D. Guberman
89. L. L. Hall
90. D. G. Harman
91. W. O. Harms
92–95. M. R. Hill
96. N. E. Hinkle
97. D. O. Hobson
98. H. W. Hoffman
99. R. W. Horton
100. W. R. Huntley
101. H. Inouye
102. D. H. Jansen
103. W. H. Jordan
104. G. W. Keilholtz
105. R. T. King
106. R. L. Klueh
107. R. W. Knight
108. J. Komatsu
109. J. A. Lane

110. J. M. Leitnaker
111. B. C. Leslie
112. T. B. Lindemer
113. A. P. Litman
114. C. T. Liu
115. H. R. Livesey
116. B. T. Loh
117. A. L. Lotts
118. C. D. Lundin
119. J. W. LuQuire
120. R. N. Lyon
121. H. G. MacPherson
122. R. E. MacPherson
123. M. M. Martin
124. W. R. Martin
125. R. W. McClung
126. H. E. McCoy, Jr.
127. H. C. McCurdy
128. R. E. McDonald
129. W. T. McDuffie
130. D. L. McElroy
131. C. J. McHargue
132. A. J. Miller
133. E. C. Miller
134. J. P. Moore
135. R. E. Moore
136. W. L. Moore
137. C. S. Morgan
138. J. G. Morgan
139. F. H. Neill
140. T. M. Nilsson
141. T. A. Nolan (K-25)
142. K. Notz
143. S. M. Ohr
144. A. R. Olsen
145. M. F. Osborne
146. P. Patriarca
147. W. H. Pechin
148. R. B. Perez
149. A. M. Perry
150. S. Peterson
151. R. A. Potter
152. R. B. Pratt
153. M. K. Preston
154. R. E. Reed
155. D. K. Reimann
156. G. A. Reimann
157. A. E. Richt
158. P. L. Rittenhouse
159. H. E. Robertson
160. M. W. Rosenthal
161. D. J. Rucker
162. C. F. Sanders
163. G. Samuels
164. A. W. Savolainen
165. J. E. Savolainen
166. A. C. Schaffhauser
167. J. L. Scott
168. J. D. Sease
169. C. E. Sessions
170. O. Sisman
171. G. M. Slaughter
172. S. D. Snyder
173. K. E. Spear
174. I. Spiewak
175. P. Spindler
176. W. G. Spoeri
177. J. E. Spruiell
178. W. J. Stelzman
179. R. L. Stephenson
180. J. O. Stiegler
181 D. A. Sundberg
182. E. J. Tenckhoff
183. V. J. Tennery
184. D. B. Trauger
185. R. L. Wagner
186. G. M. Watson
187. S. C. Weaver
188. M. S. Wechsler
189. A. M. Weinberg
190. J. R. Weir, Jr.
191. W. J. Werner
192. H. L. Whaley
193. G. D. Whitman
194. F. W. Wiffen
195. J. M. Williams
196. L. C. Williams
197. R. K. Williams
198. R. O. Williams
199. J. C. Wilson
200. R. G. Wymer
201. F. W. Young, Jr.
202. C. S. Yust
203. C. M. Adams, Jr. (Consultant)
204. Leo Brewer (Consultant)
205. L. S. Darken (Consultant)
206. J. A. Krumhansl (Consultant)

EXTERNAL DISTRIBTUION

AIR FORCE MATERIALS LABORATORY, Wright-Patterson Air Force Base

207. C. H. Armbruster
208. H. M. Burte
209. G. Glenn
210. Technical Director

AIR FORCE WEAPONS LABORATORY, Kirtland Air Force Base

211. D. Brooks

AMES LABORATORY

212. O. N. Carlson
213. W. L. Larsen
214. M. Smutz
215. F. H. Spedding

ARGONNE NATIONAL LABORATORY

216. L. Baker
217. J. H. Kittel
218. M. V. Nevitt
219. P. G. Shewmon
220. R. C. Vogel

LMFBR PROGRAM OFFICE, Argonne National Laboratory

221. A. Amorosi
222. L. Burris
223. L. Kelman
224. J. M. McKee

AEC-RDT SITE REPRESENTATIVES

225. M. E. Jackson, Argonne National Laboratory
226. D. J. Wille, Atomic Power Development Associates
227. R. L. Morgan, Atomics International
228. J. V. Levy, General Electric, Cincinnati
229. J. F. Weissenberg, General Electric, Cincinnati
230. R. H. Ball, Gulf General Atomic
231. J. E. Hebert, Idaho
232. D. A. Moss, Idaho
233. K. A. Trickett, Idaho
234. D. F. Cope, Oak Ridge National Laboratory
235. C. L. Matthews, Oak Ridge National Laboratory
236. P. G. Holsted, Pacific Northwest Laboratory
237. J. Sako, Pacific Northwest Laboratory
238. Atomic Energy Commission Library, Washington

DIVISION OF NAVAL REACTORS, AEC, Washington

239. R. H. Steele

DIVISION OF REACTOR DEVELOPMENT AND TECHNOLOGY, AEC, Washington

240. J. C. Crawford, Jr.
241. G. W. Cunningham
242. A. Giambusso
243. H. G. Hembree
244. J. R. Hunter
245. E. E. Kintner
246. W. H. Layman
247. W. H. McVey
248. J. J. Morabito
249. R. E. Pahler
250. A. J. Pressesky
251. M. A. Rosen
252. J. M. Simmons
253. E. E. Sinclair
254. A. Taboada
255. A. N. Tardiff
256. A. Van Echo
257. C. E. Weber
258. M. J. Whitman

DIVISION OF RESEARCH, AEC, Washington

259. P. W. McDaniel
260. D. K. Stevens

DIVISION OF SPACE NUCLEAR SYSTEMS, AEC, Washington

261. R. E. Anderson
262. D. Beard
263. J. F. Griffo
264. F. D. Haines
265. C. E. Johnson
266. J. A. Powers
267. F. C. Schwenk

OAK RIDGE OPERATIONS OFFICE

268. W. J. Larkin
269. Laboratory and University Division

ATOMIC POWER DEVELOPMENT ASSOCIATES

270. E. C. Kovacic
271. A. A. Shoudy

ATOMICS INTERNATIONAL

272. H. Pearlman
273. J. G. Asquith

BABCOCK AND WILCOX COMPANY, Lynchburg, Virginia 24505

274. C. Baroch
275. S. P. Grant
276. C. Johnson
277. L. Weissert

BATTELLE MEMORIAL INSTITUTE, Columbus, Ohio

278. W. Berry
279. D. Keller
280. S. J. Paprocki
281. Defense Materials Information Center

BATTELLE MEMORIAL INSTITUTE, PNL, Richland, Washington

282. A. L. Bement
283. J. J. Cadwell
284. T. T. Claudson
285. D. L. Condotta
286. E. Evans
287. B. R. Hayward
288. B. M. Johnson
289. W. E. Roake
290. D. W. Shannon
291. J. C. Tobin
292. R. G. Wheeler
293. Technical Information File

FAST FLUX TEST FACILITY, Battelle-Northwest

294. E. R. Astley

BROOKHAVEN NATIONAL LABORATORY

295. D. H. Gurinsky
296. C. Klamut

BUREAU OF MINES

297. Haruo Kato, Albany Metallurgy Research Center, P. O. Box 70, Albany, Oregon 97321
298. T. Sullivan, Bureau of Mines, Boulder City, Nevada 89005

COMBUSTION ENGINEERING

299. W. P. Chernock
300. S. S. Christopher

GENERAL ELECTRIC, Cincinnati

301. D. H. Ahmann
302. H. C. Brassfield
303. V. P. Calkins
304. E. Hoffman
305. J. McGurty
306. J. Moteff

GENERAL ELECTRIC, Nuclear Systems Programs, Cincinnati

307. E. E. Hoffman

GENERAL ELECTRIC, San Jose

308. R. Duncan
309. H. Klepfer

GENERAL ELECTRIC, Pleasanton

310. H. W. Alter

GENERAL ELECTRIC, Sunnyvale

311. K. P. Cohen
312. F. Comprelli
313. R. Skavdahl
314. C. Spalaris
315. E. L. Zebroski

GULF GENERAL ATOMIC

316. D. B. Coburn
317. A. J. Goodjohn
318. J. P. Howe
319. S. Jaye
320. J. F. Watson

IDAHO NUCLEAR CORPORATION

321. W. C. Francis

ILLINOIS INSTITUTE OF TECHNOLOGY RESEARCH INSTITUTE

322. D. J. McPherson

JET PROPULSION LABORATORY (NASA)

323. J. Davis

KNOLLS ATOMIC POWER LABORATORY

324. R. F. Wojciescak
325. Document Library

LOS ALAMOS SCIENTIFIC LABORATORY

326. R. D. Baker
327. D. B. Hall
328. J. A. Leary
329. R. Perkins
330. R. E. Peterson
331. Reports Library

MOUND LABORATORY

332. R. G. Grove

NASA, LEWIS RESEARCH CENTER

333. M. Ault
334. J.W.R. Creagh
335. J. J. Lombardo
336. T. P. Moffitt
337. T. A. Moss
338. F. E. Rom
339. L. Rosenblum
340. N. D. Sanders
341. N. Saunders
342. C. M. Scheuermann
343. H. Schwartz

NAVAL RESEARCH LABORATORY

344. J. R. Hawthorne
345. C. Serpan
346. L. E. Steele

NORTH CAROLINA UNIVERSITY, Raleigh, North Carolina 27607

347. J. Beeler
348. R. E. Dahl

NUCLEAR MATERIALS AND EQUIPMENT CORPORATION

349. C. Caldwell
350. K. Puechl

OHIO STATE UNIVERSITY, Columbus, Ohio 43212

351. M. G. Fontana
352. R. W. Staehle

RENSSELAER POLYTECHNIC INSTITUTE

353. C. B. Willingham, Jr.

SANDIA CORPORATION

354. J. Read Holland
355. J. Jacobs
356. D. R. Johnson

SAVANNAH RIVER LABORATORY

357. P. H. Permar
358. S. P. Rideout

TRW SYSTEMS (NASA), Redondo Beach, California 90278

359. H. Lurie

UNION CARBIDE CORPORATION, New York

360. J. A. Swartout

UNION CARBIDE CORPORATION, Materials Systems Division, Indianapolis

361. C. F. Leitten, Jr.

UNITED NUCLEAR CORPORATION

362. A. Strasser

UNIVERSITY OF CALIFORNIA, Lawrence Radiation Laboratory, Livermore

363. W. R. Holman
364. J. S. Kane
365. L. W. Roberts
366. A. J. Rothman
367. B. Rubin

U.S. NAVAL AIR SYSTEM COMMAND (AIR-52031B)

368. T. Kearns
369. I. Machlin

USAEC Scientific Representative, American Embassy, Box 40 FPO, N. Y. 09510

370. W.L.R. Rice

WESTINGHOUSE, Advanced Reactor Division, Waltz Mill Site

371. E. C. Bishop
372. J.C.R. Kelly
373. P. J. Levine
374. P. Murray
375. W. E. Ray
376. G. A. Whitlow

WESTINGHOUSE, Astronuclear Laboratory

377. R. T. Begley
378. D. C. Goldberg

WESTINGHOUSE, Atomic Power Division

379. T. Stern

WESTINGHOUSE, Bettis

380. R. H. Fillnow
381. P. N. Gustafson
382. Westinghouse Bettis Laboratory Library

383–604. Given distribution as shown in TID-4500 under Metals, Ceramics, and Materials category (25 copies – CFSTI)